Thermodynamic Investigations on the Dimerization and Anti-Cooperative Self-Assembly of Dipolar Merocyanines

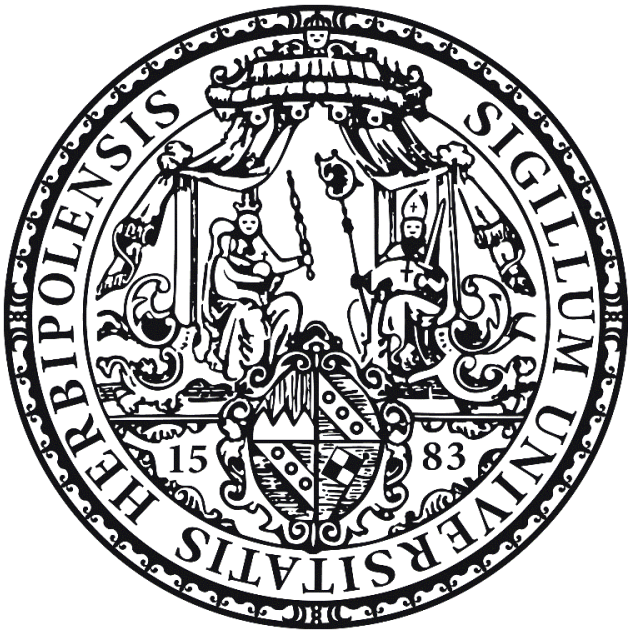

Dissertation zur Erlangung des

naturwissenschaftlichen Doktorgrades

der Julius-Maximilians-Universität Würzburg

vorgelegt von

Yvonne Wagenhäuser
(geb. Vonhausen)

aus Haßfurt

Würzburg 2024

Eingereicht bei der Fakultät für Chemie und Pharmazie am:

20.02.2024

Gutachter der schriftlichen Arbeit:

1. Gutachter: Prof. Dr. Frank Würthner

2. Gutachter: Prof. Dr. Claudia Höbartner

Prüfer des öffentlichen Promotionskolloquiums:

1. Prüfer: Prof. Dr. Frank Würthner

2. Prüfer: Prof. Dr. Claudia Höbartner

3. Prüfer: Dr. Merle Röhr

Datum des öffentlichen Promotionskolloquiums:

15.03.2024

Doktorurkunde ausgehändigt am:

_____

List of Abbreviations

1D	one dimensional
2D	two dimensional
a.u.	arbitrary units
AIEE	aggregation-induced emission enhancement
ATOP	amino-thienyl-dioxocyano-pyridine merocyanine
AFM	atomic force microscopy
CD	circular dichroism
COSY	correlation spectroscopy
CPL	circular polarized luminescence
CT	charge transfer
D	dimer
DCTB	*trans*-2-[3-(4-*tert*-butylphenyl)-2-methyl-2-propenylidene]malononitrile
DFT	density functional theory
DMF	dimethylformamide
DMSO	dimethyl sulfoxide
DNA	deoxyribonucleic acid
DOSY	diffusion ordered spectroscopy
DPFA	*N*,*N*'-diphenylformamidine
Dx	dioxane
ee	enantiomeric excess
EOAM	electrooptical absorption measurements
ESI	electron spray ionization
H	higher aggregate
HOPG	highly ordered pyrolytic graphite
HRMS	high-resolution mass spectrometry
ITC	isothermal titration calorimetry
M	monomer
MCH	methylcyclohexane
Mp	melting point
MeCN	acetonitrile
MeOH	methanol
MLR	multiple linear regression
NMR	nuclear magnetic resonance
NOESY	nuclear Overhauser effect spectroscopy
PCM	polarizable continuum model
PNA	peptide nucleic acid
ppm	parts per million
PYOP	pyridine dioxocyano-pyridine merocyanine
ROESY	rotating-frame Overhauser effect spectroscopy
rt	room temperature

S_0	electronic ground state
S_1	first electronic exited state
TD-DFT	time-dependent density functional theory
TOF	time of flight
UV/Vis	ultraviolet/visible
VPO	vapour pressure osmometry

Physical Variables and Constants

Å	ångström
Abs	absorbance
$Abs(\lambda)$	absorbance at a certain wavelength λ
α_{agg}	degree of aggregation
$\alpha_{agg}(\lambda)$	degree of aggregation calculated from experimental data at a certain wavelength λ
$\alpha_{agg\text{-}\pi}$	degree of aggregated π-surfaces
α_M	fraction of monomer
c_0	total molecular sample concentration
c_M	equilibrium monomer concentration
c_D	equilibrium dimer concentration
c_H	equilibrium higher aggregate concentration
CI	confidence interval
d	cuvette thickness
δ	chemical shift
$\Delta\varepsilon$	circular dichroism
ΔG	Gibbs energy
ΔG^0	standard molar Gibbs energy of binding
ΔG^0_{293}	standard molar Gibbs energy of binding at 293 K
$\Delta G^{0\prime}$	solvent-dependent standard molar Gibbs energy of binding
ΔH^0	standard molar binding enthalpy
$\Delta\tilde{\nu}_{Stokes}$	Stokes shift
ΔS^0	standard molar binding entropy
ε	molar extinction
$\varepsilon(\lambda)$	molar extinction at a certain wavelength λ
$\bar{\varepsilon}$	apparent molar extinction coefficient of mixture of species
ε_M	molar extinction coefficient of the chromophore as a monomer
ε_D	molar extinction coefficient of one chromophore within the dimer species
ε_H	molar extinction coefficient of one chromophore within a higher aggregate species
ε_r	static dielectric constant

f	volume fraction
Φ_{Fl}	fluorescence quantum yield
g_{lum}	emission dissymmetry factor
h	hours
Hz	Hertz
I	intensity of transmitted light
I_0	intensity of incident light
J_C	Coulomb coupling
K	equilibrium/binding/dimerization constant
K_{293}	equilibrium/binding/dimerization constant at 293 K
K_5	pentamerization constant
k_{ass}	association rate constant
K_D	dimerization constant
k_{diss}	dissociation rate constant
K_n	binding constant per binding site for n-mer formation
k_{nr}	non-radiative rate constant
k_r	radiative rate constant
λ	wavelength
λ_{ex}	excitation wavelength
λ_{em}	emission wavelength
m	linear factor describing the solvent-dependence of ΔG^0
M	molecular weight
mdeg	millidegree
MV	measurement value
$\tilde{\nu}$	wavenumber
μ_e	excited state dipole moment
μ_{eg}	transition dipole moment
μ_g	ground state dipole moment
$\rho(T)$	solvent density at a temperature T
R	universal gas constant (8.314 J $mol^{-1}K^{-1}$)
RS	residual sum of squares
S	sum of squares
SD	standard deviation
SE	standard error
σ	cooperativity factor
σ_X	uncertainty of parameter X
T	temperature
t	time
τ	fluorescence lifetime

Table of Contents

CHAPTER 1 – INTRODUCTION AND AIM OF THE THESIS 1

CHAPTER 2 – STATE OF KNOWLEDGE 7

2.1 Dimer Self-Assembly Model 7

2.1.1 Concentration-Dependent Data Evaluation 10

2.1.2 Temperature-Dependent Data Evaluation 15

2.1.3 Solvent-Dependent Data Evaluation 19

2.1.4 Fitting Data by Nonlinear Regression Analysis 21

2.1.5 Summary 30

2.2 PYOP Merocyanines as Supramolecular Building Blocks 32

2.2.1 Molecular and Dimer Properties 32

2.2.2 Functional Assemblies of the PYOP Chromophore Beyond the Dimer 39

2.2.3 Summary 47

CHAPTER 3 – CONCENTRATION-, TEMPERATURE-, AND SOLVENT-DEPENDENT SELF-ASSEMBLY: MEROCYANINE DIMERIZATION AS A SHOWCASE EXAMPLE FOR OBTAINING RELIABLE THERMODYNAMIC DATA 49

3.1 Introduction 50

3.2 Results and Discussion 53

3.2.1 Fit Functions 53

3.2.2 Concentration-Dependent Analysis 54

3.2.3 Temperature-Dependent Analysis 57

3.2.4 Solvent-Dependent Analysis 60

3.3 Conclusion 61

CHAPTER 4 – TWO-STEP ANTI-COOPERATIVE SELF-ASSEMBLY PROCESS INTO DEFINED π-STACKED DYE OLIGOMERS: INSIGHTS INTO AGGREGATION-INDUCED ENHANCED EMISSION 64

4.1 Introduction 65

4.2 Results and Discussion 68

4.2.1 Synthesis 68

4.2.2 UV/Vis Aggregation Studies 69
4.3.2 Investigation of the Aggregate Structures 78
4.2.4 Aggregation-Induced Emission Enhancement 87
4.2.5 Aggregation-Induced CPL Enhancement 91
4.3 Conclusion 92

CHAPTER 5 – SUMMARY AND CONCLUSION 94

CHAPTER 6 – ZUSAMMENFASSUNG UND FAZIT 101

CHAPTER 7 – APPENDIX 109

7.1 Appendix for Chapter 2 109
7.2 Appendix for Chapter 3 110
7.3 Appendix for Chapter 4 120

BIBLIOGRAPHY 144

INDIVIDUAL CONTRIBUTIONS 151

DANKSAGUNG 152

LIST OF PUBLICATIONS 154

CHAPTER 1

–

INTRODUCTION AND AIM OF THE THESIS

"Self-assembly is the autonomous organization of components into patterns or structures without human intervention."[1] In the field of supramolecular chemistry, "components" refers to molecular building blocks that enable distinct intermolecular interactions. The nature, directionality, and strength of these interactions can be controlled by modifying the chemical structure of these molecules, and chemists have become very skilled at these covalent modifications over the past century.[2] The assembling, however, the molecular building blocks will do by themselves. As illustrated by the awe-inspiring supramolecular systems found in nature,[3-4] it is often a fine balance of multiple weak interactions, which are, additionally, highly sensitive to the environment, that determine the thermodynamically most stable structure.[5-6] It is, therefore, not trivial to guide molecules into a desired supramolecular arrangement in solution or in the solid state. Only proper design of the molecules and the environment, based on a sound understanding of all thermodynamic (and also kinetic) parameters involved, will lead to the desired aggregate structure or solid-state material with the aspired properties. Then, self-assembly can be a very efficient bottom-up strategy which aims to place well defined building blocks at predefined locations and to achieve functionality beyond what is expected from the sum of the molecular entities. The self-assembly of dye molecules is of particular interest to supramolecular chemists, since electrical and optical functionalities often rely on extended π-conjugated systems.[7] Organic dye molecules find application in, e.g., display technology,[8] photovoltaics,[9-10] flexible materials[11-12] and sensors.[13] And for all of those applications, the device properties are strongly influenced by the packing and interactions of the functional molecules.[14]

Self-assembly under thermodynamic control can be described as chemical equilibria between monomer and aggregate species.[15-16] The equilibrium constant K is related to the thermodynamic parameters of the process: the binding enthalpy ΔH^0 and entropy ΔS^0, which are a measure of the interaction strength and changes in degrees of freedom of a system, respectively, and the Gibbs binding energy ΔG^0, which is the sum of these two contributions. The emerging aggregates can inherit a discrete oligomer size or form supramolecular polymers.

Various mathematical models are reported in literature to describe different types of self-assembly equilibria.[16-23] The most basic one is the dimerization (K_D) of a monomer, which is guided by self-complementary intermolecular interactions. But also models for larger defined-sized aggregates[24] or host-guest complexes[19] are reported. For polymeric assemblies, the simplest model is the isodesmic model,[16] which assumes every attachment of a monomer to the aggregate to have the same interaction strength, i.e., the binding constant K is equal for all association steps ($K_D = K$, Figure 1, black). For many supramolecular polymerizations, however, a difference is observed for the binding constants of the initial phase of assembly (nucleation, K_D for a dimer nucleus) and subsequent growth of the polymer (elongation, K).[18] In some cases, initially a less favoured nucleus has to be formed before highly favoured polymer growth can occur. This is called cooperative supramolecular polymerization ($K_D < K$, Figure 1, red).[22-23] Anti-cooperative self-assembly, on the other hand, is characterized by a preferred nucleus formation with a reduced tendency to further self-assemble into larger aggregate structures ($K_D > K$, Figure 1, blue).[25-26] The underlying self-assembly mechanism, which is already encoded in the individual building blocks, is tightly connected to the properties of the emerging aggregate species, like stability and size distribution.[22, 25] Figure 1 illustrates the differences that are to be expected for isodesmic, cooperative and anti-cooperative self-assembly.

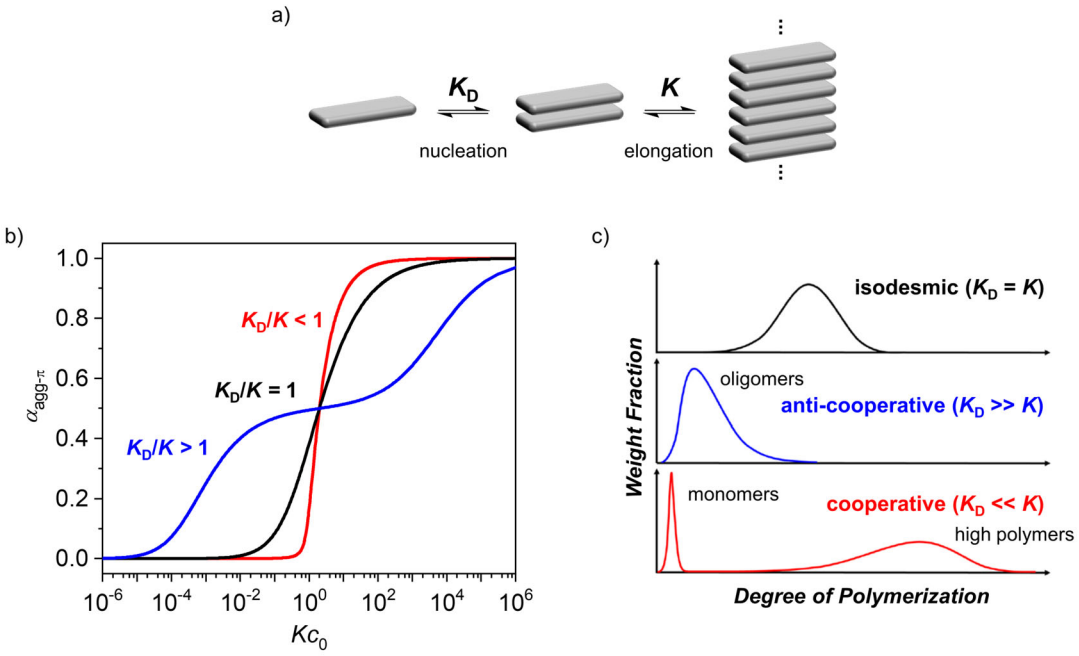

Figure 1. a) Simplified schematic representation of a self-assembly processes divided into nucleation (here dimer nucleus) and subsequent elongation, with the corresponding binding constants for nucleus formation (K_D) and polymer growth (K). b) Degree of aggregated π-surfaces ($\alpha_{agg-\pi}$) as a function of the normalized concentration Kc_0 for an anti-cooperative (blue, $K_D/K = 1000$), isodesmic (black, $K_D = K$) and cooperative (red, $K_D/K = 0.01$) self-assembly. At $\alpha_{agg-\pi} = 0.5$, predominantly dimers are present (two free and two bound π-surfaces). Based on ref. [16]. c) Qualitative length distribution (indicated by the degree of polymerization) of supramolecular polymers formed by different self-assembly mechanisms. Reprinted with permission from ref. [25]. Copyright 2018 American Chemical Society.

For isodesmic self-assembly of planar π-conjugated molecules, the degree of aggregated π-surfaces ($\alpha_{agg\text{-}\pi}$) shows a sigmoidal increase as a function of the total sample concentration c_0. For cooperative self-assembly, a characteristic critical concentration can be observed at which nucleation occurs and $\alpha_{agg\text{-}\pi}$, representing polymerization, starts to increase rapidly. The size distribution is characterized by a broad variety of extended polymers, but also a certain number of remaining monomers. For anti-cooperative self-assembly, a plateau can be observed in the graph of $\alpha_{agg\text{-}\pi}$ in Figure 1b, where within a certain concentration range predominantly the nucleus is present, in this case a dimer nucleus with $\alpha_{agg\text{-}\pi} = 0.5$. The polymers formed upon further increasing the concentration are usually shorter, with a narrower size distribution, than for a comparable isodesmic or cooperative assemblies. Cooperative supramolecular polymerization is intensely investigated for several classes of materials. Polymer growth from a relatively small number of nuclei leads to the formation of very long and stable supramolecular polymer fibers which have raised interest as functional materials in a variety of fields.[18, 27-29] The anti-cooperative self-assembly, on the other hand, has been much less investigated,[25-26, 30-38] although, it also has clear benefits for the design of interesting self-assembly structures. It can help to gain control over the formation of smaller, more defined aggregates compared to isodesmic or cooperative self-assembly. This can be advantageous for the processing of functional materials. Often the desired functionality, e.g. photophysical properties, can already be obtained from rather small sized assemblies.[24] For applications, e.g., in organic bulk heterojunction solar cells the cooperative formation of long extended aggregates during solution processing can be problematic. In mixed systems it often leads to unfavorable phase separation instead of homogeneous thin films, which significantly lowers the efficiency of the device. Furthermore, a hierarchical aggregation mechanism with firstly a nucleus formation and secondly the self-assembly of these nuclei, opens up new strategies for the stepwise construction of complex supramolecular architectures from small molecules.[30, 38] However, special molecular features are needed to induce preferred nucleus over extended polymer formation, but still allow for further self-assembly of the nuclei. This precondition is clearly met by the molecule class studied in this thesis: the dipolar merocyanines dyes (Figure 2). These light-weight molecules are interesting from a functional perspective because of their intense and often narrow charge-transfer (CT) UV/Vis absorption, which is highly sensitive to the environment. Additionally, they are also exciting as supramolecular building blocks due to their significant zwitterionic character and the resulting exceptional dipolarity (Figure 2a). Strong and directional dipole-dipole interactions between the chromophores lead to structurally defined dimers as a

supramolecular binding motif, similar to the extensively used complementary H-bonds. Due to the anti-parallel arrangement of the chromophores, the dipolarity of this dimer is significantly reduced. Further assembly can only occur through weaker dispersion interactions between the accessible π-surfaces (Figure 2c).

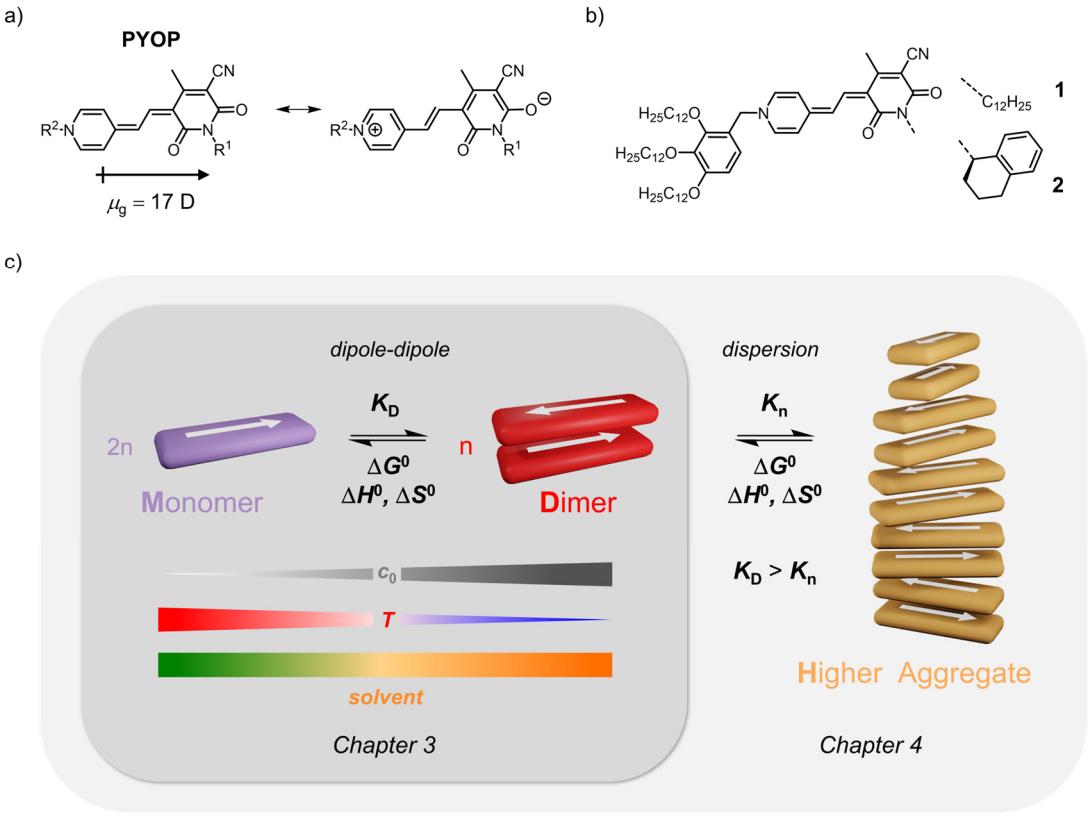

Figure 2. a) Chemical structure of the highly dipolar pyridine dioxocyano-pyridine (PYOP) merocyanine chromophore with its zwitterionic resonance structure. b) Chemical structure of merocyanines **1** and **2**, whose self-assembly is investigated in *Chapter 3* and *Chapter 4* of this thesis, respectively. c) Schematic illustration of the anti-cooperative self-assembly equilibria of merocyanine monomers (M) into an antiparallel aligned dimer nucleus (D) by dipole-dipole interactions followed by formation of a π-stacked higher aggregate (H) by dispersion interactions.

Yet, the formation of such higher merocyanine aggregates by anti-cooperative self-assembly in solution has not been explored so far. This may be due to the fact that the self-assembly of dipolar chromophores is most favoured in non-polar solvents, where the solubility of these polar molecules is typically low. Especially for anti-cooperative self-assembly, however, a large concentration range is needed to capture the entire two-step process (Figure 1b). Larger merocyanine assemblies could so far only be obtained by covalent linking of multiple chromophores into preorganized tweezers[24, 39] or flexible foldamers.[40-41]

To characterize supramolecular merocyanine systems with regard to stability (thermodynamic parameters) and the self-assembly mechanism, concentration-dependent aggregation studies by UV/Vis absorption spectroscopy so far constitute the preferred method.[42] In some cases, however, the accessible concentration range is limited by the solubility or availability of the

material or a concentration-dependent approach cannot be applied since, e.g. a folding process[43] is to be observed. Here, temperature[33-34, 36, 44-50] or solvent-dependent[51-55] studies can be alternatives, which have both successfully been applied in literature for a variety of systems. Both methods are, however, based on a series of additional assumptions, compared to the straightforward concentration-dependent evaluation of a supramolecular equilibrium, which call into question the accuracy of the derived thermodynamic parameters. The defined, and by our group well investigated,[42] merocyanine dimer formation of PYOP (PYridine diOxocyano-Pyridine) chromophore **1** (Figure 2b) is an excellent model system to have a closer look at these fundamental aspects of self-assembly studies, with regard to methodology and accuracy (*Chapter 2* and *Chapter 3*). This is an important basis for the investigation of more complex supramolecular systems (*Chapter 4*).

The aim of this thesis is, therefore, to investigate the applicability and limitations of concentration-, temperature-, and solvent-dependent aggregation studies by UV/Vis absorption spectroscopy, using the simple merocyanine dimer as a model system. The insights gained hereby will be used to elucidate the previously unreported anti-cooperative self-assembly of a highly soluble merocyanine derivative, including the structural characterization of the extended aggregate and investigation of its optical properties.

Chapter 2 is divided into two parts. In the first part, important theoretical aspects and the mathematical models for the thermodynamic evaluation of self-assembly equilibria by UV/Vis absorption spectroscopy are discussed. For the most simple example of a monomer-dimer equilibrium, the theoretical models for a concentration-, temperature- or solvent-dependent analysis are derived, and the advantages and disadvantages of the methods are addressed. Additionally, a subchapter is devoted to the theory of nonlinear regression analysis, the method of choice for fitting experimental data to a theoretical model, and a discussion on the accuracy of the obtained parameters is included. In the second part, PYOP merocyanines are introduced as dipolar supramolecular building blocks for self-assembled dye aggregates. Important molecular properties and the resulting functional properties of the chromophore and its assemblies are summarized, and an overview is given of the different aggregate structures that have previously been obtained for this dipolar dye.

In *Chapter 3*, the dimerization of PYOP merocyanine **1** serves as a simple model system to demonstrate advantages and possible sources of error for concentration-, temperature-, and

solvent-dependent self-assembly studies by UV/Vis absorption spectroscopy. Extensive datasets are presented, that allow a direct comparison of the results from these different methods.

In *Chapter 4* the anti-cooperative self-assembly of a chiral merocyanine **2** into an extended higher aggregate *via* an initially preferred dimer nucleus, was investigated. This was possible because of the exceptionally high solubility of the PYOP derivative **2** in unpolar solvents like methylcyclohexane (MCH). A variety of experimental techniques were applied to elucidate the self-assembly mechanism, including the corresponding thermodynamic parameters, as well as the aggregate structures. Aggregation-induced emission enhancement (AIEE) was observed for the higher aggregate species, accompanied by an enhancement in circularly polarized light (CPL) emission.

Chapter 5 and *Chapter 6* summarize and conclude the thesis in English and German, respectively.

Chapter 7 provides additional experimental and theoretical data for *Chapter 2*, *Chapter 3*, and *Chapter 4*. This includes the specifications on the methods and materials.

CHAPTER 2

–

STATE OF KNOWLEDGE

2.1 Dimer Self-Assembly Model[i]

Self-assembly under thermodynamic control can be described as an equilibrium between monomer and aggregate species. The most fundamental model is the self-assembly of two identical monomeric molecules (M) into a dimer (D). This two-state equilibrium can be written as:

$$2\,M \rightleftharpoons D. \qquad (1)$$

The design of structurally defined dimers is not trivial.[57] Covalent linking[58-60] or binding of two molecules in a confined cavity[61] can be tools to obtain defined dimer structures, however, there are also molecules with an inherent tendency to dimerize due to self-complementary interactions (Figure 3).

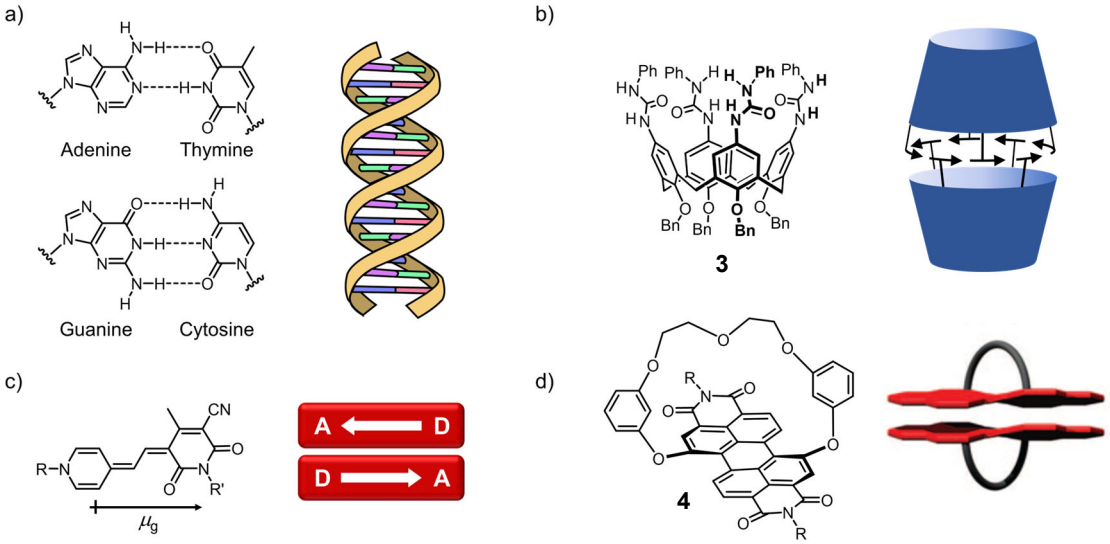

Figure 3. Examples of natural (a) and artificial (b, c, d) systems forming self-assembled dimers: a) Complementary H-bonding of oligonucleotide duplex,[62] b) self-complementary calix[4]arene **3** forming a dimer capsule by H-bonding between urea units (indicated by black arrows),[63] c) dipole-dipole interactions of merocyanine dyes, c) π-stacking of perylene bisimide **4** with sterical shielding. Reprinted with permission from ref. [64]. Copyright 2010 WILEY-VCH Verlag GmbH & Co. KGaA, Weinheim.

[i] Excerpts of this Chapter 2.1 have been published in ref. [56] Y. Vonhausen, F. Würthner, *Chem. Eur. J.* **2023**, *29*, e202300359. Adapted with permission. Copyright 2023 The Authors. Chemistry – A European Journal published by Wily VCH GmbH.

For a DNA double strand – probably the most prominent example of a supramolecular dimer – the complementary hydrogen bonding motifs of the nucleobases direct the assembly into a duplex structure (Figure 3a). The thermodynamic evaluation of melting curves of oligonucleotide double strands, according to the dimer model, is a standard technique in the field of nucleic acid chemistry to determine the stability of their secondary structure.[65]

The directionality and thermodynamic stability of complementary hydrogen bonds are also employed in many artificial supramolecular systems to achieve defined structures, like the calix[4]arene **3** dimer capsules of Rebek and co-workers (Figure 3b).[63] For merocyanines, the preferred anti-parallel dimer formation is based in the strong intermolecular dipole-dipole interactions (Figure 3c).[66] The dimerization is here the nucleation step of a highly anti-cooperative self-assembly mechanism as discussed in *Chapter 4* of this thesis. For large aromatic molecules, which tend to form extended stacks due to rather weak dispersion/π-π-interactions, the aggregation can be limited to a dimer by sterical crowding[67] or shielding of one π-surface as exemplarily shown for a bay-bridged perylene bisimide (PBI) **4** by Safont-Sempere *et al.*[64] in Figure 3d.

Geometrically defined dimers of various classes of molecules are extensively studied model systems to investigate structure-property relationships. Functional materials are usually not isolated molecules in dilute solution or in the gas phase but, e.g., gels, crystalline solids or embedded into a matrix. Therefore, their properties can no longer be explained by the covalent framework of the molecular building blocks alone but are strongly influenced by the interactions with surrounding molecules.[14] Understanding these interactions and their influence on the physical properties is fundamental for a rational design of functional materials for a specific application. Dimeric structures are an excellent starting point to unravel this complex interplay of molecular interactions and coupling between molecules in close proximity. Compared to polymeric or solid samples a small system like a dimer in solution can be more easily characterized by a wider choice of experimental techniques and theory.[68] Important insights were gained, for example, on the interplay of exciton and vibrational coupling that determine the absorption properties,[14] excited state dynamics[59, 69] including excimer formation,[70] symmetry-breaking charge separation and singlet fission,[71] or charge transport abilities.[72] Also in this *Chapter 2* and the following *Chapter 3* the monomer-dimer equilibrium will serve as a model system. The insights gained hereby are, however, not limited to the dimer example but can also be transferred to other systems that are based on other equilibrium situations, like isodesmic,[16] cooperative[22] or host-guest[19] assemblies.

Supramolecular equilibria can be shifted by different factors, e.g., the total concentration of molecules c_0, the temperature T or the solvent. Increasing the total sample concentration c_0 generally leads to assembly. Interestingly, however, for multi-component systems with competing interactions, assembly can also be induced by dilution, as shown by Meijer and co-workers[73] in a rather special example. For most supramolecular systems in organic solvents, a decrease in temperature favours assembly, since the process is usually enthalpically driven (attractive interactions between the molecules) but entropically disfavoured (loss of translational degrees of freedom upon assembly). At lower temperatures this entropy penalty becomes less significant. However, the opposite can happen to be the case, if the assembly is not enthalpically but entropically driven (e.g., liberation of solvent molecules from the solvent shell upon assembly). Especially in water, where specific solute-solvent interactions are possible, this can be of major importance.[74-75] The influence of the solvent on the equilibrium is determined by the ability of the solvent to interact with the monomer and aggregate species.[76] Solvents that interact well with the monomeric species, meaning better than the monomers with each other, can serve as "denaturation agents" for supramolecular assemblies.

By evaluating how strongly these factors influence the self-assembly equilibrium, thermodynamic parameters like the molar standard Gibbs binding energy ΔG^0 as well as the binding enthalpy ΔH^0 and entropy ΔS^0 can be determined. The shifting of the equilibrium (assembly/disassembly process) can be monitored by a variety of experimental methods, where the detected signal is proportional to the concentrations of the individual species. In this work, UV/Vis absorption spectroscopy is the method of choice as strongly absorbing merocyanine dyes with large transition dipole moments (μ_{eg}) and pronounced spectral changes upon aggregation due to exciton coupling are investigated. However, the basic principles behind the data evaluation can also be applied to datasets collected by a variety of other techniques, like fluorescence spectroscopy, nuclear magnetic resonance (NMR) or isothermal titration calorimetry (ITC).[15] The changes of an experimental observable (e.g., absorbance at a certain wavelength, shift of ^{1}H NMR signal, heat signal from ITC, …) are monitored as a function of an external influence (Figure 4, black squares). Additionally, a mathematical model (fit function) is needed, which describes the self-assembly process (changes in the observable) as a function of the external influence and the thermodynamic parameters. A fitting routine (least square regression analysis) can then be used to optimize the values for these parameters to best fit the experimental data (Figure 4, red line).[77-80]

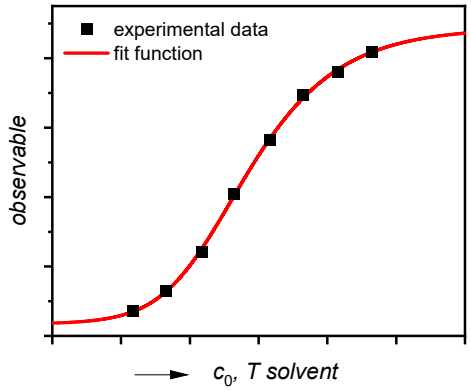

Figure 4. Schematic representation of experimental self-assembly data (black squares) and the corresponding fit function (red line) to determine thermodynamic parameters.

The derivation and application of these mathematical models is the subject of this *Chapter 2.1*. It focuses on the example of dimerization but also aims to provide guidance for the investigation of other systems.

2.1.1 Concentration-Dependent Data Evaluation

The concentration-dependent data evaluation it the most straightforward method to analyse a supramolecular equilibrium, as no additional assumptions besides mass action and mass balance law are required. The basis for the mathematical model is the self-assembly equilibrium. It defines the equilibrium constant K by the equilibrium activities of the monomer and aggregate species. However, since the activity coefficients are generally not known, the equilibrium constant defined by the equilibrium concentrations is usually employed, based on the approximation that the activity coefficients are constant under the applied conditions, in particular at the low concentrations applied for UV/Vis spectroscopy.[81] For the two-state equilibrium for dimerization, see equation (1), the mass action law applies to give:

$$c_{\mathrm{D}} \cdot k_{\mathrm{diss}} = {c_{\mathrm{M}}}^2 \cdot k_{\mathrm{ass}}, \tag{2}$$

$$K = \frac{k_{\mathrm{ass}}}{k_{\mathrm{diss}}} = \frac{c_{\mathrm{D}}}{{c_{\mathrm{M}}}^2}, \tag{3}$$

with k_{ass} and k_{diss} as the association and dissociation rate constants and c_{M} and c_{D} as the equilibrium concentration of the monomer (M) and dimer (D) species, respectively. For self-assembly equilibria, K is usually called binding constant, or in this case more specifically dimerization constant. The earliest mathematical descriptions of such monomer-dimer equilibria date back to the 1970s.[16-17, 82-84]

In thermodynamic equilibrium the Gibbs energy of the association/dissociation process is $\Delta G = 0$. Therefore, K is connected to the standard molar Gibbs energy of binding ΔG^0 by equations (4) and (5):

$$\Delta G = \Delta G^0 + RT \ln K = 0, \tag{4}$$

$$\Delta G^0 = -RT \ln K. \tag{5}$$

Here R is the universal gas constant and T the temperature. ΔG^0 applies, as indicated by the superscript "0", to the Gibbs binding energy under standard conditions, namely 1 M concentration of all components.

The equilibrium concentrations of the different species are related to the total sample concentration c_0 by the mass balance equation (6):

$$c_0 = c_\mathrm{M} + 2\, c_\mathrm{D}. \tag{6}$$

This equation takes into account that the dimer consists of two molecules. Equations (3) and (6) can be used to express the equilibrium concentration of the species c_M and c_D as a function of c_0 and K in equation (11).

$$c_\mathrm{D} = \frac{1}{2}(c_0 - c_\mathrm{M}), \tag{7}$$

$$K = \frac{\frac{1}{2}(c_0 - c_\mathrm{M})}{{c_\mathrm{M}}^2}, \tag{8}$$

$$2K{c_\mathrm{M}}^2 = c_0 - c_\mathrm{M} \;\rightarrow\; 0 = -2K{c_\mathrm{M}}^2 - c_\mathrm{M} + c_0, \tag{9}$$

$$c_\mathrm{M} = \frac{1 \pm \sqrt{1 - 4 \cdot (-2K) \cdot c_0}}{2 \cdot (-2K)}. \tag{10}$$

Only one solution of the quadratic formula (10) is physically meaningful as c_M must not assume negative values:

$$c_\mathrm{M} = \frac{-1 + \sqrt{1 + 8K \cdot c_0}}{4K}. \tag{11}$$

For other equilibrium situations the equivalent equations to (8) are not always easy to solve analytically and approximations or implicit curve fitting is needed. For UV/Vis absorption studies, the experimental observable, that is linearly dependent on the concentrations c_M and c_D, is the absorbance $Abs(\lambda)$ at a certain wavelength λ. Absorbance is defined as the decadic

logarithm of the fraction of the intensity I_0 of the incident light divided by the intensity I of the light transmitted through a sample:

$$Abs(\lambda) = \log_{10}\left(\frac{I_0}{I}\right) = \varepsilon(\lambda) \cdot c_0 \cdot d. \quad (12)$$

Instead of absorbance, however, often the molar decadic extinction coefficient $\varepsilon(\lambda)$ is plotted and evaluated that – similar to the chemical shift δ in NMR experiments – is independent of the experimental parameters of concentration c_0 and sample/cuvette thickness d. According to the Lambert-Beer law, the absorbance of an isotropic mixture of species is the sum of the contributions of the individual species, in the present case, the monomer (Abs_M) and the dimer (Abs_D):

$$Abs(\lambda) = Abs_M(\lambda) + Abs_D(\lambda), \quad (13)$$

$$\bar{\varepsilon}(\lambda) \cdot c_0 \cdot d = \varepsilon_M(\lambda) \cdot c_M \cdot d + \varepsilon_D(\lambda) \cdot 2c_D \cdot d. \quad (14)$$

Note, that ε_M and ε_D in equation (14) are both defined as the molar extinction coefficients for a single chromophore, either as a monomer or within the dimer species, respectively. This is because the extinction spectra are calculated from the absorption spectra with the concentration c_0, which represents the total molecular sample concentration. Therefore, the concentration of dimers c_D is accompanied by a factor "2" in the Lambert-Beer-law and the term "apparent" extinction coefficient $\bar{\varepsilon}$ is used in this thesis for samples with a mixture of different aggregate species to point this out. With the help of equations (6), (11) and (14) we can now also give an expression for $\bar{\varepsilon}$ as a function of the total sample concentration c_0 and K. With a constant cuvette thickness d, we can simplify and rearrange to give equation (18):

$$\bar{\varepsilon}(\lambda) \cdot c_0 = \varepsilon_M(\lambda) \cdot c_M + \varepsilon_D(\lambda) \cdot 2c_D, \quad (15)$$

$$\bar{\varepsilon}(\lambda) = \frac{1}{c_0}\left(\varepsilon_M(\lambda) \cdot c_M + \varepsilon_D(\lambda) \cdot (c_0 - c_M)\right), \quad (16)$$

$$\bar{\varepsilon}(\lambda) = \varepsilon_D(\lambda) + \left(\varepsilon_M(\lambda) - \varepsilon_D(\lambda)\right)\frac{c_M}{c_0}, \quad (17)$$

$$\bar{\varepsilon}(\lambda) = \varepsilon_D(\lambda) + \left(\varepsilon_M(\lambda) - \varepsilon_D(\lambda)\right)\frac{-1+\sqrt{1+8K \cdot c_0}}{4K c_0}. \quad (18)$$

Equation (18) is the general fit equation for the thermodynamic evaluation of the monomer-dimer equilibrium (1) by UV/Vis absorption spectroscopy. In the concentration-dependent evaluation the parameters ε_D, ε_M, and K are determined. Figure 5a illustrates how these

parameters influence the shape of the self-assembly curve: ε_D and ε_M are the limit values to which the function approaches. K shifts the curve from left to right and the turning point of the sigmoidal curve lies at K^{-1}.

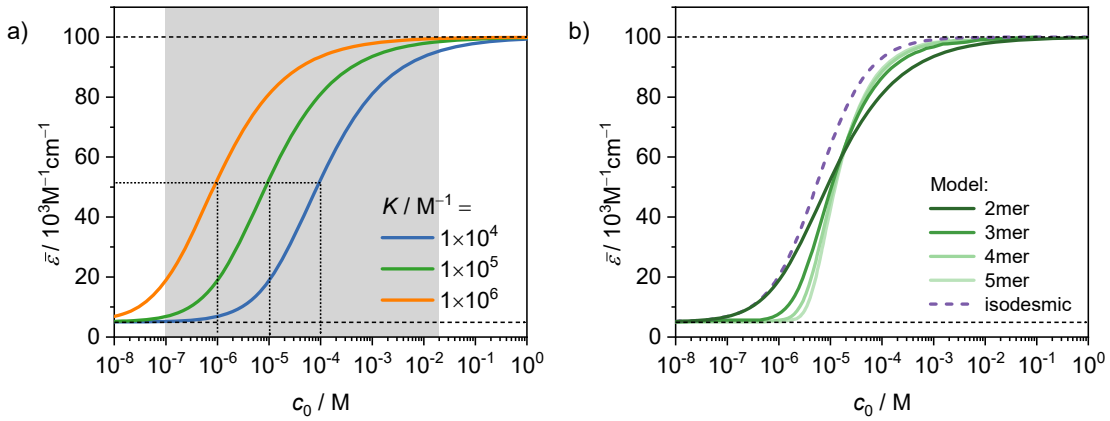

Figure 5. Simulated concentration-dependent self-assembly curves: a) For dimerization according to equation (18) for varying values of K with ε_M = 5 000 M^{-1}cm^{-1}, ε_D = 100 000 M^{-1}cm^{-1}. Grey area marks the accessible concentration range with cuvettes of 0.01mm < d < 100 mm for a standard UV/Vis spectrometer. b) For defined acyclic n-mer formation (solid lines) or isodesmic self-assembly (dashed line), according to equations (68) and (65) in the appendix, with K_n = 1×10^5 M^{-1}, ε_M = 5 000 M^{-1}cm^{-1}, ε_D = 100 000 M^{-1}cm^{-1}.

For concentration-dependent data, the shape of the curve is solely determined by the nature of the self-assembly equilibrium. Therefore, reasonable conclusions can be drawn about the self-assembly mechanism of an unknown system, depending on which model describes the experimental data best (Figure 5b).

When the extinction coefficients of the pure monomer (ε_M) and dimer (ε_D) under the applied experimental conditions are known, also the degree of aggregation α_{agg} can be evaluated instead of $\bar{\varepsilon}$. It describes the fraction of molecules incorporated into the aggregate species and is defined for this dimer case as:

$$\alpha_{agg} = \frac{2c_D}{c_0} = 1 - \frac{c_M}{c_0}. \qquad (19)$$

In the case of UV/Vis absorption spectroscopy, α_{agg} can be calculated from the apparent extinction coefficient $\bar{\varepsilon}(\lambda)$ at a certain wavelength λ with the extinction coefficients of one molecule as a monomer $\varepsilon_M(\lambda)$ or within a dimer $\varepsilon_D(\lambda)$ at this wavelength according to:

$$\alpha_{agg}(\lambda) = \frac{\bar{\varepsilon}(\lambda) - \varepsilon_M(\lambda)}{\varepsilon_D(\lambda) - \varepsilon_M(\lambda)}. \qquad (20)$$

Equation (20) can be derived directly from the Lambert-Beer law (14). With some rearrangement, we obtain equation (25), which proves that equation (19) and (20) are equivalent.

$$\bar{\varepsilon}(\lambda) \cdot c_0 = \varepsilon_{\mathrm{M}}(\lambda) \cdot (c_0 - 2c_{\mathrm{D}}) + \varepsilon_{\mathrm{D}}(\lambda) \cdot 2c_{\mathrm{D}}, \quad (21)$$

$$\bar{\varepsilon}(\lambda) \cdot c_0 = \varepsilon_{\mathrm{M}}(\lambda) \cdot c_0 - \varepsilon_{\mathrm{M}}(\lambda)\, 2c_{\mathrm{D}} + \varepsilon_{\mathrm{D}}(\lambda) \cdot 2c_{\mathrm{D}}, \quad (22)$$

$$\bar{\varepsilon}(\lambda) = \varepsilon_{\mathrm{M}}(\lambda) - \varepsilon_{\mathrm{M}}(\lambda)\, \frac{2c_{\mathrm{D}}}{c_0} + \varepsilon_{\mathrm{D}}(\lambda) \cdot \frac{2c_{\mathrm{D}}}{c_0}, \quad (23)$$

$$\bar{\varepsilon}(\lambda) - \varepsilon_{\mathrm{M}}(\lambda) = \frac{2c_{\mathrm{D}}}{c_0}\left(\varepsilon_{\mathrm{D}}(\lambda) - \varepsilon_{\mathrm{M}}(\lambda)\right), \quad (24)$$

$$\frac{\bar{\varepsilon}(\lambda) - \varepsilon_{\mathrm{M}}(\lambda)}{\varepsilon_{\mathrm{D}}(\lambda) - \varepsilon_{\mathrm{M}}(\lambda)} = \frac{2c_{\mathrm{D}}}{c_0} = \alpha_{\mathrm{agg}}(\lambda). \quad (25)$$

To evaluate the degree of aggregation α_{agg} instead of $\bar{\varepsilon}$ for a monomer-dimer equilibrium like (1) the fit equation (26) can be used:

$$\alpha_{\mathrm{agg}} = 1 - \frac{-1 + \sqrt{1 + 8K \cdot c_0}}{4Kc_0}. \quad (26)$$

Calculating $\alpha_{\mathrm{agg}}(\lambda)$ and fitting with equation (26) is only possible if ε_{M} and ε_{D} are known or can be estimated with appropriate accuracy for the system of interest. Unfortunately, this is often not the case when only a part of the self-assembly process can be monitored by the method of choice. When applying equation (18), ε_{M} and ε_{D} are additional parameters which are optimized by the fitting algorithm. Here, it is important to check whether the resultant values are in a reasonable range, e.g. $\varepsilon_{\mathrm{M/D}} \geq 0$, and appropriate boundaries should be set for the optimization of ε_{M} and ε_{D}.

The fit function (18) is applied to concentration-dependent UV/Vis absorption data of samples with a defined solvent and temperature. To gain information on the binding enthalpy (ΔH^0) and entropy (ΔS^0) contribution, the concentration-dependent measurements must be performed at different temperatures. With the values for the binding constants $K(T)$ at different temperatures T and the Gibbs-Helmholtz equation (27), the parameters ΔH^0 and ΔS^0 can be obtained by fitting K as a function of T according to equation (28):

$$\Delta G^0 = \Delta H^0 - T\Delta S^0, \quad (27)$$

$$K(T) = e^{\frac{-\Delta G^0}{RT}} = e^{\frac{-(\Delta H^0 - T\Delta S^0)}{RT}}. \quad (28)$$

Commonly, a linearized version of equation (28) is used to determine ΔH^0 and ΔS^0 from the binding constants $K(T)$ at different temperatures, i.e. the van't Hoff equation (29):

$$\ln K = -\frac{\Delta H^0}{R}\frac{1}{T} + \frac{\Delta S^0}{R}. \quad (29)$$

The values for ln$K$ as a function of T^{-1} are fitted with a linear function and ΔH^0 and ΔS^0 can be determined from the slope and intercept, respectively. A so called van't Hoff plot is useful to verify the assumption of temperature-independent ΔH^0 and ΔS^0. If ln$K$ does not change linearly with T^{-1} this assumption is wrong[75, 85] and alternative evaluation methods, which consider the heat capacity changes[86] can be found in literature.

2.1.2 Temperature-Dependent Data Evaluation

The temperature-dependent analysis has the advantage, that all thermodynamic parameters can be obtained in a single automated measurement. It is, therefore, the undisputed method of choice in the field of nucleic acid chemistry, where only very small sample amounts are available.[65, 87]

When monitoring dimerization by temperature-dependent UV/Vis absorption measurements equation (18), as derived above, still applies.

$$\bar{\varepsilon}(\lambda) = \varepsilon_{\mathrm{D}}(\lambda) + \left(\varepsilon_{\mathrm{M}}(\lambda) - \varepsilon_{\mathrm{D}}(\lambda)\right)\frac{-1+\sqrt{1+8K\cdot c_0}}{4Kc_0}. \quad (18)$$

However, the binding constant K now changes with temperature while the concentration c_0 is fixed. A straightforward way to evaluate the data is to describe the temperature-dependence of K by equation (28) with the help of the binding enthalpy ΔH^0 and entropy ΔS^0, if they can be assumed to be temperature-independent (*vide supra*).[65] This leads to equation (30), describing the temperature-dependent dimerization process:

$$\bar{\varepsilon}(\lambda) = \varepsilon_{\mathrm{D}}(\lambda) + \left(\varepsilon_{\mathrm{M}}(\lambda) - \varepsilon_{\mathrm{D}}(\lambda)\right)\frac{-1+\sqrt{1+8\,e^{-(\Delta H^0 - T\Delta S^0)/RT}\cdot c_0}}{4\,e^{-(\Delta H^0 - T\Delta S^0)/RT}\cdot c_0}. \quad (30)$$

Now, the parameters ΔH^0, ΔS^0, ε_{M} and ε_{D} are optimized by the nonlinear fitting algorithm and their influence on the self-assembly curve is illustrated in Figure 6. An increase or decrease of ΔH^0 mainly shifts the curve to higher or lower temperatures but also has a minor influence on the slope of the curve (Figure 6a). A larger entropy (ΔS^0) contribution, meaning, e.g., a larger entropy penalty upon assembly, makes the process "more sensitive" to temperature changes and leads to a steeper curve (Figure 6b).

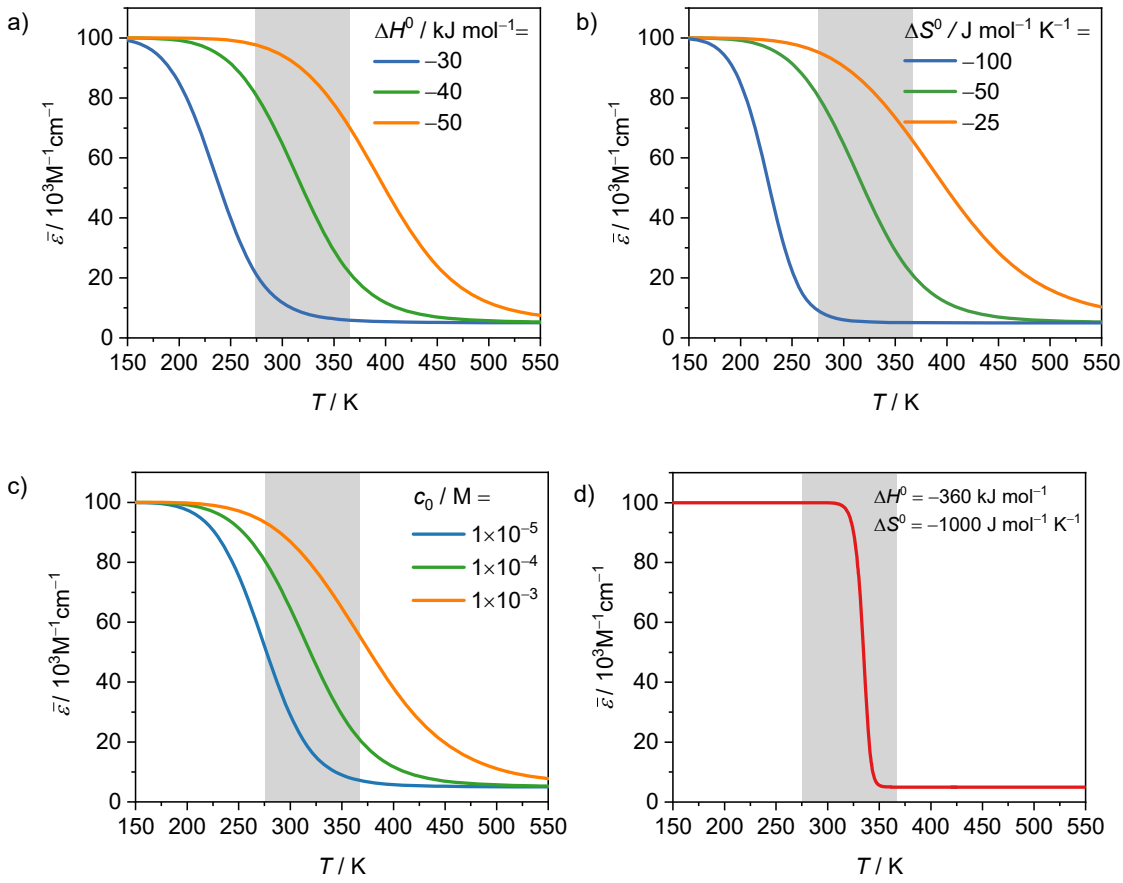

Figure 6. Simulated temperature-dependent dimer self-assembly curves for varying values of a) ΔH^0, b) ΔS^0 and c) c_0. The green curves are identical in graphs a-c. d) Exemplary values for ΔH^0 and ΔS^0 for a oligonucleotide duplex from ref. [87]. Unless stated otherwise: $\varepsilon_M = 5\,000\ M^{-1}cm^{-1}$, $\varepsilon_D = 100\,000\ M^{-1}cm^{-1}$, $\Delta H^0 = -40\ kJ\ mol^{-1}$, $\Delta S^0 = -50\ J\ mol^{-1}K^{-1}$, $c_0 = 1\times10^{-4}$ M. Marked in grey is the accessible temperature range of a standard UV/Vis spectrometer (278 – 368 K).

As evident from Figure 6, both parameters ΔH^0 and ΔS^0 can influence the shape of the curve in a similar way, thus in nonlinear regression analysis these parameters are somewhat redundant and a change in one parameter can to some degree be compensated by a change in the other (more details in section 2.1.4). Additionally, the predefined sample concentration influences the assembly curve. Decreasing c_0 increases the slope of the self-assembly curve and disassembly occurs already at lower temperatures (Figure 6c). Therefore, an adjustment of the sample concentration offers a possibility to overcome one of the disadvantages of temperature-dependent self-assembly studies, which is the (often) narrow experimentally accessible temperature range as indicated by the grey shaded area in the graphs in Figure 6. Especially for dimerization, which has a rather shallow self-assembly curve compared to other assembly models (see Figure 5b), often only a small fraction of the assembly process can be monitored by this method. There is, however, an option to fit the data of multiple samples with different concentrations (c_0) simultaneously with shared parameters (ΔH^0, ΔS^0, ε_M, ε_D) and, in this way, to cover the entire self-assembly process. Figure 6d illustrates why the

limited temperature range is less of a problem for the analysis of oligonucleotide duplexes. Both, enthalpy and entropy contribution are significantly larger in these systems than for small organic molecules.[87] This leads to a much steeper assembly curve, i.e., a transition from duplex to monomer within a narrow temperature range.

Here again, ε_M and ε_D represent the extinction coefficients of the pure monomer and dimer species which are, notably, also assumed to be temperature-independent. This is often not true, as also discussed later in Chapter 2.2.1. Temperature changes can influence the shape and position of the UV/Vis absorption band of a species (thermochromism) because of broader structural variations at higher temperature (Boltzmann distribution) and because of the temperature-dependence of solvent properties like the static dielectric constant and refractive index, which determine the interaction of the solvent with the ground and electronically excited states of a chromophore.[88] This will lead to (usually small) changes in the position and shape of the absorption band upon heating or cooling, also observed for the PYOP chromophore investigated in this thesis (see Figure 29 and Figure A59). For some chromophores, e.g., spiropyrans, even a temperature-dependent equilibrium of different molecular species exists.[89-90] In this case changes in temperature influence the chemical nature of the absorbing species and are accompanied by pronounced spectral changes upon heating or cooling. There is no easy way to accurately consider this temperature-dependence of the UV/Vis absorption spectrum of a species in a general way within the self-assembly model since the exact terms which describe the changes of $\varepsilon_M(T)$ and $\varepsilon_D(T)$ are not known. Thus, the system and collected data should be assessed carefully (as shown in *Chapter 3*) to decide whether this effect is negligible with regard to the accuracy of the derived parameters or not.

The total sample concentration c_0 can be treated to be constant as an approximation. However, c_0 is actually also temperature-dependent due to the temperature-dependent density $\rho(T)$ and concomitant volume changes of the solvent. This effect can easily be corrected in a general way by assuming a linear change of the solvent density with T. The concentration at any temperature $c_0(T)$ can be calculated from the sample concentration at a reference temperature $c_0(293\ \mathrm{K})$:

$$c_0(T) = c_0(293\ \mathrm{K}) \cdot \frac{\rho(T)}{\rho(293\ \mathrm{K})}; \tag{31}$$

where ρ(293 K) is the density of the solvent at the reference temperature. It is assumed, that in the interval between the melting and the boiling point the density $\rho(T)$ of the solvent changes linearly with the temperature T according to equation (32):

$$\rho(T) = a \cdot T + b. \tag{32}$$

The values for slope a and intercept b are determined by a linear fit of known values for the density of the solvent, in this case 1,4-dioxane, at different temperatures (Figure 7). Thus, for 1,4-dioxane equation (33) can be used to express the temperature-dependence of $c_0(T)$ as follows:

$$c_0(T) = c_0(293\ \mathrm{K}) \cdot \frac{-0.00115 \cdot T + 1.37083}{1.03392}. \tag{33}$$

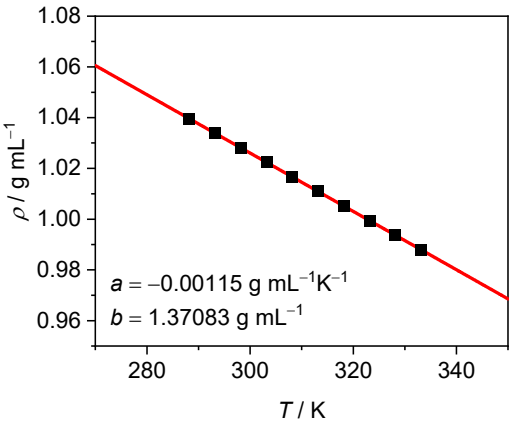

Figure 7. Linear fit (red line) for the temperature-dependence of the density (black squares) of the solvent 1,4-dioxane (R^2 = 0.99999).

Employing this expression (33) for the temperature-dependent molecular sample concentration $c_0(T)$ in equation (30) leads to the fit equation (34) for temperature-dependent UV/Vis extinction data in 1,4-dioxane:

$$\bar{\varepsilon}(\lambda) = \varepsilon_\mathrm{D}(\lambda) + \left(\varepsilon_\mathrm{M}(\lambda) - \varepsilon_\mathrm{D}(\lambda)\right) \frac{-1 + \sqrt{1 + 8\, e^{-(\Delta H^0 - T\Delta S^0)/RT} \cdot c_0(293\ \mathrm{K}) \cdot \frac{-0.00115 \cdot T + 1.37083}{1.03392}}}{4\, e^{-(\Delta H^0 - T\Delta S^0)/RT} \cdot c_0(293\ \mathrm{K}) \cdot \frac{-0.00115 \cdot T + 1.37083}{1.03392}}. \tag{34}$$

In *Chapter 3* of this thesis, this density-corrected version of the temperature-dependent fit function was applied. Admittedly, however, the influence of this correction on the values of the optimized parameters is rather small (e.g., ΔH^0 = –43.5 kJ mol^{-1}, ΔS^0 = –48.7 J mol^{-1}K^{-1}

(density corrected) *vs.* $\Delta H^0 = -44.4$ kJ mol^{-1}, $\Delta S^0 = -51.8$ J mol^{-1}K^{-1} (not density corrected), for the temperature-dependent studies discussed for merocyanine **1** in *Chapter 3*).

In the literature, also slightly different approaches can be found to evaluate temperature-dependent self-assembly data. Often the parameter of the melting temperature T_m is introduced which is defined as the temperature at which $\alpha_{agg} = 0.5$.[18, 22, 65, 87, 91] Examples and more details can be found in the cited literature. However, also for those approaches equation (28) and the assumed temperature-independence of ΔH^0 and ΔS^0 is the basis.

2.1.3 Solvent-Dependent Data Evaluation

In solvent-dependent UV/Vis absorption studies, the (dis)assembly process is monitored by changing the mixing ratio of two solvents while keeping a fixed concentration and a defined temperature: a "bad" solvent, which favours the aggregated species and a "good" solvent, where the monomeric species is well solubilized. This often allows to find conditions, where the entire self-assembly process can be monitored, even for more complex, multi-step processes.[30] Additionally, this analysis method also allows the quantification of the degree of folding strength in foldamers, which can of course not be determined concentration-dependent.[43]

Here, the fundamental equation (18) also applies. The total sample concentration c_0 is assumed to be constant while again the binding constant $K(f)$ changes with the mixing ratio of the two solvents. To describe this solvent-dependence of K, it is assumed, that the Gibbs binding energy $\Delta G^{0\prime}$ in the solvent mixtures changes linearly with the volume fraction f of the denaturating "good" solvent.[51, 76, 92]

$$K(f) = e^{\frac{-\Delta G^{0\prime}}{RT}} = e^{\frac{-(\Delta G^0 + m \cdot f)}{RT}}. \qquad (35)$$

In equation (35) ΔG^0 is the Gibbs binding energy in the pure starting solvent and m is a linear factor, describing how strongly the second solvent influences the self-assembly equilibrium. For various types of supramolecular interactions linear free energy relationships (LFER) between ΔG^0 and different solvent polarity scales could be demonstrated.[76] However, for some solvents and solutes the assumption that ΔG^0 changes linearly with the mixing ratio might not be the best approximation, especially if specific solvent effects are involved.[53, 74] This should be considered when choosing the solvent system.

By using expression (35) for K in the general equation (18), equation (36) is obtained as a fit function for the solvent-dependent dimerization process:

$$\bar{\varepsilon}(\lambda) = \varepsilon_D(\lambda) + \left(\varepsilon_M(\lambda) - \varepsilon_D(\lambda)\right) \frac{-1+\sqrt{1 + 8\, e^{-(\Delta G^0 + m \cdot f)/RT} \cdot c_0}}{4\, e^{-(\Delta G^0 + m \cdot f)/RT} \cdot c_0}. \qquad (36)$$

Figure 8 illustrates how the parameters in this equation influence the self-assembly curve.

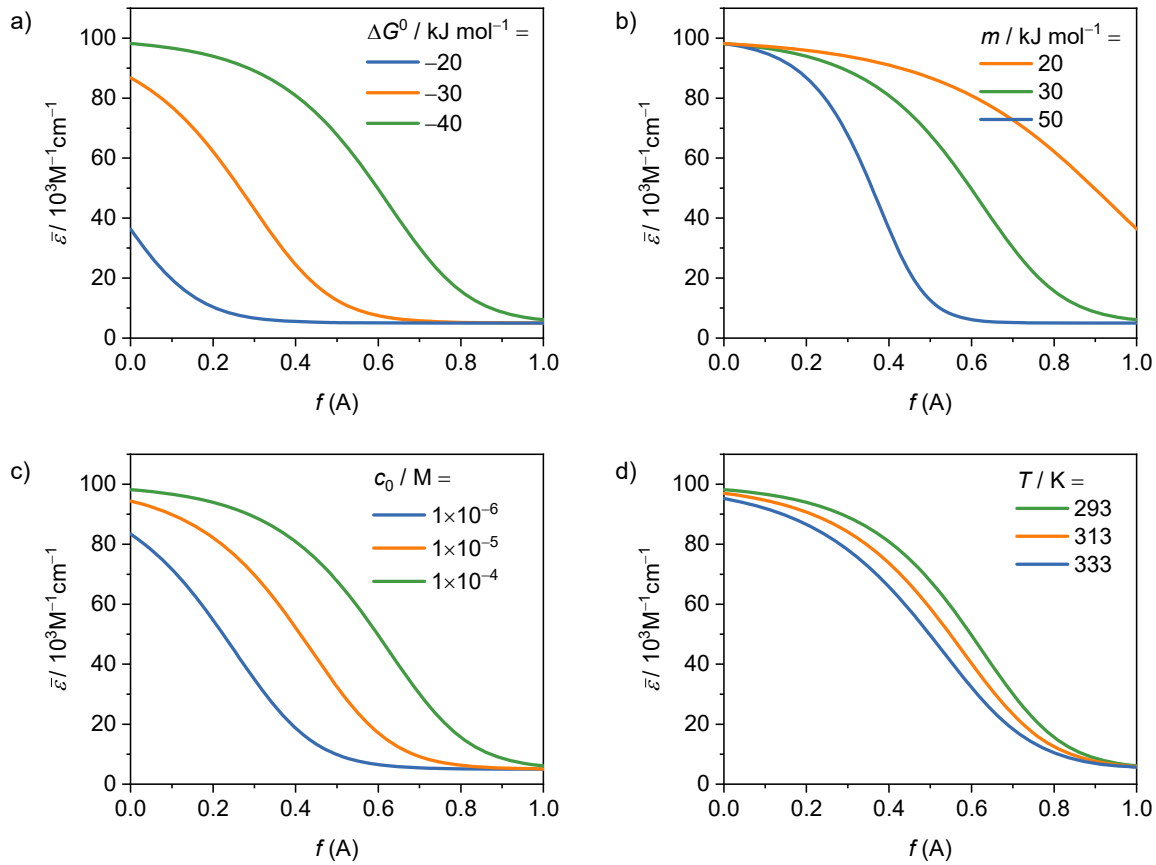

Figure 8. Simulated solvent-dependent dimer self-assembly curves for varying values of a) ΔG^0, b) m, c) c_0, and d) T, with ε_M = 5 000 $M^{-1}cm^{-1}$, ε_D = 100 000 $M^{-1}cm^{-1}$, ΔG^0 = –40 kJ mol^{-1}, m = 30 kJ mol^{-1}, $c_0 = 1\times10^{-4}$ M and T = 293 K, if not stated otherwise. f is the volume fraction of solvent A in mixtures of two solvents A and B. The green curves are identical in all graphs.

In comparison to concentration- or temperature-dependent self-assembly studies, solvent-dependent experiments have the advantage, that it is often easier to find conditions, where the entire self-assembly process can be monitored. In this regard, some background knowledge on the behaviour of the components in different solvents is beneficial. The only prerequisite is that two miscible solvents have to be found where at the same sample concentration either the fully aggregated or the monomeric state is present.

To prepare samples with varying f, stock solutions of the two solvents with identical c_0 can be mixed in different volume ratios. Either defined volumes of both solutions are mixed or a

defined volume of one solution is added, and the second solution is used to fill up the sample to a defined volume. It is assumed that the volume of the two solvents is additive. This is an approximation, since solvents generally shrink or expand to some degree upon mixing.[93] For the first mixing method, this effect will lead to an error in c_0, for the second to an error in the assumed f. Since this effect is rather small for many solvents and time-consuming investigation of the mixing properties of the solvent compositions would be needed to correct it, this is usually neglected.

The parameters to be optimized by the nonlinear fitting algorithm are ΔG^0, m, ε_M and ε_D. Again, the model assumes that the absorption properties of the individual species are not influenced by the solvent and therefore $\varepsilon_M(f)$ and $\varepsilon_D(f)$ are constant. However, this is not true for many chromophores, especially for dipolar ones like the merocyanines discussed here, and serious errors are to be expected with this assumption. The reason is that solvents of different polarity interact differently with the ground and electronically excited states of molecules, leading to spectral shifts and changes in the shape of the UV/Vis absorption band (solvatochromism, see also section 2.2.1).[88, 94-96] Ignoring this will distort the results for the derived parameters, yet there is no easy way to correct the self-assembly model for these solvent-dependent changes, since no general term can be given for $\varepsilon_M(f)$ and $\varepsilon_D(f)$ to accurately describe this complex phenomenon. Since a more or less pronounced solvatochromic shift is given for all dyes and π-conjugated molecules, this should be kept in mind and considered when choosing the two solvents.

2.1.4 Fitting Data by Nonlinear Regression Analysis

Nonlinear regression is a tool for fitting experimental data to a nonlinear equation to determine the values of one or more parameters.[78] A gradual development can be observed for the approaches to evaluate self-assembly data. In times of less computational power, linearized models, where parameters can be derived from the slope and intercept of a linear fit, were the easiest accessible method.[65, 80] With increasing availability of nonlinear regression programmes, UV/Vis absorption data were evaluated by nonlinear fitting. Initially mainly to the simpler models for dimerization or isodesmic assembly. The fit was performed for data at one selected wavelength but often the thermodynamic parameters were reported as an average of the results from several wavelengths.[64, 66] With increasing computational power this approach was extended to a global fit over all data within a selected absorption range. This method provides the binding constant that gives the overall best fit of

experimental and calculated spectra as well as calculated UV/Vis absorption spectra for the individual monomer and dimer species.[24, 26, 97] Simultaneous fitting of multiple data sets can also be useful to, e.g., evaluate temperature-dependent UV/Vis absorption data from multiple samples with different concentrations simultaneously. The most recent developments with regard to data analysis deal with a better error estimation for the derived thermodynamic parameters by so called Monte-Carlo or "bootstrapping" methods.[98-99] Several specialized computer programs are now available online, for the analysis of UV/Vis or NMR self-assembly data. For example, Bindfit,[100] SIVUU[101] or HySS.[102] They are easy to use, but also "black boxes" and limited in their application by the models that have been included. In this thesis the more general data analysis program OriginPro[103] was used, which allows the implementation of user defined explicit and implicit fit functions, as well as simultaneous fitting with shared parameters of up to 100 data sets.

The method of nonlinear regression analysis is well established. However, it can produce misleading results when used inappropriately. The theory behind the method, including a discussion of errors, is, therefore, shortly summarized in the following and important aspects for the analysis of self-assembly data are highlighted.

Theory of Nonlinear Regression

The goal of the method is, to find the parameter values for a model equation that minimize the sum of the squares (S) of the distances of the experimental data points (y_{exp}) to the theoretical curve (y_{theo}):

$$S = \sum_i \left[\left(y_{i,exp} - y_{i,theo} \right)^2 \right]. \quad (37)$$

Since the square of distances is minimized, this is called a least-square method. Nonlinear regression is based on a set of assumptions, and one should check whether they are true for the investigated system or "at least not badly violated".[80] For the optimization it is assumed that the experimental errors of the data points are only in the dependent variable (y) and the independent variable (x) is known precisely, that errors are Gaussian (normally distributed) and, if no weighing scheme is applied, not related to the values of x or y. For UV/Vis data the y value, the absorbance, is usually very precise[104] and the scatter of the data points come rather from an error in x (concentration, temperature, solvent mixing ratio). As this contradicts the assumptions of the fitting method, it is especially important to be as precise as possible during the sample preparation. The problem of finding optimized parameter values that

minimize S must be solved iteratively. The procedure starts with an initial guess and systematically adjusts the parameter values to improve the fit of the curve to the data until no more (or only negligible) improvement occurs. For an equation with two parameters A and B, this can be visualized as a three-dimensional surface map (Figure 9).

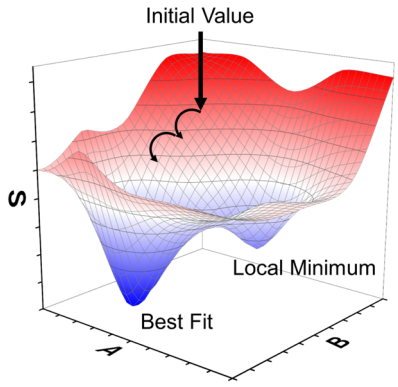

Figure 9. Topographical analogy of nonlinear regression with two parameters A and B and the goal to minimize the sum of squares S. The importance of choosing suitable initial values for the optimization is illustrated by the presence of a local and a global (best fit) minimum.

Each pair of possible values for the parameters A and B is associated with a single sum of squares (S) value. The shape of the surface is determined by the respective fit function. When there are more than two parameters the topographical analogy cannot be visualized anymore, but the mathematical principles remain the same. Starting from the initial guess the nonlinear regression procedure iteratively moves along the surface by altering the values of the parameters. Figure 9 also highlights the importance of selecting appropriate initial parameter values for the optimization. Poorly selected starting values can cause the nonlinear regression to converge to a wrong solution (local minimum) or not to converge at all.

Suitability of the Applied Model

Once the parameter values are optimized the question: “How good is the fit?”, needs to be answered. There are two parts to this. First, whether a good model was chosen to describe the experimental data, and second, how accurate the optimized values of the parameters are (see next section). There are several indicators for how well the model describes the experimental data. The most intuitive is a comparison of the fitting curve and the experimental data points. In Figure 10a the experimental data points are slightly better described by the curve according to the dimer model (red) than the isodesmic model (black). This is further illustrated in the residuals plot (Figure 10b), which depicts the distance of each experimental data point to the optimized curve.

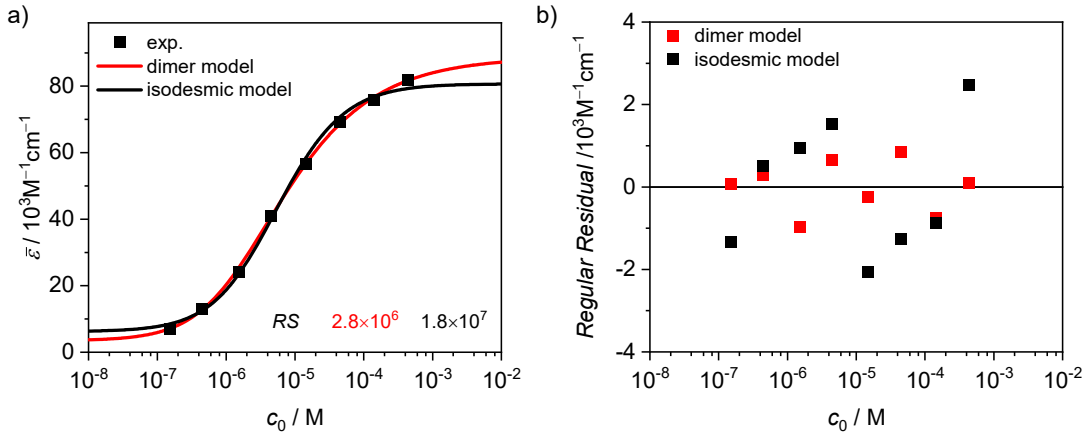

Figure 10. a) Exemplary concentration-dependent UV/Vis absorption data for the dimerization of a merocyanine (black squares) with optimized fit curves according to the dimer (red) and isodesmic model (black) and the residual sum of squares (*RS*) for both fits. b) Residuals plot for the fit curves depicted in a).

If the applied model is appropriate the residuals should only be influenced by random experimental error and, therefore, be randomly distributed as positive or negative. The superior fit of the dimer model is particularly evident for the first and the last data points, which describe the start and end points of the self-assembly process. This exemplarily demonstrates, how important it is to record experimental data for a large portion of the assembly process, including data points for the (almost) fully monomeric and (almost) fully aggregated state, to differentiate between self-assembly mechanisms based on the quality of the fit of different models. The analysis report of the nonlinear regression program usually gives several values that contain information on the quality of the fit.[105] The residual sum of squares (*RS*) is simply the sum of the square of all the vertical deviations of the data points to the fitting regression line. It can, therefore, be used to compare the fit of two different models to the same dataset.

Accuracy of the Optimized Parameter Values

The second important point to think about is the accuracy of the parameter values which are obtained. This includes two aspects: How precisely can the fit predict the true parameter value based on the given dataset (fit error), as well as, how accurate is the given dataset (experimental error)? Errors can be categorized into gross errors (mistakes, e.g., preparation of a sample with a wrong concentration), systematic errors (e.g., UV/Vis absorption data influenced by solvatochromism) and random errors (result of the sum of unavoidable inaccuracies during the experiment).[79] Data points suffering from a gross error should be excluded from the analysis if they can be identified as such without doubt. Systematic errors are problematic for the analysis as they are not easily detected. Only comparing the results with a different experimental method can help in this regard. The uncertainty, that is finally

given for a parameter value usually only refers to the random errors which are considered by evaluating the amount of scatter and the number of the available data points during fitting (fit error) or by repeating the experiment multiple times (experimental error).

Regarding the fit error many programs report standard errors (*SE*) and confidence intervals (*CI*) for the optimized parameter values. The standard errors of nonlinear regression analysis, often called asymptotic standard errors, are approximated and their calculation is complex. They consider the scatter of the data points (smaller *SE* for less scattered data), the number of data points (smaller *SE* for more data points) and how well the parameters are defined by the available experimental data points (*x* range). The standard error can be used to calculate the confidence interval, which is more intuitive to interpret: the 95% *CI*, for example, gives a range where, based on the available experimental data, you can be 95% sure that the true parameter value lies within. Or in other words: the fit predicts that if the experiment is repeated multiple times, in 95% of the cases the optimized parameter values will be in this range. The confidence interval is calculated from the standard error by equation (38).

$$CI = BestFit \pm t^* \cdot SE. \tag{38}$$

The constant t^* depends on the amount of confidence (e.g. 95% or 99%) and on the degrees of freedom, which are the number of experimental data points minus the number of parameters in the model. Tabulated values for t^* can be found in most statistics books and are usually in the range of ~2.[80] Both *SE* and *CI* are approximated values and always determined symmetrical around the optimized *BestFit* value. They are based on several assumptions which are not strictly fulfilled for spectrophotometric self-assembly data and, thus, usually underestimate the true error for the calculated binding parameters.[98-99] Therefore, these values should only be considered as indicators for the accuracy of the derived parameters. *SE* which are in the range of or even larger than the parameter value itself indicate that something is wrong, e.g. a bad model was chosen or there is not enough experimental data to define the parameters accurately. The best method to determine the uncertainty of all parameters is to repeat the respective experiment multiple (*n*) times and determine the mean value $\bar{x}$ as well as the experimental standard deviation *SD* of the individual optimized parameter values x_i:[79]

$$SD = \sqrt{\frac{\sum_{i=1}^{n}(x_i-\bar{x})^2}{n-1}}. \tag{39}$$

However, for a reasonable estimate at least three repetitions are needed and more would be required for truly statistically significant results.[19] As this is unrealistic in most cases, other

methods have been suggested in the literature to obtain statistically meaningful confidence limits. Monte Carlo simulations are recommended by Thordarson and co-workers[19, 98]. The idea is to derive many artificial datasets from the results of one experimental dataset by adding random scattering. Then, each of the artificial datasets is evaluated and the individual optimized parameter values are a numerical approximation of the distribution function of this parameter. The standard uncertainty is the interval covering 68.3% of the values. The prerequisite for this is, however, that reasonable values for the uncertainty of the experimental data points are given. Recently, Vander Griend and co-workers proposed an even more sophisticated method called bootstrapping.[99] This method, similar to the Monte Carlo method, also generates a large number of artificial datasets from one experimental dataset to determine the confidence intervals of the parameters. However, without the need for the user to specify the uncertainty of the individual data points. A drawback of both methods is that user friendly availability in common data analysis software is still limited.

If a parameter *C* is derived from two parameters *A* and *B* that have an uncertainty of $\sigma_{A/B}$, σ_C must be determined by applying the law of error propagation according to equation (40). Equation (40) is a commonly used simplification which assumes that σ_A and σ_B are independent:[106]

$$\sigma_C = \sqrt{\left(\frac{\partial C}{\partial A}\right)^2 {\sigma_A}^2 + \left(\frac{\partial C}{\partial B}\right)^2 {\sigma_B}^2}\,. \tag{40}$$

For example, the uncertainty of ΔG^0 derived from *K* according to equation (5) is:

$$\sigma_{\Delta G^0} = \frac{RT}{K} \cdot \sigma_K\,, \tag{41}$$

and derived from ΔH^0 and ΔS^0 according to equation (27):

$$\sigma_{\Delta G^0} = \sqrt{{\sigma_{\Delta H^0}}^2 + T^2 \cdot {\sigma_{\Delta S^0}}^2}. \tag{42}$$

The parameters of a model are usually not entirely independent. Changing one parameter value will make the fit of the model to the experimental data worse, but this can often partially be compensated by adjusting the value of another parameter. The degree to which two parameters can compensate changes in one another is shown by a value ranging from −1 to 1 in the correlation matrix. Values of ±1 mean that an increase/decrease in one parameter value can completely be compensated by increase/decrease of the other parameter value. A value of 0 means the two parameters are not correlated at all. Parameters in most models are

somewhat related and values of ±0.8 are common. Higher correlations of ±0.9 or even ±0.99 mean that the parameters are not defined unambiguously by the data, which results in larger standard errors. The problem can sometimes be mitigated by applying suitable boundaries for parameter values and collecting data for a wider range of x. For example, the parameters ΔH^0 and ΔS^0 in the temperature-dependent fit equation for dimerization (30) are highly correlated with correlation coefficients > 0.99. To illustrate this, UV/Vis absorption datasets with an identical number of data points were simulated with $\varepsilon_M = 5\,000\ M^{-1}cm^{-1}$, $\varepsilon_D = 100\,000\ M^{-1}cm^{-1}$, $\Delta H^0 = -40\ kJ\ mol^{-1}$, $\Delta S^0 = -50\ J\ mol^{-1}K^{-1}$ and $c_0 = 1\times10^{-4}$ M for four different α_{agg} regimes of a dimer self-assembly process (I-IV, Figure 11a-d).

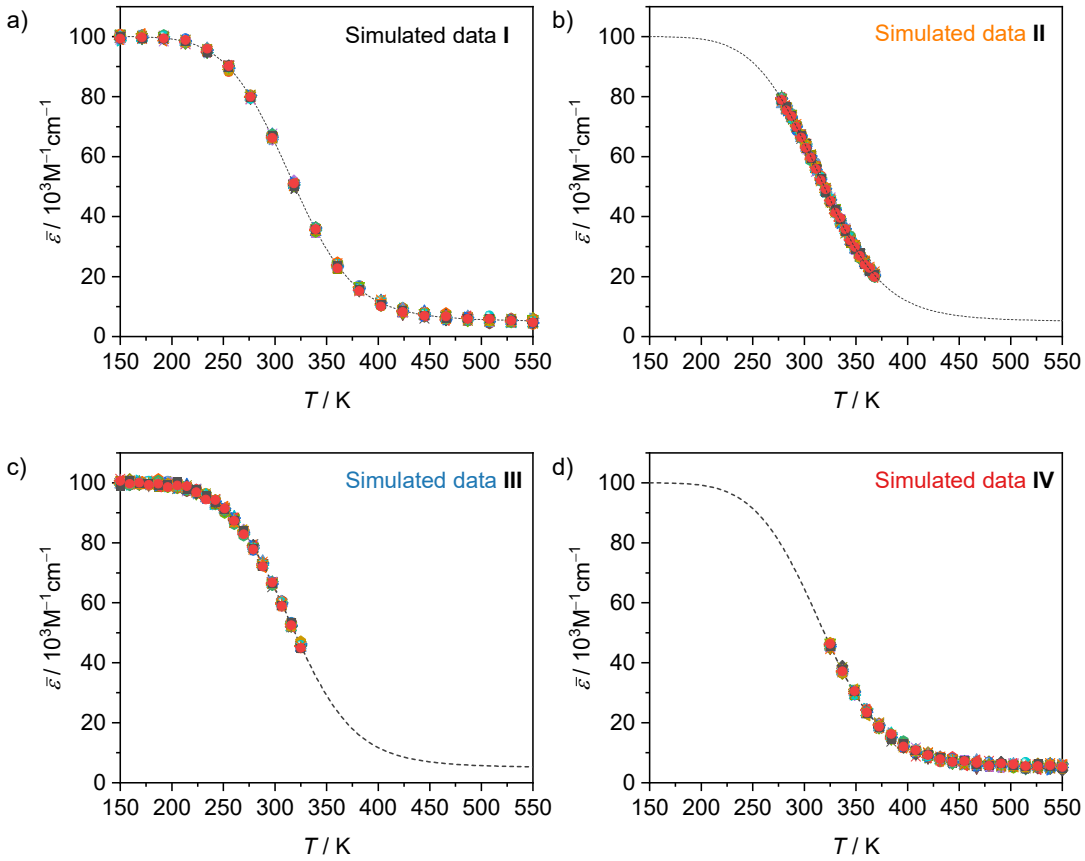

Figure 11. a-d) Simulated UV/Vis absorption datasets for temperature-dependent dimerization with $\varepsilon_M = 5\,000\ M^{-1}cm^{-1}$, $\varepsilon_D = 100\,000\ M^{-1}cm^{-1}$, $\Delta H^0 = -40\ kJ\ mol^{-1}$, $\Delta S^0 = -50\ J\ mol^{-1}K^{-1}$ and $c_0 = 1\times10^{-4}$ M. Random scatter with a standard deviation of 500 $M^{-1}cm^{-1}$ was added so 50 slightly different datasets were obtained for each regime I-IV.

Monte Carlo simulations were performed by adding random y-scatter with a standard deviation of 500 $M^{-1}cm^{-1}$ to these data so that 50 slightly different datasets, representing, e.g., multiple repetitions of an experiment, were obtained for each regime. All datasets were fitted with equation (30) (initial parameter values: $\Delta H^0 = -40\ kJ\ mol^{-1}$, $\Delta S^0 = -50\ J\ mol^{-1}K^{-1}$, $\varepsilon_{M/D} \geq 0$). The results are depicted in Figure 12.

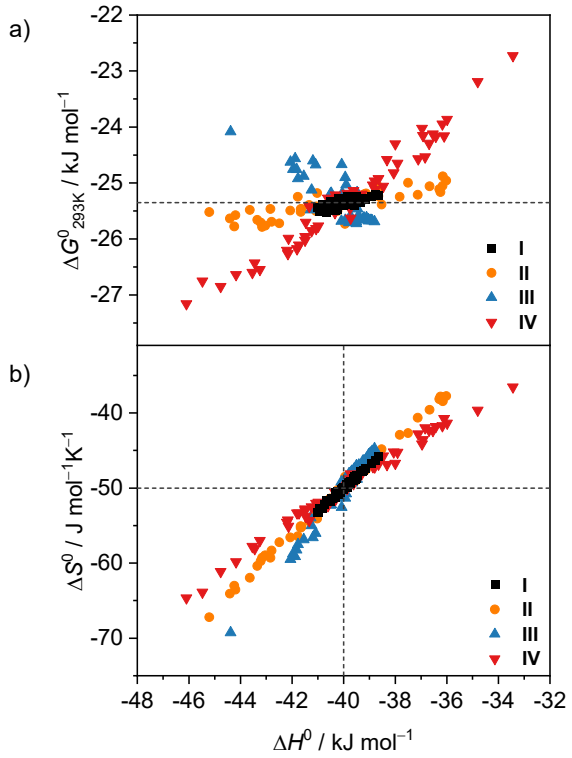

Figure 12. Fit results of the simulated datasets shown in Figure 11 a-d. with equation (30). For every regime (I: black, II: orange, III: blue, IV: red) each 50 different data sets were evaluated and fit results for the thermodynamic parameters are plotted as: a) ΔG^0 calculated from ΔH^0 and corresponding ΔS^0. b) Optimized parameter values for ΔS^0 in comparison to the corresponding optimized parameter value of ΔH^0 from the same fit. Dashed grey lines mark the "true" values for ΔH^0, ΔS^0 and ΔG^0 that were used to simulate the data sets.

Figure 12b clearly illustrates that the results for ΔH^0 and ΔS^0 which are obtained from a fit are not independent. Despite only small random changes between the 50 simulated data sets for each regime, the 50 different optimized parameter values for ΔH^0 and ΔS^0 vary significantly and show a linear correlation. The differences in the optimized parameter values for ΔH^0 and ΔS^0 compensate each other when calculating ΔG^0. The values for ΔG^0, therefore, show much less variation between the data sets (Figure 12a) and are, especially also for simulated dataset II always quite close to the true value of $\Delta G^0_{293K} = -25.4$ kJ mol^{-1}.

The most accurate result with the smallest standard deviation is obtained if the experimental data points cover the entire temperature range of the self-assembly process (simulated data I, Table 1).

Table 1. Optimized parameter values given as *mean*±*SD* of the 50 individual fit results for the simulated data sets I-IV depicted in Figure 11. Data were simulated with $\Delta H^0 = -40$ kJ mol^{-1}, $\Delta S^0 = -50$ J mol^{-1}K^{-1}, $\Delta G^0_{293K} = -25.4$ kJ mol^{-1}.

	α_{agg}	ΔH^0 /kJ mol^{-1}	ΔS^0 /J mol^{-1}K^{-1}	ΔG^0_{293} /kJ mol^{-1}
Input		–40	–50	–25.4
Simulated data I	1 – 0	–39.9±0.6	–49.8±1.7	–25.3±0.1
Simulated data II	0.8 – 0.15	–40.4±2.5	–51.4±8.0	–25.4±0.2
Simulated data III	1 – 0.4	–40.1±1.1	–50.6±4.9	–25.3±0.4
Simulated data IV	0.4 – 0	–39.8±2.8	–49.6±6.4	–25.3±1.0

In summary, more data points that cover as much as possible of the self-assembly process are advantageous for model comparison as well as parameter accuracy. The number of data points can also be increased by using multiple independent datasets and fitting them together with shared parameters. The standard error *SE* and derived confidence interval *CI* from the fit are indicators of the accuracy of the optimized parameter values. However, they only estimate (and usually underestimate) the random experimental errors, based on the scattering of the data points. To obtain a more meaningful assessment of the parameter accuracy, experiments should be performed multiple times (at least 3×), and, if possible, even by multiple different experimental methods. When giving parameter values in the form $M \pm e$, it is important to clarify what e is (*SE*, *CI* or *SD*) and how it was determined.

2.1.5 Summary

In this *Chapter 2.1* the fit equations for the nonlinear regression analysis of concentration-, temperature-, and solvent-dependent UV/Vis absorption self-assembly data of thermodynamically controlled dimer formation were derived based on mass balance and mass action law. Each of these methods has advantages and disadvantages (Table 2) that have to be considered when deciding on the most appropriate way to analyse a self-assembly equilibrium, meaning the method which will provide the most accurate thermodynamic parameter values.

Table 2. Summary on concentration-, temperature-, and solvent-dependent UV/Vis absorption studies for the determination of thermodynamic parameters of self-assembly equilibria. Some aspects are marked as clear advantages (+) and disadvantages (–).

	Concentration-Dependent	**Temperature-Dependent**	**Solvent-Dependent**
Sample preparation	dilution series with multiple cuvettes	only one sample needed +	mixing two stock solutions of identical concentration
Range (UV/Vis)[a)]	five orders of magnitude limited by solubility	5 – 95 °C –	controlled by choice of solvent +
Sources of errors	compound not fully dissolved at high concentrations	precipitation upon cooling decomposition upon heating sample not equilibrated before measurement solvent evaporation during measurement	unknown density of solvent mixtures change of composition due to evaporation of more volatile solvent
Fit Parameters	K, $\varepsilon_{M/D}$	ΔH^0, ΔS^0, $\varepsilon_{M/D}$	ΔG^0, m, $\varepsilon_{M/D}$
Data evaluation	straightforward shape of self-assembly curve only dependent on model +	$\varepsilon_{M/D}$ assumed temp.-independent ΔH^0 and ΔS^0 assumed temp.-independent	$\varepsilon_{M/D}$ assumed solvent-independent linear dependence of ΔG^0 and f assumed –

a) Five orders of magnitude for the concentration refers to the availability of standard UV/Vis absorption cuvettes with 0.01 mm < d < 100 mm. The temperature range of 5 – 95 °C is the accessible range of a Peltier element with a water cooling system as implemented in a standard UV/Vis spectrometer. However, of course also the solvents melting and boiling point pose limitations.

The concentration-dependent analysis is the most straightforward, with no additional assumptions needed. It is the most reliable method, when trying to elucidate the self-assembly mechanism of an unknown system by model comparison. However, sample preparation is more elaborate and for UV/Vis spectroscopy a set of cuvettes with different path lengths is needed. The temperature-dependent analysis has the advantage that all thermodynamic parameters can be obtained from a single sample in a single automated measurement. However, the accessible temperature-range is often quite limited by the instrument and the melting and boiling point of the solvent. Furthermore, the assumptions of temperature-independent $\varepsilon_{M/D}$ as well as ΔH^0 and ΔS^0 must apply. Solvent-dependent studies often allow the monitoring of the entire self-assembly process from the monomeric to the fully aggregated state, which can be a problem for concentration- and temperature-dependent experiments. It is important, however, to carefully consider whether the assumption of solvent-independent $\varepsilon_{M/D}$ is acceptable. The same holds true for the approximation of a linear relation of the binding energy ΔG^0 and the solvent mixing ratio f.

Ultimately, the experimental data of each individual system need to be studied carefully to evaluate how to determine the thermodynamic parameters most accurately and the parameter values should always be given in conjunction with their corresponding accuracy. For good results from nonlinear regression analysis, it is advantageous to cover a large portion of the self-assembly process with the experimental data points. This chapter is a guide on what points need to be considered, with a focus on self-assembly studies by UV/Vis spectroscopy. To gain a comprehensive understanding of the self-assembly process, these UV/Vis spectroscopic studies are usually supplemented by other experimental techniques for structure and size determination as well as theory.

2.2 PYOP Merocyanines as Supramolecular Building Blocks

Merocyanine dyes are a versatile class of neutral, unsymmetric, dipolar chromophores.[107] They find application in electro-optics[10, 108-109] and sensing[87, 110-114]. For supramolecular chemistry, they are very interesting chromophores as they constitute supramolecular and functional building block at the same time. Their large molecular ground state dipole moment (μ_g) causes strong binding by dipole-dipole interactions between the chromophores, and the highly polarizable π-system with a large transition dipole moment (μ_{eg}) is reflected in strong UV/Vis absorption and pronounced excitonic coupling of the chromophores within aggregate species. The optical and self-assembly properties of particularly the PYOP (PYridin diOxocyano-Pyridine) merocyanine, which is used in this thesis, are discussed in the following.

2.2.1 Molecular and Dimer Properties

Electronic Structure of PYOP Merocyanines

The interesting properties of merocyanines, like dipolarity, high extinction coefficients, narrow absorption bands in the visible range and exceptional sensitivity of the optical features on the environment, are a result of their chemical structure.[42] An electron-rich donor and an electron-deficient acceptor unit are connected by a conjugated polymethine chain. Resonance structures can be formulated in a neutral (polyene) as well as in zwitterionic (betaine) form (Figure 13a).

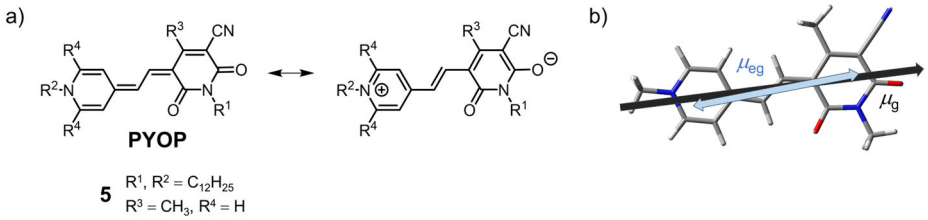

Figure 13. a) General chemical structure of a pyridine dioxocyano-pyridine (PYOP) merocyanine with its zwitterionic resonance structure. b) Geometry-optimized structure (B97D3/def2SVP, PCM: CH_2Cl_2) of the PYOP chromophore (R^1, R^2, $R^3 = CH_3$, $R^4 = H$). Bold arrows indicate the orientation of the ground state dipole moment μ_g as obtained from the DFT calculations (black), and the transition dipole moment μ_{eg} (light blue) from TD-DFT calculations (ωB97/def2SVP, PCM: CH_2Cl_2).

With increasing electron donating or accepting strength of the functional groups, and also with increasing polarity of the solvent environment, the zwitterionic structure gains in importance. Merocyanines can be classified based on the resonance parameter c^2,[96, 115] which indicates the contribution of the two resonance structures in the ground state. If the chromophore is more polyene like $c^2 < 0.5$, and for more betaine like chromophores $c^2 > 0.5$.

The perfect intermediate between the two extremes, is the so called 'cyanine limit' ($c^2 = 0.5$), which is characterized by a lack of bond length alternation between the formal carbon-carbon single and double bonds. The electronic structure determines the absorption properties of merocyanine dyes.[116] Merocyanines close to the cyanine limit show, similar to cyanines, no bond length alternation and, therefore, a more rigid fully conjugated carbon-carbon chain. In addition, the change in molecular geometry between the ground and excited states is rather small. Therefore, the absorption band is characterized by little vibronic fine structure with a narrow most intense band for the 0-0 vibronic transition. For polyene- and betaine-like merocyanines, additional symmetric torsional vibrations around the carbon-carbon single bonds of the polymethine chain are less hindered and more structural changes occur upon excitation. This results in unstructured and rather broad absorption bands.[117] Electronic excitation of merocyanines is characterized as an intramolecular charge transfer process. It is generally accompanied by an increase in dipolarity for merocyanines in the $c^2 < 0.5$ regime and, conversely, a decrease in dipolarity for $c^2 > 0.5$ merocyanines. For merocyanines with $c^2 \sim 0.5$, the dipolarity hardly changes upon excitation.[107]

The chromophore exclusively used in this thesis features a strong pyridine donor and dioxocyano-pyridine acceptor (therefore abbreviated as PYOP, Figure 13a). The result is an exceptionally high monomer (M) ground state dipole moment of $\mu_g(M) = 17.1$ D,[66] as determined by electrooptical absorption (EOA) measurements in 1,4-dioxane, which is oriented along the long axis of the molecule (Figure 13b, black arrow). This value is among the highest reported for merocyanine dyes.[66, 116, 118-119] Despite the high polarity, the chromophore is still soluble enough, even in organic solvents of low polarity, for UV/Vis absorption studies ($c_0 > 3\times10^{-4}$ M in 1,4-dioxane, for **5**). The chromophore can be functionalized in various positions (R^1, R^2, R^3, R^4 in Figure 13a), without significantly changing the optical properties of the monomer.[66]

The dipolarity or this chromophore reduces upon excitation to $\mu_e(M) = 12.6$ D.[66] The large transition dipole moment $\mu_{eg}(M)$ is also oriented along the long axis of the molecule (Figure 13b, blue arrow). A transition dipole moment of $\mu_{eg}(M) = 10.7$ D was determined from the UV/Vis absorption band of the monomeric PYOP derivative **2** in 1,4-dioxane (see *Chapter 4*). With these values a resonance parameter of $c^2 = 0.60$ can be calculated for the PYOP chromophore in 1,4-dioxane, according to:[96]

$$c^2 = \frac{1}{2}\left[1 - \Delta\mu\left(4{\mu_{eg}}^2 + \Delta\mu^2\right)^{-1/2}\right], \quad (43)$$

$$\Delta\mu = \mu_e - \mu_g. \quad (44)$$

It categorizes the chromophore, just like the famous Brooker merocyanine,[111] as "beyond the cyanine limit", even in unpolar solvents like 1,4-dioxane. This is in line with the negative solvatochromism observed for the UV/Vis absorption of this chromophore and mostly unstructured absorption bands, which are discussed further below.

Dimer Formation by Dipole-Dipole Interactions

Due to their dipolarity merocyanines readily form anti-parallel face-to-face stacked dimers by strong intermolecular dipole-dipole interactions (Figure 14a) with high binding constants in solution ($K = 1.4\times10^5$ M^{-1} in 1,4-dioxane for PYOP **5**).[66]

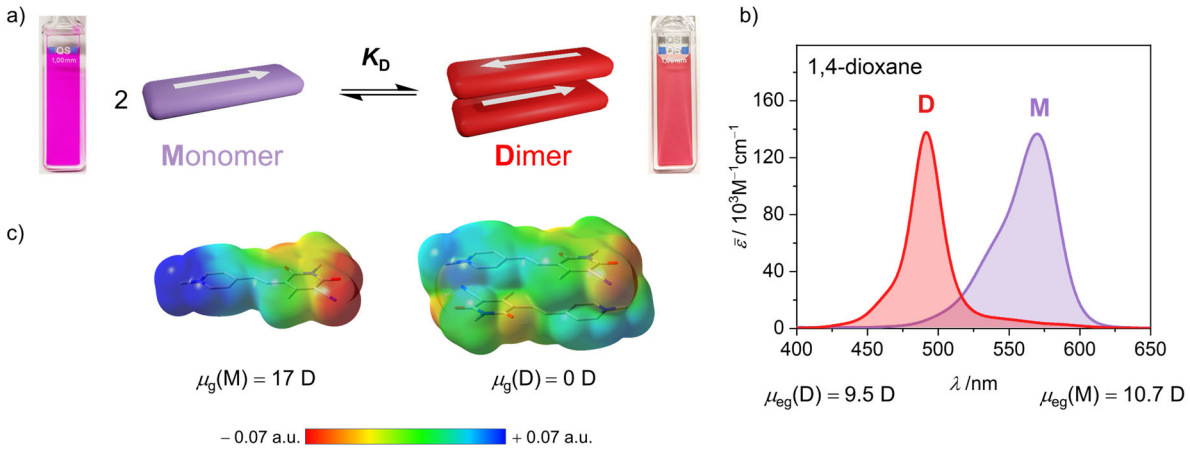

Figure 14. a) Schematic monomer-dimer equilibrium of dipolar merocyanines. Arrows indicate μ_g. Pictures of cuvettes show solutions of the PYOP merocyanine **1** ($c_0 = 2\times10^{-4}$ M) monomer in CH_2Cl_2 (left) and dimer in 1,4-dioxane (right). b) Calculated monomer (M) and dimer (D) UV/Vis absorption spectra of a PYOP merocyanine **1** in 1,4-dioxane (293 K) as deduced form a global fit analysis of concentration-dependent spectra. The transition dipole moment of the monomer μ_{eg}(M) and dimer μ_{eg}(D), were determined from the integrated UV/Vis absorption band as described in *Chapter 4*. c) Electrostatic surface potential of geometry-optimized (B97D3/def2SVP, PCM: CH_2Cl_2) PYOP monomer (M) and anti-parallel dimer (D). The μ_g(M) of the monomer was determined experimentally by EOAM measurements in 1,4-dioxane,[66] μ_g(D) of the dimer was calculated by DFT.

This dimerization can easily be monitored by UV/Vis absorption spectroscopy. The sample concentration range that is needed to monitor the process in solvents of intermediate polarity is ideal for this analytical method. Upon increasing the sample concentration, the monomer absorption band (λ_{max}(M) = 570 nm, 1,4-dioxane) decreases and a hypsochromically shifted absorption band of the dimer (λ_{max}(D) = 492 nm, 1,4-dioxane) gains in intensity (Figure 14b). Würthner and co-workers showed, that for this dimerization electrostatic (dipole-dipole) interactions are the main driving force.[66] A simple linear correlation was observed between the dipolarity μ_g^2(M) and the Gibbs dimerization energy for sterically uncrowded linear

merocyanines as well as a strong dependence of the binding strength on the solvent polarity. The anti-parallel face-to-face structure of these dimers was proven in solution by ^{1}H ^{1}H ROESY NMR and also in the solid state the preferred anti-parallel stacking was observed by X-ray crystallography.[66] Since the molecular ground state dipole moments compensate each other upon assembly the ground state dipole moment of the dimer is significantly reduced ($\mu_g(D) \sim 0$, Figure 14c). This was also demonstrated experimentally through concentration-dependent dipole measurements.[66, 120] The driving force for further self-assembly is, therefore, significantly reduced after dimer formation. It was shown that anti-parallel merocyanine dimerization is a very useful supramolecular synthon, not only to investigate defined dimers but also to construct more elaborate supramolecular architectures. The binding is strong and directional, similar to, e.g. triple hydrogen bonds, which allows the design of monomer building blocks that form assemblies of predictable geometry.[42] Selected examples based on the PYOP chromophore are presented in *Chapter 2.2.2*.

Exciton Coupling Theory

The formation of PYOP dimers in solution is accompanied by distinct spectral and subsequent color changes (Figure 14a,b). The dimer exhibits a hypsochromic shift of the absorption maximum compared to the monomer ($\Delta\tilde{\nu} \sim 2800\ cm^{-1}$ in 1,4-dioxane). Due to the unstructured absorption bands and the pronounced shift, PYOP monomer and aggregate species are easily distinguishable solely from the UV/Vis absorption spectrum. For merocyanines, which often exhibit only weak vibronic coupling and have a large molecular transition dipole moment that leads to strong Coulomb exciton coupling, these spectral changes are often well described within the conventional molecular exciton theory,[14] as introduced by Davydov[121] and Kasha[122]. Merocyanines are a textbook example of so-called H-type aggregates, which are characterized by a hypsochromic shift of the absorption band compared to the monomer and a “side-by-side” or “card-stack” arrangement of the chromophores. Conversely, aggregates with a bathochromic absorption shift are referred to as J-type aggregates and are often associated with a “head-to-tail” arrangement of chromophores (Figure 15a). For merocyanines also a few examples of J-aggregates are reported in literature[123-127] but due to the directionality of the dipole-dipole interactions the H-type assemblies are much more common for this dye class and, therefore, exclusively discussed here. Within Kasha’s exciton theory, Coulomb coupling (J_c) of the transition dipoles (μ_{eg}, point-dipole approximation) of two neighboring chromophores leads to a splitting of $2|J_c|$ of

the degenerated excited states into two excitonic states (Figure 15b). Vibronic coupling is hereby not considered.[14, 128]

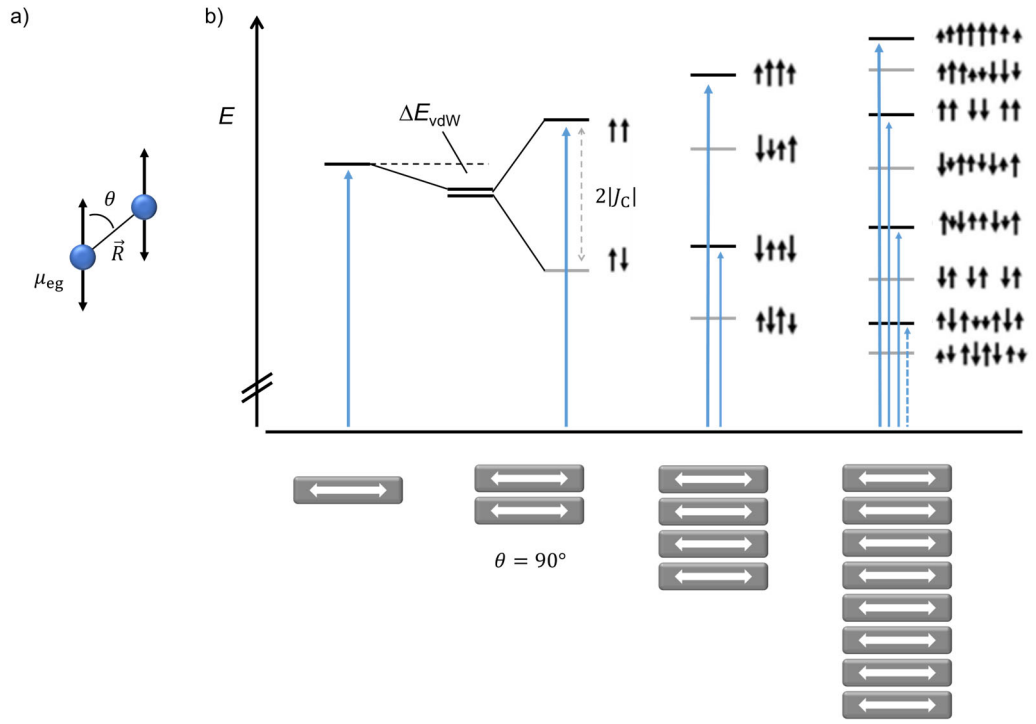

Figure 15. a) Relative orientation of the transition dipole moments (μ_{eg}, double headed arrows) differentiating between H- ($54.7° < \theta < 90°$) and J-aggregates ($\theta < 54.7°$) under the point dipole approximation.[128] b) Energy levels of calculated exciton states with allowed (black states) and forbidden (grey states) electronic transitions (light blue arrows). The black single headed arrows illustrate the in- and out-of-phase coupling of the transition dipole moments. Adapted with permission from ref. [24]. Copyright 2019, American Chemical Society.

The coupling J_c hereby mainly depends on the square of the transition dipole moment (μ_{eg}^2), the relative orientation (θ) and the center-to-center distance (R) of the two chromophores (Figure 15a):

$$J_C = \frac{\mu_{eg}^2(1-3\cos^2\theta)}{4\pi\varepsilon_r R^3}, \qquad (45)$$

with the dielectric constant of the medium ε_r. The two exciton states are composed of the in-phase and out-of-phase linear combination of the two local excited states (indicated by the single headed black arrows in Figure 15b). The higher energy in-phase state exhibits an enhanced transition dipole moment relative to the monomer, while, for a perfect H-dimer, the transition to the lower energy out-of-phase state is symmetry forbidden. This results in the mentioned pronounced hypsochromic shift of the absorption maximum of the PYOP dimer relative to the monomer. This conventional exciton theory can also be applied to more extended π-stacks (Figure 15b). The coupling of N parallel aligned identical transition dipole moments leads to a splitting of the excited state into N non-degenerate exciton states.[24] For

H-type aggregates the highest (N^{th}) exciton state always has the largest oscillator strength as all transition dipole moments are coupled in phase. The transitions to the lower exciton states can be partially allowed due to incomplete annihilation of the transition dipole moments or due to rotational displacements from a perfect H-stack. Increase of the stack size is accompanied by an increase of the hypsochromic shift and plateau is predicted by theory[24] for the energy of the highest excited state with increasing stack size. This was experimentally confirmed by the observed shifts of absorption bands for a series of Amino-Thienyl-diOxocyano-Pyridine (ATOP) merocyanine stacks of defined size up to eight chromophores by Kirchner *et al.*[24] and a series of PYOP merocyanine foldamers of up to five chromophores by Hu *et al.*[40, 129] (see also *Chapter 2.2.2*).

Solvatochromism

The absorption (and emission) properties of merocyanines are strongly influenced by the environment, i.e., the solvent.[95] Especially famous examples are Brooker's dye[111] and Reichardt's dye[130], which were both used to elucidate solvent polarity effects and to establish solvent polarity scales. As mentioned in *Chapter 2.1*, solvatochromism is an important consideration and a potentially serious problem for self-assembly research by solvent-dependent UV/Vis absorption studies. Therefore, this effect will be discussed here in more detail for the PYOP chromophore (Figure 16).

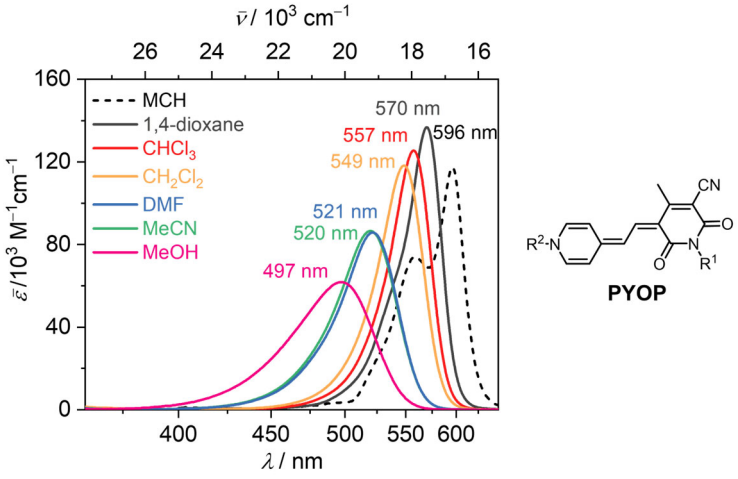

Figure 16. UV/Vis absorption spectra ($\bar{\nu}$ scale) of monomeric PYOP merocyanine **1** in 1,4-dioxane (calculated from concentration-dependent data), $CHCl_3$ (calculated from concentration-dependent data), CH_2Cl_2 ($c_0 = 1\times10^{-5}$ M), DMF ($c_0 = 3\times10^{-6}$ M), MeCN ($c_0 = 1\times10^{-5}$ M) and MeOH ($c_0 = 3\times10^{-6}$ M) at 293 K. The spectrum in MCH is the calculated monomer spectrum of merocyanine **2** from the concentration-dependent data at 353 K. The wavelength of the respective absorption maximum is given in the same color.

The solvent influences the position of the UV/Vis absorption band as well as its shape and vibronic structure. For PYOP merocyanines a hypsochromic shift is observed for solvents of

increasing polarity (negative solvatochromism), from $\lambda_{max} = 596$ nm in methylcyclohexane (MCH) to $\lambda_{max} = 497$ nm in methanol (MeOH) which scales to $\Delta\tilde{\nu} \sim 3500\ cm^{-1}$. The absorption bands are unstructured in all solvents of Figure 16, except for the lowest polarity solvent MCH where a vibronic fine structure is resolved. This indicates that the solvent influences the electronic ground state structure of the dipolar chromophore.

The shifting of the absorption band in different solvents is, however, primarily a result of changes in the solvation energies that stabilize the ground (S_0) and electronically excited (S_1) state of the dye molecule (Figure 17).[88, 94]

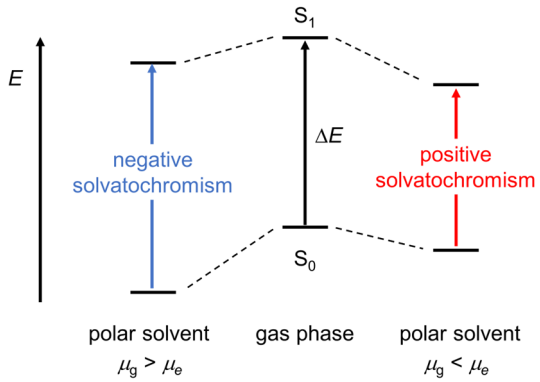

Figure 17. Stabilization of the electronic ground (S_0) and excited state (S_1) energies of a dye molecule by solvation. The cases of increasing ($\mu_g < \mu_e$) or decreasing ($\mu_g > \mu_e$) polarity of the chromophore upon excitation are differentiated. Adapted with permission from ref. [76]. Copyright 2022, American Chemical Society.

Excluding specific solvation effects such as H-bonding, the stabilization is mainly the result of dipole-dipole and dispersion interactions between the solute and solvent, which corelate with the dipole moment and polarizability of the involved molecules, respectively. For highly dipolar molecules, like the merocyanine dyes discussed in this thesis, the stabilization of S_0 and S_1 is mainly attributed to dipole-(induced) dipole interactions between the dye and solvent molecules.[131] Therefore, the stabilizing interactions with the solvent are usually the stronger the more dipolar the chromophore in its respective electronic ground or excited state ($\mu_{g/e}$) and the more polar the solvent. In case of the PYOP chromophore, the dipolarity decreases upon excitation ($\mu_g > \mu_e$, left case in Figure 17). Therefore, the ground state is better stabilized by the solvent sphere, than the less polar excited state and a hypsochromic shift of the absorption band can be observed in solvents of increasing polarity (Figure 16).

For merocyanine chromophores which are very close to the cyanine limit in solvents of intermediate polarity the situation of $\mu_g > \mu_e$ *vs.* $\mu_g < \mu_e$ can also switch between different solvents. This leads to an initial hypsochromic shift followed by a bathochromic shift upon increasing the solvent polarity (inverted solvatochromism).[96]

2.2.2 Functional Assemblies of the PYOP Chromophore Beyond the Dimer

PYOP chromophore building blocks allowed the Würthner group to construct a variety of functional supramolecular architectures beyond the initially observed anti-parallel dimer.[66] By suitable functionalization with sterical and solubilizing groups as well as covalent linkers a variety of aggregate structures could be achieved, like cyclic aggregates,[132] π-stacks of defined size[39-41, 129, 133] and supramolecular polymers.[134-135] To achieve larger structures beyond a merocyanine dimer stack, so far always monomer building blocks comprising at least two covalently linked chromophore units were used. A selection is presented in the following.

Cyclic Trimer out of Dimers

The predictable geometry of the merocyanine dimer motif was used by Lohr *et al.*[132] to construct a cyclic assembly of bis(merocyanine) **6**. The calix[4]arene linker arranges the two dipolar chromophores in an ideal geometry to form a cyclic trimer (Figure 18a,b). The well-defined isosbestic point confirms an equilibrium between only two defined species with distinct absorption properties, the monomer (M) and cyclic trimer (T). The hypsochromic shift of the UV/Vis absorption maximum from 556 nm to 490 nm ($CHCl_3$, Figure 18c) is indicative of exciton coupling between independent pairs of π-stacked PYOP chromophores in the aggregate. A trimerization constant of $K_T = 1.9\times10^9\ M^{-2}$ was determined based on a $3M \rightleftharpoons T$ equilibrium. The discrete trimer assembly was observed by mass spectrometry and scanning tunnelling microscopy (STM). Additionally, an increased thermodynamic stability was observed for the cyclic trimer of bis(merocyanine) **6** compared to a dimer of the reference PYOP merocyanine **5** ($K_D = 590\ M^{-1}$) in $CHCl_3$.

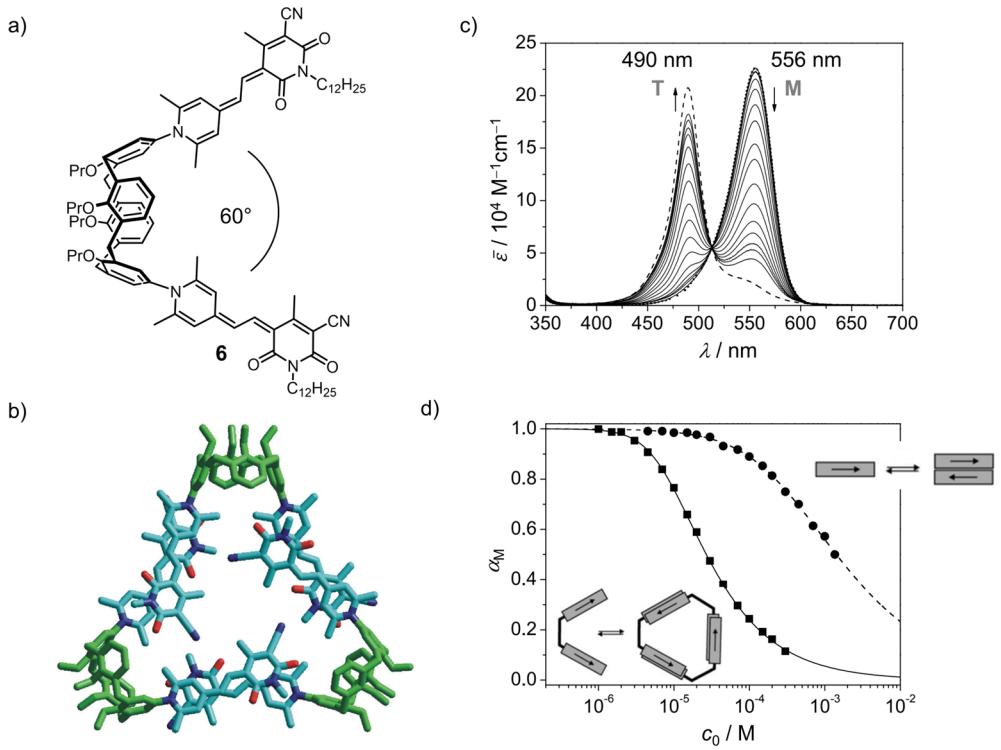

Figure 18. a) Chemical structure of the calix[4]arene-tethered bis(merocyanine) **6**. b) Geometry-optimized (MM+) molecular model of the cyclic trimer aggregate. c) Concentration-dependent UV/vis absorption spectra of **6** in $CHCl_3$ (298 K). d) Fraction of monomer calculated from concentration-dependent UV/Vis absorption data ($CHCl_3$, 298 K) for the trimerization of the bis(merocyanine) **6** (squares) and the dimerization of reference monomer **5** (circles). Adapted with permission from ref. [132]. Copyright 2009 WILEY-VCH Verlag GmbH & Co. KGaA, Weinheim.

This is evident from the concentration at which half of the molecules are incorporated into an aggregate ($\alpha_M = 0.5$, Figure 18d) and can be rationalized by chelate cooperativity introduced by the multiple binding sites in the cyclic assembly. This additionally supports the proposed formation of a distinct cyclic structure instead of a linear polymer.

Defined Tetramer Stacks

The first extended merocyanine π-stacks beyond a dimer, also based on the PYOP chromophore, were reported by Lohr *et al.* in 2009.[39] Four tweezer molecules, **7a**, **7b**, **8a**, **8b**, were synthesized (Figure 19a). In these systems two merocyanine chromophores are covalently linked either at the donor or the acceptor moiety with a naphthalene or diphenylmethane spacer. The preorganization by the spacer units arranges the PYOP chromophores at a bit more than two times the π-π-distance within a monomer building block (7.4 Å for **7** and 9.1 Å for **8**). This leads to self-assembly into tetramer stacks of anti-parallel oriented chromophores as exemplarily shown for **7b** in Figure 19b. The process was monitored by concentration-dependent UV/Vis absorption spectroscopy in $CHCl_3$ (298 K, Figure 19c).

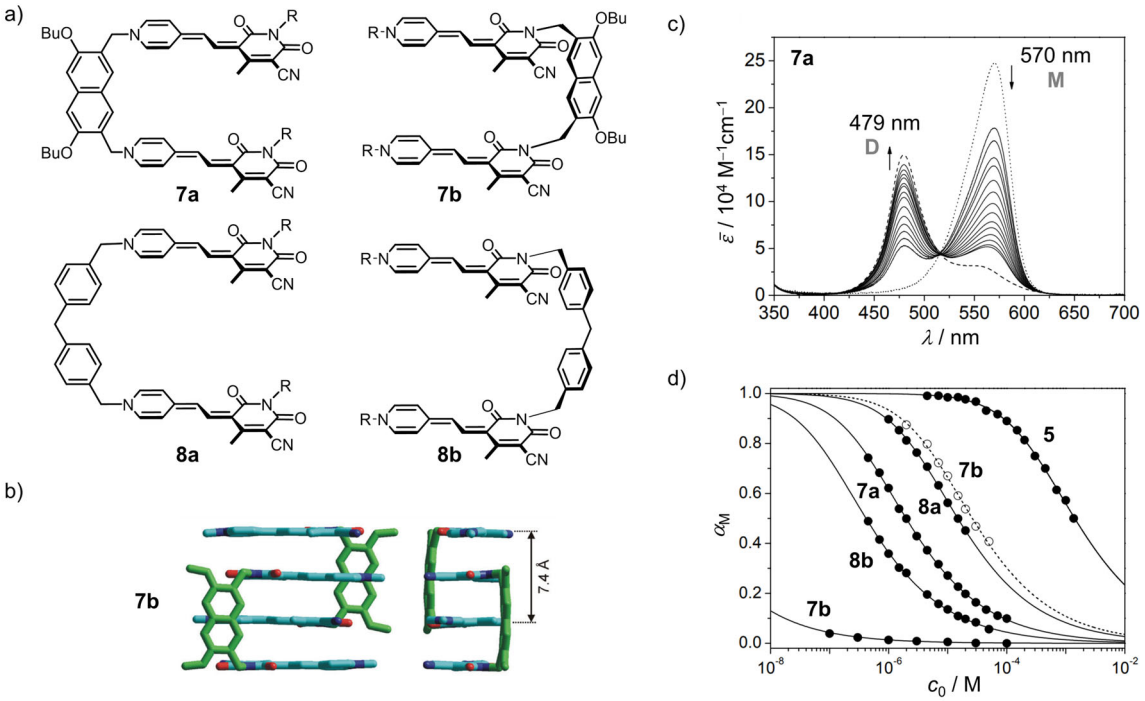

Figure 19. a) Chemical structures of bis(merocyanine) tweezers **7a**, **7b**, **8a** and **8b**. b) Geometry optimized (MM+) structure of the **7b** dimer. c) Concentration-dependent UV/Vis absorption spectra of **7a** in $CHCl_3$ (298 K). d) Fraction of monomer (α_M) calculated form UV/Vis absorption spectra of reference merocyanine **5** and **7a**, **7b**, **8a**, **8b** in $CHCl_3$ (solid circles) and **7b** in 1,2-dichloroethane (open circles) at 298 K with fit according to the dimer model. Adapted with permission from ref. [39]. Copyright 2009 WILEY-VCH Verlag GmbH & Co. KGaA, Weinheim.

The hypsochromic shift of the main UV/Vis absorption band of the tetramer stacks (460 – 488 nm) exceeds the shift of a PYOP dimer stack (λ_{max} = 490 nm) and increases in the sequence **7a**, **7b**, **8a**, **8b** (Table 3).

Table 3. Dimerization constants (K_D) and Gibbs binding energy (ΔG^0) as well as UV/Vis absorption maxima of monomer (M) and dimer (D) species from concentration-dependent self-assembly studies of **7a**, **7b**, **8a**, **8b** in $CHCl_3$ (298 K).

	K_D / M^{-1}	$-\Delta G^0$ / kJ mol^{-1}	λ_{max}(M) / nm	λ_{max}(D) / nm
Ref (5)	590	15.8	559	490
8a	6.2×10^4	27.3	569	488
7a	4.5×10^5	32.3	570	479
8b	2.1×10^6	36.1	558	466
7b	$> 10^9$	> 50	555	460

Interestingly, the binding constant K_D increases in the same order, so that the more strongly bound tetramers also exhibit the strongest exciton coupling. Attachment of the spacer at the pyridone acceptor seems advantageous for a tight PYOP stack formation. In combination with the ideal double π-π-stacking distance of the naphthalene spacer unit this leads to an

exceptionally high dimerization constant ($K_D > 10^9$ M^{-1}) for **7b** in $CHCl_3$ which could not be precisely determined anymore by UV/Vis absorption spectroscopy (Figure 19d). This also results in the most hypsochromically shifted absorption maximum within this tetramer series at $\lambda_{max} = 460$ nm. In accordance with equation (45) this illustrates the high sensitivity and significant influence of the chromophore arrangement on the exciton coupling.

Merocyanine Duplex Structures

In the next example the concept of backbone directed self-assembly was extended to larger systems. The similarity of merocyanine dipole-dipole interactions and the complementary hydrogen bonding of nucleobases, with regard to strength and directionality, inspired Liu *et al.*[133] to synthesize merocyanine analogues to peptide nucleic acid (PNA) oligonucleotides and investigate their duplex formation (Figure 20).

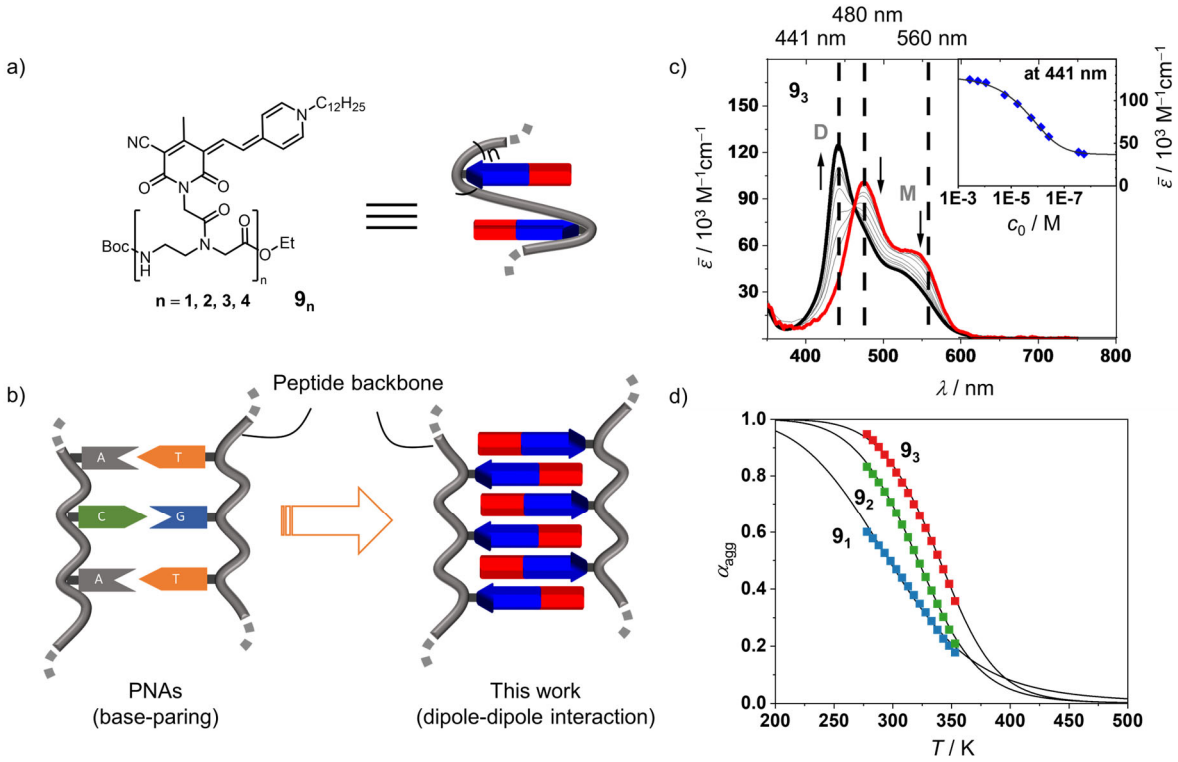

Figure 20. a) Chemical as well as schematic structure of peptide merocyanine oligomers $\mathbf{9_n}$. b) Concept of peptide backbone directed self-assembly of peptide nucleic acid (PNA) and peptide merocyanine oligomers into duplex structures. c) Concentration-dependent UV/Vis absorption spectra of $\mathbf{9_3}$ in $CHCl_3$ (298 K). Inset shows the concentration-dependent extinction coefficient at 441 nm with fit according to the dimer model. d) Comparison of the temperature-dependent degree of aggregation (α_{agg}) of $\mathbf{9_1}$, $\mathbf{9_2}$ and $\mathbf{9_3}$ in 1,4-dioxane/DMSO 95:5 ($c_0 = 1.2\times10^{-5}$ M), with fit according to the dimer model. Adapted with permission from ref. [133]. Copyright 2022 The Authors. Angewandte Chemie International Edition published by Wiley-VCH GmbH.

One up to four PYOP chromophores were covalently linked to a peptide backbone (Figure 20a). Double strand formation by dipole-dipole interaction was observed for $\mathbf{9_{1\text{-}3}}$. The self-assembly of these oligomers was investigated by concentration-dependent UV/Vis

absorption measurements in $CHCl_3$ (298 K) and evaluated successfully with the dimer model (Figure 20c). Binding constants of 3.0×10^5, 1.1×10^6 and 3.8×10^5 M^{-1} were determined for **9₁**, **9₂** and **9₃**, respectively. The similar magnitude of these values is at first glance surprising, especially in comparison to the bis(merocyanine) tweezers of Lohr *et.al.*[39] presented above. However, the present system features much more structural flexibility due to the peptide backbone. Temperature-dependent UV/Vis absorption studies (melting curves in 1,4 dioxane/DMSO 95:5, Figure 20d) indicated that the enthalpic gain indeed increases as expected with the number of interacting dipolar PYOP chromophores. However, the concomitant increase of the entropy penalty reduces the binding strength for the larger systems. Furthermore, the intermolecular duplex formation of **9₂** and **9₃** has to compete with an intramolecular folding process, as evident from the UV/Vis absorption band at ~ 480 nm for monomeric **9₂** and **9₃** in $CHCl_3$. For the tetramer **9₄** the flexible peptide backbone was not able to guide the assembly into a defined duplex anymore. The data suggests the presence of a mixture of folded monomeric and self-assembled species of **9₄** in $CHCl_3$ solutions of varying concentration.

Merocyanine Foldamer Series

Even larger but still defined PYOP π-stacks were obtained in a foldamer series of Hu and Schulz *et al.*[40-41, 129] Up to six chromophores were covalently connected by peptide chemistry with a pyridinedicarboxylic acid spacer (Figure 21a,b).

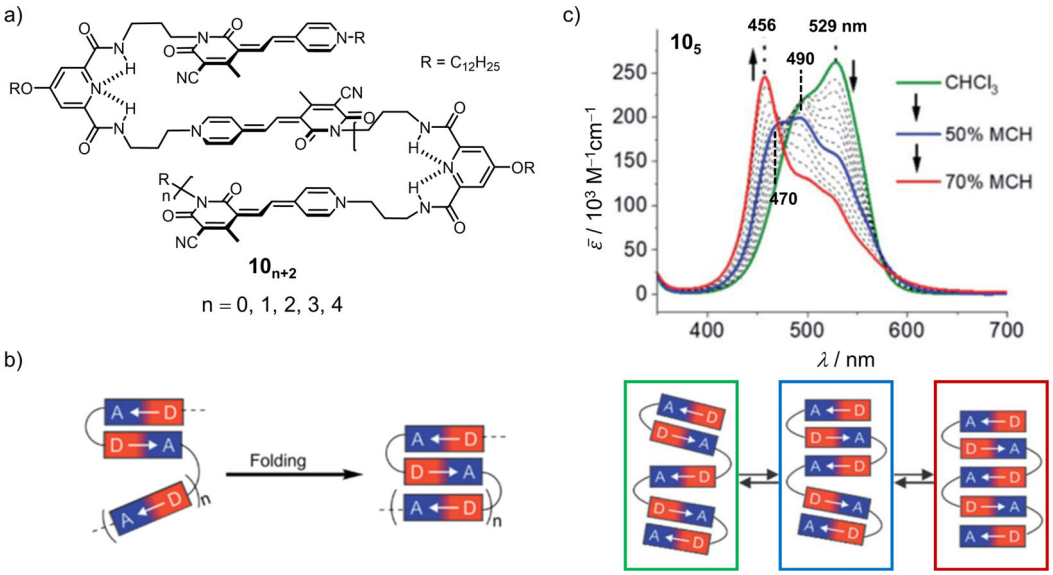

Figure 21. a) Chemical and b) schematic structure of merocyanines foldamers **10n+2**. c) Solvent-dependent UV/Vis absorption spectra of **10₅** in $CHCl_3$/MCH mixtures (293 K) and schematic structures of the corresponding step-wise folding stages. Adapted from ref. [40] with permission from the Royal Society of Chemistry.

The turn-unit connecting neighbouring chromophores promoted anti-parallel π-stacking by preorganization through intramolecular H-bonding. For the pentamer **10$_5$**, step-wise folding was observed in solvent-dependent UV/Vis absorption studies ($CHCl_3$ → $CHCl_3$/MCH 3:7, Figure 21c). The gradual formation of stacks of increasing size was clearly indicated by the appearance of more and more hypsochromically shifted absorption bands. The spectrum in pure $CHCl_3$ exhibits two absorption maxima, which can be rationalized by a mixture of strongly H-type coupled dimer stacks (λ_{max} = 490 nm) and only weakly coupled single chromophores (λ_{max} = 529 nm) in a partly folded structure. Upon decreasing the polarity ($CHCl_3$/MCH 1:1) the band at 529 nm decreases and an additional band at 470 nm appears, which corresponds presumably to a trimer stack. Upon further decrease of the solvent polarity a narrow absorption band at 456 nm gains in intensity, indicating rigidification of the five exciton coupled chromophores in the fully folded pentamer stack. A similar folding behaviour with the same corresponding UV/Vis absorption bands was also observed for the other PYOP foldamers of different length (**10$_{2\text{-}6}$**). Although a detailed thermodynamic analysis of the folding process was not possible, it was evident from the UV/Vis absorption spectra, that the driving force to form the fully folded stack was significantly higher for the trimer and pentamer compared to the tetramer and hexamer. The oligomers with an even number of chromophores preferably formed dimer stacks (λ_{max} ~ 490 nm) with reduced electrostatic interactions between these dimer units due to cancelation of the anti-parallel aligned molecular dipole moments.

Polymeric Merocyanine Assemblies

Fernández *et al*.[134] observed the formation of supramolecular lamellae from a *p*-xylene-connected bis(merocyanine) **11** (Figure 22). The self-assembly was monitored by temperature- as well as concentration-dependent UV/Vis absorption measurements in $CHCl_3$. Decrease of the monomer (M) absorption band at 587 nm and formation of an aggregate species (H) with a hypsochromically shifted absorption band at 462 nm was observed (Figure 22c). Compared to the other results for UV/Vis absorption spectra of this PYOP chromophore, this is in the range expected for a tightly packed H-type tetramer stack.[39] A well-defined isosbestic point indicates an equilibrium between only two distinct species. The temperature- as well as solvent-dependent datasets revealed a cooperative self-assembly mechanism with a large nucleus size of 8-10 monomers. Evaluation of the concentration-dependent data gave a binding constant for elongation of $K = 1.6\times10^6$ M^{-1} ($CHCl_3$, 298 K).

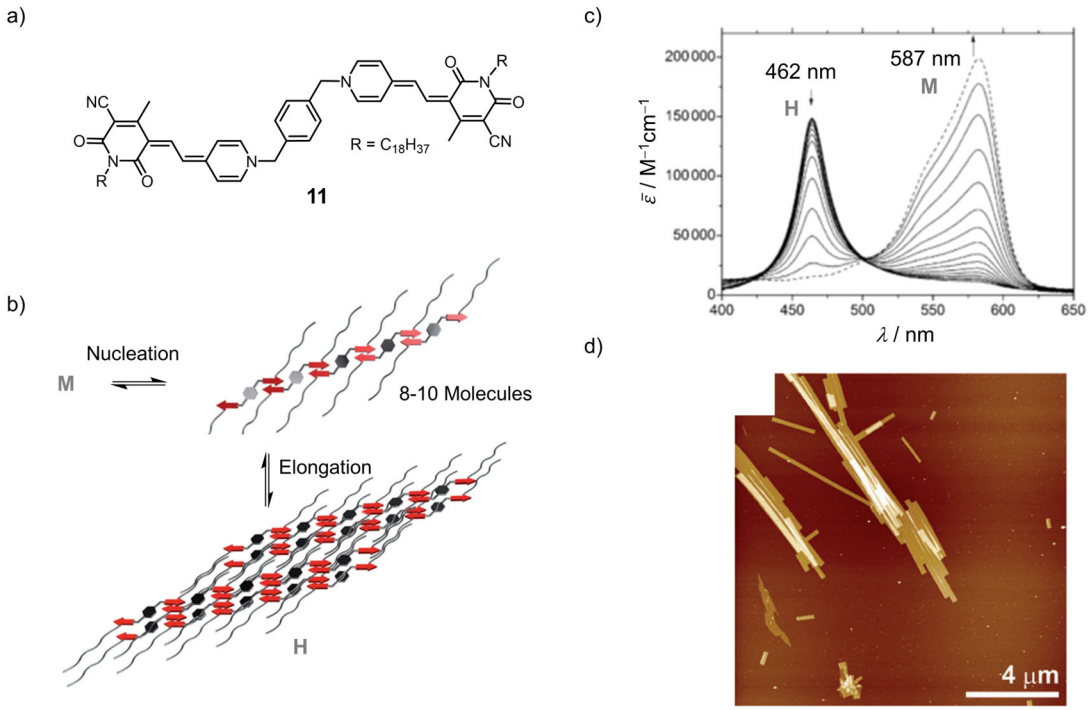

Figure 22. a) Chemical structure of bis(merocyanine) **11** monomer (M). b) Schematic structures proposed for nucleus and lamellar higher aggregate (H) formed by cooperative self-assembly of **11**. Red arrows indicate the orientation of the dipolar merocyanine chromophores. c) Concentration-dependent UV/Vis absorption spectra of **11** in $CHCl_3$ (298 K). Arrows indicate spectral changes upon dilution. d) AFM height image of drop-casted $CHCl_3$ solution of **11** on Mica. Adapted with permission from ref. [134]. Copyright 2013 WILEY-VCH Verlag GmbH & Co. KGaA, Weinheim.

By changing the connectivity of the two PYOP chromophores to *m*-xylene, helical rod like assemblies were obtained already in 2003 (Figure 23). Yao and Lohr *et al.*[135-139] investigated the self-assembly of bis(merocyanine) **12** in solvent mixtures of different polarity. In solvents of intermediate polarity, a mixture of non-aggregated dyes (M, $\lambda_{max} \sim 570$ nm) and self-assembled dimers (D, $\lambda_{max} \sim 480$ nm) were observed. The presence of dimer units indicates in this case the formation of a single stranded supramolecular polymer due to the bifunctionality of the monomer. In unpolar solvents, a strongly hypsochromically shifted narrow aggregate band at $\lambda_{max} \sim 447$ nm emerged. The formation of this higher aggregate species (H) is a kinetic process and was studied in more detail by solvent- and time-dependent UV/Vis absorption measurements. By attaching chiral side chains to **12** the helicity of the aggregate fibres could be controlled. Time-dependent circular dichroism (CD) studies revealed, that after initial formation of a kinetically preferred aggregate structure, slow rearrangement of the chromophores occurs, which reverts the sign of the bisignate CD signal without significantly changing the UV/Vis absorption spectrum.

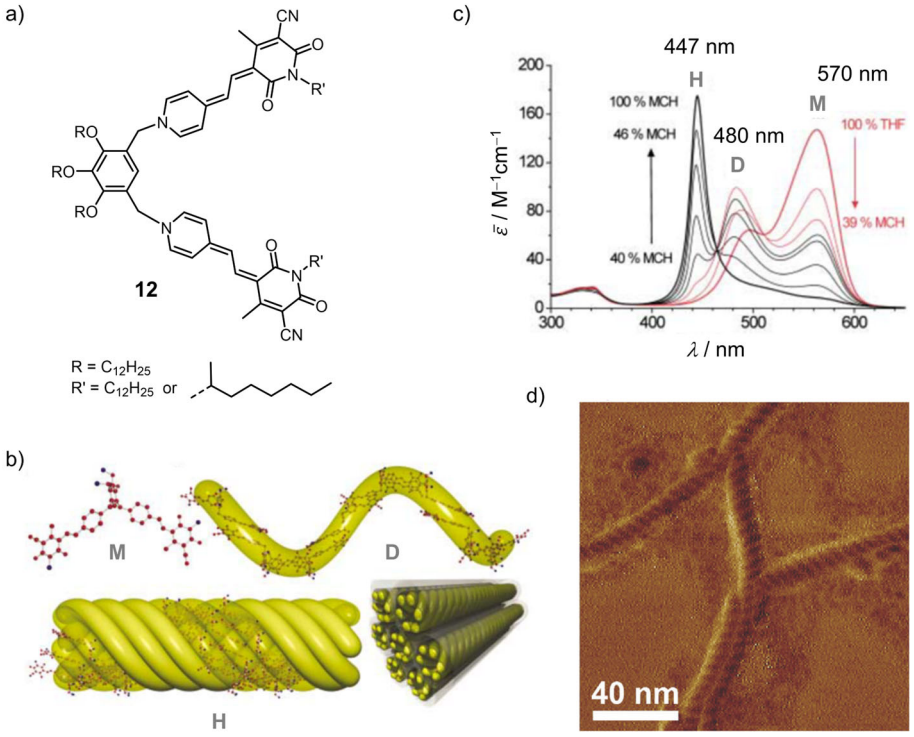

Figure 23. a) Chemical structure of bis(merocyanine) **12**. Achiral and chiral derivatives were investigated. b) Proposed self-assembly mechanism of monomers (M) into single stranded polymers through dimerization of the chromophore units (D) and subsequent formation of helical fibres (H). c) Solvent-dependent UV/Vis absorption spectra of **12** in MCH/THF mixtures (298 K). d) AFM phase image of spin-coated solutions of **12** in MCH/THF 7:3 onto HOPG. Adapted with permission from ref. [136]. Copyright 2003 WILEY-VCH Verlag GmbH & Co. KGaA, Weinheim. And ref. [137]. Copyright 2005 WILEY-VCH Verlag GmbH & Co. KGaA, Weinheim

The previously introduced folda-pentamer $\mathbf{10_5}$ (P) of Hu *et al.*[129] also formed a higher aggregate species (H), with a narrow and strongly hypsochromically shifted UV/Vis absorption band in unpolar environment ($CHCl_3$/MCH 8:2, Figure 24). The kinetic formation of this aggregate, with an absorption band at 399 nm, was monitored by time-dependent UV/Vis absorption measurements (Figure 24c). The absorption maximum is further hypsochromically shifted than expected for an extended single strand of π-stacked PYOP merocyanines, based on the data of the other investigated systems of defined size.[24, 40, 133] With increasing size of the PYOP chromophore π-stacks, the shift of the UV/Vis absorption maximum seems to saturate after about six chromophores at $\lambda_{max} \sim 440$ nm (see also Figure 25).

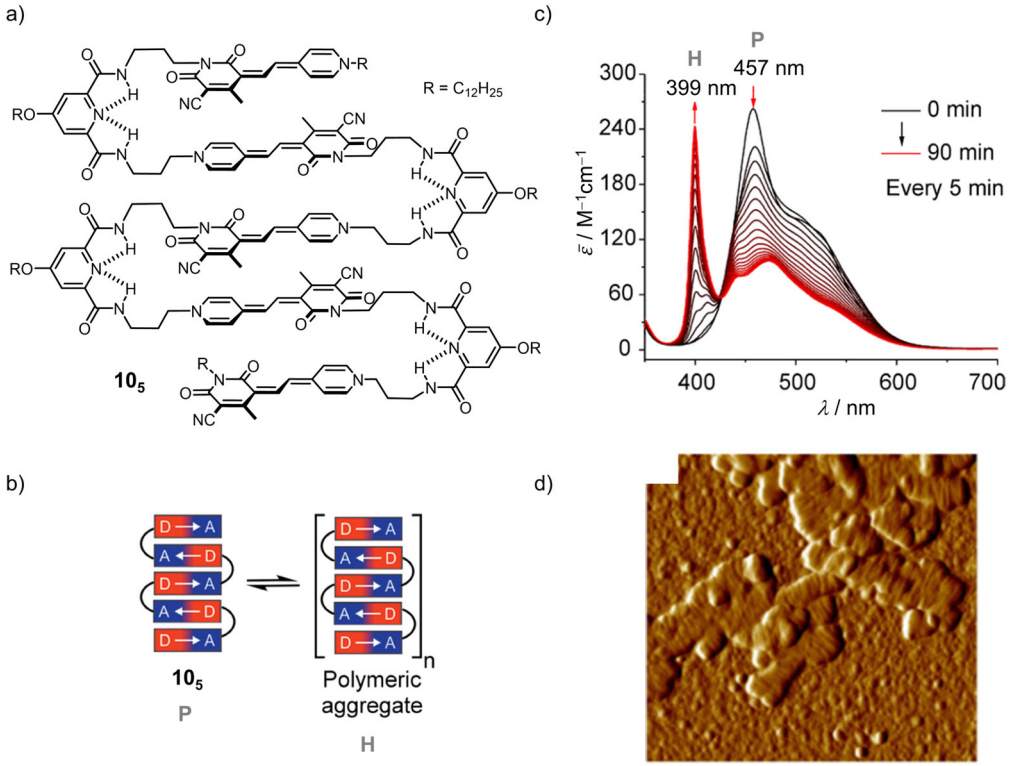

Figure 24. a) Chemical structure of folda-pentamer **10**$_5$. b) Schematic representation of **10**$_5$ as fully folded monomer (P) and higher aggregate (H) of unknown structure. c) Time-dependent UV/Vis absorption spectra of the self-assembly of **10**$_5$ into a higher aggregate in MCH/$CHCl_3$ 8:2 (323 K). d) AFM image (amplitude) of the higher aggregate of **10**$_5$ spin-coated from MCH/$CHCl_3$ 8:2 solution onto silicon wafer (SiO_x). Adapted with permission from ref. [129]. Copyright 2020, American Chemical Society.

Structure elucidation of those polymeric assemblies is very challenging. The analytical methods to investigate the molecular arrangement within supramolecular polymers are very limited. Often only assumptions, based on previous results and comparable systems, are possible. In this regard, the characteristic changes in the UV/Vis absorption spectrum of PYOP assemblies can be a helpful first indication on the number of coupled chromophores. However, to draw reliable conclusions, sound structure-property relationships provided by additional experimental techniques and including the effects of the environment, are needed. This field leaves room for further investigations.

2.2.3 Summary

The PYOP merocyanine is a highly interesting chromophore for supramolecular chemistry. Its easy synthetic functionalizability at multiple positions of the chromophore core (R^1, R^2, R^3, R^4, Figure 13a) allows the design of a variety of building blocks for all kinds of supramolecular architectures based on single- or multi-chromophore monomers. PYOP stands out among the merocyanines because of its exceptionally high molecular ground state dipole moment (μ_g = 17 D), which results in strong and highly directional intermolecular interactions

between the chromophores even in polar solvents like $CHCl_3$ ($K_D = 590\ M^{-1}$ for **5**, 298 K). The large transition dipole moment ($\mu_{eg} = 10.7$ D) and associated intense and mainly unstructured absorption band at 559 nm ($\varepsilon_{max} = 125\,000\ M^{-1}cm^{-1}$, **5** in $CHCl_3$), which is highly sensitive to the environment (negative solvatochromism, strong exciton coupling), make it also interesting from a functional point of view. Strong exciton coupling ($\sim \mu_{eg}^2$), which is for this chromophore usually well described by the simple Kasha model, gives rise to pronounced spectral changes upon aggregate formation which can easily be studied by UV/Vis absorption spectroscopy to elucidate the self-assembly mechanism and deduce the arrangement and number of π-stacked chromophores.

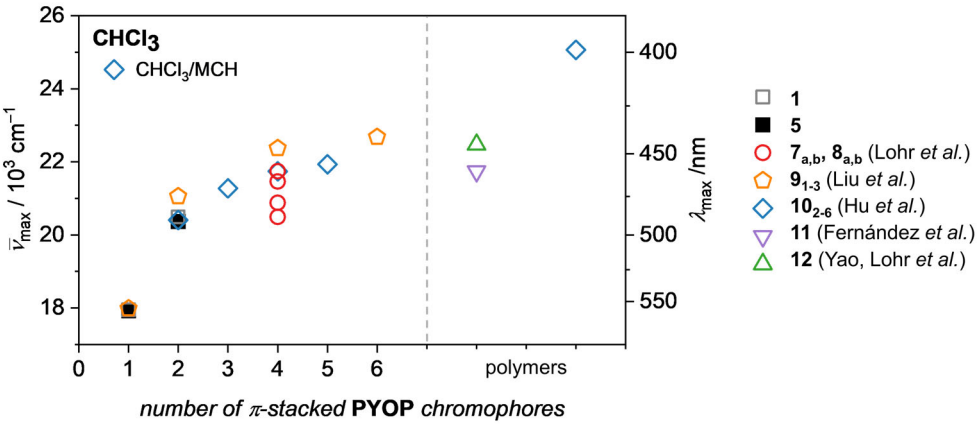

Figure 25. Maxima of UV/Vis absorption bands of the different PYOP merocyanine species presented in *Chapter 2.2.2*, as well as reference merocyanines **1** and **5**, ordered by number of π-stacked chromophores as proposed by the aggregate structure model. All values are from $CHCl_3$ solutions, except for $\mathbf{10}_{2\text{-}6}$ which are from $CHCl_3$/MCH solvent mixtures.

The values for the UV/Vis absorption maxima of the different defined or polymeric H-type coupled PYOP assemblies presented in this chapter, are summarized in Figure 25 (all values in $CHCl_3$ or $CHCl_3$/MCH). Clear structure-property trends can be observed. Both, the number and arrangement of interacting chromophores strongly influence the position of the UV/Vis absorption band. Particularly for a series of structurally similar assemblies, this can provide a very convenient insight into the chromophore arrangement within an aggregate species by simply recording a UV/Vis absorption spectrum.

For the present thesis, the interesting supramolecular and functional properties in combination with the extensive background-knowledge on this chromophore represented in *Chapter 2.2* make PYOP a very useful tool to investigate fundamental aspects of supramolecular self-assembly.

CHAPTER 3

–

CONCENTRATION-, TEMPERATURE-, AND SOLVENT-DEPENDENT SELF-ASSEMBLY: MEROCYANINE DIMERIZATION AS A SHOWCASE EXAMPLE FOR OBTAINING RELIABLE THERMODYNAMIC DATA

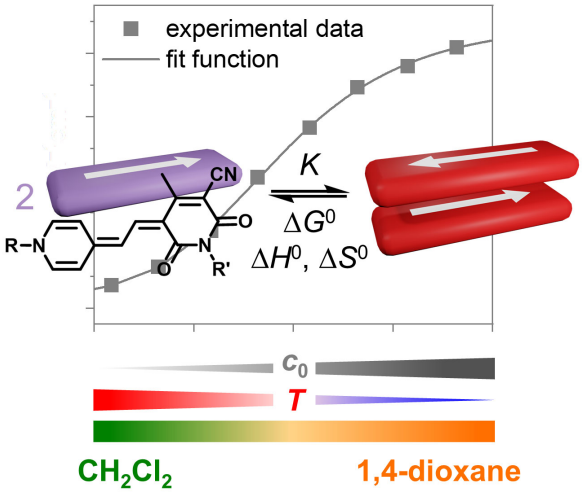

This chapter and the associated supporting information have been published in:

Y. Vonhausen, F. Würthner, *Chem. Eur. J.* **2023**, *29*, e202300359.

Abstract. Mathematical models for the concentration-, temperature-, and solvent-dependent analysis of self-assembly equilibria are derived for the most simple case of dimer formation, to highlight the assumptions these models and the thus determined thermodynamic parameters are based on. The three models were applied to UV/Vis absorption data for the dimerization of a highly dipolar merocyanine dye in 1,4-dioxane. Isothermal titration calorimetry (ITC) dilution experiments were performed as an independent reference technique. While the

concentration-dependent analysis is according to our studies the most reliable method, also the less time-consuming temperature-dependent evaluation can give accurate results in the present example, despite small thermochromic effects. In contrast, the strong negative solvatochromism of the merocyanine tampers with the results from the solvent-dependent evaluation. Even though the studies presented in this work are limited to the monomer-dimer equilibrium of a dipolar dye, the basic principles can be transferred to other chromophores and different self-assembly models, including those for supramolecular polymerization.

3.1 Introduction

In the field of supramolecular chemistry, the thermodynamic parameters ΔG^0 (Gibbs energy of binding), ΔH^0 (binding enthalpy) and ΔS^0 (binding entropy) and in particular the association constants K at room temperature are of utmost importance to characterize self-assembly processes.[15] However, whilst a plethora of articles is available that in a critical way discuss the theoretical and experimental aspects of relevance for the thermodynamic characterization of host-guest systems,[19, 98, 140-141] self-assembly did not receive comparable attention from the fundamental point of view. Whilst it is obvious that the perfect method, such as the constant-host titration for host-guest systems, covering the whole range from pure host up to almost entirely present host-guest complex,[19] is not adaptable to self-assembly processes, we will here address the critical aspects of solvent- and temperature-dependent analyses that became more and more common recently in the elucidation of self-assembly processes into larger aggregates, also called supramolecular polymers. Compared to conventional concentration-dependent studies as preferred in our research on dye aggregates,[66, 142] these methods appear simpler to perform and in some cases are indeed the only viable option, for instance in cases of insufficient solubility or instrumental limitations on the applicable concentration range. Here, temperature[33-34, 36, 44-50] or solvent-dependent[51-55] studies can be alternatives, which have both successfully been applied in literature for a variety of systems. For complex self-assembly systems often only a mixture of different techniques and conditions can provide a full understanding of the self-assembly process.[25, 30, 143-144] Temperature-dependent measurements have the advantage that all thermodynamic parameters can be obtained from one individual sample at a given concentration in a single automated measurement. It is the method of choice for studies on duplex formation in nucleic acid chemistry, where usually only small sample amounts are available.[65] For the other two

approaches, more time (and compound) consuming sample preparation is necessary. In solvent-dependent measurements, the range of (dis)assembling force can be tuned for every system by the choice of two solvents with contrasting solvation properties, often simplified by the dielectric constant (ε_r).[76] By gradually changing the solvent mixture from a "bad" solvent where the fully aggregated species is present to a "good" solvent, where all molecules are in the monomeric state, the entire aggregation process can be monitored. The accessible concentration and temperature range, on the other hand, usually set much tighter boundaries. So it is often not possible to reach both end-points of the self-assembly process by these approaches. Also for solvent- and temperature-dependent studies it has to be emphasized that simple intramolecular folding processes might generate similar spectral changes as intermolecular aggregate formation.[43, 145] Thus, whilst each of the available methods of concentration-, temperature-, and solvent-dependent experiments has advantages, it is important to understand and mind the underlying assumptions behind the data evaluation models to derive reliable results.

With this goal in mind, we study here a most simple showcase example, i.e. dimerization as the most simple self-assembly process. For this study we chose merocyanine dyes, whose strong and directional dipole-dipole interactions lead to the formation of structurally well-defined dimer aggregates for which the antiparallel orientation affords a cancellation of the dyes' large ground state dipole moments (μ_g(M) = 17 D, Figure 26a).[42, 66] Therefore, whilst dimerization is strongly favoured by pronounced dipole-dipole interactions, elongation into extended dye aggregates is disfavoured by the reduced electrostatic surface potential and concomitant lack of dipolarity of the respective dimers.

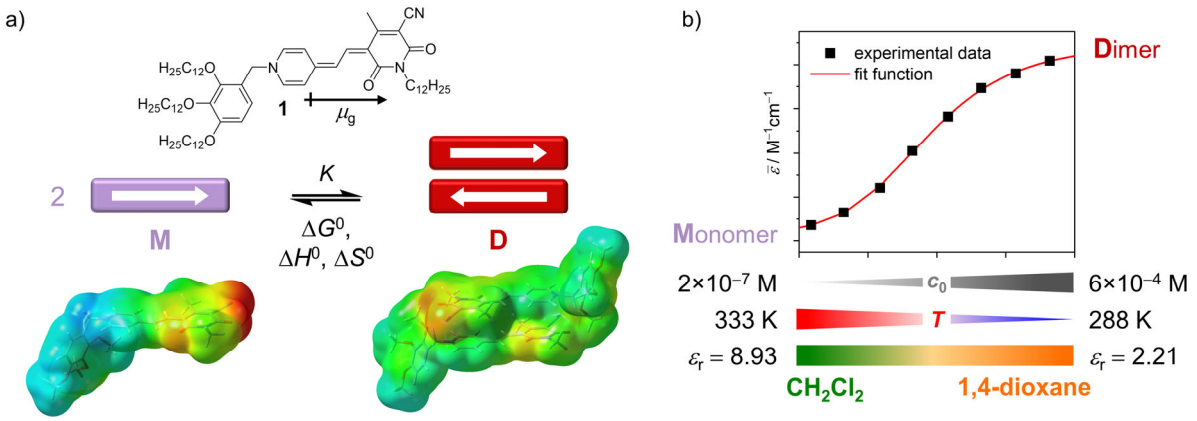

Figure 26. a) Monomer (M) – dimer (D) equilibrium of merocyanine **1** with electrostatic surface potential (DFT) of both species visualizing the reduction in dipolarity upon dimerization. b) Schematic representation of experimental self-assembly data (black squares) and the corresponding fit function (red line) to determine thermodynamic parameters for the dimerization of **1**.

In our earlier research we have gained detailed insights in the structure of these dimer aggregates and the very high preference of these dyes for dimerization over further elongation.[146-147] Accordingly, within the studies carried out here we can ignore further growth into larger oligomers and thereby explore the fundamental critical aspects for a most simple monomer-dimer self-assembly system. Additionally, the characteristic changes in the absorption properties of the π-stacked merocyanine chromophores due to H-type exciton coupling upon dimerization[42, 148] allow easy monitoring of the self-assembly process by UV/Vis spectroscopy. Therefore, highly dipolar merocyanine derivatives are frequently used in the field of supramolecular chemistry to construct elaborate aggregate structures, which help to elucidate important structure-property relationships.[14, 149] To investigate the aggregation mechanism of such systems and to determine the thermodynamic parameters for the self-assembly process, concentration-dependent UV/Vis absorption measurements were hitherto applied as the most straightforward method.[16] To assess the suitability of the other approaches for the investigation of merocyanine dye self-assembly into discrete dimer species, an extensive UV/Vis absorption study is presented in this work. It allows a direct comparison of the results from concentration-, temperature-, and solvent-dependent measurements for the dimerization of merocyanine **1**[150] in 1,4-dioxane. Additionally isothermal titration calorimetry (ITC) dilution experiments were performed to obtain reference values for K and ΔH^0 from an independent technique.

To illustrate the principles behind the evaluation of concentration-, temperature-, or solvent-dependent self-assembly data all necessary equations were derived step by step in *Chapter 2.1* for this simplest case of dimer formation, and the assumptions the models are based on were pointed out. Even though this work focuses on a specific example, it is emphasized that the same principles and assumptions also apply for other self-assembly processes, e.g. isodesmic and cooperative polymerization[18, 21] or host-guest systems[19]. Only the mathematical description of the supramolecular equilibrium has to be adapted accordingly. Thus, we hope these studies on merocyanine dimerization provide an easy introduction to the topic, which can help readers, especially people new to the field, to find the best suited method to investigate the self-assembly of their system of interest.

3.2 Results and Discussion

Merocyanine **1**, which was employed in the following studies, was synthesised according to literature known procedure.[150] This donor-acceptor chromophore is known to dimerize in solvents of intermediate polarity like 1,4-dioxane mainly driven by strong dipole-dipole interactions ($K \sim 10^4 - 10^5$ M^{-1}).[66] The intense UV/Vis absorption ($\mu_{eg}(M) \sim 11$ D)[146] and defined spectroscopic changes upon aggregate formation due to H-type exciton coupling make it a well suited probe for self-assembly studies by UV/Vis spectroscopy. For the monomeric chromophore of **1** a large molecular ground state dipole moment of $\mu_g(M) = 17$ D has been determined by electrooptical absorption measurements.[66] In accordance with a decrease of the dipole moment upon excitation ($\mu_e(M) = 13$ D) the charge transfer (CT) UV/Vis absorption band of the monomer species shows a pronounced negative solvatochromism (blue shift in solvents of higher polarity). Also for the dimer species a less pronounced negative solvatochromism has been observed.[146] Three repetitions were performed for each concentration-, temperature- and solvent-dependent UV/Vis absorption study. Due to the high accuracy of the instrument and sample preparation, the standard deviation between independent runs was in the same range or even smaller than the fit error (Table A8, A10 and A11). It must be noted, however, that this fit error only represents how well the data points match the optimized theoretical curve. It does not necessarily give any information on how close the result is to the "true" value.

3.2.1 Fit Functions

The chemical equilibrium of two identical monomeric molecules (M) forming a dimer (D) a two-state equilibrium can be written as:[17]

$$2\,M \rightleftharpoons D \qquad (1)$$

The fit equations used to evaluate the influence of concentration, temperature, and solvent on this equilibrium are summarized in the following. For a detailed derivation and discussion of those equations see *Chapters 2.1.1 – 2.1.3*. The general term which describes the experimental apparent extinction coefficient $\bar{\varepsilon}$ at a certain wavelength λ as a function of the dimerization constant K, the total sample concentration c_0 and the extinction coefficients of the pure monomer (ε_M) and dimer (ε_D) species is given by equation (18).

$$\bar{\varepsilon}(\lambda) = \varepsilon_{\mathrm{D}}(\lambda) + \left(\varepsilon_{\mathrm{M}}(\lambda) - \varepsilon_{\mathrm{D}}(\lambda)\right) \frac{-1+\sqrt{1+8K\cdot c_0}}{4Kc_0}. \tag{18}$$

The temperature dependence of the binding constant K can be described by:

$$K(T) = e^{\frac{-\Delta G^0}{RT}} = e^{\frac{-(\Delta H^0 - T\Delta S^0)}{RT}}, \tag{28}$$

with the binding enthalpy ΔH^0 and binding entropy ΔS^0, which are assumed to be temperature independent. This gives fit equation (30) for the evaluation of temperature-dependent UV/Vis absorption data for a dimer self-assembly.

$$\bar{\varepsilon}(\lambda) = \varepsilon_{\mathrm{D}}(\lambda) + \left(\varepsilon_{\mathrm{M}}(\lambda) - \varepsilon_{\mathrm{D}}(\lambda)\right) \frac{-1+\sqrt{1+8\,e^{-(\Delta H^0 - T\Delta S^0)/RT}\cdot c_0}}{4\,e^{-(\Delta H^0 - T\Delta S^0)/RT}\cdot c_0}. \tag{30}$$

The small temperature-dependence of the sample concentration c_0 can be included in the analysis and was done here as described in *Chapter 2.1.2*, by equation (34).

The solvent-dependence of K can be approximated by assuming a linear relation of the binding energy $\Delta G^{0\prime}$ in a specific solvent mixture, and the fraction of denaturating solvent f:

$$K = e^{\frac{-\Delta G^{0\prime}}{RT}} = e^{\frac{-(\Delta G^0 + m\cdot f)}{RT}}. \tag{35}$$

In equation (35) ΔG^0 is the Gibbs binding energy in the pure starting solvent and m is a linear factor, describing how strongly the second solvent influences the self-assembly equilibrium. By using this term for K in equation (18), we obtain equation (36) as a fit function for the solvent-dependent dimerization process.

$$\bar{\varepsilon}(\lambda) = \varepsilon_{\mathrm{D}}(\lambda) + \left(\varepsilon_{\mathrm{M}}(\lambda) - \varepsilon_{\mathrm{D}}(\lambda)\right) \frac{-1+\sqrt{1+8\,e^{-(\Delta G^0 + m\cdot f)/RT}\cdot c_0}}{4\,e^{-(\Delta G^0 + m\cdot f)/RT}\cdot c_0}. \tag{36}$$

3.2.2 Concentration-Dependent Analysis

The step-wise concentration-dependent measurements (from $c_0 = 6.3\times10^{-4}$ down to 2.0×10^{-7} M) of merocyanine **1** in 1,4-dioxane at 293 K in cuvettes of 0.1 up to 100 mm thickness show the transition from predominantly aggregate (λ_{max} = 492 nm, α_{agg} = 0.96) to monomer (λ_{max} = 570 nm, α_{agg} = 0.06) species upon dilution (Figure 27a). The single absorption band of the aggregate species at 492 nm clearly indicates the presence of dimers of this chromophore and excludes the presence of larger oligomers, as H-type coupling of more

than two chromophores would be accompanied by an even further blue shifted absorption maximum.[40]

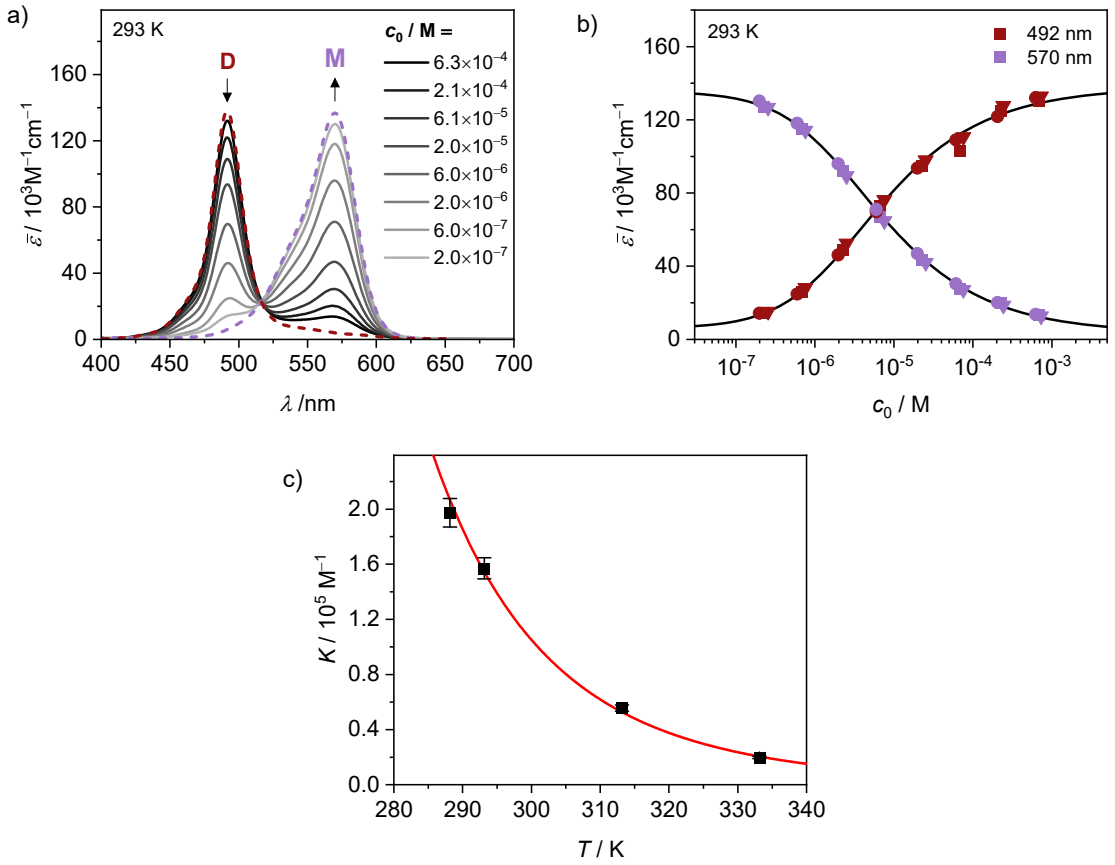

Figure 27. a) Concentration-dependent UV/Vis absorption spectra of **1** in 1,4-dioxane at 293 K ($c_0 = 6.3\times10^{-4}$ to 2.0×10^{-7} M, solid lines) and calculated (dashed lines) monomer (M, violet) and dimer (D, red) spectra from global fit analysis. b) Changes in absorption at 492 nm (red symbols) and 570 nm (violet symbols) with simultaneous fit of three datasets at each two wavelengths according to equation (18). c) Fit of K as a function of T according to equation (28) for the determination of ΔH^0 and ΔS^0.

A well-defined isosbestic point at $\lambda = 516$ nm confirms the presence of a two-state equilibrium. The changes in apparent molar extinction coefficient $\bar{\varepsilon}(c_0)$ as a function of the total sample concentration c_0 at two different wavelengths of 570 nm and 492 nm for the monomer and dimer absorption maxima, respectively, are fitted with equation (18) (Figure 27b). The values for K obtained at those two wavelengths are, as expected from the model, very similar: $(1.7\pm0.03)\times10^5$ M^{-1} and $(1.4\pm0.1)\times10^5$ M^{-1}, respectively. The fit results for K should in general be independent of the wavelength at which the fit is performed (see also Figure 31c), therefore, it makes sense to determine the binding constant as an average of the data from multiple wavelengths. By performing a simultaneous fit of three independent concentration-dependent datasets, at each two wavelengths (492 and 570 nm) $K_{293} = (1.6\pm0.1)\times10^5$ M^{-1} is obtained. This corresponds to a molar standard Gibbs binding

energy of $\Delta G^0_{293} = -29.1 \pm 0.1$ kJ mol^{-1}. The concentration-dependent spectra were additionally recorded and evaluated at 288, 313 and 333 K (Figure A55). Binding constants of $K_{288} = (2.0 \pm 0.1) \times 10^5$ M^{-1}, $K_{313} = (5.6 \pm 0.2) \times 10^4$ M^{-1} and $K_{333} = (2.0 \pm 0.1) \times 10^4$ M^{-1} were obtained. By fitting the temperature-dependence of K as a function of T (Figure 27c) according to equation (28) the binding enthalpy was determined to be $\Delta H^0 = -41.0 \pm 1.4$ kJ mol^{-1} and the entropy penalty upon dimerization $\Delta S^0 = -40.5 \pm 4.3$ J mol^{-1} K^{-1}. Very similar results were obtained from a classical van't Hoff analysis (Figure A54).

These data are in good agreement with the results from ITC dissociation experiments[151-152] of the dimer of merocyanine **1** in 1,4-dioxane at 293 K (Figure 28).

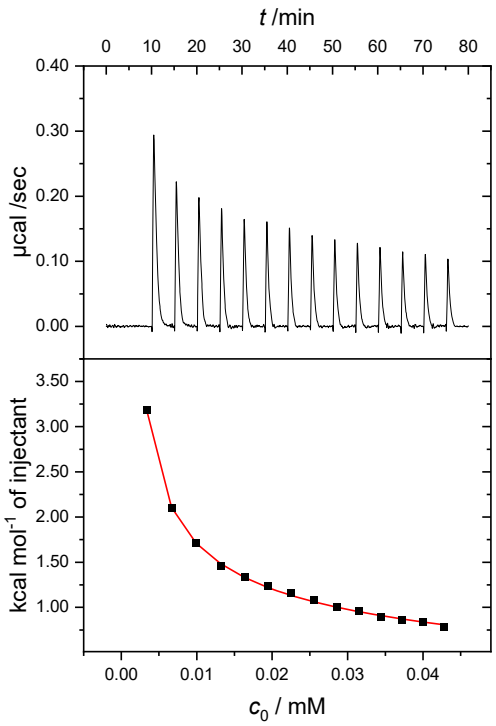

Figure 28. ITC-dilution data for the dissociation of dimers of **1** in 1,4-dioxane at 293 K.

A concentrated solution of **1** in 1,4-dioxane ($c_0 = 2 \times 10^{-4}$ M, $\alpha_{agg} = 0.88$) is sequentially injected into a calorimeter cell initially containing pure solvent. The concentration of the stock solution was limited by the solubility of the compound, which lead to a comparatively low signal to noise ratio. The dissociation of dimers upon dilution causes endothermic heat pulses which were evaluated as a mean ± standard deviation of five measurements (Table A7). This gave similar values for the binding constant ($K_{293} = (1.8 \pm 0.7) \times 10^5$ M^{-1}) and

a similar binding enthalpy of $\Delta H^0 = -44.0 \pm 6.4$ kJ mol^{-1} compared to the concentration-dependent UV/Vis measurements.

3.2.3 Temperature-Dependent Analysis

For the temperature-dependent measurements of merocyanine **1** in 1,4-dioxane the accessible temperature range was limited by the melting point of the solvent, the instruments accessible temperature range and a slow decomposition of the compound at elevated temperatures of > 343 K. Therefore, studies were performed between 288 to 333 K with a heating rate of 2 °C/min for three samples with different c_0 of 2×10^{-4}, 2×10^{-5} and 2×10^{-6} M (Figure 29).

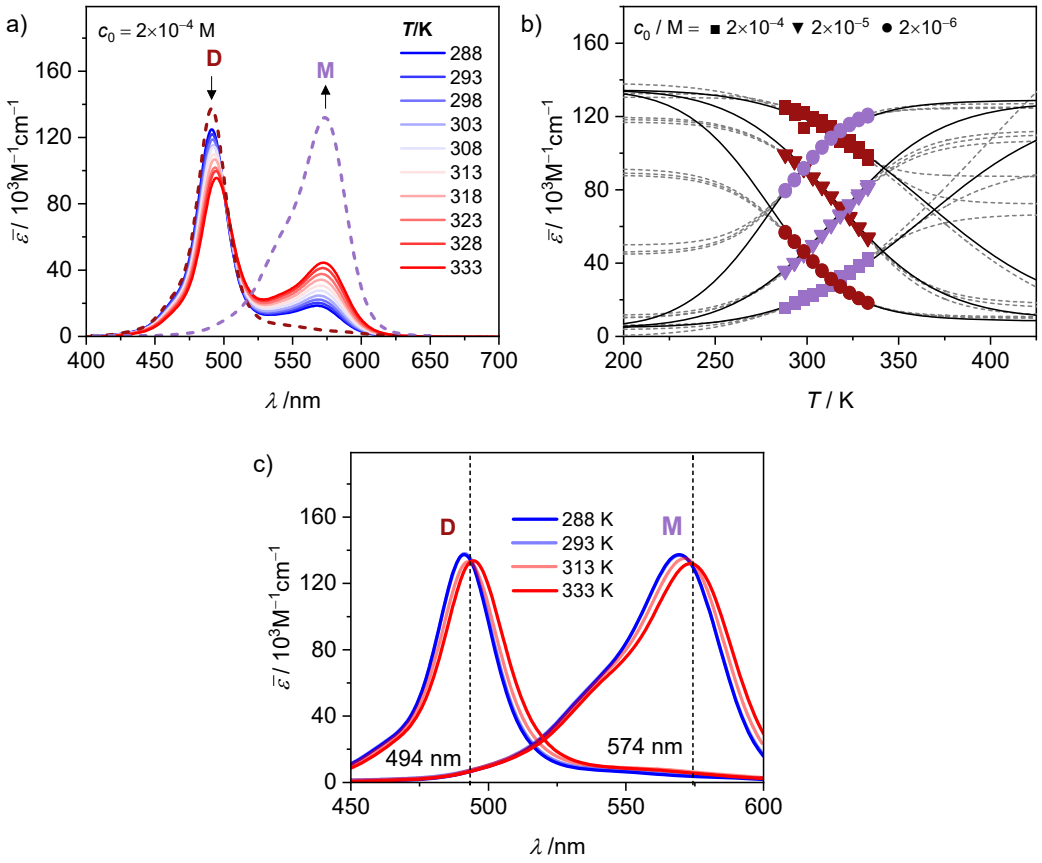

Figure 29. a) Temperature-dependent UV/Vis absorption spectra of **1** in 1,4-dioxane ($c_0 = 2\times10^{-4}$ M, 288 to 333 K, solid lines) as well as calculated spectra (dashed lines) for dimer (D, red) and monomer (M, violet) from global fit analysis of concentration-dependent data at 288 and 333 K, respectively. b) Changes in absorption at 494 (red) and 574 nm (violet) for each three measurements of samples with $c_0 = 2\times10^{-4}$ M (squares), 2×10^{-5} M (triangles) or 2×10^{-6} M (circles) with individual (dashed lines) and simultaneous (solid lines) fit functions according to equation (34). c) Calculated dimer and monomer spectra from global fit analysis of concentration-dependent data at different temperatures.

Successive heating and cooling cycles were measured and did not show significant hysteresis between the data points (Figure A56), verifying that the process is reversible and the system was given enough time to reach the thermodynamic equilibrium for each measurement. With increasing temperature, the same spectral changes can be observed as upon dilution, i.e. the

dimer absorption band at ~490 nm drops in intensity and the monomer band at ~570 nm rises (Figure 29a). However, whilst such a simple temperature-dependent study is less time-consuming than the former concentration-dependent study, in the present example it cannot ensure a good coverage of the self-assembly process from mostly aggregate to mostly monomeric species. This might be less of a problem for systems where a larger temperature-range can be applied or which follow a "steeper" self-assembly curve, e.g., due to cooperativity[45] or a high entropy contribution like in the case of oligonucleotide double strand formation[65]. In the illustrated case, due to the limited temperature range, only a small portion of the initial dimers is disassembled upon heating for the sample at $c_0 = 2\times10^{-4}$ M ($\alpha_{agg} = 0.91 - 0.71$). Thus, fitting the observed changes $\bar{\varepsilon}(T)$ of a single dataset to equation (34) did not give meaningful results (Table A9). The standard errors for the optimized parameters are very large due to the small range of the theoretical curve covered by the experimental data points and the asymptotic values for ε_M and ε_D are not always in the expected range (Figure 29b, dashed lines). For the system on hand the quality of the evaluation can be improved significantly by performing the temperature-dependent measurements for several samples with different concentrations. The datasets of three samples with concentrations of $c_0 = 2\times10^{-4}$, 2×10^{-5} and 2×10^{-6} M combined cover a meaningful fraction of the self-assembly process ($\alpha_{agg} = 0.91 - 0.07$). They all share the parameters ΔH^0 and ΔS^0 and can be fitted simultaneously according to equation (34) (Table A10).

From a simultaneous fit of 18 datasets (three repetitions for three concentrations at each 494 and 574 nm) averaged values of $\Delta H^0 = -43.5\pm0.4$ kJ mol^{-1} and $\Delta S^0 = -48.7\pm1.4$ J mol^{-1} K^{-1} were obtained (Figure 29b, solid lines). These are similar to the results from the concentration-dependent studies and the ITC experiment (Table 4). A $\Delta G^0_{293} = -29.2\pm0.6$ kJ mol^{-1} and $K_{293} = (1.6\pm0.4)\times10^5$ M^{-1} can be calculated from this. However, when looking at Figure 29c it becomes clear that those two wavelengths were particularly well chosen for our data evaluation based on our earlier results from concentration-dependent studies. Figure 29c shows a comparison of the calculated spectra of pure monomer and dimer at different temperatures. They clearly show a spectral shift and change of the width of the absorption bands of both species due to thermochromism. Also in the temperature-dependent experimental spectra shown in Figure 29a a gradual shifting of the two band maxima can be observed: for the dimer from 491 nm (288 K) to 495 nm (333 K) and for the monomer from 569 nm (288 K) to 573 nm (333 K). Those changes are not considered by the fit, which assumes ε_M and ε_D to be temperature independent. At the selected

wavelengths 494 nm and 574 nm, the temperature-dependent changes in ε_M and ε_D are, however, very small (< 3%), which is the reason for the good agreement of the results from temperature- and concentration-dependent measurements as well as ITC. However, when the fit is performed at other wavelengths fluctuating results for ΔH^0 (–34.2 to –56.0 kJ mol^{-1}) and ΔS^0 (–19.9 to –92.8 J mol^{-1} K^{-1}) are obtained. The fluctuations of ΔH^0 and ΔS^0 are not independent and follow the same trend (Figure 30).

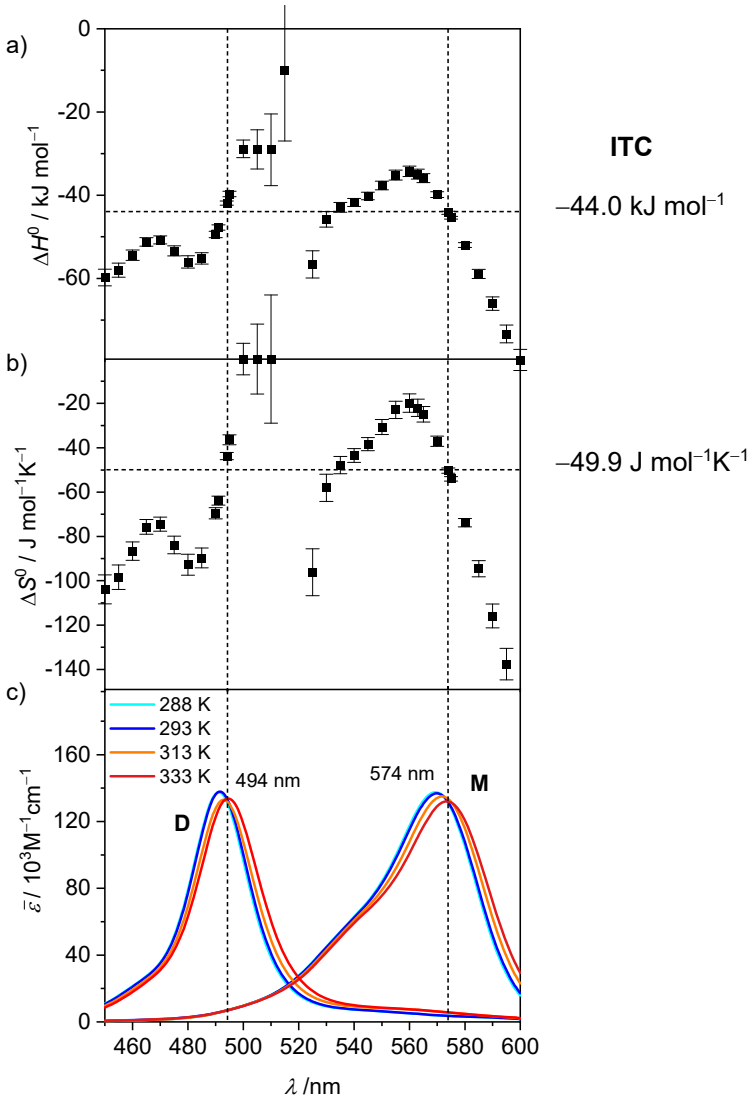

Figure 30. Fit results with standard errors for a) ΔH^0 and b) ΔS^0 according to equation (34) at different wavelengths, from simultaneous fit analysis of three temperature-dependent UV/Vis absorption datasets of **1** in 1,4-dioxane with different concentrations ($c_0 = 2\times10^{-4}$, 2×10^{-5} and 2×10^{-6} M) with shared parameters. Values from ITC are marked as reference with horizontal lines. c) Calculated dimer (D) and monomer (M) UV/Vis absorption spectra at different temperatures: 288 K (turquoise), 293 K (blue), 313 K (orange) and 333 K (red). The vertical lines mark 494 and 574 nm.

Thus, when calculating ΔG^0_{293} the resulting value is fairly constant, independent of the wavelength at which the fit is performed (see also Figure 31c). We interpret this in a way that the optimized values for ΔH^0 and ΔS^0 are very sensitive to the shape of the self-assembly

curve, since both parameters can influence the inflection point of the melting curve and the slope at this point.[91] For the nonlinear regression, a change in one parameter can thus to some degree be compensated by a corresponding change in the other and the results are therefore strongly influenced by the small errors due to thermochromism which distort the shape of aggregation curve. The resulting values for ΔG^0, which is the sum of both contributions, seem to be less sensitive to those small deviations in the experimental data. This phenomenon of apparent ΔH^0 and ΔS^0 compensation has also been discussed for ITC data.[153]

3.2.4 Solvent-Dependent Analysis

To obtain solvent-dependent data two stock solutions of merocyanine **1** in 1,4-dioxane and CH_2Cl_2 with identical concentrations (c_0 = 6.2×10^{-4} M) were mixed in different ratios and measured at 293 K. By this the transition from almost completely dimeric species in 1,4-dioxane (α_{agg} = 0.97) to fully monomeric ones in CH_2Cl_2 (α_{agg} = 0) can be monitored (Figure 31a). When performing the fit of $\bar{\varepsilon}(f)$ according to equation (36) at different wavelengths, e.g., at the maximum of the dimer (491 nm in 1,4-dioxane) and monomer (549 nm in CH_2Cl_2) absorption band, quite different results are obtained for ΔG^0_{293} in 1,4-dioxane. For the wavelengths mentioned: -20.1 ± 0.4 kJ mol^{-1} and -27.5 ± 1.5 kJ mol^{-1}, respectively. Three independent repetitions of this solvent-dependent study were performed with samples of slightly different concentrations (Figure A57, Table A11). All of them gave very similar results. A $\Delta G^0_{293} = -26.6\pm0.8$ kJ mol^{-1} which corresponds to $K_{293} = (5.6\pm1.8)\times10^4$ M^{-1} is obtained from the simultaneous fit of all three datasets at the two chosen wavelengths. This is a bit lower compared to the reference values from ITC and the concentration-dependent evaluation (Table 4). The solvent-dependent data evaluation suffers a similar problem as the temperature-dependent: ε_M and ε_D are assumed to be solvent-independent, yet due to the pronounced negative solvatochromism of the dipolar merocyanine they are not. This is obvious when comparing the UV/Vis absorption spectra of the monomer of **1** in CH_2Cl_2 and in 1,4-dioxane (Figure 31a). The band maximum is shifted from 570 nm in the less polar 1,4-dioxane (ε_r = 2.21) to 549 nm in the more polar CH_2Cl_2 (ε_r = 8.93) accompanied by a slight broadening of the band and decrease in intensity.

Comparing the ΔG^0_{293} values obtained from fits at different wavelengths additionally illustrates this problem caused by solvatochromism (Figure 31c).

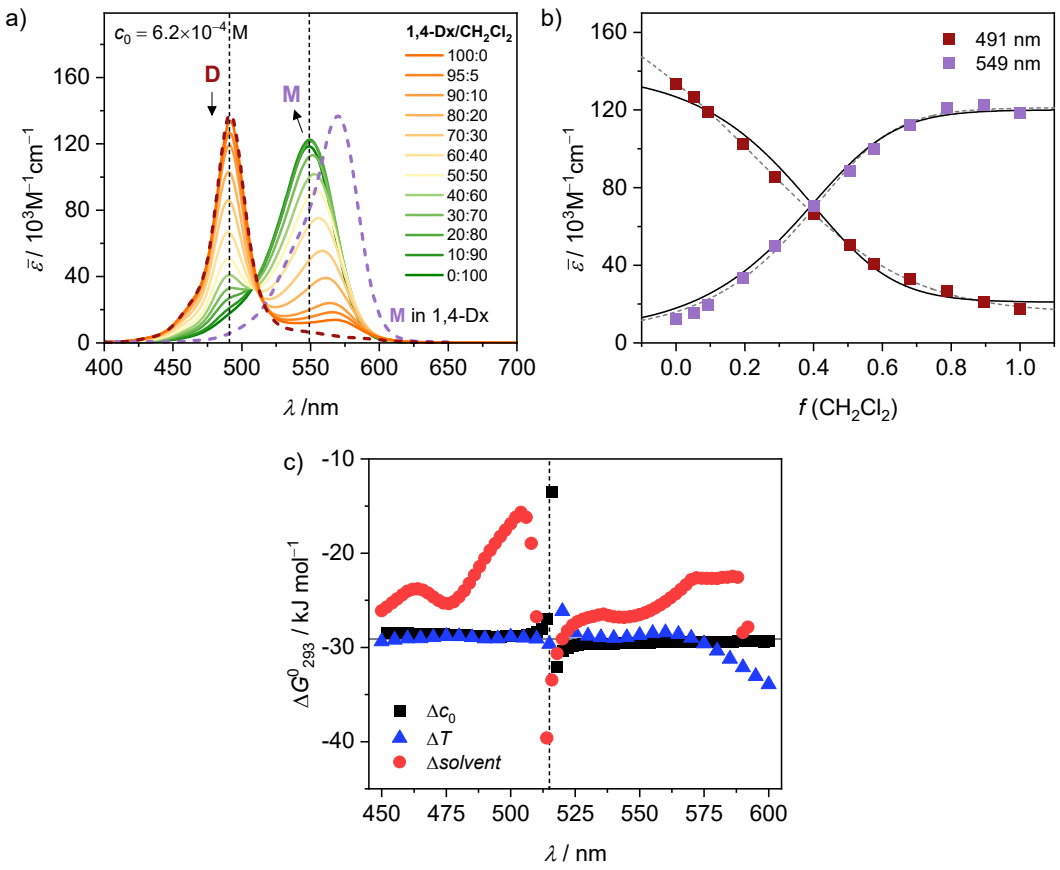

Figure 31. a) Solvent-dependent UV/Vis absorption spectra of **1** in mixtures of 1,4-dioxane and CH_2Cl_2 ($c_0 = 6.2\times10^{-4}$ M, 293 K, solid lines) as well as calculated (dashed lines) dimer (D, red) and monomer (M, violet) spectra of **1** in 1,4-dioxane. Vertical lines mark 491 and 549 nm. b) Changes in absorption at 491 nm (red symbols) and 549 nm (violet symbols) as a function of the volume fraction f of CH_2Cl_2, with individual (dashed lines) and simultaneous (solid lines) fit at two wavelengths according to equation (36). c) Results for ΔG^0_{293} from concentration- (black squares), temperature- (blue triangles) or solvent-dependent (red circles) data evaluation at different wavelengths. The dashed line marks the (pseudo)isosbestic point.

For the concentration- and temperature-dependent evaluation relatively constant results are obtained from fits over the whole absorption range (450 – 600 nm), except around the (pseudo)isosbestic point. For the solvent-dependent evaluation, on the other hand, the ΔG^0 is underestimated in the present example and the results vary significantly between –26.8 and –16.5 kJ mol^{-1} depending on the wavelength at which the fit is performed.

3.3 Conclusion

In this chapter, concentration-, temperature- and solvent-dependent UV/Vis absorption studies were performed for the well-defined dimerization process of merocyanine **1** in 1,4-dioxane (Table 4). Additionally, ITC dilution experiments provided reference thermodynamic values by an independent method. Thus, for the first time a direct comparison of these common

methods applied for the elucidation of self-assembly processes into dye aggregates and supramolecular polymers has been performed.

Table 4. Summarized results of the thermodynamic parameters for the dimerization of **1** in 1,4-dioxane from ITC in comparison with concentration- (c_0), temperature- (T) and solvent-dependent (f) UV/Vis absorption data analysis.

	ΔH^0 /kJ mol^{-1}	ΔS^0 /J mol^{-1}K^{-1}	K_{293} /10^5 M^{-1}	ΔG^0_{293} /kJ mol^{-1}
ITC (c_0)	–44.0±6.4	–49.9±19	1.8±0.7	–29.4±0.9
UV/Vis (c_0)	–41.0±1.4	–40.5±4.3	1.6±0.1	–29.1±0.1
UV/Vis (T)	–43.5±0.4	–48.7±1.4	1.6±0.4	–29.2±0.6
UV/Vis (f)	–	–	0.6±0.2	–26.6±0.8

The positive outcome is that the thermodynamic parameters acquired from concentration- and temperature-dependent measurements are in good agreement with those from ITC studies. Of particular importance is that the more simple temperature-dependent studies gave correct values for the binding constant K if thermochromic effects in the absorption spectra of the monomer and dimer of **1** are avoided by the proper choice of the wavelength used for the analysis. For a fit performed at wavelengths where the temperature-dependent changes in the absorption spectra are small, the values for binding enthalpy ΔH^0 and entropy ΔS^0 were in excellent agreement with the results independently obtained by ITC. For other wavelengths, however, fluctuating values for ΔH^0 and ΔS^0 were obtained. Here even the relatively small thermochromic effects falsified the results up to 30%. In the solvent-dependent studies, the pronounced negative solvatochromism of **1** tampered with the analysis, leading to a general underestimation of ΔG^0 with a strong dependence on the wavelength at which the fit is performed.

To draw a more general conclusion: Concentration-dependent measurements are the most recommended way to investigate self-assembly equilibria. When temperature- or solvent-dependent UV/Vis absorption data are evaluated the results should be interpreted with care and the effects of thermochromism and solvatochromism should be considered. A gradual shift of the maxima of the UV/Vis absorption bands with temperature or solvent, for example, can indicate that the observed changes are not (only) due to an assembly process. A rational selection of the wavelength at which the fit is performed might help to make these effects negligible. Additionally, for the temperature-dependent analysis it should be kept in mind,

that it is usually assumed that ΔH^0 and ΔS^0 are temperature-independent. For the solvent-dependent analysis it is important, that no specific solute/solvent interactions should be involved, so that a linear change of ΔG^0 with the solvent ratio can be approximated. It is noteworthy that in particular solvent mixtures involving water[74, 154-155] often deviate from such a linearity due to specific solvation. Taking further into consideration that also folding processes may afford similar spectral changes upon change of the solvent composition due to intramolecular aggregation[43], the method of solvent variation is the least recommended one which should always be complemented by further techniques to ensure that indeed self-assembly is the main process that is monitored. Last but not least it should be mentioned that the self-assembly mechanism might not always be conclusively known and is therefore an additional factor of uncertainty. The more parameters in the fit the less certain one can be that a good fit indicates a correct choice of mathematical model. A good agreement of concentration-dependent data to the theoretical model, where only one parameter K can be optimised (assuming that both ε_M and ε_D can at least be estimated), is a strong indication that the supposed aggregation mechanism is correct. For the temperature and solvent dependent model, which employ each two parameters, one should be more careful with such conclusions. If these issues are kept in mind, temperature- as well as solvent-dependent measurements are valid alternatives, if concentration-dependent studies are not an option, at least to get a reliable approximation for the Gibbs binding energy ΔG^0 of a self-assembly equilibrium.

CHAPTER 4

–

TWO-STEP ANTI-COOPERATIVE SELF-ASSEMBLY PROCESS INTO DEFINED π-STACKED DYE OLIGOMERS: INSIGHTS INTO AGGREGATION-INDUCED ENHANCED EMISSION

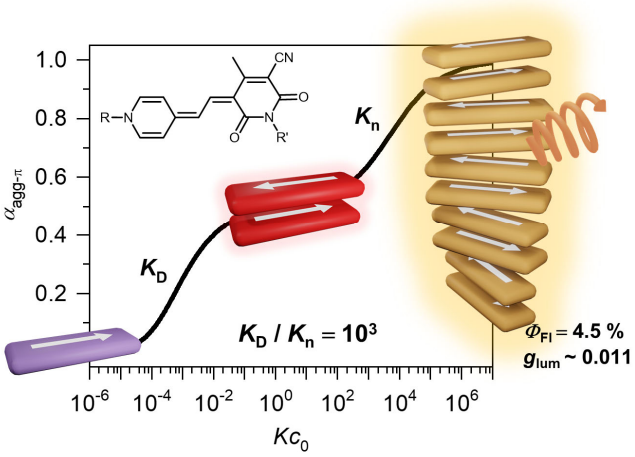

This chapter and the associated supporting information have been published in:[ii]

Y. Vonhausen, A. Lohr, M. Stolte, F. Würthner, *Chem. Sci.* **2021**, *12*, 12302-12314.

Abstract. Aggregation-induced emission enhancement (AIEE) phenomena received great popularity during the last decade but in most cases insights into the packing structure – fluorescence properties remained scarce. Here, an almost non-fluorescent merocyanine dye was equipped with large solubilizing substituents, which allowed the investigation of its aggregation behaviour in unpolar solvents over a large concentration range (10^{-2} – 10^{-7} M). In depth analysis of the self-assembly process by concentration-dependent UV/Vis spectroscopy at different temperatures revealed a two-step anti-cooperative aggregation mechanism. In the first step a co-facially stacked dimer is formed driven by dipole-dipole interactions. In a second step these dimers self-assemble to give an oligomer stack consisting of about ten dyes.

[ii] Parts of the results have been described in: Y. Vonhausen, Master Thesis, Julius-Maximilians-Universität Würzburg, **2019**.

Concentration- and temperature-dependent UV/Vis spectroscopy provided insight into the thermodynamic parameters and allowed to identify conditions where either the monomer, the dimer or the decamer prevails. The centrosymmetric dimer structure could be proven by 2D NMR spectroscopy. For the larger decamer atomic force microscopy (AFM), diffusion ordered spectroscopy (DOSY) and vapour pressure osmometric (VPO) measurements consistently indicated that it is of small and defined size. Fluorescence, circular dichroism (CD) and circularly polarized luminescence (CPL) spectroscopy provided insights into the photofunctional properties of the dye aggregates. Starting from an essentially non-fluorescent monomer (Φ_{Fl} = 0.23 %) a strong AIEE effect with excimer-type fluorescence (large Stokes shift, increased fluorescence lifetime) is observed upon formation of the dimer (Φ_{Fl} = 2.3%) and decamer (Φ_{Fl} = 4.5%) stack. This increase in fluorescence is accompanied for both aggregates by an aggregation-induced CPL enhancement with a strong increase of the g_{lum} from ~ 0.001 for the dimer up to ~ 0.011 for the higher aggregate. Analysis of the radiative and non-radiative decay rates corroborates the interpretation that the AIEE effect originates from a pronounced decrease of the non-radiative rate due to π–π–stacking induced rigidification that outmatches the effect of the reduced radiative rate that originates from the H-type exciton coupling in the co-facially stacked dyes.

4.1 Introduction

Organic materials, especially dyes and pigments, have gained considerable interest for high performance technology applications like organic solar cells or other optoelectronic devices[7] as they promise low costs and easy and versatile processing. The desired properties of those organic functional materials are, however, tightly connected to interactions between the molecules in the solid state. Therefore, predicting and controlling the *inter*molecular arrangement along with understanding structure – property relationships, is a key step toward tailor-made functional organic materials.[14, 156] For this, defined dye aggregates in solution can play an important role as model systems of reduced complexity. Already by investigating rather simple dimer systems, fundamental insights can be gained on processes like aggregation-induced enhanced emission (AIEE)[157], symmetry-breaking charge separation[59] or singlet fission[158]. For a better understanding, especially of solid-state materials, however, the investigation of larger systems is crucial. Oligomeric systems of defined size and geometry have the advantage, that multi-chromophore interactions can be studied in solution

without the drawbacks of possible phase separation or gel formation that can occur upon formation of polymeric structures. The deliberate formation of defined-sized aggregate stacks, however, is quite challenging. Good results were obtained by connecting dye molecules to covalent backbones[159-161] that favour a specific arrangement or by using templating effects[162-163]. Another, less explored, method to form small-sized aggregates, which does not require the addition of templates or the covalent linking of chromophores, is taking advantage of an anti-cooperative aggregation mechanism. The self-assembly mechanism[18], which is encoded in the molecular building blocks, dictates important properties like stability, size and size distribution of the emerging aggregates.[16, 23] Three classical cases are differentiated: isodesmic, cooperative and anti-cooperative aggregation (Figure 32).

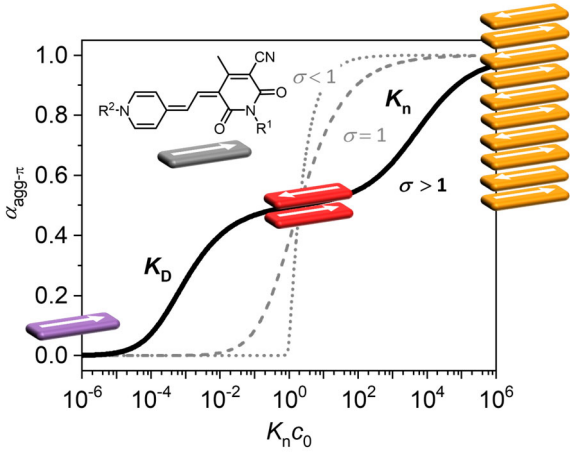

Figure 32. Degree of aggregated π-faces ($\alpha_{agg-\pi}$) as a function of $K_n c_0$ according to the isodesmic (dashed grey line), cooperative (dotted grey line) and anti-cooperative (solid black line) model with a dimer nucleus, governed by the cooperativity parameter $\sigma = K_D/K_n$. Inset shows the dipolar chromophore of merocyanine **2**.

In the case of isodesmic aggregation, all binding sites (e.g. both π-faces of a chromophore) are equivalent and independent and thus the binding constant K is equal for every individual binding event upon self-assembly. This usually leads to oligomeric aggregates with large polydispersity. In case of cooperative aggregation, first an unfavourable nucleation step (e.g. dimer formation, K_D) has to occur at a critical concentration or temperature before polymerization (K_n) takes place starting from a relatively small amount of nuclei ($K_D < K_n$). The resulting aggregates are much longer, i.e. supramolecular polymers, compared to those obtained by isodesmic aggregation.[22] Because these features are often desirable for functional supramolecular polymers cooperative self-assembly has been widely explored.[28-29] To study intermolecular interactions and their influence on optical or electronic properties, however, small and well-defined aggregates of a discrete number of chromophores are preferred. Here an anti-cooperative aggregation mechanism can be advantageous, since it is characterized by a preferred nucleus formation and less favoured further aggregation ($K_D >$

K_n) of those nuclei. Thus, rather small-sized aggregates with a narrow size distribution can be obtained[25, 34, 48]. When plotting the degree of aggregated π-faces ($\alpha_{agg-\pi}$) as a function of the dimensionless concentration Kc_0, a characteristic curve is obtained for the anti-cooperative model (Figure 32, black line), with a plateau at the concentration range, where predominantly the nucleus species is present ($\alpha_{agg-\pi} = 0.5$ for dimer case). Anti-cooperativity requires special molecular features that allow two competing *inter*molecular interactions, a strong one (e.g., H-bonding[26, 30] or dipole-dipole[31] interactions) leading to nucleus formation and a weaker one causing further self-assembly (often dispersion forces). Alternatively, the reduced binding strength for further self-assembly of the nuclei is caused by increasing sterical hindrance of bulky substituents[25, 33, 164-167] or electrostatic repulsion[48]. In this case smaller stack sizes of less than twenty chromophores have been realized. Clearly, such step-wise aggregation also provides interesting possibilities for the construction of complex structures out of relatively simple molecular building blocks[30], which can bring us one step closer toward the engineering of sophisticated supramolecular nanostructures as they can currently only be found in nature[2].

Here we will show that the utilization of both concepts, i.e. preferential nucleation and sterical encumbrance to limit growth, can afford a hierarchical growth process to realize upon increasing concentration two defined aggregate species whose functional properties could be characterized. A most suitable class of molecules for the exploration of this concept are dipolar merocyanines[42] which provide a textbook example for anti-cooperative self-assembly. Because of their significant zwitterionic character and the resulting large molecular ground state dipole moment (μ_g) of ~ 17 D for the dipolar chromophore of merocyanine **2**, dimerization is favoured due to strong, directional dipole-dipole interactions between antiparallel oriented chromophores.[66] Since the molecular ground state dipole moments compensate each other in the dimer, further aggregation is only driven by the weaker dispersion forces between the remaining two free π-faces. Owing to the significant decrease of binding strength stacking of more than two chromophores has never been observed for individual merocyanines in solution but only for bis-merocyanines with tweezer like structures[24, 39, 43] or foldamers[129] whose self-assembly could be directed into a broad variety of supramolecular oligomers and polymers. Here, by introduction of a large solubilizing substituent ("wedge")[168] with three dodecyl chains for the first time the self-assembly of the single chromophore merocyanine **2** could be investigated over a concentration range of five orders of magnitude in very unpolar solvents like MCH, where aggregation is highly

favoured. By this means, the stepwise growth into dimers and a larger aggregate species was observed in solvent- and concentration-dependent UV/Vis studies. The aggregation mechanism and the structures of the emerging aggregates were studied in detail to provide an illustrative example for the formation of defined, small-sized aggregates by stepwise anti-cooperative self-assembly.

4.2 Results and Discussion

4.2.1 Synthesis

Merocyanine **2** was synthesized according to Scheme 1.[iii]

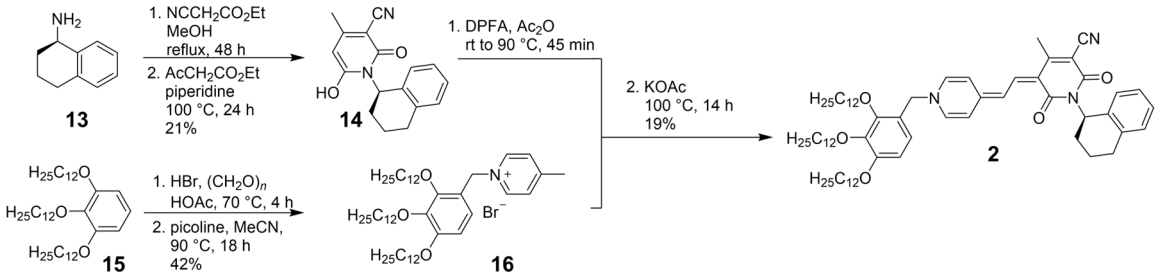

Scheme 1. Synthesis of enantiopure merocyanine **2**.

Firstly, the enantiopure amine **13** (*ee* 99.3%) was used to synthesize pyridone **14** by a sequence of condensation reactions.[66] By this means a rigid chiral center was intruduced at the acceptor moiety, which due to the close proximity to the chromophore π-core should directly affect the structure of the emerging aggregates. 4-Methylpyridinium salt **16** was obtained from 1,2,3-tris(dodecyloxy)-benzene **15** according to literature known procedure.[150] The reaction of pyridone **14** with *N*,*N*′-diphenylformamidine (DPFA) and precursor **16** gave the desired merocyanine **2** in 19% yield after purification by column chromatography. This method has been established for the synthesis of other merocyanine dyes in our earlier work.[150, 169] For details on synthetic procedures and characterization of literature unknown compounds by melting point, NMR, high resolution mass spectrometry (HRMS) and elemental analysis see the Appendix.

[iii] Synthesis was performed by A. Lohr.

4.2.2 UV/Vis Aggregation Studies

In general, the magnitude of the binding constant for a self-assembly process strongly depends on the solvent and its ability to solubilize and interact with the monomeric and aggregated species. For dipolar merocyanines, aggregation is favoured in unpolar solvents because the dipole-dipole interactions between the chromophores are stronger in unpolar compared to more polar environments. Accordingly, in the polar solvent dichloromethane (CH_2Cl_2), monomers prevail at all concentrations. Next, in concentration-dependent UV/Vis studies of **2** in 1,4-dioxane (Figure 33a,b) only the formation of antiparallel aligned dimers (D) driven by strong dipole-dipole interactions [66] can be observed ($K_D = 4.0\times10^4$ M^{-1}).

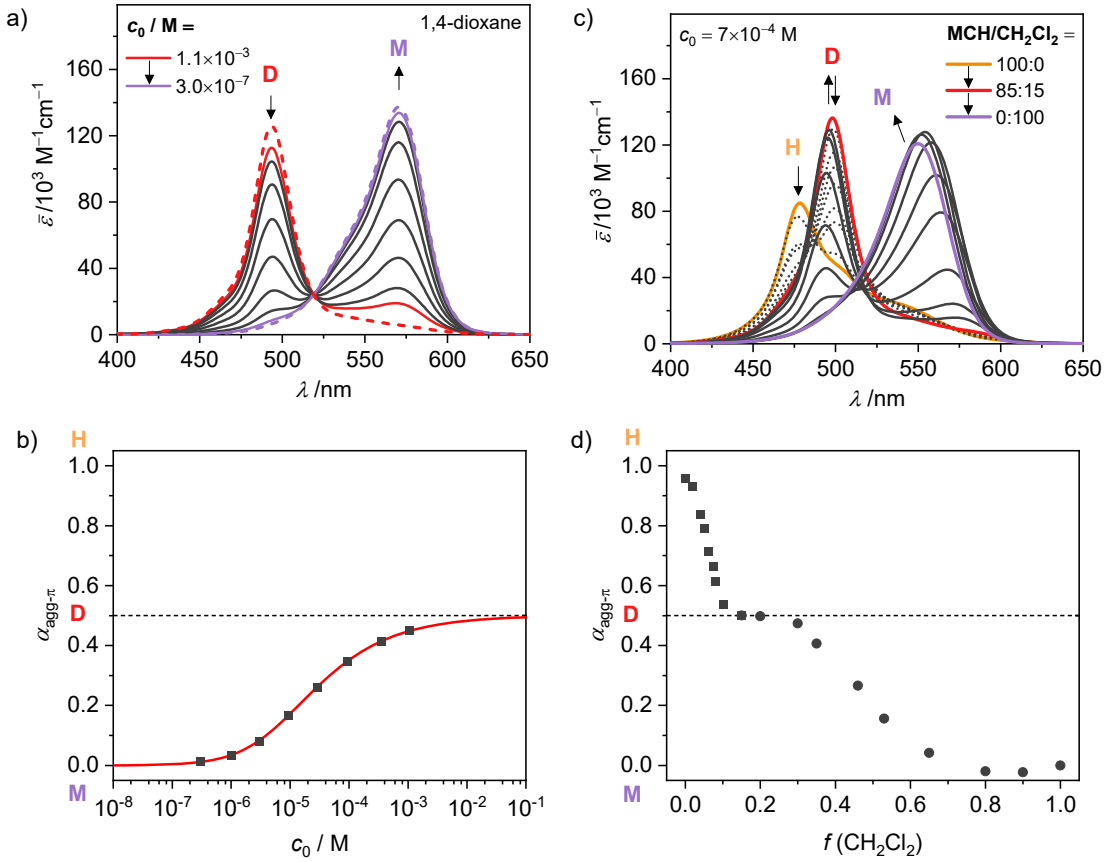

Figure 33. a) Concentration-dependent UV/Vis absorption spectra (solid lines) of merocyanine **2** in 1,4-dioxane at 298 K. Arrows indicate the spectral changes upon decreasing the concentration from $c_0 = 1.1\times10^{-3}$ to 3.0×10^{-7} M. Dashed spectra are calculated spectra for the individual monomer (M, violet) and dimer (D, red) species from global fit analysis according to the dimer model. b) Concentration-dependent degree of aggregated π-faces ($\alpha_{agg-\pi}$) calculated from the concentration-dependent UV/Vis spectra at 571 nm (black squares) and the dimerization isotherm (red line) based on the dimerization constant obtained from global fit analysis. c) Solvent-dependent UV/Vis absorption spectra of merocyanine **2** in mixtures of CH_2Cl_2 and MCH ($c_0 = 7.2\times10^{-4}$ M, 298 K). Arrows indicate spectral changes upon increasing the volume fraction of CH_2Cl_2 from 0% to 15% (dotted lines) and to 100% (solid lines). The spectra with a CH_2Cl_2 content of 0% (orange), 15% (red) and 100% (violet) are marked in color. d) $\alpha_{agg-\pi}$ as a function of the volume fraction of CH_2Cl_2 calculated from the solvent-dependent UV/Vis spectra at 550 nm (M⇌D, circles) or 498 nm (D⇌H, squares).

To trigger further aggregation of these dimer species, a solvent with even lower polarity like methylcyclohexane (MCH) is needed. In solvent-dependent UV/Vis studies (Figure 33c,d) the

polarity of the environment of **2** was stepwise decreased by successively changing the mixing ratio of polar CH_2Cl_2 and unpolar MCH. Significant spectral changes are observed as aggregate formation becomes more and more favoured.In pure dichloromethane, only the monomeric species (M) is present, as evident from the strong charge transfer (CT) absorption band at $\lambda_{max}(CH_2Cl_2) = 549$ nm[39, 66] (Figure 33c, violet line). When increasing the volume fraction of MCH to about 90%, the appearance of a hypsochromically shifted absorption band, indicating H-type exciton coupling[128, 170] can be observed at $\lambda_{max}(CH_2Cl_2/MCH\ 1:9) = 498$ nm (Figure 33c, red line). These results resemble the monomer-dimer equilibrium of **2**, also observed in the concentration-dependent UV/Vis studies in 1,4-dioxane (Figure 33a). Upon further reduction of the solvent polarity up to pure MCH an even more blue shifted absorption maximum arises at $\lambda_{max}(MCH) = 477$ nm (Figure 33c, orange line), which suggests the formation of an extended aggregate (H) with more than two interacting chromophores[24, 39]. Especially the strong solvatochromism of the push-pull chromophore[96] hinders in depth evaluation, due to the strong shifts and changes in the shape of the absorption band. When comparing the absorption spectra of the monomer of merocyanine **2** in different solvents with increasing polarity (Figure A58, see also Figure 16), a pronounced negative solvatochromism can be observed. This is in accordance with the decrease in dipole moment upon optical excitation reported in literature for this kind of dipolar chromophore ($\mu_g = 17.1$ D, $\mu_e = 12.6$ D).[66] Also for the dimer a negative but smaller solvatochromic effect can be observed.

However, the exceptionally high solubility of merocyanine **2** even in aliphatic solvents (> 10 mg mL^{-1}) allowed us to perform concentration-dependent UV/Vis studies in the unpolar solvent MCH over a large concentration range to investigate aggregation of this chromophore beyond the dimer species. The spectroscopic studies were performed in a concentration range of 1.0×10^{-2} to 9.8×10^{-8} M using cuvettes with an optical path length between 0.01 and 100 mm to sustain a suitable optical density. Since the chromophores tend to adsorb to glass surfaces in the low-polar MCH environment, silanized glassware (for silanization procedure see the Appendix) had to be used. Furthermore, samples in MCH showed some kinetic effects and needed time to equilibrate after concentration or temperature change (Figure A60 and Figure A61). Accordingly, the samples were always measured several times in varying time intervals, to ensure the equilibrium state had been reached. The samples in MCH needed several hours to equilibrate after dilution and were allowed to equilibrate at room temperature overnight. After temperature change, the individual samples were measured in intervals of 5

to 10 minutes until no more changes could be observed in the respective absorption spectrum (approximately 5 to 30 min). As shown in Figure 34, these concentration-dependent studies in MCH showed the same process as the solvent-dependent measurements.

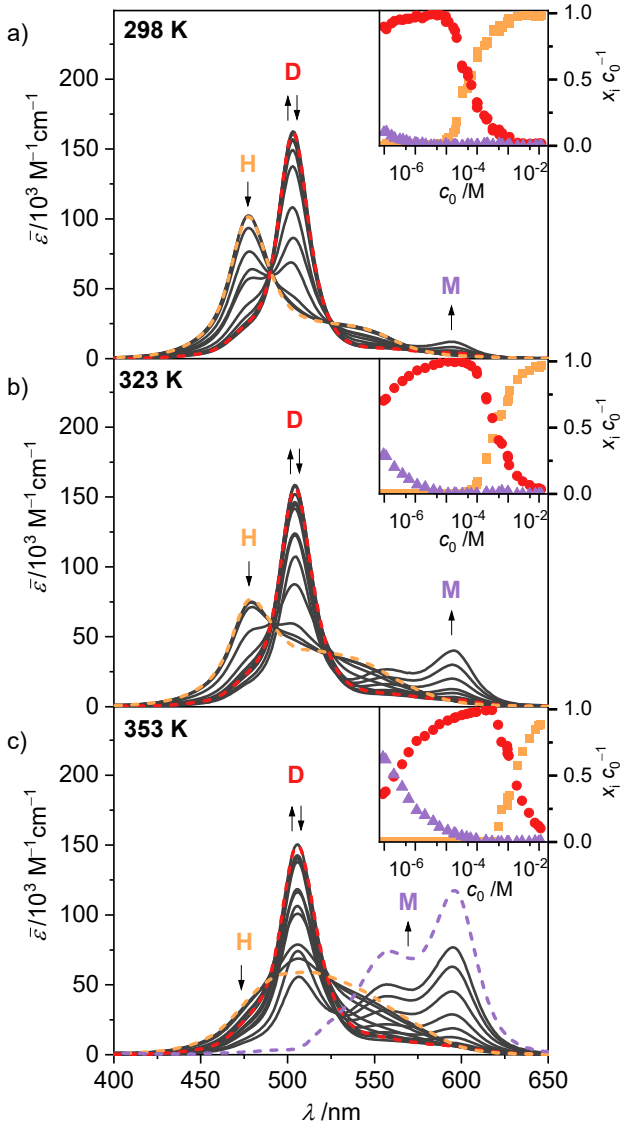

Figure 34. Concentration-dependent UV/Vis absorption spectra (solid lines) of merocyanine **2** in MCH at a) 298 K, b) 323 K and c) 353 K. Arrows indicate the spectral changes during the disassembly process from higher aggregates (H) to dimers (D) and monomers (M) upon decreasing the concentration from $c_0 = 1.0\times10^{-2}$ to 9.8×10^{-8} M. Colored spectra are calculated spectra of the individual species from global fit analysis according to the dimer (2M ⇌ D) and pentamer (5D ⇌ H) models. Insets show the concentration-dependent fraction of molecules x_i c_0^{-1} of **2** present as higher aggregate (orange), dimer (red) and monomer (violet) in MCH at the respective temperatures according to multiple linear regression analysis.

In the unpolar solvent MCH the tendency of the dipolar merocyanine **2** to aggregate is so strong, that even at the lowest concentration accessible for UV/Vis studies ($c_0 = 9.8\times10^{-8}$ M) almost no monomers (λ_{max}(M) = 596 nm) are present at 298 K. However, when performing concentration-dependent measurements at elevated temperatures of 323 K and 353 K, disassembly is induced, and an increasing amount of monomer is formed in the most dilute

samples (Figure 34). The dominant peak at $\lambda_{max}(D) = 503$ nm can be assigned to the dimeric species. Upon increasing the concentration, a further hypsochromically shifted absorption band at $\lambda_{max}(H) = 477$ nm rises, indicating the formation of a higher aggregate species. At all temperatures a concentration range exists ($c_0 \sim 6\times10^{-6}$ M at 298 K, $c_0 \sim 1\times10^{-5}$ M at 323 K and $c_0 \sim 2\times10^{-4}$ M at 353 K) where almost exclusively dimer absorption can be observed. Thus, the dimer is the intermediate species in a two-step aggregation process. This preferred dimerization is expected, as the dipolar chromophores can firstly self-assemble into antiparallel dimers due to strong electrostatic dipole-dipole interactions while further aggregation into larger species is only guided by weaker dispersion forces, as the ground state dipole moment of the dimer is close to zero. Isosbestic points for the concentration-dependent spectra showing the transition from monomer to dimer, as well as from dimer to higher aggregate indicate the presence of two equilibria between each two defined species. The spectroscopic data at 353 K, showing the transition between monomer and dimer ($c_0 = 9.1\times10^{-8}$ to 6.1×10^{-5} M), could be fitted globally (see Appendix for more information) according to the dimer model[16] (Figure A62). A dimerization constant of $K_D(353\text{ K}) = 4.5\times10^6$ M^{-1} was determined.

The concentration-dependent data showing the dimer – higher aggregate transition were best described by aggregation models for small, defined sized aggregates (trimer, tetramer and pentamer model[24], Figure A63 – A65). The differences in the quality of the fit obtained for these models are small and seem to vary slightly with temperature and concentration. Together with the ill match of the fit according to the isodesmic model[16] (Figure A63 – A65) this is a first indication that the higher aggregate formed by merocyanine **2** is indeed not an extended π-stacked supramolecular polymer. It is possible that the size of the higher aggregates is not uniform, but smaller (trimer of dimers = hexamer) for higher temperatures and lower concentrations, where binding constants are smaller and the substituents enjoy a higher mobility, i.e. entropy, and larger (pentamer of dimers = decamer) for the opposite conditions. For the following evaluations, the pentamer fit is used as an approximation to describe a 5D ⇌ H equilibrium since it gave the overall best match to the experimental data. Binding constants per binding site of $K_5(298\text{ K}) = 6.0\times10^4$ M^{-1}, $K_5(323\text{ K}) = 7.5\times10^3$ M^{-1} and $K_5(353\text{ K}) = 1.8\times10^3$ M^{-1} were obtained from global fit analysis. Thus, at 353 K the aggregation constant K_5 is more than three orders of magnitude smaller than the dimerization constant K_D at the same temperature, resulting in a value of $\sigma > 10^3$ for the degree of anti-

cooperativity. The summarized UV/Vis spectroscopic data of merocyanine **2** in CH_2Cl_2, 1,4-dioxane and MCH at different temperatures can be found in Table 5.

Table 5. Summarized UV/Vis spectroscopic data of monomer (M), dimer (D) and higher aggregate (H) species of merocyanine **2** in CH_2Cl_2, 1,4-dioxane and MCH at 298 K, 323 K and 353 K after analysis of the anti-cooperative aggregation.

Solvent		CH_2Cl_2	1,4-dioxane	MCH		
T	/K	298	298	298	323	353
K_D(M-D)	/M^{-1}	-	4.0×10^{4}[a]	4.0×10^{8}[b]	4.0×10^{7}[b]	4.5×10^{6}[a]
K_5(D-H)	/M^{-1}	-	-	6.0×10^{4}[a]	7.5×10^{3}[a]	1.8×10^{3}[a]
$\sigma = K_D/K_5$	/1	-	-	6700	5300	2500
$-\Delta G^0$(M-D)[c]	/kJ mol^{-1}	-	26.3	49.1	47.0	45.0
$-\Delta G^0$(D-H)[c]	/kJ mol^{-1}	-	-	27.3	24.0	22.0
λ_{max}(M)[d]	/nm	549	571	596	596	596
λ_{max}(D)[d]	/nm	-	494	503	504	506
λ_{max}(H)[d]	/nm	-	-	477	479	505
ε_{max}(M)[d]	/M^{-1} cm^{-1}	116000	137000	117000	117000	117000
ε_{max}(D)[d]	/M^{-1} cm^{-1}	-	126000	162000	156000	150000
ε_{max}(H)[d]	/M^{-1} cm^{-1}	-	-	101000	77000	59000
$\lambda_{isosbestic}$(M-D)	/nm	-	519	525	528	530
$\lambda_{isosbestic}$(D-H)	/nm	-		489	490	489
μ_{eg}(M)[d]	/D	10.4	10.7	10.8	10.8	10.8
μ_{eg}(D)[d]	/D	-	9.5	9.5	9.7	9.7
μ_{eg}(H)[d]	/D	-	-	9.7	9.9	10.1

[a] global fit analysis, [b] estimated according to dimer model from $\alpha_{agg\text{-}\pi}$, [c] determined from K_D or K_5 by Gibbs-Helmholtz equation, [d] all values correspond to monomeric units within the aggregate; for information on the determination of μ_{eg} see Appendix.

The shape of the higher aggregate absorption band changes remarkably upon heating (Figure 34, Figure A59). While the absorption spectrum at 298 K shows a pronounced maximum at 477 nm as expected for co-facially stacked H-aggregates, the spectrum at 353 K exhibits a broad, ill-defined absorption band with a maximum at around 500 nm. These spectroscopic changes can be rationalized by a more disordered and less tight packing of the higher aggregate at higher temperatures, probably due to increased flexibility and mobility of the substituents. This shifting of the maximum of the higher aggregate band into the range of the dimer absorption indicates, that at elevated temperatures the chromophores are not packed with equal and close distances anymore but rather into preferred dimer-pairs whose contact to other dimer-pairs is less defined and/or more distant. So, while at 298 K exciton coupling occurs between all the chromophores of the stack, leading to the hypsochromically shifted H-band, at 353 K the coupling between only two chromophores seems to be the most prominent. At 323 K either an intermediate higher aggregate form might be present or a mixture of the more tightly packed low and the more loosely packed high temperature form, since the UV/Vis absorption spectrum shows a sharp H-band at 479 nm as well as a more pronounced

shoulder at > 500 nm. The structural rearrangement in the higher aggregate structure upon heating is also characterized by an activation energy. Accordingly, time-dependent UV/Vis experiments reveal a period of about 1.5 h to return to the original room temperature (298 K) H-aggregate species (Figure A61). The absorption spectrum of the dimer shows only a slight broadening and red shift for increased temperatures. For the monomer no significant temperature-dependence of the shape of the absorption is observed in the experimental data, thus the calculated monomer spectrum from global fit analysis of the data at 353 K according to the dimer model is used for further evaluation of spectroscopic data at all temperatures.

Multiple linear regression (MLR) analysis was used to determine the concentration of molecules present as monomer (x_M), dimer (x_D) and higher aggregate (x_H) in the sample solutions at different concentrations c_0 for each dataset at the applied temperature. Based on Lambert-Beer's law (46) the absorbance $Abs(\lambda)$ can be deconvoluted into the contributions of the individual species (ε_M, ε_D and ε_H) for each cuvette thickness (d).

$$Abs(\lambda) = c_0 \varepsilon(\lambda) d = [x_M\, \varepsilon_M(\lambda) + x_D\, \varepsilon_D(\lambda) + x_H\, \varepsilon_H(\lambda)]d. \quad (46)$$

By MLR analysis the factors x_M, x_D and x_H (which are defined to be ≥ 0) were obtained. Please note, that x_D and x_H are not the actual concentrations of dimer and higher aggregate but the concentration of monomeric molecules present as dimer (D) or higher aggregate (H) species as defined by the way the extinction coefficient is calculated. The spectra calculated according to equation (46) from the extinction spectra of the individual species and the coefficients obtained by MLR analysis are in excellent agreement with the experimental spectra (representative spectra depicted in Figure 35). Additionally, the calculated total concentration $c_\Sigma = x_M + x_D + x_H$ matches the experimentally balanced concentration c_0 well (Figure 35, insets), which confirms the validity of the method.

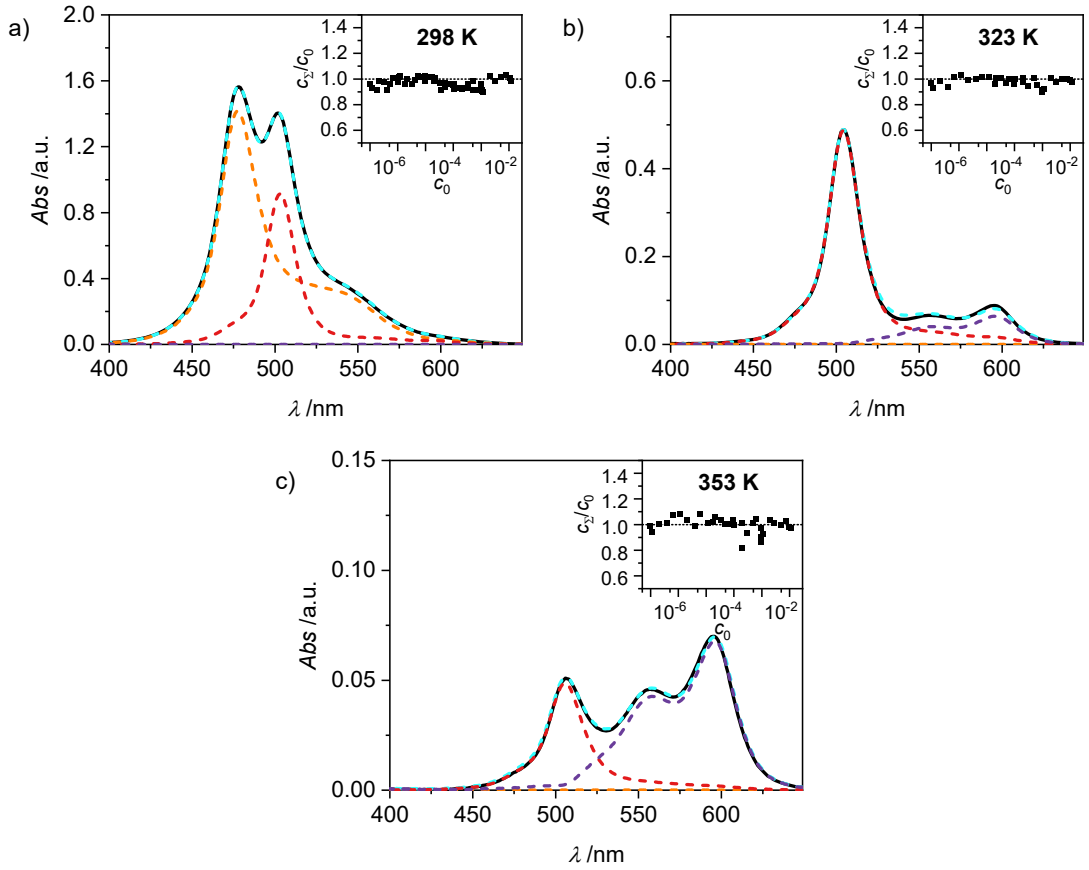

Figure 35. Experimental UV/Vis absorption spectra (black solid line) of merocyanine **2** and calculated spectra according to equation (46) (turquoise dashed line) as well as the partial contributions of monomer (violet dashed line), dimer (red dashed line) and higher aggregate (orange dashed line) at a) $c_0 = 1.0\times10^{-4}$ M (298 K), b) $c_0 = 3.9\times10^{-7}$ M (323 K) and c) $c_0 = 9.8\times10^{-8}$ M (353 K). Insets show the deviation of the calculated total concentration $c_\Sigma = x_M + x_D + x_H$ from MLR analysis with respect to the balanced concentration c_0.

The concentration-dependent fraction of molecules present as monomer, dimer or higher aggregate ($x_i\ c_0^{-1}$) are depicted in the insets of Figure 34. Notably, for all three temperatures a concentration range exists, where almost exclusively dimers (> 99%) are present. This strict separation of the aggregation process into two consecutive steps allows us to calculate the degree of aggregated π-faces ($\alpha_{agg\text{-}\pi}$) independently for both equilibria, namely the dimerization (2M ⇌ D) as well as the further self-assembly (5D ⇌ H) at higher concentrations. In general, $\alpha_{agg\text{-}\pi}$ is defined as

$$\alpha_{agg-\pi} = \frac{N_{occupied\ \pi-faces}}{N_{total\ \pi-faces}}, \qquad (47)$$

which can be applied to the two equilibria of interest. For the dimerization of two monomers (M) according to 2M ⇌ D applies:

$$c_0 = c_M + 2c_D. \quad (48)$$

$$c_0 \cdot \bar{\varepsilon} = c_M \cdot \varepsilon_M + 2\, c_D \cdot \varepsilon_D \rightarrow \frac{2\, c_D}{c_0} = \frac{\bar{\varepsilon} - \varepsilon_M}{\varepsilon_D - \varepsilon_M}. \quad (49)$$

$$\alpha_{agg-\pi}(2M \rightleftharpoons D) = \frac{2\, c_D}{2\, c_0} = \left(\frac{\bar{\varepsilon} - \varepsilon_M}{\varepsilon_D - \varepsilon_M}\right) \cdot 0.5. \quad (50)$$

For the formation of a higher aggregate (H) out of five dimers (D) according to 5D ⇌ H applies:

$$c_0 = 2c_D + 10c_H. \quad (51)$$

$$c_0 \cdot \bar{\varepsilon} = 2\, c_D \cdot \varepsilon_D + 10\, c_H \cdot \varepsilon_H \rightarrow \frac{10\, c_H}{c_0} = \frac{\bar{\varepsilon} - \varepsilon_D}{\varepsilon_H - \varepsilon_D}. \quad (52)$$

$$\alpha_{agg-\pi}(5D \rightleftharpoons H) = \frac{20\, c_H + 2\, c_D}{2\, c_0} = \quad (53)$$

$$\frac{10\, c_H + c_0}{2\, c_0} = \left(\frac{10\, c_H}{c_0}\right) \cdot 0.5 + \frac{c_0}{2\, c_0} = \left(\frac{\bar{\varepsilon} - \varepsilon_D}{\varepsilon_H - \varepsilon_D}\right) \cdot 0.5 + 0.5.$$

For simplification, it is assumed that for the higher aggregate species all π-faces are occupied so $\alpha_{agg-\pi} = 1$ is defined for the fully aggregated state. Please note, that this would indeed only be true for a cyclic arrangement of molecules or an infinite stack. The experimental apparent extinction coefficient $\bar{\varepsilon}$ of a sample with the concentration c_0 is taken at the maximum of the dimer (5D ⇌ H) or the monomer (2M ⇌ D) band. The monomer (ε_M), dimer (ε_D) and higher aggregate (ε_H) extinction coefficients are obtained from the spectra of the individual species calculated by global fit analysis. Up to the concentration at which the absorption band of the dimer reaches its maximum, $\alpha_{agg-\pi}$ was calculated according to equation (50), above that equation (53) was used. The data points from the concentration-dependent UV/Vis studies at 298 K, 323 K, and 353 K nicely follow the trend expected for anti-cooperative aggregation behaviour schematically illustrated in Figure 32, with a plateau at $\alpha_{agg-\pi} = 0.5$ where predominantly the dimer species is present (Figure 36). The experimental data for the initial dimerization of merocyanine **2** at 353 K nicely match the theoretical curve for $\alpha_{agg-\pi}$ according to the dimer model[16] (54) with K_D(353 K) = 4.5×10^6 M^{-1} from global fit analysis.

$$\alpha_{agg-\pi}(2M \rightleftharpoons D) = \frac{4K_D c_0 + 1 - \sqrt{8K_D c_0 + 1}}{4K_D c_0} \cdot 0.5. \quad (54)$$

Although $\alpha_{agg-\pi}$ only decreases to a value of 0.43 and 0.34 for the measurements at 298 K and 323 K, respectively, the dimerization constants can be estimated by comparing simulated curves for different K_D-values with the experimental data points. The dimerization constant at

298 K can thus be assessed to be around $K_D(298\ K) = 4.0\times10^8\ M^{-1}$ (Figure 36, black dashed line).

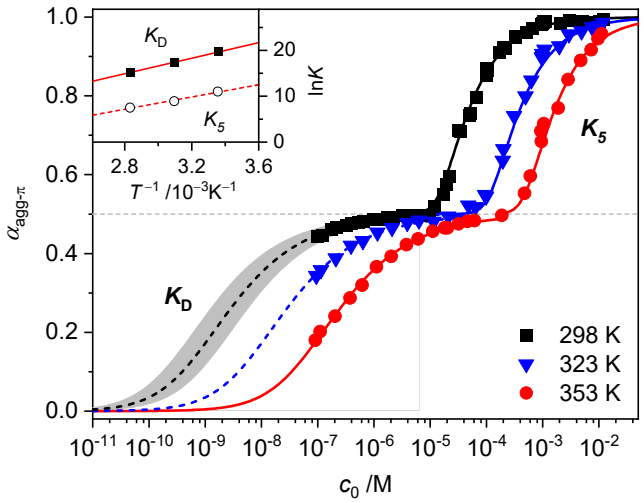

Figure 36. Fraction of aggregated π-faces $\alpha_{agg-\pi}$ of merocyanine **2** in MCH calculated from spectroscopic data at 298 K (black symbols), 323 K (blue symbols) and 353 K (red symbols) according to equation (50) and (53). Simulated curves according to dimer ($\alpha_{agg-\pi} < 0.5$, equation (54)) and pentamer model ($\alpha_{agg-\pi} > 0.5$, equation (55) and (56)) calculated with binding constants from global fit analysis (solid lines) or estimated binding constants (dashed lines) are shown for comparison. Grey area marks a range of $\alpha_{agg-\pi}$ for $9.0\times10^8\ M^{-1} > K_D > 2.0\times10^8\ M^{-1}$. Inset shows the van't Hoff plot for the calculation of thermodynamic parameters for dimerization (K_D) and formation of the higher aggregate (K_5).

For comparison, the gray area in Figure 36 marks a range of $\alpha_{agg-\pi}$ for $9.0\times10^8\ M^{-1} > K_D > 2.0\times10^8\ M^{-1}$. In the same way the binding constant at 323 K was estimated to $K_D(353\ K) = 4.0\times10^7\ M^{-1}$, which is in accordance to the decrease in K_D expected for increasing temperatures. Furthermore, the simulated curves for the 5D ⇌ H equilibrium according to the pentamer model are shown in Figure 36. Since the pentamer model consists of a fifth-order equation, no simple expression can be given for $\alpha_{agg-\pi}$. However, the degree of aggregated π-faces can be simulated according to equation (55) (compare with equation (53) for derivation).

$$\alpha_{agg-\pi}(5D \rightleftharpoons H) = \left(\frac{10\,c_H}{c_0}\right)\cdot 0.5 + 0.5. \qquad (55)$$

The concentration of higher aggregate c_H can be calculated for different total molecular concentrations c_0 by finding the zero-crossings of equation (56), or implicit curve fitting methods can be used.

$$K_5 = \sqrt[4]{\frac{c_H}{{c_D}^5}} = \sqrt[4]{\frac{c_H}{((c_0 - 10c_H)\cdot 0.5)^5}}. \qquad (56)$$

With the binding constants for dimerization and further aggregation, the cooperativity parameter $\sigma = K_D/K_5$ of the self-assembly process of merocyanine **2** in MCH can be

calculated to: $\sigma(298\ \mathrm{K}) = 6700$, $\sigma(323\ \mathrm{K}) = 5300$ and $\sigma(353\ \mathrm{K}) = 2500$. It quantifies the high degree of anti-cooperativity in this system.

In order to determine the thermodynamic parameters for the dimerization (K_D) and aggregation (K_5) process, the binding constants at the three different temperatures were used in a van't Hoff plot (Figure 36, inset). The values for both K_D and K_5 meet the expected linear relation for ln$K$ and T^{-1}. However, the results of the van't Hoff plot for K_5 should be interpreted with caution, since the structure of the higher aggregate might be different at elevated temperatures (*vide supra*). Thus, it is not certain that a reasonable comparability is given for the K_5 values at different temperatures. The determined entropy penalty for the formation of the higher aggregate ($\Delta S^0 = -96.4\ \mathrm{J\ K^{-1}mol^{-1}}$) is higher than for the dimerization ($\Delta S^0 = -74.4\ \mathrm{J\ K^{-1}mol^{-1}}$), since more building blocks are involved in the process. As expected, dimerization is enthalpically more favoured ($\Delta H^0 = -71.5\ \mathrm{kJ\ mol^{-1}}$) than the formation of the higher aggregate ($\Delta H^0 = -55.7\ \mathrm{kJ\ mol^{-1}}$), which can be explained by the strong dipole-dipole interaction within the dimer. The Gibbs free energy changes ΔG^0 obtained from this analysis for dimer ($\Delta G^0(353\ \mathrm{K}) = -45.2\ \mathrm{kJ\ mol^{-1}}$) and higher aggregate ($\Delta G^0(298\ \mathrm{K}) = -27.0\ \mathrm{kJ\ mol^{-1}}$) formation match the values calculated from the binding constants from global fit analysis at the respective temperatures (Table 5) very well. The highly negative ΔG^0 values again confirm the exceptionally strong binding of the dipolar merocyanine chromophores in MCH compared to other solvents.[66]

4.3.2 Investigation of the Aggregate Structures

To correlate the spectroscopic findings as well as the investigated anti-cooperative growth mechanism with structural parameters it is essential to deduce the number of molecules which form the aggregate species as well as the respective molecular arrangement within the defined assembly. The formation of a small-sized higher aggregate species indicated by the fitting results of the spectroscopic data was confirmed by AFM, DOSY and VPO measurements. The higher aggregate sample for AFM imaging was prepared by diluting a MCH solution of merocyanine **2** at a concentration of $c_0 = 9.7\times10^{-4}$ M to 0.5×10^{-4} M, and immediately spin-coating it onto silicon wafer functionalized with *n*-tetradecylphosphonic acid (TPA). Time-dependent UV/Vis studies have shown that due to kinetic effects the higher aggregate is still the dominant species for at least ten minutes after dilution at 298 K (Figure A60). The AFM images show very uniform small particles of 2.3 ± 0.2 nm height and 7-9 nm diameter (Figure 37b). Also for dimer-samples small homogeneous particles were observed

(Figure 37a). The respective height of 0.9 ± 0.2 nm matches well the height of two π-stacked molecules on the substrate surface. The average diameter is measured to be 4.5 nm, however, this value is not reliable since the diameter of objects smaller than the tip radius (< 7 nm) is overestimated in AFM measurements due to the tip-broadening effect[171-172].

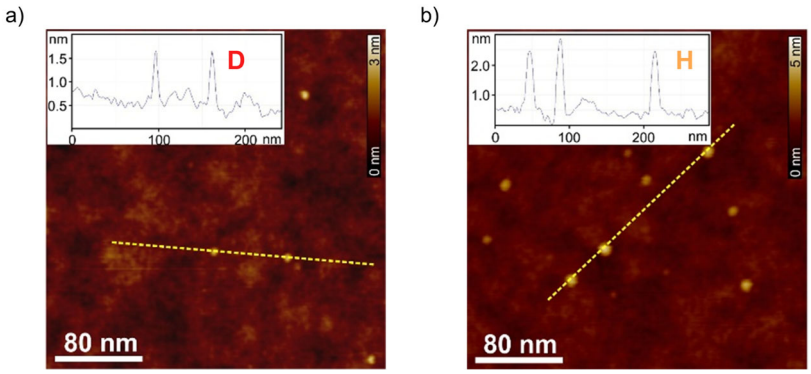

Figure 37. AFM height images of a) dimer samples of merocyanine **2** in MCH ($c_0 = 8.7\times10^{-6}$ M) spin-coated onto TPA-functionalized SiO_x/AlO_x substrates and b) higher aggregate sample of merocyanine **2** in MCH diluted from $c_0 = 9.7\times10^{-4}$ M to $c_0 = 0.5\times10^{-4}$ M and subsequent spin-coating onto TPA-functionalized SiO_x/AlO_x substrates. Insets show the respective cross-section analysis of the yellow dashed lines.

Vapor pressure osmometry (VPO) measurements were performed in MCH at 318 K to determine the average molar mass of the higher aggregate of merocyanine **2** ($M_{monomer}$ = 1026.55 g/mol) and thus the average number of molecules incorporated in those aggregates. This method allows to determine the total osmolality of solutions. Solutions containing solutes have lower vapor pressure than the pure solvent, which leads to a vapor pressure difference, and thus to a temperature difference (ΔT) at the thermistors during the measurement. This ΔT is proportional to the number of particles dissolved in the solution. Benzil (M = 210.23 g/mol) and polystyrene PS5270 (M_n = 5270 g/mol) were used as standards to determine the relation of measurement value (MV) and osmolality for the device and the applied measurement conditions. MCH was used as solvent and the measurements were performed at 318 K to ensure saturation of the gas phase of the cell with solvent vapor.

To evaluate the data two different methods can be applied. The first one assumes a linear relation between MV and the number of particles. A linear fit was applied to the data of the two standards with a fixed intercept at $y = 0$. With the slope s of these fit curves, the concentration c in mol kg^{-1} (moles of particles per kg solution) of unknown samples can be directly determined from the measurement value MV according to equation (57). In this way, the average number $<X_n>$ of molecules incorporated in these particles can be calculated.

$$c\left(\frac{mol}{kg}\right) = \frac{MV}{s\left(\frac{kg}{mol}\right)}. \qquad (57)$$

The slope obtained from the linear fit of benzil and PS5270 reference measurements was identical (s = 562 kg mol^{-1}) and <X_n> was calculated for samples with different concentrations (in g of compound per kg solution, Figure 38a).

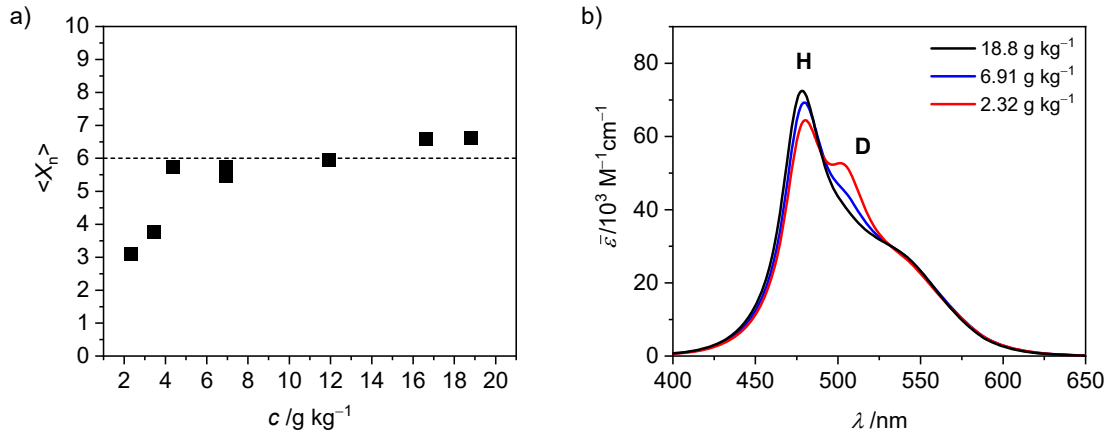

Figure 38. a) Average number of molecules incorporated into the higher aggregate of merocyanine **2** (MCH, 318 K) calculated from the VPO measurement values (*MV*) of samples of **2** with varying concentrations. A linear relation between *MV* and particle concentration is assumed. b) UV/Vis absorption spectra of samples of merocyanine **2** in MCH at 318 K used for VPO measurements.

The value rises with concentration up to <X_n> = 6.6. This is in accordance with the fact, that in the lower concentrated samples at 318 K mixtures of dimer and higher aggregates are present according to the UV/Vis spectra (Figure 38b).

The second way to evaluate the data from VPO measurements considers that for large molecules (M > 500 g/mol) the relation between MV and the number of particles is not necessarily linear. It is recommended to use a standard with a similar molecular weight as expected for the analyte (here PS5270). The measurement values MV divided by the concentration (in mol/kg for the reference and in g/kg for the analyte) are plotted against the concentration (Figure 39). A linear fit is applied. For the data of merocyanine **1**, the data points for the two lowest concentrations are excluded, since these samples are not fully aggregated under the measurement conditions. K_{cal} and K_{meas} are obtained as the intercept at c = 0. The molecular weight of the analyte can then be calculated according to:

$$M = \frac{K_{cal}}{K_{meas}}. \qquad (58)$$

By this, an average weight of the higher aggregate particles of M = 6339 g/mol was obtained, which corresponds to <X_n> = 6.2.

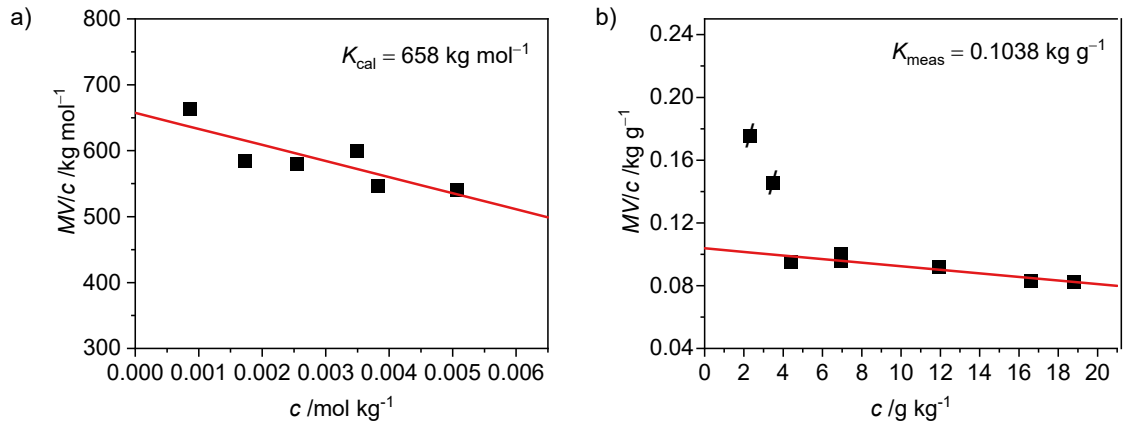

Figure 39. VPO measurement values (*MV*) divided by the concentration *c* as a function of the sample concentration of a) the reference PS5270 and b) merocyanine **2** in MCH at 318 K. The *K* values are the interpolated *y*-values of the linear fit at $c = 0$.

Thus, both evaluation methods gave very similar results, indicating an average number of six molecules (trimer of dimers) for the higher aggregate species formed by merocyanine **2** in MCH at 318 K. This value is at the lower end of the range expected for the higher aggregate size according to the fitting results of the UV/Vis data (*vide supra*), but considering the error of the method and the elevated temperatures needed for the measurements it is still supporting our previous assumptions.

^{1}H DOSY measurements of the higher aggregate in MCH-d_{14} ($c_0 = 1.0\times10^{-3}$ M, 295 K) emphasize the uniformity of the aggregate particles with a hydrodynamic radius of 2.4 nm according to the Stokes-Einstein equation (Figure 40b).

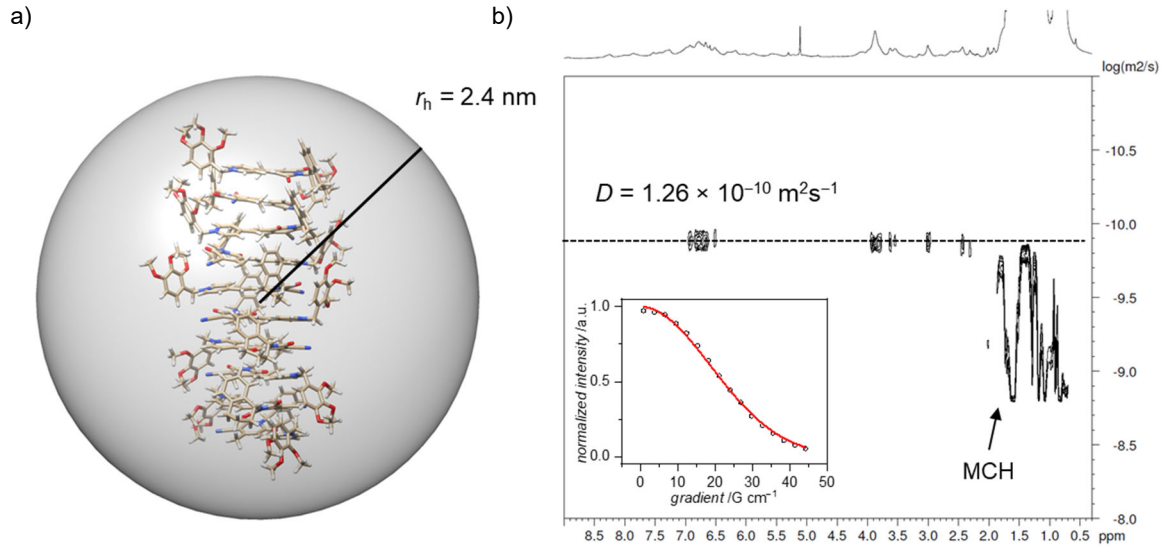

Figure 40. Illustration of the geometry-optimized decamer stack of merocyanine **2** (PM7, dodecyl chains replaced by methyl groups) as well as the hydrodynamic radius (transparent grey sphere) as obtained from the Stokes-Einstein equation deduced from b) the ^{1}H DOSY NMR (600 MHz, 295 K) spectrum of **2** in MCH-d_{14} ($c_0 = 1.0\times10^{-3}$ M). Inset shows a representative attenuation curve for the integral from 6.86 – 6.62 ppm with the respective fit.

This is in good agreement with the particle size observed by AFM. The hydrodynamic radius matches the size of a geometry-optimized stack of ten merocyanine **2** chromophores (i.e. five dimers) considering that the large solubilizing substituents were neglected in the calculations (Figure 40a). For the dimer (MCH-d_{14}, $c_0 = 2.3\times10^{-4}$ M, 348 K) a hydrodynamic radius of 1.0 nm was calculated from the diffusion coefficient. Also this value agrees well, with the size of the geometry optimized dimer-structure of **2** (Figure 41).

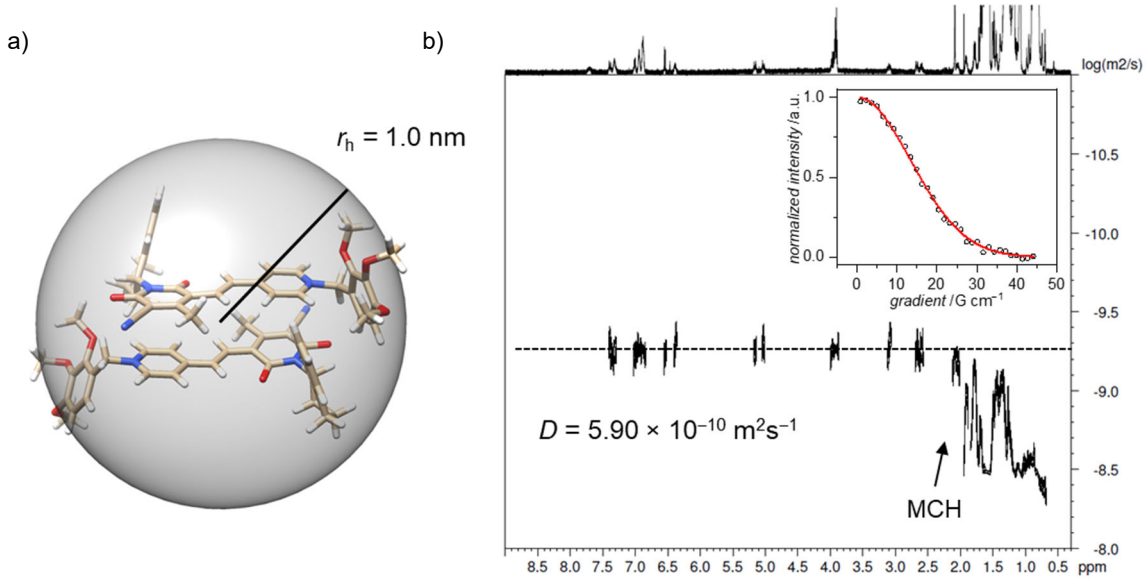

Figure 41. Illustration of the geometry-optimized dimer structure of merocyanine **2** (B97D3/def2SVP) as well as the hydrodynamic radius (transparent grey sphere) as obtained from the Stokes-Einstein equation deduced from b) the ^{1}H DOSY NMR (600 MHz, 348 K) spectrum of **2** in MCH-d_{14} ($c_0 = 2.3\times10^{-4}$ M). Inset shows a representative attenuation curve for the integral from 7.07 – 6.80 ppm with the respective fit.

As the global fitting of the spectroscopic data as well as AFM, VPO and DOSY measurements all indicate the formation of a small-sized oligomeric higher aggregate consisting of six to ten molecules, we took the efforts to get a better understanding of the arrangement of the chromophores within this species. To elucidate the structure of the dimer and the higher aggregate formed by merocyanine **2** in MCH, 1D and 2D NMR spectra were recorded (see Appendix). All peaks in the ^{1}H NMR spectra of the monomer and dimer could be assigned to the respective protons with the help of correlation spectroscopy (COSY), nuclear Overhauser effect spectroscopy or rotating frame Overhauser effect spectroscopy (NOESY or ROESY), and heteronuclear single quantum coherence (HSQC) experiments (Table A13). The proton spectrum of the dimer (MCH-d_{14}, $c_0 = 2.2\times10^{-4}$ M, 348 K) is well resolved and shows only one set of signals revealing a high symmetry of the dimer structure with two equivalent chromophores (Figure 42b).

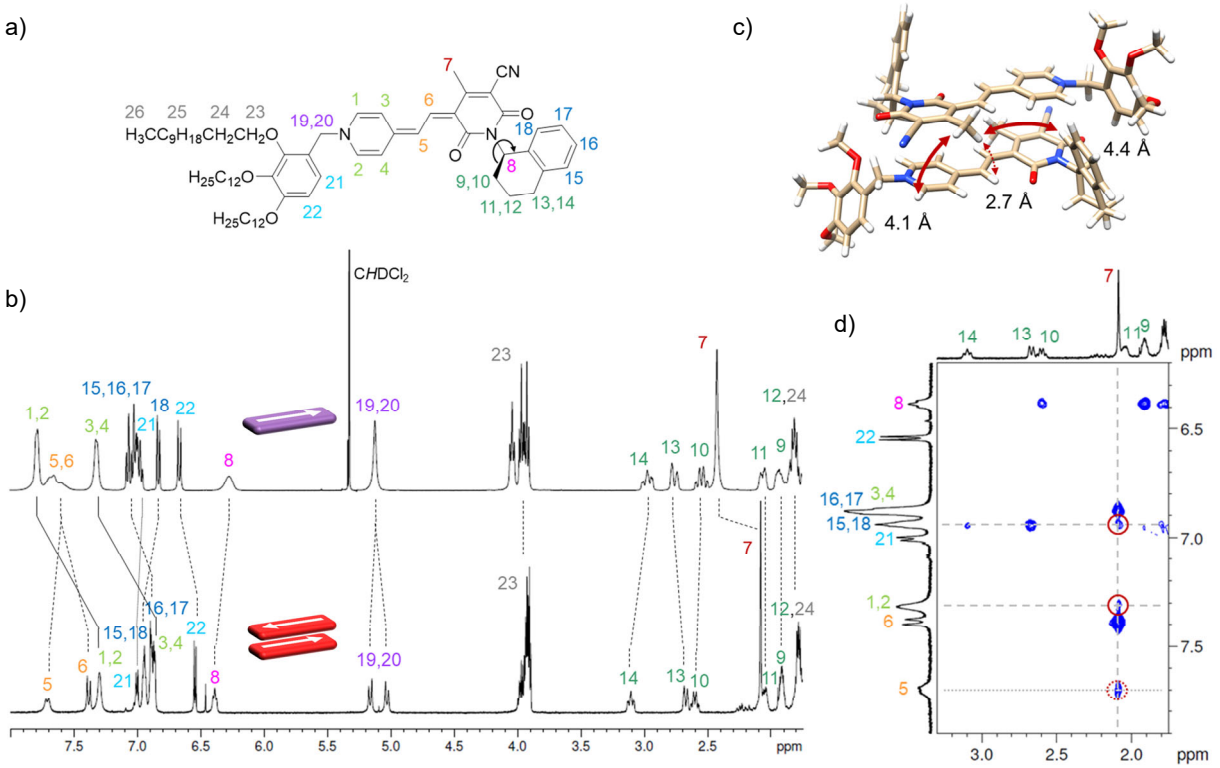

Figure 42. a) Molecular structure of merocyanine **2** with proton assignment in color. b) Relevant section of the ^{1}H NMR spectra of the monomer (top) of **2** in CD_2Cl_2 at 295 K ($c_0 = 9.7\times10^{-4}$ M, 400 MHz) and the dimer (bottom) in MCH-d_{14} at 348 K ($c_0 = 2.2\times10^{-4}$ M, 600 MHz). c) Geometry-optimized dimer structure (B97D3/def2SVP) with distances given for protons showing *inter*molecular NOE cross peaks with the protons 7 of the CH_3 group. d) Section of the ^{1}H ^{1}H NOESY NMR (600 MHz) spectrum of the dimer of **2** ($c_0 = 2.7\times10^{-4}$ M) in MCH-d_{14} at 348 K. For complete spectrum see Figure A72.

In comparison to the monomer ^{1}H spectrum (Figure 42b, CD_2Cl_2, $c_0 = 9.7\times10^{-4}$ M, 295 K), only the signal for the two protons 19 and 20 splits in the dimer spectrum as these protons are now closer to a stereogenic centre and the difference in the chemical environment of those diastereotopic protons is increased within the dimer structure compared to the monomeric species. For the proton 8 at the chiral carbon, only one signal can be observed for the monomer as well as for the dimer. In principle the chiral tetralin substituent can point toward the interior or exterior of the double π-stack with proton 8 pointing either towards the outer or the inner neighbouring carbonyl group. As only one signal can be observed for proton 8 in the monomer as well as in the dimer ^{1}H spectrum, fast rotation around the marked C–N (Figure 42a) bond is expected for both cases. This is further augmented by a calculated rotational barrier around this C–N bond of only 52 kJ mol^{-1} (B97D3/def2SVP) for the monomer in the gas phase, leading to a half-life of $\tau_{1/2}(298\ \text{K}) = 2.1\times10^{-4}$ sec, which is fast on the NMR timescale of this process.

The defined molecular arrangement of the dipolar chromophores within the dimer could be further elucidated by NOE spectroscopy. In the dimer ^{1}H ^{1}H NOESY NMR spectrum

(MCH-d_{14}, $c_0 = 2.7\times10^{-4}$ M, 348 K) several cross signals can be found, where no signals are expected for the monomer, indicating *inter*molecular proximity of the protons. Especially the sharp proton signal of the CH_3-group 7 of the acceptor unit is well suited to detect those *inter*molecular proximities and gives defined NOE cross peaks with the outer pyridine protons (1, 2) and the aromatic proton 18 of the tetralin substituent (Figure 42d). Notably, these cross signals are not observed in the spectrum of the monomer (Figure A71), which corroborates the presence of *inter*molecular through space couplings. The results are in accordance with the geometry-optimized structure (Figure 42c) indicating close spatial proximity between the mentioned protons. Additionally, cross signals can be observed between the protons 7 and both methine bridge protons (5, 6). Even though the *intra*molecular distance between 7 and 5 is with 4.9 Å also still just within the NOE range the much closer *inter*molecular contact between those protons can explain the relatively high intensity of the cross signal observed between those protons (Figure 42d). A similar intermolecular arrangement has also been observed in the crystal structure of the same merocyanine chromophore equipped with other substituents.[66]

Unfortunately, the proton spectrum of the higher aggregate in MCH-d_{14} at 295 K shows broad peaks (Figure 43), which prohibits an unambiguous proton assignment like for the dimer species.

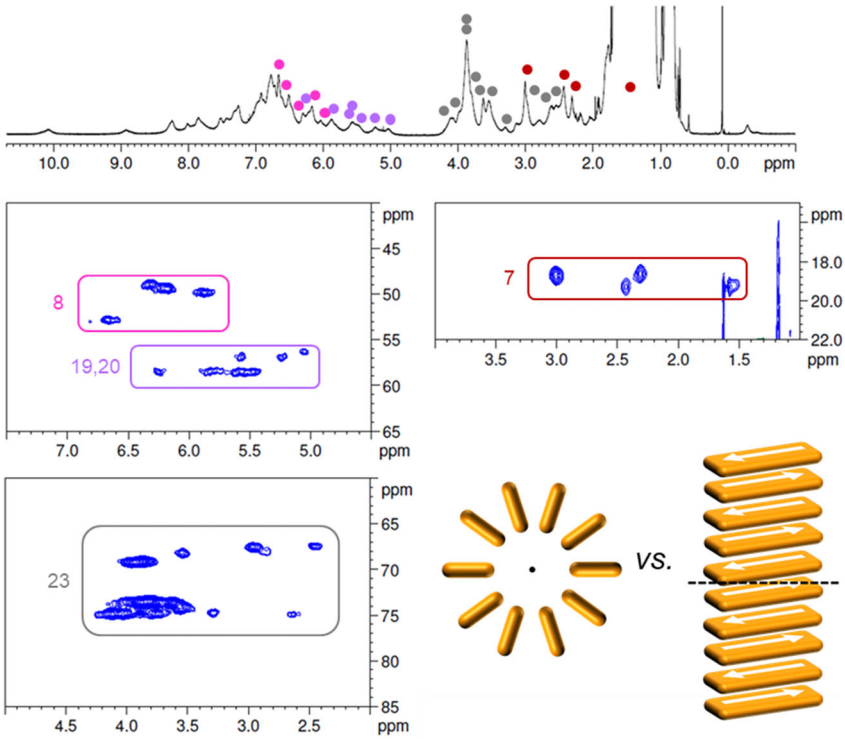

Figure 43. ^{1}H as well as sections of the ^{1}H ^{13}C HSQC NMR (600 MHz) spectrum (for complete spectrum see Figure A75) of the higher aggregate of **2** ($c_0 = 2.1\times10^{-3}$ M) in MCH-d_{14} at 295 K. Signals of protons with characteristic ^{13}C shift could be assigned in the HSQC spectrum of the higher aggregate and are marked in color. Sketch of cyclic *vs.* linear arrangement of ten chromophores visualizes the lower degree of symmetry of the linear stack.

Still, some information can be deduced from the HSQC spectrum of the higher aggregate. Since ^{13}C shifts are in general hardly influenced by aggregation (Table A13), some proton signals can be assigned in the higher aggregate ^{1}H spectrum based on the HSQC spectrum (Figure 43). This works especially well for the protons 7 ($\delta_C(D) = 18.2$ ppm), 8 ($\delta_C(D) = 49.9$ ppm), 19/20 ($\delta_C(D) = 58.9$ ppm), and 23 ($\delta_C(D) = 69.6$, 73.9, 74.2 ppm) as the corresponding carbon atoms have a characteristic shift in comparison to the other carbons of the molecules. Notably, defined sets of cross signals can be observed in the HSQC of the higher aggregate. For the protons 7 of the methyl group at least four signals (red labels in Figure 43) can be assigned and also for the other protons (labelled in different colors in Figure 43) several sets of signals are observed. The signal sets cover a wide range of about 1.5 ppm, indicating large variation in the electronic environment of the chromophores within the higher aggregate. This condition is realized in a linear stack of chromophores, where the environment of the outer molecules differs significantly from that of the inner ones. In contrast, a cyclic structure does not seem reasonable since due to the higher symmetry less signals are expected (illustration in Figure 43). For our structure proposal of the higher aggregate the linear arrangement is therefore favoured over a cyclic arrangement of chromophores. The limited size of the stack to presumably a decamer (*vide supra*) can be explained by the significant sterical demand of the peripheral solubilizing trialkoxyphenyl brushes, which cannot be accommodated within the close repeat distance, demanded by the π-stacked dimers, hindering the further growth to an extended assembly (Figure A77). These sterical effects[164-167] in combination with the preferred formation of small-sized aggregates by the anti-cooperative aggregation mechanism[25, 33-34] can well explain the formation of oligomers of rather defined size instead of extended π-stacks.

Additional information on the relative arrangement of chromophores within an aggregate can be gained from CD spectroscopy. While the CD signals of the monomer and the dimer of **2** are very weak, the CD spectrum of the higher aggregate shows a much stronger bisignate signal with positive Cotton effect (Figure 44), indicating a *P*-helical arrangement of the chromophores according to the exciton chirality method.[173] The CD band exhibits two maxima at $\lambda = 575$ nm and $\lambda = 537$ nm in the wavelength range of the shoulder of the higher aggregate absorption band and a minimum at $\lambda = 477$ nm which coinsides well with the absorption maximum.

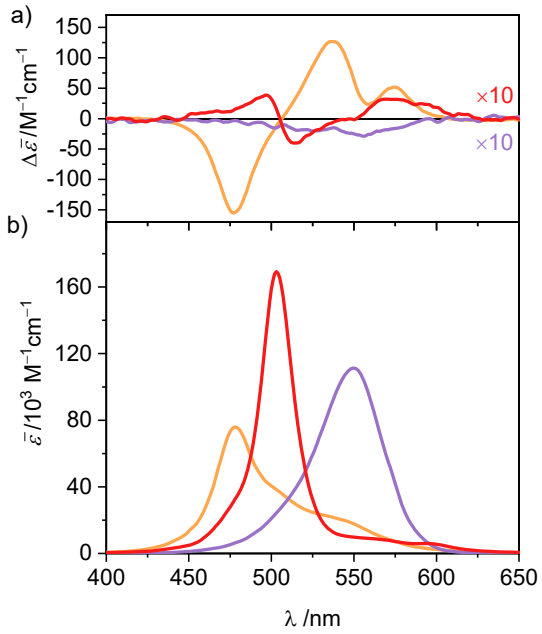

Figure 44 a) CD and b) UV/Vis absorption spectra of the monomer ($c_0 = 7.2\times10^{-6}$ M, violet line) of merocyanine **2** in dichloromethane, as well as the dimer ($c_0 = 6.5\times10^{-6}$ M, red line) in MCH and the higher aggregate ($c_0 = 1.0\times10^{-3}$ M, orange line) in MCH at 298 K. The monomer and dimer CD spectra are depicted with ten-fold increased intensity.

The simulated CD spectrum by time-dependent density functional theory (TD-DFT) calculations on the geometry-optimized decamer stack with *P*-helicity indeed reproduces the experimental spectrum quite well (Figure 45).

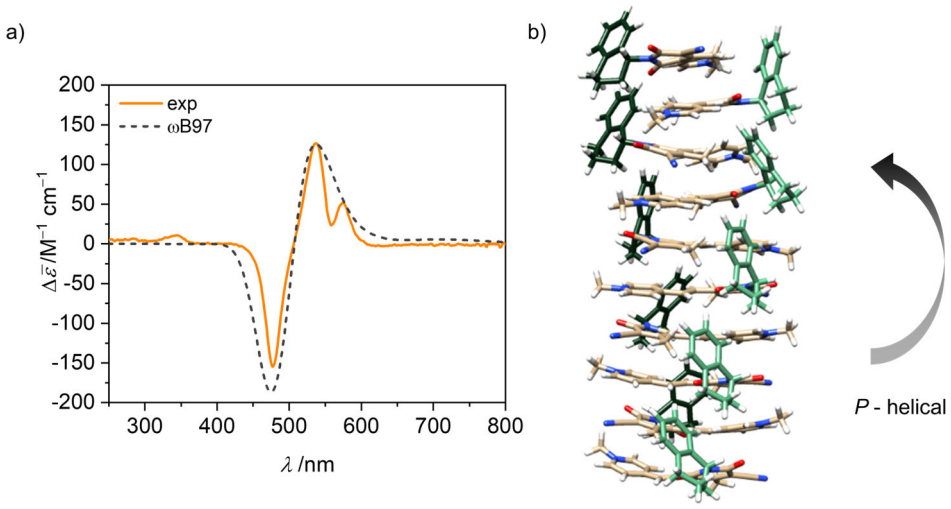

Figure 45. a) Experimental CD spectrum of the higher aggregate of **2** in MCH (orange, $c_0 = 1.0\times10^{-3}$ M, 298 K) in comparison with calculated CD spectrum (dashed grey) of the structure shown in b) calculated by TD-DFT with the ωB97 functional (def2SVP, PCM, 15 states, half with at half height = 0.18 eV, shifted 0.64 eV toward lower energies and intensity corrected to fit the maximum of the experimental spectrum). b) Geometry-optimized structure of a decamer stack of **2** (PM7, trialkoxypheny substituents replaced by methyl groups after structure optimization to reduce computational effort for the TD-DFT calculations).

This gives further evidence that our proposed structure for the higher aggregate is a reasonable approximation for the true arrangement in solution. Note that vibronic coupling is

not considered by our employed TD-DFT method so that the vibronic fine structure at $\lambda > 500$ nm is not reproduced by the simulations.

4.2.4 Aggregation-Induced Emission Enhancement

Aggregation-induced emission (AIE)[174] and aggregation-induced emission enhancement (AIEE)[175] for organic nanoparticles became popular research fields during the last two decades. Both terms describe a related phenomenon, i.e. an increase of luminescence upon aggregation. Whilst the original example for which the term AIEE was coined described an increase of fluorescence with the formation of nanoparticles composed of π-stacked "aggregated" dyes (similar as in Scheibe's J-aggregates[176]) with relevance for the design of luminescent organic semiconductors[157, 177], no π-π-stacking was involved in nanoparticles of 1-methyl-1,2,3,4,5-pentaphenylsilole dye for which the term AIE was coined.[174] Indeed, for these aggregates the fluorescence enhancement did not originate from dye-dye interactions upon aggregation but from the restriction of motions that promote the non-radiative decay.[178] Like for AIEE also for this phenomenon of AIE multiple examples from old literature were already available including fluorescence enhancements in viscous media, upon cooling, upon solidification or by fixation of the π-scaffold with covalent bridges.[179] However, because both of these as well as the majority of all other known AIE and AIEE molecules only allow the investigation of either the molecular state or the often poorly characterized nanoparticle state, the latter often consisting of thousands of molecules and including heterogeneity, few insights are provided by these studies on the origin of the fluorescence enhancement upon dye aggregation. In this regard the dimers and decamers of merocyanine **2** offer a unique opportunity to acquire further insights into the emergence of fluorescence beyond previously studied merocyanine dimers[180] and solid state materials[181]. The fluorescence properties of the monomer, dimer and higher aggregate species were investigated, and the summarized results can be found in Table 6.

Monomeric merocyanine dyes usually show only poor fluorescence due to a fast non-radiative deactivation pathway through a bond-twisting mechanism ($\Phi_{Fl}(M) \sim 0.1\%$)[182-185]. Rigidification of the π-system by dimerization[180], stacking[39] or in the solid state[181] can enhance the emission strength and accordingly merocyanines were also utilized in aggregation-induced emission studies[186]. The monomer emission of **2** could not be investigated in MCH since low sample concentrations of $< 10^{-7}$ M are required to obtain

significant amount of monomer, which however resulted in no detectable monomer emission at elevated temperatures of 353 K, where a monomer content of > 65 % can be reached.

Table 6. Summarized fluorescence data of monomer (M), dimer (D) and higher aggregate (H) of merocyanine **2** in solution and in the solid state (A, B) at room temperature.

	Species	λ_{em} /nm	$\Delta\bar{\nu}_{Stokes}$ /cm^{-1}	τ[a] /ns	Φ_{Fl} /%	k_r 10^6 s^{-1}	k_{nr} 10^6 s^{-1}
CH_2Cl_2	M[b]	587	1200	< 0.2	0.23	> 11.5[g]	> 5000[g]
MCH	D[c]	720	6000	7.6	2.3	3.0	129
	H[d]	706	6800	11.5	4.5	3.9	83.1
Solid	A[e]	710	-	2.3 (27%), 8.1(73%)	4.9	-[h]	-[h]
	B[f]	710	-	1.7 (28%), 5.1 (72%)	7.5	-[h]	-[h]

[a] Decay curves can be found in Figure A76. [b] $c_0 = 7\times10^{-7}$ M, OD = 0.08. [c] $c_0 = 2\times10^{-6}$ M, OD = 0.25; it was verified with a more dilute sample (OD < 0.03) that excitation spectrum is free of reabsorption effects. [d] $c_0 = 1\times10^{-3}$ M, OD = 0.9, front face setup. [e] Freeze-dried higher aggregate solution of **2** in cyclohexane ($c_0 = 1\times10^{-3}$ M). [f] Solid after evaporation of CH_2Cl_2 and drying *in vacuo*. [g] Only a lower limit for k_r and k_{nr} is given, as the fluorescence lifetime is below the instrument response time of the TCSPC setup. [h] Not evaluated because the biexponential decay suggests the presence of a mixture of monomer-like and aggregate species.

The fluorescence properties of the monomer where therefore studied in CH_2Cl_2, where at all concentrations suitable for spectroscopy exclusively the monomeric species is present (Figure 46, violet). The monomer's emission spectrum with maximum at $\lambda_{em}(M) = 587$ nm is mirror-imaged to the monomer absorption with a Stokes shift ($\Delta\tilde{\nu}_{Stokes}$) of 1200 cm^{-1}. As expected, a very short lifetime ($\tau < 0.2$ ns) and a low quantum yield of $\Phi_{Fl}(M) = 0.23\%$ could be determined for the monomer species.

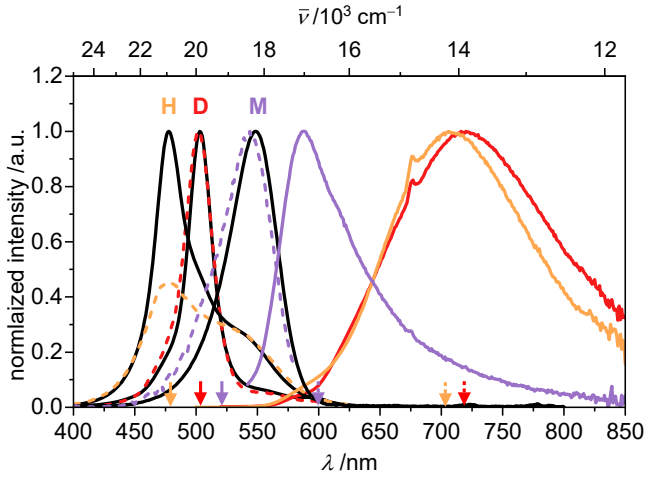

Figure 46. Normalized UV/Vis absorption (solid black lines), fluorescence (solid colored line) and excitation (dashed colored lines) spectra of the monomer (violet, $c_0 = 6.6\times10^{-7}$ M, $\lambda_{ex} = 520$ nm, $\lambda_{em} = 600$ nm) of **2** in CH_2Cl_2, as well as the dimer (red, $c_0 = 1.7\times10^{-6}$ M, $\lambda_{ex} = 502$ nm, $\lambda_{em} = 720$ nm) and the higher aggregate (orange, $c_0 = 1.0\times10^{-3}$ M, $\lambda_{ex} = 478$ nm, $\lambda_{em} = 703$ nm, front face setup) of **2** in MCH all recorded at room temperature.

The dimer of **2** in MCH shows a structureless broad excimer emission band at λ_{em} = 720 nm (λ_{ex} = 502 nm, c_0 = 1.7×10^{-6} M, 295 K) with large $\Delta\tilde{\nu}_{Stokes}$ = 6000 cm^{-1} (Figure 46, red) and a lifetime of the excited state of 7.6 ns. Even though the dimer is more emissive than the monomer the fluorescence intensity is still comparably low. Accordingly, a quantum yield of Φ_{Fl}(D) = 2.3% could be determined for the dimer in MCH. Interestingly, for the higher aggregate of merocyanine **2** in MCH an even further increased fluorescence intensity and lifetime of τ = 11.5 ns were observed compared to the dimer. The fluorescence spectrum of the higher aggregate also shows similar to the dimer a broad excimer band at λ_{em}(H) = 706 nm (λ_{ex} = 478 nm, c_0 = 1.0×10^{-3} M, 295 K) with an even larger $\Delta\tilde{\nu}_{Stokes}$ of 6800 cm^{-1} (Figure 46, orange). The emission spectrum resembles the dimer emission, which might indicate a localization of the initially formed exciton into excited dimers (excimers).[187] Due to the high sample concentration, the measurements suffer from reabsorption effects, even though a front face setup was used to keep the sample thickness as small as possible. These effects are less pronounced in the emission spectrum, due to the large $\Delta\tilde{\nu}_{Stokes}$, but clearly visible in the excitation spectrum of the higher aggregate. As the fluorescence quantum yield of the higher aggregate of merocyanine **2** could not be determined directly, it was estimated relative to the quantum yield of the dimer. For this the kinetic stability of the aggregate upon dilution was exploited. A concentrated higher aggregate solution of merocyanine **2** (c_0 = 1.0×10^{-3} M) was diluted to a concentration where predominantly dimers are present under equilibrium conditions at room temperature (c_0 = 1.0×10^{-5} M). The spectral changes of the emission were monitored over time (Figure 47).

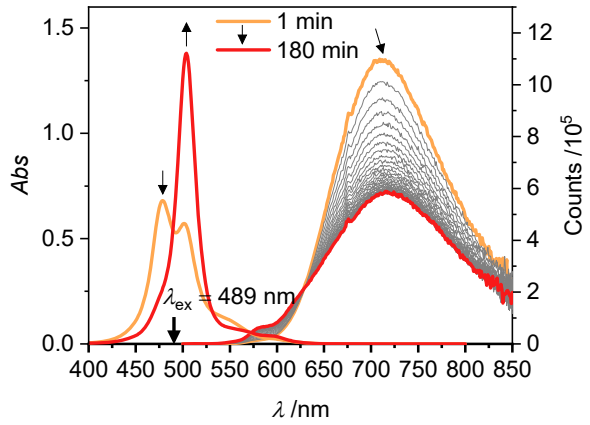

Figure 47. Time-dependent UV/Vis absorption and fluorescence (λ_{ex} = 489 nm) spectra of merocyanine **2** in MCH at room temperature, 1 min (orange line) to 180 min (red line) after dilution from c_0 = 1.0×10^{-3} M to c_0 = 1.0×10^{-5} M.

Upon disassembly into dimers, the fluorescence intensity decreases and the emission maximum shifts to 719 nm. Since the excitation wavelength was set at the isosbestic point at

489 nm, the sample always absorbs a constant amount of photons and the intensity of the emission can be directly correlated to the varying higher aggregate and dimer ratio. The fluorescence quantum yield Φ_{Fl} is proportional to the integral A of the emission spectrum (equation (59)). A system of linear equations can be formulated as equations (60) and (61), where A_1 and A_2 are the areas under the emission band at two different times, which were chosen as 1 min (27% of dimer and 73% of higher aggregate) and 180 min (97% dimer and 3% higher aggregate) after dilution, respectively. x_H and x_D are the fraction of molecules present as higher aggregate (H) or dimer (D) at the observed time, according to multiple linear regression analysis of the corresponding absorption spectrum.

$$\Phi_{Fl} \propto A . \tag{59}$$

$$A_1 = x_{H1} \cdot a_H + x_{D1} \cdot a_D . \tag{60}$$

$$A_2 = x_{H2} \cdot a_H + x_{D2} \cdot a_D . \tag{61}$$

Accordingly, a_H and a_D are the integrals of the theoretical emission bands of 100 % higher aggregate or 100% dimer, respectively, which are proportional to the respective quantum yields of the species. Since the quantum yield of the dimer is known to be $\Phi_{Fl}(D) = 2.3\%$, which is proportional to a_D, the quantum yield of the higher aggregate can be determined relative to this by solving the system of linear equations and comparing a_D and a_H. By this method a quantum yield of about $\Phi_{Fl}(H) = 4.5\%$ was determined for the H-aggregated dye stack.

With the available data for fluorescence quantum yields and fluorescence lifetimes for the monomer and the two aggregate species, further insights into the radiative (k_r) and non-radiative (k_{nr}) decay rates could be obtained (Table 6). These data clearly indicate that the rigidification of the dyes within the aggregate state affords a pronounced decrease of the non-radiative rate whilst the reduction of the radiative rate due to H-type coupling has a weaker impact. In this regard merocyanine **2** dimer and oligomer aggregates might be considered as soluble relatives to *para*-distyrylbenzene-based emissive solid state H-aggregates.[177]

Merocyanine **2** was also found to be emissive in the solid state. Two different solid samples were investigated: A solution of the higher aggregate of **2** in cyclohexane ($c_0 = 1\times10^{-3}$ M, Figure A66) was freeze-dried and for the resulting solid an absolute quantum yield of $\Phi_{Fl} = 4.9\%$, similar to the quantum yield of the higher aggregate in MCH, was determined with the integration sphere. A solid sample of **2**, obtained by evaporation of a CH_2Cl_2

solution, gave an even larger absolute quantum yield of $\Phi_{Fl} = 7.5\%$. Both solid samples show similar broad excimer like emission spectra with maxima at $\lambda_{em} = 710$ nm (Figure 48).

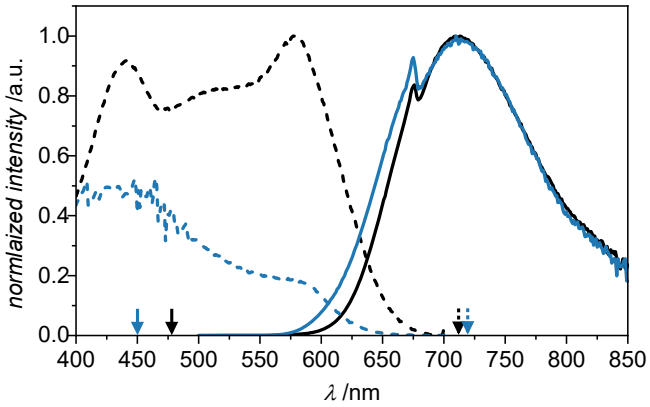

Figure 48. Fluorescence (dotted line) and excitation (dashed line) spectra of solid samples of merocyanine **2**. Blue: evaporation of CH_2Cl_2 solution ($\lambda_{ex} = 450$ nm, $\lambda_{em} = 720$ nm). Black: Freeze-dried cyclohexane solution ($\lambda_{ex} = 478$ nm, $\lambda_{em} = 712$ nm). All recorded at room temperature with a front face setup.

Also in the solid state a significant decrease of the non-radiative rate due to rigidification seems to be the main reason for the increased fluorescence intensity compared to the monomeric molecule in solution.

4.2.5 Aggregation-Induced CPL Enhancement

Circular polarized luminescence (CPL) describes the phenomenon of differential emission intensity of right and left circularly polarized light. While CD spectroscopy provides insights about the ground state of chiral systems, CPL can grant information about the relaxed excited state. The extend of chiral fluorescence dissymmetry is quantified by the anisotropy factor $g_{lum} = 2(I_L - I_R)/ (I_L + I_R)$, with I_L and I_R being the intensities of left and right circularly polarized light, respectively. Molecular organic systems usually exhibit relatively low g_{lum} values of $10^{-4} - 10^{-2}$.[188] It has, however, been observed that chiral excimer formation[189] or in general the formation of chiral aggregated structures[190-191] can enhance the g_{lum} value of a system significantly. Intrigued by these reports in literature, we investigated the CPL properties of the aggregate species of merocyanine **2**. For the monomer of **2** as expected no CPL was detectable, due to the low fluorescence intensity and the very week CD signal (Figure 44). For the dimer in MCH ($c_0 = 6.7\times10^{-6}$ M) a CPL signal with negative Cotton effect is detected (Figure 49, red line) with a g_{lum} value of 0.001 at 720 nm. The CPL spectrum of the higher aggregate in MCH ($c_0 = 1.2\times10^{-3}$ M, Figure 49, orange line) exhibits a strong negative signal with a significantly increased g_{lum} of up to 0.011 at 700 nm. Such preferential right circularly polarized fluorescence (negative CPL signal) for a right-handed

excimer configuration, as proposed for our higher aggregate, has also been observed for pyrene excimers of right-handed screw sense.[192] The g_{lum} value of the higher aggregate of **2** is in the same order as the highest values reported on multi-chromophore aggregates in solution[190] and confirms the usefulness of chiral helical assemblies to enhance the efficiency of CPL by AIEE.

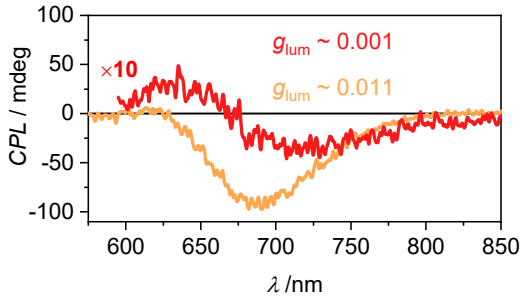

Figure 49. CPL spectra of the dimer (red, $c_0 = 6.7\times10^{-6}$ M, $\lambda_{ex} = 480$ nm) and the higher aggregate (orange, $c_0 = 1.2\times10^{-3}$ M, $\lambda_{ex} = 470$ nm) of merocyanine **2** in MCH recorded at room temperature. The dimer spectrum is depicted with ten-fold increased intensity.

4.3 Conclusion

Solvent- and concentration-dependent UV/Vis studies of merocyanine **2** revealed an anti-cooperative aggregation mechanism that consists of a two-step process. In the first step a dimer (2M ⇌ D) is formed due to strong dipole-dipole interactions followed by further self-assembly of those dimers into a larger oligomer π-stack by weaker dispersion forces. Due to the pronounced difference in the thermodynamic driving force for dimerization versus further oligomerization a concentration range exists where almost exclusively the dimer species is present (> 99%). This allowed us to fully evaluate and quantify the two processes, dimerization and higher aggregate formation, separately. The spectroscopic data for the formation of the higher aggregate was best described by a pentamer fit (5D ⇌ H) and a cooperativity value σ of up to 6700 at 298 K was determined.

NOE NMR spectroscopy provided precise insight into the molecular arrangement of the antiparallel aligned chromophores within the dimer aggregate. Regarding the structure of the higher aggregate, its rather small size of six to ten chromophores was consistently indicated by AFM, VPO and DOSY NMR measurements. We propose a *P*-helical stack, build from discrete dimer units based on 1D and 2D NMR experiments as well as the strong CD signal of the higher aggregate, which could be nicely reproduced by TD-DFT calculations. The increasing sterical demand of the solubilizing trialkoxyphenyl substituents limit the growth of

the stack size, as also observed in other literature examples[25, 33-34, 164-166]. An aliphatic shell can be formed around the polar chromophore core by the dodecyl chains, which would also explain the exceptionally high solubility of the compound even in MCH.

Based on our careful studies of the solvent-, concentration-, temperature-, and time-dependence of the aggregation process of dipolar merocyanine **2** we were able to investigate the fluorescence properties of the individual aggregate species. Accordingly, almost non-emissive merocyanine dyes show aggregation-induced emission enhancement (AIEE) behaviour upon dimerization and the fluorescence is further increased upon growth into larger aggregates. This AIEE behaviour is rationalized by the tight π-π-stacking of the merocyanine dyes in antiparallel dimeric units and further rigidification within more extended oligomeric π-stacks. Increased fluorescence lifetimes and larger Stokes shifts corroborate that the emission can be classified as excimer-type. Thus, this well-characterized two-step dye aggregate system provided valuable insights into the emergence of fluorescence by decrease of the non-radiative decay rates upon aggregation. The system additionally exhibited enhanced CPL for the higher aggregate compared to the dimer species, with a large g_{lum} value as high as 0.011.

CHAPTER 5

–

SUMMARY AND CONCLUSION

Dipolar merocyanines are very attractive supramolecular building blocks, as they combine interesting functional properties with strong, directional intermolecular interactions. The pyridine dioxocyano-pyridine (PYOP) chromophore (*Chapter 2.2*), used in this thesis, stands out because of its exceptionally high ground state dipole moment ($\mu_g \sim 17$ D), in combination with the option to retain good solubility also in unpolar solvents, by decoration with solubilizing groups (Figure 50a).

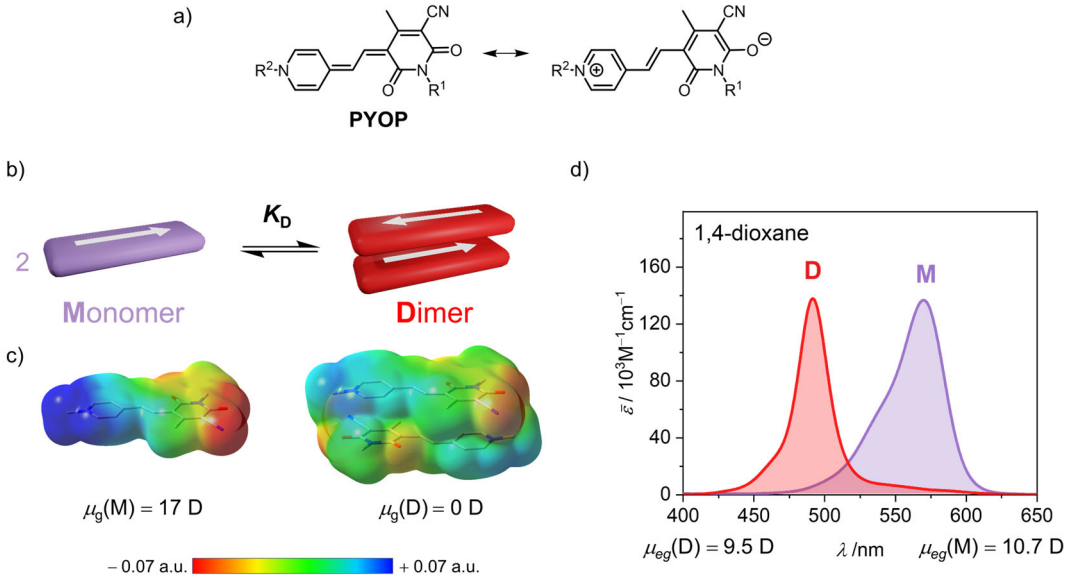

Figure 50. a) Chemical structure of the pyridine dioxocyano-pyridine (PYOP) merocyanine with its zwitterionic resonance structure. b) Schematic monomer-dimer equilibrium of the highly dipolar chromophore. Arrows indicate μ_g. c) Electrostatic surface potential of the geometry-optimized (B97D3/def2SVP, PCM: CH_2Cl_2) monomer and anti-parallel dimer. d) UV/Vis absorption spectra of the PYOP **1** monomer (M) and dimer (D) in 1,4-dioxane (293 K).

The reliable binding motif of anti-parallel π-stacking due to dipole-dipole interactions has allowed the design of molecular building blocks that form assemblies of predictable geometry. The intense unstructured charge transfer UV/Vis absorption band ($\mu_{eg} \sim 10.7$ D) is a result of the dominant contribution of the zwitterionic resonance structure which brings the PYOP chromophore just beyond the cyanine limit in solvents of low polarity ($c^2 = 0.60$, 1,4-dioxane). The high sensitivity of the $S_0 - S_1$ UV/Vis absorption band to the environment manifests itself in a pronounced negative solvatochromism and strong H-type exciton coupling within π-stacked PYOP assemblies. In accordance with the classical molecular

exciton theory, an increasing hypsochromic shift of the dominant absorption band of these H-aggregates can be observed as the stack size increases up to about six chromophores, where it levels out at about $\lambda_{max} \sim 440$ nm ($CHCl_3$). This allows a uniquely simple estimation of the number of interacting chromophores within the self-assembled structure from a single UV/Vis absorption spectrum of an aggregate.

The defined and well investigated PYOP dimer formation was employed in this thesis to probe the applicability and limitations of concentration-, temperature-, and solvent-dependent self-assembly studies (*Chapter 3*). Straightforward theoretical models to evaluate datasets of concentration-, temperature-, and solvent-dependent UV/Vis absorption by nonlinear regression analysis were derived for the case of dimer formation (*Chapter 2.1*). Although the dimer model is well known and widely applied in literature, this detailed derivation is helpful to understand assumptions and potential problems of the different approaches for the determination of thermodynamic parameters. This helps to decide on the most appropriate method to analyse a system of interest. In this regard it should be noted that covering a large portion of the self-assembly process with the experimental data is a prerequisite for the accuracy of the analysis. Additionally, many of the insights can also be transferred to other self-assembly systems like supramolecular polymerization or host-guest interactions.

The concentration-dependent analysis is the most straightforward method to investigate self-assembly equilibria. No additional assumptions, besides mass balance and mass action law, are required. Since it includes the least number of parameters (only K, if $\varepsilon_{M/D}$ are known), it is the most, or even only, reliable method, to elucidate the self-assembly mechanism of an unknown system by model comparison. To cover a large concentration range, however, the compound must be soluble enough and generally sample amounts at least in the low mg scale must be available.

The temperature-dependent analysis has the advantage that all thermodynamic parameters ΔG^0, ΔH^0 and ΔS^0 can be obtained from a single sample in one automated measurement. However, the accessible temperature-range is experimentally often quite limited and dependent on the solvent. For systems which do not show the transition from monomer to aggregate in a narrow temperature range, as given for, e.g., cooperative aggregation or processes with a high entropy contribution, often not the entire self-assembly process can be monitored. Furthermore, the assumptions of temperature-independent extinction coefficients of the individual species as well as temperature-independent ΔH^0 and ΔS^0 must be met. Monte

Carlo simulations of data sets demonstrated that even minor changes in experimental data can significantly impact the optimized values for ΔH^0 and ΔS^0. This is due to the redundancy of these two parameters within the model framework and even small thermochromic effects can significantly influence the results. The ΔG^0 value, calculated from ΔH^0 and ΔS^0, is, however, still rather reliable.

Solvent-dependent studies can often cover the entire self-assembly process from monomeric ($\alpha_{agg} = 0$) to the fully aggregated state ($\alpha_{agg} = 1$). However, for dyes with strong solvatochromic effects, such as the dipolar merocyanines investigated in this thesis, the results are affected. Also, the assumption of a linear relation of the binding energy ΔG^0 and the fraction of denaturating solvent *f*, which is based on linear free energy relationships between ΔG^0 and the solvent polarity, can lead to errors. Especially when specific solvent effects are involved.

For the evaluation of experimental data by nonlinear regression, general data analysis software can be used, where user-defined fit models and known parameters can be implemented as desired. Alternatively, multiple specialized programs for analysing self-assembly data are available online. While the latter programs are usually more user-friendly, they have the disadvantage of being a "black box" where only pre-implemented models can be used without the option for the user to adapt models or parameters for a specific system.

In *Chapter 3* comprehensive UV/Vis absorption datasets are presented for the dimerization of merocyanine derivative **1** in 1,4-dioxane (Figure 51a), which allowed for the first time a direct comparison of the results derived from concentration- (Figure 51b), temperature- (Figure 51c), and solvent-dependent (Figure 51d) self-assembly studies.

The results for the binding constant *K* and corresponding ΔG^0 from the concentration- and temperature-dependent analysis were in very good agreement, also in comparison to the results from ITC (Figure 51f). For the temperature-dependent analysis, though, multiple datasets of samples with different concentration had to be evaluated simultaneously to cover a meaningful part of the self-assembly process. Furthermore, a significant dependence of the optimized parameters ΔH^0 and ΔS^0 on the wavelength chosen for the analysis was observed (Figure 51e). This can be rationalized by the small thermochromic shifts of both the monomer and the dimer UV/Vis absorption band. The results from the solvent-dependent evaluation showed the largest deviation (Figure 51f), as expected for the highly solvatochromic merocyanine dye.

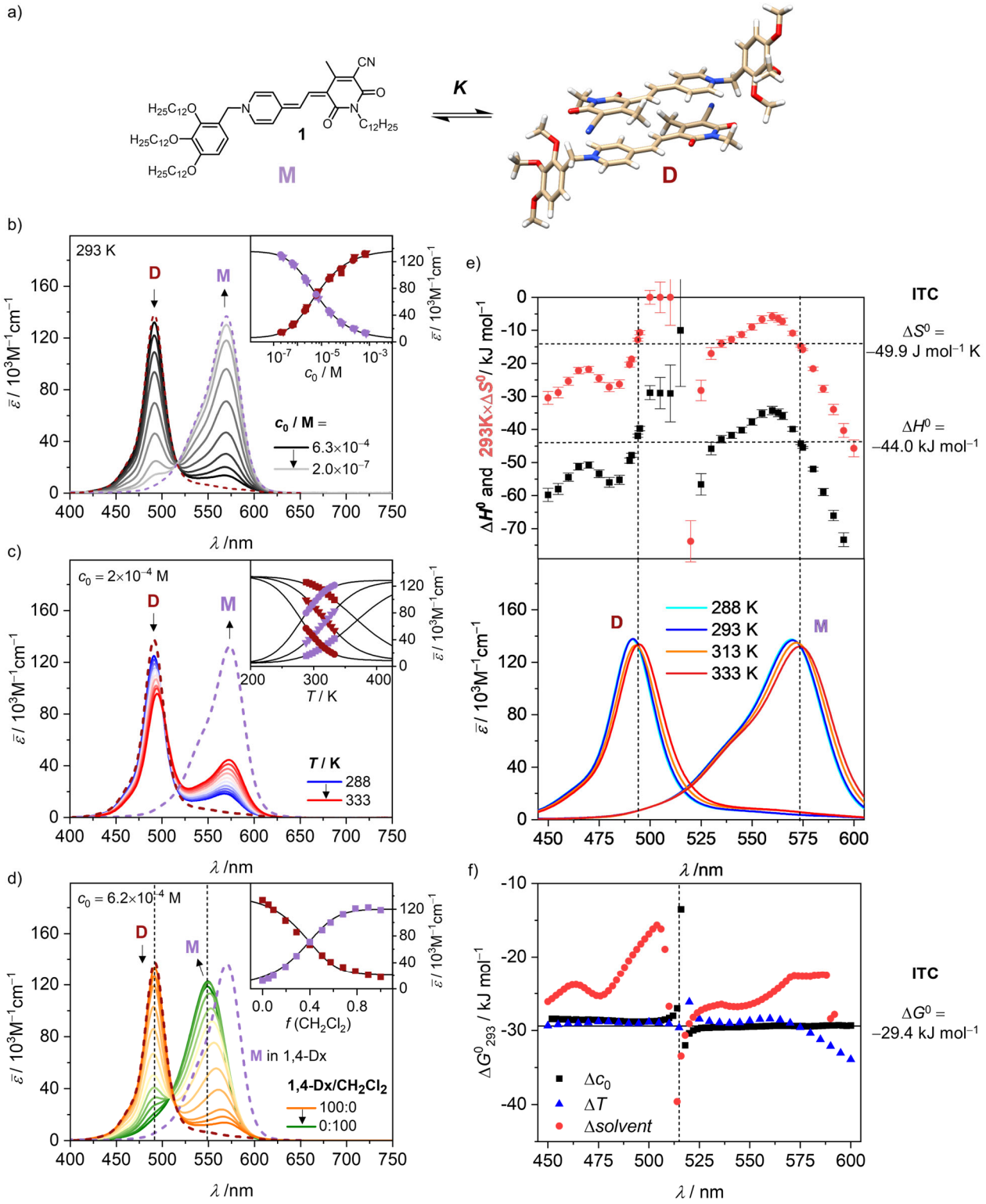

Figure 51. a) Chemical structure of merocyanine **1** monomer (M) and geometry optimized (B97D3/def2SVP, PCM: 1,4-dioxane) dimer (D). Dodecyl chains were substituted with CH_3. b-d) Concentration-, temperature-, and solvent-dependent UV/Vis absorption spectra of **1**. Calculated spectra of the monomer (M) and the dimer (D) in 1,4-dioxane are depicted with dashed lines. e) Results for ΔH^0 and ΔS^0 from temperature-dependent analysis at different wavelengths in comparison to results from ITC. On the bottom the calculated monomer and dimer spectra at different temperatures are shown. f) Results for ΔG^0 at 293 K from concentration- (black), temperature- (blue), and solvent-dependent (red) analysis at different wavelengths. The vertical line marks the wavelength of the (pseudo)isosbestic point.

However, even here by evaluation at 491 and 549 nm (dashed lines, Figure 51d) the deviation for ΔG^0 was only 2.5 kJ mol^{-1} (9%) with respect to the results from the concentration-dependent analysis (ΔG^0 = 29.1 kJ mol^{-1}). Thus, despite the strong solvatochromism of the dipolar chromophore, it can still be considered a reliable method for estimating the binding strength. Furthermore, multiple repetitions of the concentration-, temperature-, and solvent-dependent studies provided insight into the reproducibility of the results and possible sources of experimental errors. In all cases, the deviations of the results were small ($\Delta\Delta G^0 < 0.4$ kJ mol^{-1}) and within the same range as the fit error from the nonlinear regression analysis.

The insights from these studies were an important basis for the in-depth investigation of a more complex supramolecular system in *Chapter 4*, as a single method is often not enough to capture the full picture of a more complicated self-assembly process. To elucidate the anti-cooperative self-assembly of the chiral merocyanine **2** (Figure 52), a combination of multiple techniques had to be applied.

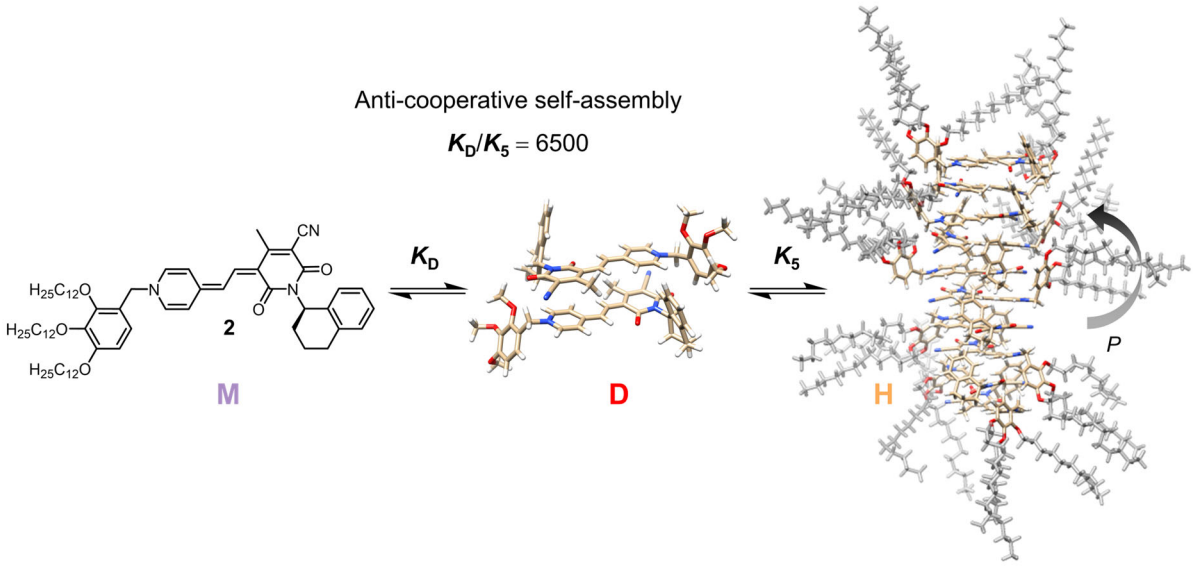

Figure 52. Anti-cooperative self-assembly of PYOP **2** monomers (M) into antiparallel dimers (D) and a *P*-helical π-stacked higher aggregate (H) of about ten chromophores. Dodecyl chains were added manually (in grey) to the optimized higher aggregate stack to illustrate the aliphatic shell formed by the solubilizing substituents around the polar chromophore core.

Solvent-dependent UV/Vis absorption studies in CH_2Cl_2/MCH mixtures showed the step-wise assembly of the merocyanine monomer (λ_{max}(M) = 549 nm, CH_2Cl_2) to first a dimer (λ_{max}(D) = 498 nm, CH_2Cl_2/MCH 15:85) by dipole-dipole interactions, and then a π-stacked higher aggregate (λ_{max}(H) = 477 nm, MCH), with pronounced H-type coupling (Figure 53a,b).

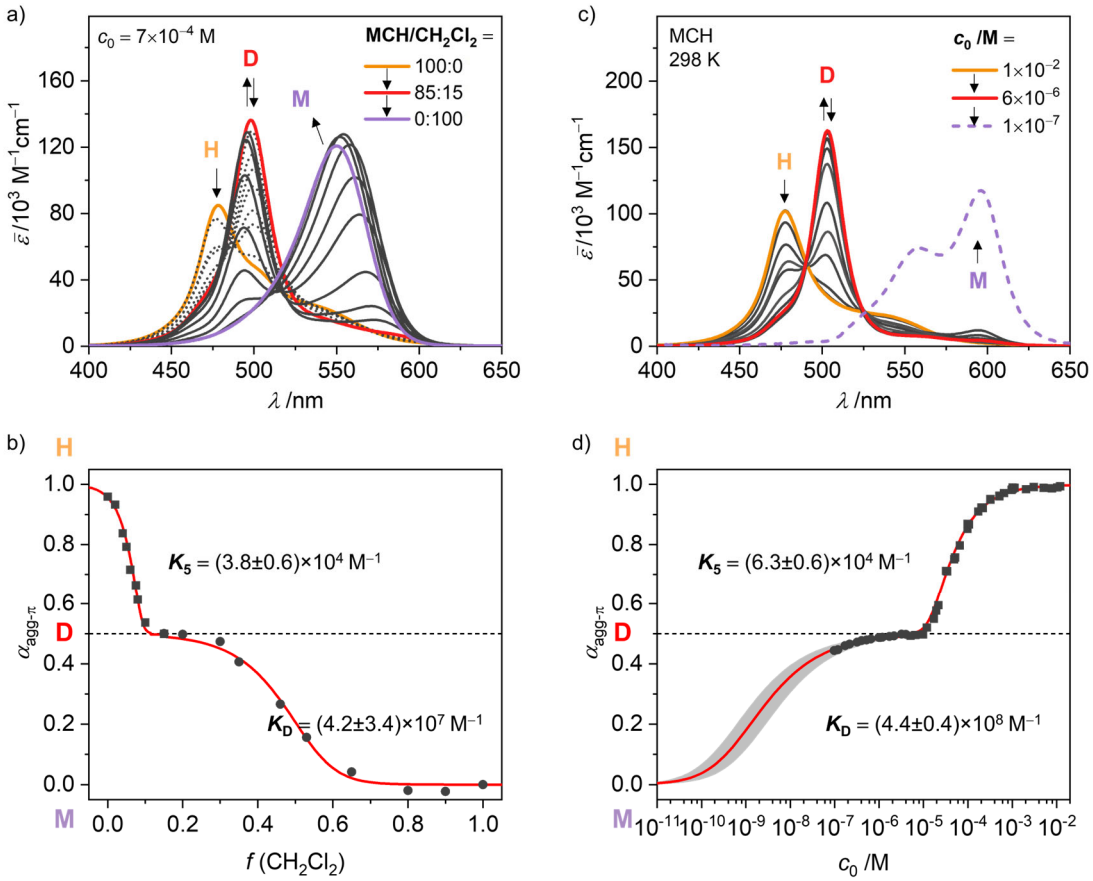

Figure 53. a) Solvent-dependent UV/Vis absorption spectra of **2** and b) corresponding degree of aggregated π-surfaces calculated at 550 nm (M⇌D, circles) or 498 nm (D⇌H, squares), with derived binding constants (± standard error) for the nucleation (K_D) and elongation (K_5). c) Concentration-dependent UV/Vis absorption spectra of **2** and d) corresponding degree of aggregated π-surfaces ($\alpha_{agg-\pi}$) calculated at 596 nm (M⇌D, circles) or 503 nm (D⇌H, squares), with derived binding constants (± standard error) for the nucleation (K_D) and elongation (K_5).

The thermodynamic evaluation of this data, however, suffered from the severe solvatochromism, especially of the monomeric species (λ_{max}(M, CH_2Cl_2) = 549 nm, λ_{max}(M, MCH) = 596 nm). Therefore, concentration-dependent studies were performed (Figure 53c,d) at three different temperatures (298, 323, 353 K) to elucidate the self-assembly mechanism and determine reliable thermodynamic parameters. The studies at elevated temperatures were hereby necessary, to obtain experimental data over a larger $\alpha_{agg-\pi}$-range. Due to the pronounced difference in the thermodynamic driving force for dimerization and higher aggregate formation ($K_D/K_5 = 6500$) a concentration range exists in MCH where almost exclusively the dimer species of **2** is present, before further self-assembly by dispersion interactions occurs. Therefore, the data could be evaluated independently for the two self-assembly steps. The self-assembly of dimers into the higher aggregate could not be described by the isodesmic model but was fitted satisfactorily to a pentamer model. This rather small size of about ten π-stacked PYOP chromophores was, furthermore, consistently indicated by AFM, VPO and DOSY NMR measurements. Based on 1D and 2D NMR data as

well as the strong bisignate CD signal of the higher aggregate in combination with TD-DFT calculations, a *P*-helical stack is proposed as its structure (Figure 52). The small size can be rationalized by the anti-cooperative self-assembly mechanism and the sterical demand of the solubilizing trialkoxyphenyl and the chiral tetralin substituents. Additionally, the aliphatic shell formed by the solubilizing chains around the polar chromophore stack, can account for the exceptionally high solubility of **2** in MCH (> 15 mg mL^{-1}). These combined studies of the self-assembly process enabled the identification of suitable conditions for the investigation of fluorescence properties of the individual aggregate species. Aggregation-induced emission enhancement was observed for the almost non-emissive monomer ($\Phi_{Fl}(M) = 0.23\%$), which can be rationalized by the increasing rigidification within the dimer ($\Phi_{Fl}(D) = 2.3\%$) and the higher aggregate ($\Phi_{Fl}(H) = 4.5\%$). The helical chirality of the PYOP decamer stack, furthermore, gave rise to a strong CPL signal with a large g_{lum} value of 0.011.

The important conclusion of this thesis is that the temperature- and solvent-dependent analyses are valid alternatives to the classical concentration-dependent analysis to determine thermodynamic parameters of self-assembly equilibria. Although, for a specific supramolecular system, one approach might be favourable over the others for a variety of reasons. The experimental limitations often demand a combination of techniques to fully elucidate a self-assembly process and to gain insights in the aggregate structure. The anti-cooperative merocyanine self-assembly, which was described here for the first time for the PYOP merocyanine **2**, is no exception. Besides the interest in the merocyanine assemblies from a structural and functional point of view, the insights gained from the presented studies can also be transferred to other self-assembly systems and be a guide to find the most appropriate analysis technique.

CHAPTER 6

–

ZUSAMMENFASSUNG UND FAZIT

Dipolare Merocyanine sind sehr attraktive supramolekulare Bausteine, da sie interessante funktionale Eigenschaften mit starken, gerichteten zwischenmolekularen Wechselwirkungen vereinen. Der Pyridin-dioxocyano-pyridin (PYOP)-Chromophor (*Kapitel 2.2*), welcher in dieser Arbeit verwendet wurde, zeichnet sich durch sein besonders starkes Grundzustands-dipolmoment ($\mu_g \sim 17$ D) aus, in Kombination mit der Möglichkeit durch Funktionalisierung mit löslichkeitsvermittelnden Gruppen dennoch gute Löslichkeit zu bewahren (Abbildung 1).

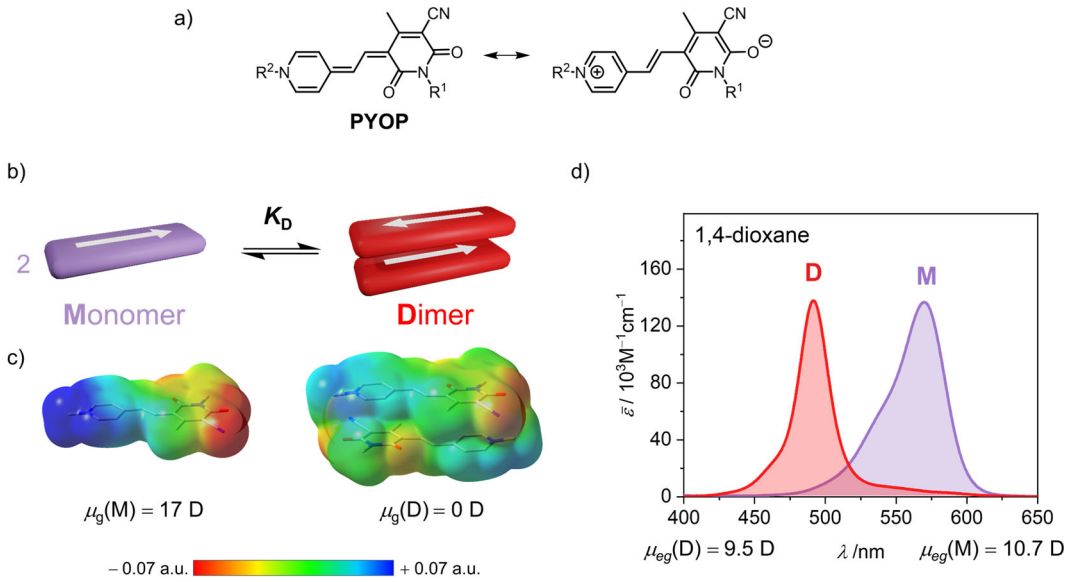

Abbildung 1. a) Chemische Struktur des Pyridin-dioxocyano-pyridin (PYOP)-Merocyanins mit seiner zwitterionischen Resonanzstruktur. b) Schematisches Monomer-Dimer Gleichgewicht des dipolaren Chromophors. Die Pfeile zeigen μ_g an. c) Elektrostatische Potentialoberflächen von Geometrie-optimiertem (B97D3/def2SVP, PCM: CH_2Cl_2) Monomer und anti-parallelem Dimer. d) UV/Vis Absorptionsspektren des PYOP **1** Monomers (M) und Dimers (D) in 1,4-Dioxan (293 K).

Das zuverlässige Bindungsmotiv der durch Dipol-Dipol Wechselwirkungen anti-parallel π-gestapelten Merocyanine ermöglicht es, gezielt molekulare Bausteine zu entwerfen, welche sich zu Strukturen von vorhersagbarer Geometrie zusammenlagern. Der dominante Beitrag der zwitterionischen Resonanzstruktur führt zu einer intensiven, unstrukturierten Charge-Transfer UV/Vis-Absorptionsbande ($\mu_{eg} \sim 10.7$ D) und bringt den PYOP Chromophor leicht jenseits des Cyanin-Limits in unpolaren Lösungsmitteln ($c^2 = 0.60$, 1,4-Dioxan). Die Sensitivität der S_0 - S_1 UV/Vis-Absorptionsbande gegenüber der Umgebung zeigt sich in der ausgeprägten negativen Solvatochromie und einer starken H-artigen excitonischen Kopplung

in π-gestapelten Aggregaten. In Übereinstimmung mit klassischer Excitonen-Theorie kann eine zunehmende hypsochrome Verschiebung der dominanten Absorptionsbande mit zunehmender Größe der H-Aggregate beobachtet werden, bis bei etwa sechs Chromophoren und $\lambda_{max} \sim 440$ nm ein Plateau erreicht wird. Dies ermöglicht eine einmalig einfache Abschätzung, der Anzahl an wechselwirkenden Chromophoren innerhalb einer Aggregatstruktur, basierend auf einem einzigen UV/Vis-Absorptionsspektrum.

Das definierte und gut untersuchte Beispiel des PYOP-Dimers wurde in dieser Arbeit verwendet, um die Anwendbarkeit und die Grenzen von konzentrations-, temperatur- und lösungsmittelabhängigen Aggregationsstudien auszutesten (*Kapitel 3*). Theoretische Modelle zur thermodynamischen Auswertung von konzentrations-, temperatur- und lösungsmittelabhängigen Studien mittels nichtlinearer Regression wurden für das Beispiel der Dimerisierung hergeleitet (*Kapitel 2*). Obwohl das Dimer-Modell literaturbekannt ist, ist diese detaillierte Herleitung hilfreich, um die Annahmen zu verstehen, die dem Modell zugrunde liegen. So können potenzielle Problemquellen der verschiedenen Methoden erkannt und die geeignetste Methode zur Bestimmung der thermodynamischen Parameter für ein bestimmtes System ausgewählt werden. Hierbei sollte man beachten, dass es sich für die Aussagekraft der Analyse klar als zuträglich erwiesen hat, wenn ein möglichst großer Bereich des Aggregationssprozesses von den experimentellen Daten abgedeckt werden kann. Viele der hier gewonnen Erkenntnisse lassen sich auch auf andere Systeme wie supramolekulare Polymere oder Wirt-Gast-Komplexe übertragen.

Die konzentrationsabhängige Analyse ist die direkteste Methode, um ein supramolekulares Gleichgewicht zu untersuchen. Sie erfordert keine zusätzlichen Annahmen, außer dem Massenerhalt und dem Massenwirkungsgesetz. Da das konzentrationsabhängige mathematische Modell die wenigsten Parameter enthält (nur K, wenn $\varepsilon_{M/D}$ bekannt), ist es die zuverlässigste, wenn nicht sogar die einzig zuverlässige, Methode, um den Aggregationsmechanismus durch einen Vergleich der experimentellen Daten mit verschiedenen Modellen aufzuklären. Allerdings muss die zu untersuchende Verbindung hierbei löslich genug sein, damit ein großer Teil des Aggregationsprozesses in den Studien abgebildet werden kann und es werden üblicherweise Substanzmengen im niedrigen mg Bereich benötig.

Die temperaturabhängige Analyse hat den Vorteil, dass alle thermodynamischen Parameter ΔG^0, ΔH^0 und ΔS^0 in einer einzigen automatisierten Messung einer einzelnen Probe erhalten

werden können. Allerdings ist der experimentell zugängliche Temperaturbereich oft sehr eingeschränkt und abhängig von dem verwendeten Lösungsmittel. Für Systeme, bei denen der Übergang vom Monomer zum Aggregat nicht in einem engen Temperaturbereich erfolgt, z.B. aufgrund von Kooperativität oder einem großen Entropie-Beitrag, ist es oft nicht möglich den gesamten Aggreationsprozess abzubilden. Zusätzlich sollten die Annahmen, dass sowohl die Extinktionskoeffizienten der einzelnen Spezies sowie ΔH^0 und ΔS^0 temperaturunabhängig sind, zutreffen. Mittels Monte Carlo Simulationen konnte gezeigt werden, dass selbst kleine Änderungen in den experimentellen Daten die erhaltenen Werte von ΔH^0 und ΔS^0 deutlich beeinflussen können. Dies liegt daran, dass die beiden Parameter im mathematischen Modell nicht völlig unabhängig voneinander sind. Selbst geringfügige thermochrome Veränderungen können daher die Ergebnisse für ΔH^0 und ΔS^0 beeinflussen. Die ΔG^0-Werte, die sich aus ΔH^0 und ΔS^0 berechnen lassen, sind allerding dennoch recht zuverlässig. Mittels lösungsmittelabhängiger Studien ist es oft am einfachsten, den vollständigen Prozess vom Monomer ($\alpha_{agg} = 0$) bis zum Aggregat ($\alpha_{agg} = 1$) abzubilden. Für stark solvatochrome Farbstoffe wie die hier untersuchten dipolaren Merocyanine werden die Ergebnisse allerdings deutlich verfälscht. Auch die Annahme einer linearen Abhängigkeit der Bindungsenergie ΔG^0 und der Lösungsmittelzusammensetzung *f*, die auf linearen Freie-Energie Beziehungen zwischen ΔG^0 und der Lösungsmittelpolarität beruhen, kann zu Abweichungen führen, vor allem, wenn spezifische Lösungsmitteleffekte involviert sind. Die Auswertung der experimentellen Daten erfolgt mittels nichtlinearer Regression. Hierfür können diverse Datenauswertungsprogramme genutzt werden, in die sich benutzerdefinierte Modelle inklusive bekannter Parameter implementieren lassen. Alternativ gibt es auch eine Auswahl von spezialisierten Programmen zur Auswertung von Aggregationsdaten im Internet. Diese sind zwar deutlich benutzerfreundlicher, aber auch „Black Boxes“, deren voreingestellte Modelle und Parameter in der Regel nicht vom Nutzer für ein spezielles System angepasst werden können.

In *Kapitel 3* wurden umfangreiche UV/Vis-Absorptionsstudien für die Dimerisierung von Merocyanin **1** in 1,4-Dioxan vorgestellt (Abbildung 2a), welche zum ersten Mal einen direkten Vergleich zwischen den Ergebnissen von konzentrations- (Abbildung 2b), temperatur- (Abbildung 2c) und lösungsmittelabhängigen (Abbildung 2d) Aggregationsstudien ermöglichten. Die Ergebnisse für die Bindungskonstante *K* und dem dazugehörigen ΔG^0-Wert aus der konzentrations- und temperaturabhängigen Analyse

stimmen mit den Ergebnissen der isothermalen Titrationskalorimetrie (ITC) überein (Abbildung 2f).

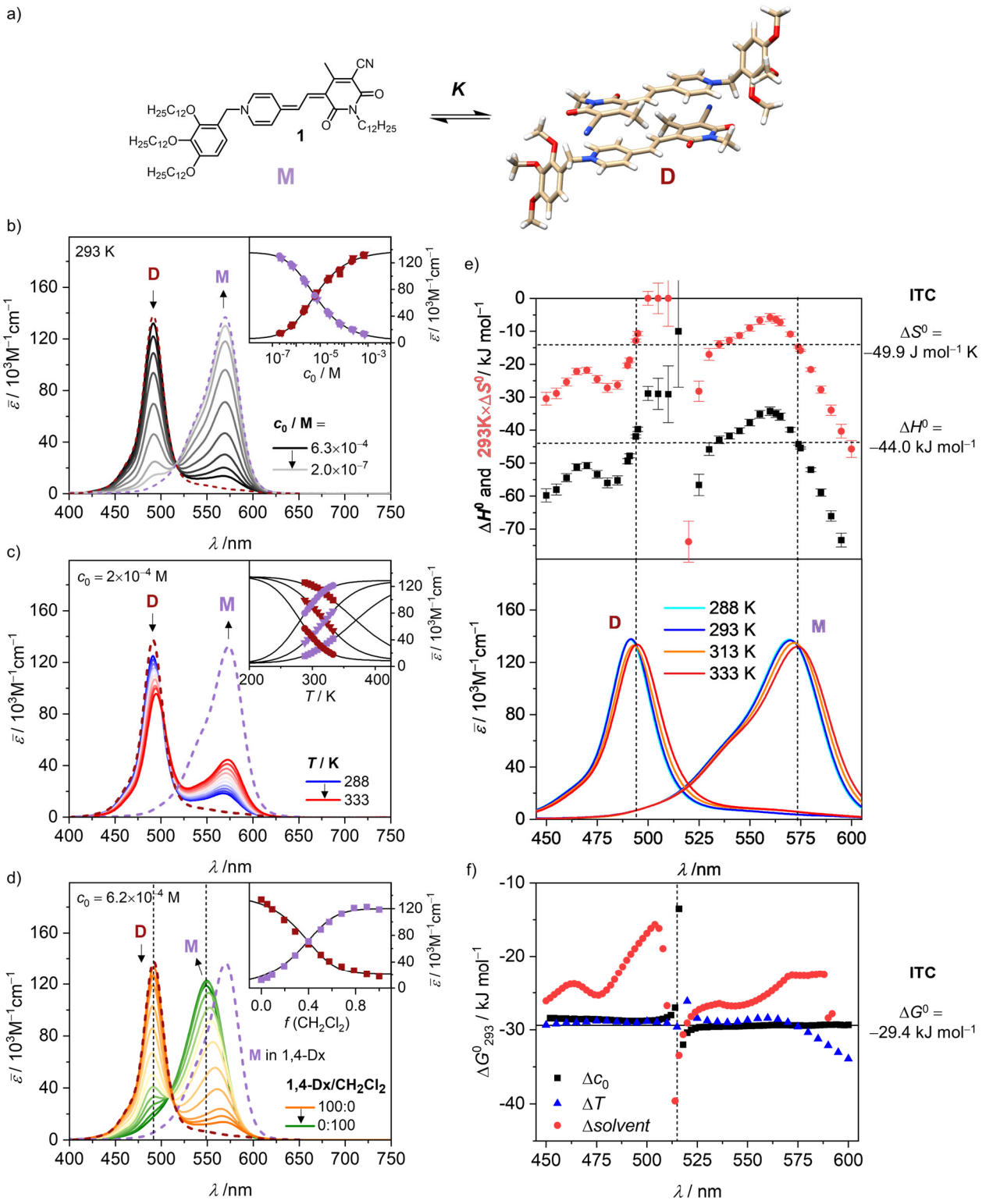

Abbildung 2. a) Chemische Struktur von Merocyanin **1** Monomer (M) und Geometrie-optimiertes Dimer (D). Dodecylketten wurden durch CH_3 ersetzt. b-d) Konzentrations-, temperatur- und lösungsmittelabhängige UV/Vis-Absorptionsspektren von **1**. Berechnete Monomer- (M) und Dimer- (D) Spektren sind mit gestrichelten Linien dargestellt. e) Werte für ΔH^0 and ΔS^0 von der temperaturabhängigen Auswertung der Daten bei unterschiedlichen Wellenlängen im Vergleich mit den Ergebnissen der ITC. Unten sind die berechnete Monomer- und Dimer-Spektren bei verschiedenen Temperaturen gezeigt. f) Werte für ΔG^0 bei 293 K aus der konzentrations- (schwarz), temperatur- (blau) und lösungsmittelabhängigen Analyse bei verschiedenen Wellenlängen. Die vertikale Linie markiert den (pseudo)isosbestischen Punkt.

Bei der temperaturabhängigen Auswertung mussten allerdings mehrere Datensätze von Proben mit unterschiedlichen Konzentrationen zusammen ausgewertet werden, um einen aussagekräftigen Bereich des Aggregationsprozesses abzudecken. Außerdem wurde eine deutliche Abhängigkeit der Ergebnisse für ΔH^0 und ΔS^0 von der Wellenlänge festgestellt, die für die Auswertung gewählt wurde (Abbildung 2e). Dies liegt an der kleinen thermochromen Verschiebung der Monomer- und Dimer-Absorptionsbande. Die Ergebnisse der lösungsmittelabhängigen Studien zeigten, wie für den stark solvatochromen Chromophor erwartet, die größte Abweichung (Abbildung 2f). Allerdings beträgt die Abweichung für ΔG^0 selbst hier nur 2.5 kJ mol^{-1} (9%), bei Auswertung bei 491 und 549 nm (gestrichelte Linien, Abbildung 2d), im Vergleich zur konzentrationsabhängigen Auswertung (ΔG^0 = 29.1 kJ mol^{-1}). Trotz der ausgeprägten Solvatochromie sind die lösungsmittelabhängigen Studien also geeignet, um die Bindungsstärke eines Systems abzuschätzen. Mehrmalige Wiederholung der Experimente erlaubte eine Abschätzung der Reproduzierbarkeit der Ergebnisse und möglicher Fehlerquellen. Die Ergebnisse schwankten hierbei in allen Fällen nur geringfügig ($\Delta\Delta G^0 < 0.4$ kJ mol^{-1}) und in der gleichen Größenordnung wie der Fehler der nichtlinearen Regression.

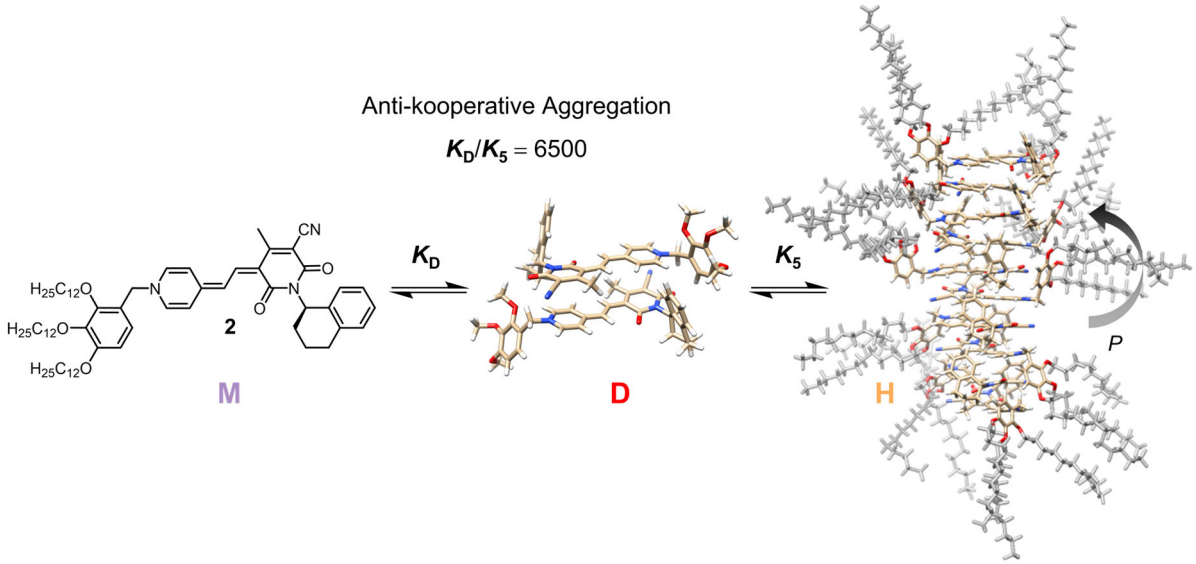

Abbildung 3. Anti-kooperative Aggregation des PYOP **2** Monomers (M) zu antiparallelen Dimeren (D) und *P*-helikalien höheren Aggregaten (H) aus ca. zehn Chromophoren. Die Dodecylketten wurden manuell (in Grau) zum optimierten Aggregatstapel hinzugefügt, um die aliphatische Hülle zu veranschaulichen, die sich durch die löslichkeitsvermittelnden Gruppen um den polaren Chromophor-Stapel bildet.

Die Erkenntnisse aus diesen Studien waren eine wichtige Grundlage für die Untersuchung eines komplexeren supramolekularen Systems in *Kapitel 4*. Eine einzelne Methode ist oft nicht ausreichend, um einen mehrstufigen Aggregationsprozess vollständig aufzuklären, und auch zur Aufklärung der anti-kooperativen Aggregation des chiralen Merocyanins **2**

(Abbildung 3), wurde eine Kombination verschiedener Techniken angewandt. Lösungsmittelabhängige UV/Vis-Absorptionsstudien in CH_2Cl_2/MCH Mischungen zeigten die stufenweise Zusammenlagerung der Merocyanin-Monomere (λ_{max}(M) = 549 nm, CH_2Cl_2) zuerst durch Dipol-Dipol Wechselwirkungen zu Dimeren (λ_{max}(D) = 498 nm, CH_2Cl_2/MCH 15:85) und dann zu größeren π-Stapeln (λ_{max}(H) = 477 nm, MCH) mit ausgeprägter H-Kopplung (Abbildung 4a,b).

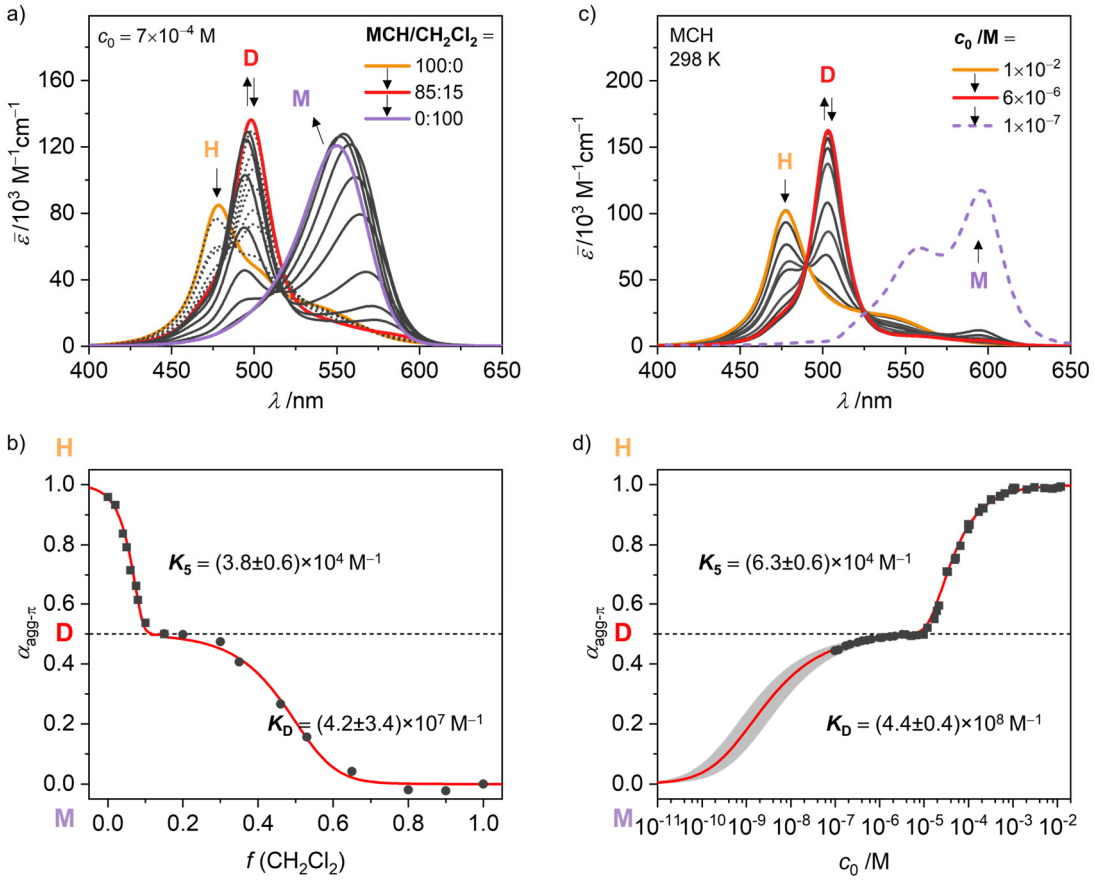

Abbildung 4. a) Lösungsmittelabhängige UV/Vis-Absorptionsspektren von **2** und b) dazugehöriger π-Flächen-Aggregationsgrad ($\alpha_{agg-\pi}$) berechnet bei 550 nm (M⇌D, Kreise) oder 498 nm (D⇌H, Quadrate), mit den daraus ermittelten Bindungskonstanten (± Standardfehler) für die Dimerisierung (K_D) und höhere Aggregatbildung (K_5). c) Konzentrationsabhängige UV/Vis-Absorptionsspektren von **2** und d) dazugehöriger π-Flächen-Aggregationsgrad ($\alpha_{agg-\pi}$) berechnet bei 596 nm (M⇌D, Kreise) oder 503 nm (D⇌H, Quadrate), mit den daraus ermittelten Bindungskonstanten (± Standardfehler) für die Dimerisierung (K_D) und höhere Aggregatbildung (K_5).

Die thermodynamische Auswertung dieser Daten leidet allerdings unter der ausgeprägten Solvatochromie, vor allem der Monomer-Spezies (λ_{max}(M, CH_2Cl_2) = 549 nm, λ_{max}(M, MCH) = 596 nm). Daher wurden stattdessen konzentrationsabhängige Studien bei verschiedenen Temperaturen durchgeführt (Abbildung 4c,d), um den Aggregationsmechanismus aufzuklären und verlässliche thermodynamische Parameter zu bestimmen. Die Studien bei höheren Temperaturen waren notwendig, um mit den experimentellen Daten einen größeren $\alpha_{agg-\pi}$-Bereich abdecken zu können. Aufgrund des

ausgeprägten Unterschieds in der thermodynamischen Triebkraft für die Dimerisierung und die Bildung höherer Aggregate ($K_D/K_5 = 6500$) gibt es in MCH einen Konzentrationsbereich, in dem fast ausschließlich die dimere Spezies vorhanden ist, bevor eine weitere Zusammenlagerung durch Dispersionswechselwirkungen erfolgt. Dies ermöglichte eine unabhängige Auswertung der Daten für die beiden Aggregationsschritte. Der Zusammenschluss von Dimeren zum höheren Aggregat ließ sich nicht durch das isodesmische Modell beschreiben, sondern durch ein Pentamer-Modell. Diese Größe von etwa zehn π-gestapelten PYOP-Chromophoren wurde außerdem durch AFM-, VPO- und DOSY-NMR-Messungen bestätigt. Basierend auf 1D- und 2D-NMR-Daten und dem CD-Signal des höheren Aggregats mit positivem Cotton-Effekt in Kombination mit TD-DFT Rechnungen, wurde ein *P*-helikaler π-Stapel als Struktur angenommen (Abbildung 3). Die geringe Größe lässt sich durch den anti-kooperativen Aggregationsmechanismus und den sterischen Anspruch der lösungsvermittelnden Trialkoxyphenyl- und der chiralen Tetralin-Substituenten erklären. Die durch diese Substituenten ausgebildete aliphatische Hülle um den polaren Chromophorstapel kann außerdem die ungewöhnlich hohe Löslichkeit der Verbindung **2** in MCH erklären (> 15 mg mL^{-1}). Die detaillierte Untersuchung des Selbstorganisationsprozesses ermöglichte die Identifizierung geeigneter Bedingungen für die Untersuchung der Fluoreszenzeigenschaften der einzelnen Aggregatspezies. Für das nahezu nicht emittierende Monomer ($\Phi_{Fl}(M) = 0.23\%$) wurde durch zunehmende Rigidisierung im Dimer ($\Phi_{Fl}(D) = 2.3\%$) und im höherem Aggregat ($\Phi_{Fl}(H) = 4.5\%$) eine durch Aggregation induzierte Emissionssteigerung beobachtet. Die helikale Chiralität des PYOP-Decamer-Stapels führte außerdem zu einem starken CPL Signal mit einem hohen g_{lum}-Wert von 0.011.

Das wichtige Fazit dieser Arbeit ist, dass sowohl temperatur- als auch lösungsmittelabhängige Studien valide Alternativen zu den klassischen konzentrationsabhängigen Untersuchungen sind, mit denen thermodynamische Parameter von Selbstorganisations-Gleichgewichten bestimmt werden können. Wobei für ein bestimmtes supramolekulares System eine der Methoden aus verschiedenen Gründen vorteilhafter sein kann als die anderen. Üblicherweise gegebene experimentelle Beschränkungen erfordern oft den kombinierten Einsatz von Techniken, um einen Selbstorganisationsprozess und die Aggregatstrukturen vollständig aufzuklären. Die anti-kooperative Merocyanin-Selbstorganisation, die hier zum ersten Mal für das PYOP-Merocyanin **2** beschrieben wurde, ist keine Ausnahme. Neben dem Interesse an den Merocyanin-Aggregaten aus struktureller und funktioneller Sicht können die aus den vorgestellten Studien gewonnenen Erkenntnisse auch auf andere Selbstassemblierungs-

systeme übertragen werden und als Leitfaden für die Suche nach der am besten geeigneten Analysemethode dienen.

CHAPTER 7

–

APPENDIX

7.1 Appendix for Chapter 2

Isodesmic Model

For the simulated curves according to the isodesmic aggregation $M_{n-1} + M \rightleftharpoons M_n$, the following equations apply:[16]

$$c_n = K^{n-1}\, {c_1}^n, \tag{62}$$

$$c_0 = (c_1 + 2K{c_1}^2 + 3K^2\, {c_1}^3 + \cdots + nK^{n-1}\, {c_1}^n) = \frac{c_1}{(1-Kc_1)^2}, \tag{63}$$

$$c_1 = \frac{2Kc_T+1-\sqrt{4Kc_T+1}}{2K^2c_T}, \tag{64}$$

$$\bar{\varepsilon} = \varepsilon_n + (\varepsilon_1 - \varepsilon_n)\frac{2Kc_0+1-\sqrt{4Kc_0+1}}{2K^2{c_0}^2}. \tag{65}$$

Here c_1 and c_n are the equilibrium concentrations of 1-mer and n-mer, and ε_1 and ε_n their respective extinction coefficients. K is the binding constant, which is assumed to be equal for all association steps.

Defined n-Mer Formation

For the formation of a defined linear n-mer applies the simplified two-species equilibrium $n\,M \rightleftharpoons M_n$.[24]

$$c_0 = c_1 + n\,c_n, \tag{66}$$

$$c_0 \cdot \bar{\varepsilon} = c_1 \cdot \varepsilon_1 + n\,c_n \cdot \varepsilon_n, \tag{67}$$

$$K_n = \sqrt[n-1]{\frac{c_n}{{c_1}^n}} = \sqrt[n-1]{\frac{\left(c_0 - \frac{c_0(\bar{\varepsilon}-\varepsilon_n)}{(\varepsilon_1-\varepsilon_n)}\right)\cdot\frac{1}{n}}{\left(\frac{c_0(\bar{\varepsilon}-\varepsilon_n)}{(\varepsilon_1-\varepsilon_n)}\right)^n}}. \tag{68}$$

Here c_1 and c_n are the equilibrium concentrations of 1-mer and n-mer, and ε_1 and ε_n their respective extinction coefficients. K_n is the binding constant per binding site. Implicit curve simulations and fitting according to this model was performed with OriginPro.[103]

7.2 Appendix for Chapter 3

Materials and Methods

Chemicals

Merocyanine **1** was synthesised according to literature known procedure.[150] All solvents used were of spectroscopy grade.

UV/Vis Spectroscopy

UV/Vis absorption spectra were recorded on a JASCO V-770 spectrometer with a spectral bandwidth of 1 nm and a scan rate of 200 nm/min (photometric accuracy ±0.0025). Quartz cells (Hellma Analytics) with path length of 0.1 – 100 mm were used to keep the absorbance of the samples in a suitable regime for the instrumental setup (0.3 – 1.7). The temperature was controlled either by a Peltier element (JASCO PAC-743R) with a temperature-control accuracy of ± 1 K for cells ≤ 10 mm thickness or with a LAUDA Alpha RA 8 thermostat for cells > 10 mm thickness.

For concentration-dependent studies, a stock solution was subsequently diluted to adjust the desired concentration. The highest concentration is limited by the solubility of the compound and the lowest accessible concentration by the sensitivity of the instrument and the maximum path length of the available cuvettes. For the highest concentrated solution the compound weight was determined with an Ultra-Micro balance XP2U from METTLER TOLEDO (accuracy ± 0.1 µg). The added solvent volume was determined from the weight (XP205 balance from METTLER TOLEDO, accuracy ± 0.01 mg) and the solvent density. This solution was diluted to ~1/3 and ~1/10 by mixing the stock solution with pure solvent. The exact mixing ratio and therefore concentration of diluted samples was determined from the weight of the stock solution and the solvent added. The solution with about ~1/10 of the concentration of the initial stock solution was used as the new stock solution for the subsequent dilution steps and so on.

Temperature-dependent measurements were performed with a heating rate of 2 °C/min and a delay time of 1 min before the measurement upon reaching the desired temperature. First the

heating curve was recorded, then the cooling curve. No significant hysteresis was observed between heating and cooling. The data acquired upon heating was used for evaluation. For the solvent-dependent measurements equally concentrated stock solutions of **1** in 1,4-dioxane and CH_2Cl_2 were mixed in different volume ratios. The exact ratio was determined by weighing and it is assumed that the volume of the two solvents is additive. It was always verified by repeated measurements that the samples were equilibrated after concentration-, temperature- or solvent change. Apparent molar extinction coefficients ($\bar{\varepsilon}$) were calculated according to the Lambert-Beer law and the concentrations are density corrected for the respective temperatures.

UV/Vis Absorption Data Evaluation

Fitting of the experimental UV/Vis absorption data was performed with OriginPro 2020[103]. Either the nonlinear curve fitting tool was used or the "Global Fit with Multiple Functions" application (both with Levenberg-Marquardt iteration algorithm). Suitable starting values were chosen for the required parameters and the resultant values are given with the approximated standard error from the fit. The error of derived parameters (marked in grey in the tables of the SI) was determined by propagation of errors. If multiple datasets were fitted simultaneously always as many parameters as possible were shared between as many datasets as possible, e.g., same K for all datasets, and $\varepsilon_{M/D}$ shared for all of the datasets from the same wavelength. Concentration-dependent data was additionally fitted globally over the whole absorption range (400 – 650 nm) with a LabView fitting routine as introduced in previous work[26, 97] to obtain calculated UV/Vis absorption spectra of the pure monomer and dimer species.

Isothermal Titration Calorimetry

ITC measurements were performed using a MicroCal VP-ITC (GEHealthcare, USA). Stirring rate was 307 rpm. The temperature of the sample solution and solvent was adjusted to the respective temperature (293 K) prior to the measurement using a MicroCal ThermoVac (GE Healthcare, USA). The enthalpograms were derived by integrating the raw heat signals and were fitted with the calorimetric fitting routines embedded in the Origin 7.0 for ITC software package from MicroCal, LLC. Results for the thermodynamic parameters are given as mean ± standard deviation from five repetitions of the experiment, since this standard deviation was significantly larger than the individual fit errors.

Dilution ITC experiments[151] were performed by sequential injection (14×20 µL, 5 min intervals) of a concentrated solution of merocyanine **1** in 1,4-dioxane ($c_0 = 2\times10^{-4}$ M, concentration limited by solubility) into the stirred calorimeter cell ($V = 1.4$ mL) initially containing pure 1,4-dioxane. The integrals of the series of endothermic heat pulses was analysed using MicroCal Origin for ITC software according to a pre-implemented dimer dissociation model as described in the MicroCal manual to give the dissociation constant $K_{diss} = 1/K$ and the standard molar enthalpy of dissociation $\Delta H^0_{diss} = -\Delta H^0$.

Heats of dilution data for the monomer-dimer equilibrium (1) is analysed as follows. It applies

$$K_{\mathrm{diss}} = \frac{{c_{\mathrm{M}}}^2}{c_{\mathrm{D}}} \tag{69}$$

and therefore the total molecular sample concentration in the cell after the ith injection c_i can be expressed as the sum of the monomer concentration $c_{M,i}$ in the cell plus two times the dimer concentration $c_{D,i}$:

$$c_{\mathrm{i}} = {K_{\mathrm{diss}}}^{\frac{1}{2}}\, {c_{\mathrm{D,i}}}^{\frac{1}{2}} + 2 \cdot c_{\mathrm{D,i}} \tag{70}$$

A similar expression applies to the fixed concentration c_{syr} of the solution in the syringe.

$$c_{\mathrm{syr}} = {K_{\mathrm{diss}}}^{\frac{1}{2}}\, {c_{\mathrm{D,syr}}}^{\frac{1}{2}} + 2 \cdot c_{\mathrm{D,syr}} \tag{71}$$

Since c_{syr} is known, c_i can be determined with the injection volume V_i and the initial solvent volume in the cell V_0. Now $c_{D,syr}$ and $c_{D,i}$ can be determined from equations (70) and (71) if a value for K_{diss} is assigned.

The heat release q_i during the ith injection will be

$$q_{\mathrm{i}} = \Delta H_{\mathrm{diss}}\, c_{\mathrm{D,syr}}\; V_{\mathrm{i}} - \Delta H_{\mathrm{diss}} \left(c_{\mathrm{D,i}} - c_{\mathrm{D,i-1}}\right) \left(V_0 + \frac{V_{\mathrm{i}}}{2}\right) \tag{72}$$

The first term in equation (72) is the heat content of the aggregate contained in the injection volume. The second term is the heat content due to the difference in dimers present in the cell before and after the injection. The $(V_0 + V_i/2)$ factor is a correction for an effective volume, which takes into account the dilution of compound in the part of the cell which is sensed calorimetrically due to the increasing amount of solvent in the cell with each injection.

Equations (70) – (72) are solved simultaneously for the experimental values of q_i by iterative optimization of the parameters K_{diss} and ΔH^0_{diss}.

Computational Details

Geometry-optimization for the monomer (M) and dimer (D) of merocyanine **1** was performed at the density functional theory (DFT) level using the B97D3 functional[193] including dispersion correction and the def2-SVP basis[194] as implemented in the Gaussian 16 program package[195]. The polarizable continuum model (PCM)[196-198] was used with 1,4-dioxane as solvent. Dodecyl chains were replaced by methyl groups to reduce computational effort. Frequency calculations were performed to verify the optimized geometries as stationary minima. The electrostatic surface potential were calculated for the geometry-optimized structures of the monomer and dimer at the DFT level employing the same functional and basis set as for the geometry-optimization and visualized using GaussView 6[199]. For the monomer and the dimer the same color scale of –0.08 a.u. (red) to +0.08 a.u. (blue) was chosen.

Van't Hoff Plot

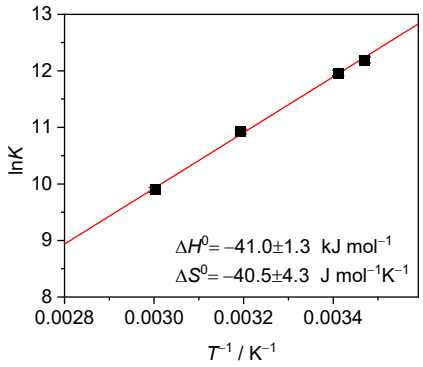

Figure A54. Van't Hoff plot (black squares) with linear fit (red line) according to equation (29) and fit results for ΔH^0 and ΔS^0.

Concentration-Dependent UV/Vis Absorption Spectra at Different Temperatures

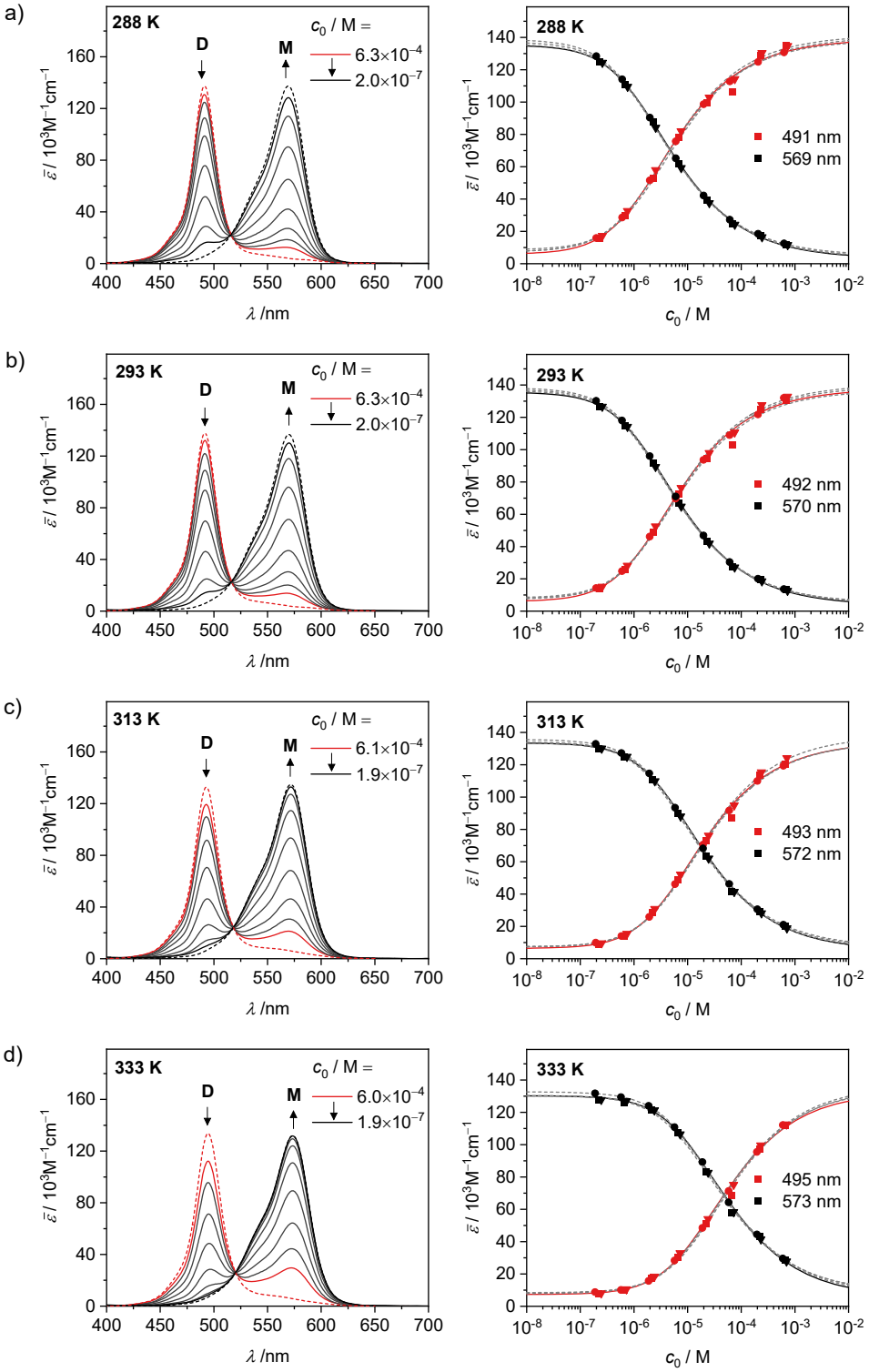

Figure A55. Concentration-dependent analysis at different temperatures: a) 288 K, b) 293 K, c) 313 K, d) 333 K. Left: Concentration-dependent UV/Vis absorption spectra of **1** in 1,4-dioxane (solid lines) and calculated (dashed lines) monomer (M, black) and dimer (D, red) spectra from global fit analysis. Right: Optical changes at the maximum of the dimer (red symbols) and monomer (black symbols) absorption band from three independent dilution series (■,▼,●) with respective fit curves from individual fits (dashed lines) and simultaneous fit of all datasets (solid lines) according to equation (18).

Temperature-Dependent UV/Vis Absorption Spectra at Different Concentrations

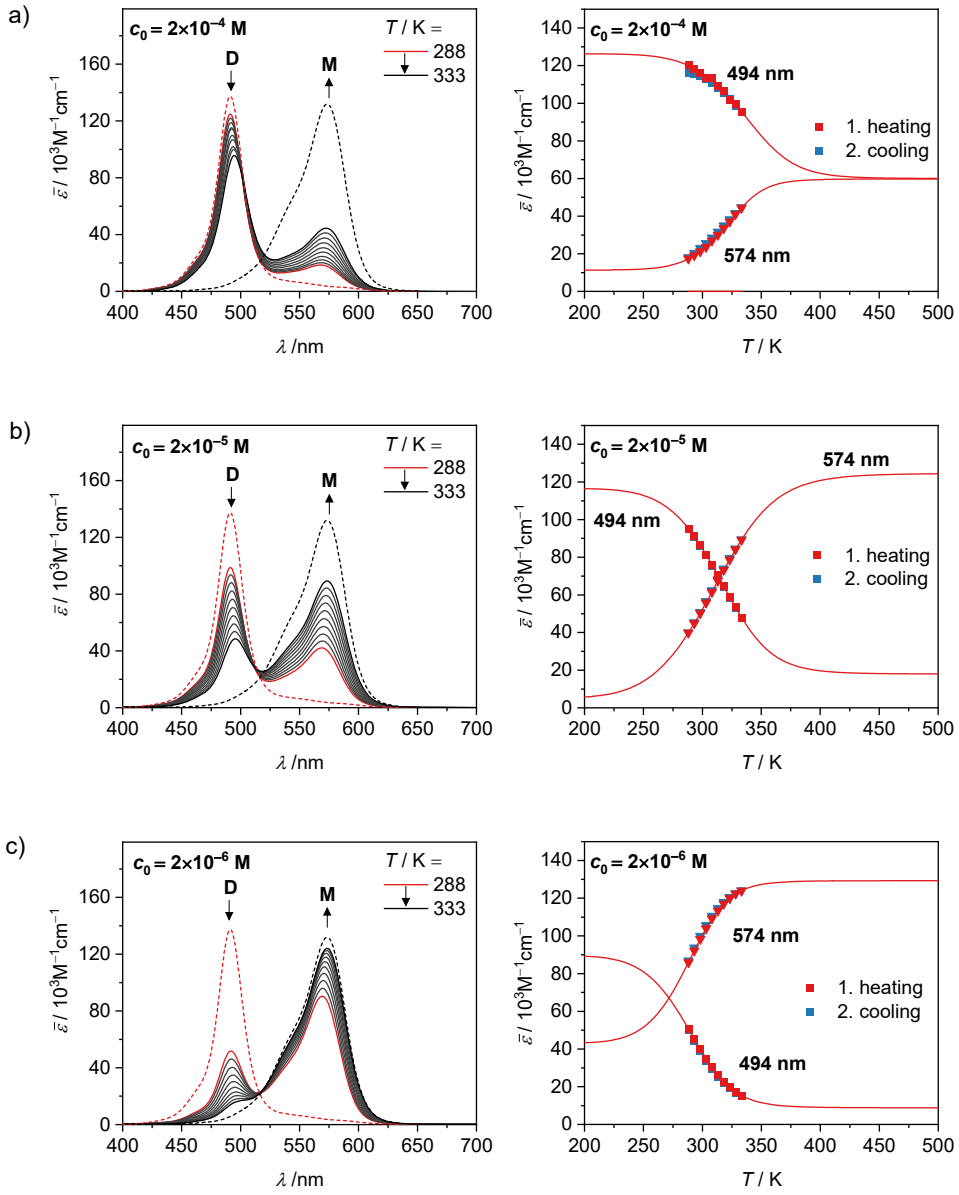

Figure A56. Temperature-dependent analysis at different concentrations: a) 2×10^{-4} M, b) 2×10^{-5} M, c) 2×10^{-6} M. Left: UV/Vis absorption spectra of samples of **1** in 1,4-dioxane (solid lines) as well as calculated dimer (D, red dashed line) and monomer (M, black dashed line) spectra from global fit analysis of concentration dependent data at 288 and 333 K, respectively. Right: Experimental data points of heating (red squares) and cooling (blue squares) experiments at two different wavelengths with fit for heating curve according to equation (34).

Solvent-Dependent UV/Vis Absorption Data

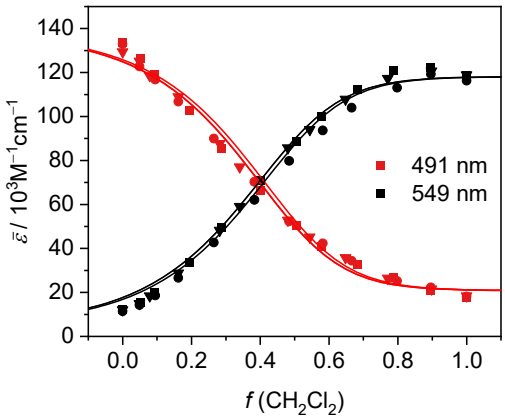

Figure A57. Solvent-dependent UV/Vis absorption data of three independent studies of **1** in mixtures of 1,4-dioxane/CH_2Cl_2 ($c_0 = 6.2\times10^{-4}$ M ■, 6.3×10^{-4} M ▼, $c_0 = 7.3\times10^{-4}$ M ●) at two wavelengths with fit curves from a simultaneous fit of all six datasets according to equation (36).

Summarized Fit Results from Isothermal Titration Calorimetry (ITC)

Table A7. Fit results with standard errors (±) of five ITC dilution experiments of different stock solutions of **1** in 1,4-dioxane with initial concentrations of c_0 = 2.2 to 2.4×10^{-4} M (293 K). In the last row the mean ± standard deviation (SD) of the values above is given.

	ΔH^0 /kJ mol^{-1}	ΔS^0 /J mol^{-1}K^{-1}	K_{293} /10^5 M^{-1}	ΔG^0_{293} /kJ mol^{-1}
I	–43.6±0.8	–49.4±0.6	1.58±0.13	–29.2±0.2
II	–42.3±2.1	–45.6±2.0	1.47±0.34	–29.0±0.6
III	–37.5±0.5	–31.1±0.5	1.14±0.07	–28.4±0.2
IV	–42.0±2.3	–41.6±1.9	2.07±0.47	–29.8±0.5
V	–54.6±4.4	–81.9±2.4	2.92±0.85	–30.7±0.7
Mean±SD	–44.0±6.4	–49.9±19	1.84±0.69	–29.4±0.9

Summarized Fit Results from Concentration-Dependent Data Evaluation at 293 K

Table A8. Fit results with standard fit errors (±) from three independent concentration-dependent UV/Vis absorption studies (I-III, $c_0 \sim 7\times10^{-4}$ to 2×10^{-7} M) of **1** in 1,4-dioxane at 293 K by analysis of individual datasets at important wavelengths or by a simultaneous fit of multiple datasets with shared parameter *K*. In the last row the mean ± standard deviation (SD) of the values above is given.

293 K	λ /nm	K /10^5 M^{-1}	ΔG^0 /kJ mol^{-1}	K /10^5 M^{-1}	ΔG^0 /kJ mol^{-1}	K /10^5 M^{-1}	ΔG^0 /kJ mol^{-1}
I	492	1.38±0.12	–28.8±0.2	1.55±0.09	–29.1±0.1	1.57±0.08	–29.1±0.1
	570	1.73±0.03	–29.4±0.05				
II	492	1.43±0.21	–28.9±0.3	1.58±0.12	–29.2±0.2		
	570	1.75±0.06	–29.4±0.09				
III	492	1.41±0.34	–28.9±0.6	1.58±0.19	–29.2±0.3		
	570	1.75±0.11	–29.4±0.1				
Mean ± SD		1.57±0.19	–29.1±0.03	1.57±0.02	–29.1±0.03		

The same samples were additionally measured at 288, 313 and 333 K. Evaluation of these datasets showed the same trends as shown here for the data at 293 K. For the fit of *K vs. T* and the van't Hoff Plot the binding constants from the simultaneous fit of all six datasets were used.

While it is no surprise that the temperature- and solvent-dependent studies give different results for an analysis at different wavelengths, due to the changing influence of thermochromism and solvatochromism, it can be noted, that also for the concentration-dependent analysis clearly different results are obtained from the analysis of different absorption bands. If any wavelength of the dimer absorption band is evaluated a $K \sim 1.4\times10^5$ M^{-1} is obtained while for the monomer band $K \sim 1.7\times10^5$ M^{-1}. This difference is small, but larger than the fit error.

Summarized Fit Results from Temperature-Dependent Data Evaluation

Table A9. Fit results with standard errors (±) from temperature-dependent UV/Vis absorption data of **1** in 1,4-dioxane from each three measurements (I, II and III) of samples with different concentrations c_0 by individual analysis at important wavelengths. In the last row the mean ± standard deviation (SD) of the values above is given.

c_0 /M		λ /nm	ΔH^0 /kJ mol^{-1}	ΔS^0 /J mol^{-1}K^{-1}	ΔG^0_{293} /kJ mol^{-1}	K_{293} /10^5 M^{-1}
2×10^{-4}	I	494	–77.8±10.7	–165.8±42.2	–29.3±16.3	1.66±11.1
		574	–47.3±10.1	–68.0±41.2	–27.3±15.7	0.74±4.80
	II	494	–78.0±23.1	–179.0±80.3	–25.6±33.0	0.36±4.89
		574	–58.8±17.3	–112.0±63.5	–26.0±25.4	0.43±4.48
	III	494	–40.2±22.1	–39.9±62.5	–28.5±37.3	1.22±18.7
		574	–36.2±5.9	–18.5±56.9	–30.8±22.5	3.11±28.7
2×10^{-5}	I	494	–54.9±2.0	–82.7±7.2	–30.6±2.9	2.90±3.47
		574	–53.1±1.1	–81.1±3.7	–29.3±1.5	1.67±1.05
	II	494	–57.6±1.0	–90.9±3.7	–31.0±1.5	3.32±2.04
		574	–52.9±1.0	–80.5±3.5	–29.3±1.5	1.69±1.01
	III	494	–55.7±1.7	–84.1±6.0	–31.1±2.4	3.54±3.51
		574	–53.2±1.1	–82.8±3.8	–29.0±1.6	1.46±0.95
2×10^{-6}	I	494	–58.2±1.8	–90.3±5.5	–31.8±2.4	4.59±4.53
		574	–64.5±1.5	–112.4±4.5	–31.6±2.0	4.25±3.43
	II	494	–56.1±1.3	–83.2±3.9	–31.7±1.7	4.45±3.13
		574	–69.5±0.8	–129.2±2.5	–31.7±1.1	4.47±2.06
	III	494	–58.7±1.1	–92.0±3.4	–31.8±1.5	4.61±2.78
		574	–64.6±0.7	–113.3±2.2	–31.4±1.0	4.02±1.64
Mean ± SD			–57.6±10.9	–94.8±38.2	–29.9±2.0	2.69±1.54

Table A10. Fit results with standard errors (±) of three repetitions (I, II, III) of temperature-dependent UV/Vis absorption data of **1** in 1,4-dioxane by simultaneous analysis of each three samples with different concentrations at important wavelengths. In the last row the mean ± standard deviation of the values above is given.

	c_0 /M	λ /nm	ΔH^0 /kJ mol^{-1}	ΔS^0 /J mol^{-1}K^{-1}	ΔG^0_{293} /kJ mol^{-1}	K_{293} /10^5 M^{-1}
I	2×10^{-4}, 2×10^{-5} 2×10^{-6} M	494 and 574 nm	−43.1±0.6	−47.7±2.1	−29.1±0.9	1.54±0.53
II	2×10^{-4}, 2×10^{-5} 2×10^{-6} M	494 and 574 nm	−43.6±0.7	−48.9±2.3	−29.3±1.0	1.67±0.66
III	2×10^{-4}, 2×10^{-5} 2×10^{-6} M	494 and 574 nm	−43.8±0.7	−49.3±2.2	−29.3±0.9	1.70±0.64
Mean ± SD			−43.5±0.4	−48.7±0.8	−29.2±0.1	1.63±0.08

Summarized Fit Results from Solvent-Dependent Data Evaluation

Table A11. Fit results with standard errors (±) for the dimerization of **1** in 1,4-dioxane at 293 K from three independent solvent-dependent UV/Vis absorption studies (I $c_0 = 6.2\times10^{-4}$ M, II $c_0 = 6.3\times10^{-4}$ M, III $c_0 = 7.3\times10^{-4}$ M) in mixtures of 1,4-dioxane/CH_2Cl_2 by analysis of individual datasets at important wavelengths or by a simultaneous fit of multiple datasets with shared parameters. In the last row the mean ± standard deviation of the values above is given.

293 K	λ /nm	ΔG^0 (m) /kJ mol^{-1}	K /10^4 M^{-1}	ΔG^0 (m) /kJ mol^{-1}	K /10^4 M^{-1}	ΔG^0 (m) /kJ mol^{-1}	K /10^4 M^{-1}
I	491	−20.1±0.4 (13.5±0.7)	0.38±0.07	−26.7±1.5 (24.7±3.0)	5.65±3.52	−26.6±0.8 (24.6±1.6)	5.57±1.83
	549	−27.5±1.5 (28.5±3.0)	8.10±4.91				
II	491	−21.6±0.6 (15.8±1.1)	0.72±0.18	−26.8±1.3 (25.0±2.6)	5.92±3.08		
	549	−27.5±1.4 (26.0±2.8)	7.94±4.47				
III	491	−19.8±0.6 (13.3±1.0)	0.34±0.09	−26.4±1.5 (24.2±3.2)	5.10±3.38		
	549	−27.2±1.6 (24.8±3.1)	7.13±4.63				
Mean ± SD		−24.0±3.8	4.10±3.98	−26.6 ±0.2	5.56±0.42		

Bounds were set for ε_D(549 nm) to be ≥ 5000 M^{-1}cm^{-1}.

7.3 Appendix for Chapter 4

Materials and Methods

Chemicals

Solvents and chemicals were obtained from commercial suppliers and used without further purification, unless otherwise stated. The solvents for UV/Vis absorption, circular dichroism (CD), fluorescence spectroscopy, circular polarized luminescence (CPL), vapor pressure osmometry (VPO) measurements as well as atomic force microscopy (AFM) were of spectroscopic grade and used as received. 1,2,3-Tris(dodecyloxy)benzene **16** was synthesised according to literature known procedure.[200] Chiral amine **13**[201] was a gracious donation by Prof. Dr. Klaus Ditrich from the BASF SE in Ludwigshafen, Germany, and had an enantiomeric excess of 99.3%.

Chromatography

Column chromatography was performed on silica gel (Merck Silica 60, particle size 0.04 – 0.063 mm).

Melting Points

Melting points were determined on a Linkam TP 94 heating stage and are uncorrected.

Elemental Analysis

Elemental analyses were conducted on a CHNS 932 analyser (Leco Instruments GmbH)

NMR-Spectroscopy

All spectra were recorded in deuterated solvents at a Bruker Avance III HD 400 or Bruker Avance III HD 600 spectrometer (Germany) using either a 5 mm BBFO probe or a 5 mm DCH cryo-probe, both equipped with z-gradient and a temperature control unit. Chemical shifts are reported in ppm relative to residual solvent signal. For multiplicities, abbreviations are used as follows: s = singlet, d = doublet, t = triplet, m = multiplet, br = broad.

The nuclear Overhauser effect spectrum (^{1}H ^{1}H NOESY) of the dimer of **2** was recorded using the noesygpphpp sequence with a mixing time (d8) of 600 ms. The rotating frame Overhauser effect spectrum (^{1}H ^{1}H ROESY) of the monomer of **2** was recorded using the roesyphpr.2 sequence with a mixing time (p15) of 300 ms.

Diffusion ordered spectroscopy (DOSY) experiments were recorded on a Bruker Avance III HD 600 with a BBFO probe with z gradient and a maximum gradient strength of 50 G cm^{-1}. The DOSY spectra were acquired using the dstebpgp3s (without rotation) or ledbpgp2s (with rotation) pulse sequence. For all experiments, the diffusion gradients were linearly incremented in 32 steps from 2 to 98%. The diffusion time (d20) was set to 50 ms. In case of the dimer of **2** the dstebpgp3s spectrum was evaluated which includes convention compensation. For the higher aggregate no difference was observed between the sequences so the ledbpgp2s spectrum was used for evaluation. Diffusion coefficients were determined by monoexponential fit of the attenuation curves for several peak integrals and averaging of the values. To calculate the hydrodynamic radius according to the Stokes-Einstein equation the value for the dynamic viscosity of undeuterated MCH at the respective temperature was used[202]. Data processing was performed with the TopSpin 3.5 pl 7 software.

Mass Spectrometry

High-resolution ESI-TOF mass spectrometry for the characterization of compounds **14** and **2** was performed on a microTOF focus instrument (Bruker Daltonics) in positive mode with methanol (MeOH) or acetonitrile (MeCN) as solvent.

UV/Vis Spectroscopy

UV/Vis absorption spectra were recorded on a JASCO V-670 or V-770 spectrometer with a spectral bandwidth of 2 nm and a scan rate of 200 nm/min. The temperature was controlled either by a Peltier element (JASCO) or with a NCP-706 thermostat. Quartz cells (Hellma Analytics) with the following path length were used: 0.01 mm ($c_0 = 1.0\times10^{-2}$ to 2.0×10^{-3} M), 0.1 mm ($c_0 = 1.0\times10^{-3}$ to 1.7×10^{-4} M), 2 mm ($c_0 = 1.0\times10^{-4}$ to 1.7×10^{-5} M), 10 mm ($c_0 = 1.2\times10^{-5}$ to 2.2×10^{-6} M), 50 mm ($c_0 = 1.2\times10^{-6}$ to 5.2×10^{-7} M), 100 mm ($c_0 = 4.0\times10^{-7}$ to 9.8×10^{-8} M). Samples in MCH were prepared in silanized vials and measured in silanized cuvettes (except for cuvettes with a path length of $d < 2$ mm). For concentration-dependent studies, stock solutions were subsequently diluted to adjust the desired concentration. Solutions in MCH were allowed to equilibrate at rt overnight after dilution and 5 to 30 min after a temperature change, before starting the measurement. Repeated measurements were performed to check whether equilibration was complete. Apparent extinction coefficients were calculated according to the Lambert-Beer law and are density corrected for the respective temperatures.

The electronic transition dipole moments (μ_{eg}) were calculated according to equation (73). I_A is the integrated absorption, N_A the Avogadro constant, ε_0 the vacuum permittivity, c_0 the speed of light in vacuum and h the Planck constant.

$$\left|\mu_{eg}^2\right| = \frac{3\,I_A}{S}, \tag{73}$$

With S defined as:

$$S = \frac{2\pi^2 N_A}{\varepsilon_0 c_0 h \ln 10} = 2.9356 \times 10^{60}\ \frac{1}{\text{mol C}^2}. \tag{74}$$

CD Spectroscopy

CD was measured on a JASCO J-810 spectropolarimeter with a spectral bandwidth of 1 nm and a scan rate of 200 nm/min, using the same solvents and quartz cells as for the UV/Vis measurements.

Fluorescence Spectroscopy

Fluorescence spectroscopy was carried out with an FLS-980-D2D2-ST spectrometer (Edinburgh Instruments Ltd., UK). Spectra were corrected against the photomultiplier sensitivity and the lamp intensity. Conventional fluorescence quartz cells (Hellma Analytics) with 10 mm path length were used for standard measurements of solutions. To measure concentrated solutions ($c_0 > 1.0\times10^{-4}$ M) a cylindrical cuvette (Hellma Analytics) with a path length of 0.1 mm was used in front-face setup (22.5°). All sample were measured with excitation polarizer 0° and emission polarizer 54.7° (magic angle). The spectral bandwidth was increased until sufficient signal to noise ratio was obtained (5 – 12 nm). To determine relative fluorescence quantum yields the average value at four different excitation wavelengths was used. For the dimer of merocyanine **2** in MCH (λ_{ex} = 485, 490, 495 and 500 nm) *N,N′*-Bis(2,6-diisopropylphenyl)perylene-3,4:9,10-bis(dicarboximide) in $CHCl_3$ was used as a reference (Φ_{Fl} = 100%)[203]. For the monomer of **2** in CH_2Cl_2 (λ_{ex} = 515, 520, 525 and 530 nm) *N,N′*-Bis(2,6-diisopropylphenyl)-1,6,7,12-tetraphenoxyperylene-3,4:9,10-bis(dicarboximide) in $CHCl_3$ was used as a reference (Φ_{Fl} = 96%)[203]. All fluorescence lifetimes were determined with an EPL picosecond pulsed diode laser (λ_{ex} = 505.8 nm) for time-correlated single photon counting (TCSPC) with an Edinburgh Instruments FLS980-D2D2-ST spectrometer under magic angle conditions (54.7°). To obtain emission and excitation spectra of merocyanine **2** in the solid state, the solid sample was manually applied

on a quartz surface and measured in front-face setup with the FLS-980-D2D2-ST spectrometer (Edinburgh Instruments Ltd., UK). Absolute quantum yields of the solid material were determined on a Hamamatsu Absolute PL Quantum Yield Measurement System *CC9920-02*.

CPL Spectroscopy

CPL spectra were recorded with a customised JASCO CPL-300/J-1500 hybrid spectrometer. The dimer sample was measured in a conventional fluorescence quartz cell (Hellma Analytics) with 10 mm path length. The excitation and emission bandwidth were set to 36 nm and 11 nm, respectively. The HAT photomultiplier current was 995 V and the spectrum was recorded with a scan speed of 50 nm/min and a D.I.T. of 2 sec. 30 accumulations were measured.

For the higher aggregate sample in MCH a cylindrical cuvette (Hellma Analytics) with a path length of 1 mm was used. The excitation and emission bandwidth were set to 36 nm and 10 nm, respectively. The HAT photomultiplier current was 950 V and the spectrum was recorded with a scan speed of 50 nm/min and a D.I.T. of 2 sec. 3 accumulations were measured.

Atomic Force Microscopy

AFM measurements were performed under ambient conditions using a Bruker Multimode 8 SPM system operating in tapping mode in air. Silica cantilevers (OMCL-AC200TS, Olympus) with a resonance frequency of ~150 kHz and a spring constant of ~10 N m^{-1} were used. The solution of the sample in MCH was spin-coated onto *n*-tetradecylphosphonic acid(TPA)-modified Si/SiO_2 (100 nm)/AlO_x (8 nm) substrates.

VPO Measurement

The vapor pressure osmometry measurements were performed on a KNAUER osmometer with a universal temperature measurement unit. For the measurements in MCH the measurement chamber was heated to 318 K and the chamber lid with the syringes to 320 K. Benzil (M = 210.23 g/mol) was purchased from Merck KGaA, Darmstadt Germany. The polystyrene standard PS5270 was purchased from PSS – Polymer Standards Service, Mainz, Germany. The number average molar mass is given as M_n = 5270 g/mol. Samples in MCH were prepared by diluting the most concentrated solution and allowed to equilibrate overnight.

The measurement value (*MV*) of a sample was determined as the average of three to five measurements.

Computational Details

Geometry-optimization for monomer (M) and dimer (D) of merocyanine **2** was performed at the density functional theory (DFT) level using the B97D3 functional[193] including dispersion correction and the def2-SVP basis set[194] as implemented in the Gaussian 16 program package[195]. The polarizable continuum model (PCM)[196-198] was used with MCH as solvent. Dodecyl chains were replaced by methyl groups to reduce computational effort. Frequency calculations were performed to verify the optimized geometries as stationary minima. The rotational barrier around the C–N bond of the tetralin substituent of the monomer in the gas phase was calculated by performing a relaxed potential energy surface scan for a 180° rotation around this bond in 5° steps and calculating the energy difference between the highest and lowest energy structure. For this the B97D3 functional[193] and the def2-SVP basis set[194] was used.

Due to the large size of the proposed decamer stack (H), the geometry was optimized using the semi-empirical PM7 Hamiltonian[204] within the MOPAC software package[205], which also accounts for dispersion interaction. Dodecyl chains were replaced by methyl groups to reduce computational effort. Frequency calculations were performed to verify the optimized geometry as a stationary minimum. TD-DFT calculations were performed on the geometry-optimized decamer stack (the benzene substituents were replaced by methyl groups after structure optimization to reduce computational effort for TD-DFT calculations) using the ωB97[206] functional and the def2SVP basis set[194] as implemented in the Gaussian 16 program package[195]. The polarizable continuum model (PCM)[196-198] was used with MCH as solvent. The oscillator strength for the first 15 states were calculated and the CD spectrum was simulated with the help of GaussView 5[207]. The half with at half hight was set to 0.18 eV and the spectrum was shifted 0.64 eV to lower energies to fit the experimental maximum.

Synthesis and Characterization

Hydroxypyridone 14

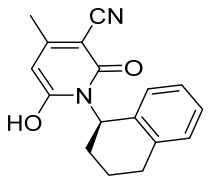

Ethyl cyanoacetate (1.15 g, 10.2 mmol) and chiral amine **13** (1.47 g, 10.0 mmol) were refluxed in MeOH (10 mL) for 48 h. The solvent was evaporated under reduced pressure. Ethyl acetoacetate (1.27 mL, ρ = 1.06 g/mL, 10.0 mmol) and piperidine (1 mL, ρ = 0.86 g/mL, 10.1 mmol) were added, and the mixture was stirred at 100 °C for 24 h. The solvent was removed under reduced pressure and the residue dissolved in MeOH. The pH value was adjusted to 1 with 32% aqueous HCl. After precipitation at room temperature, the product was filtered off, washed with distilled water and diethylether and dried *in vacuo*. Recrystallization from an ethyl acetate ethanol mixture gave the pure pyridone **14**.

Yield: 580 mg (2.07 mmol, 21%).

Mp: 250–252 °C.

^{1}H NMR (400 MHz, DMSO-d_6, 295 K): δ = 7.08 (m, 3H), 6.65 (d, J = 6.7 Hz, 1H), 6.36 (br, 1H), 5.96 (br, 1H), 5.48 (br, 1H), 2.76 (m, 2H), 2.33 (m, 1H), 2.21 (s, 3H), 2.00 (m, 2H), 1.76 (m, 1H) ppm.

^{13}C NMR (101 MHz, DMSO-d_6, 295 K): δ = 161.5, 160.7, 158.5, 137.0, 136.2, 128.8, 126.1, 126.0, 124.2, 117.8, 93.5, 88.0, 51.0, 29.0, 26.6, 22.6, 20.5 ppm.

HRMS (ESI, pos. mode, MeOH): m/z calcd. for $C_{17}H_{16}N_2O_2Na$ ($[M+Na]^+$) 303.11040, found 303.11039.

Anal. calcd. for $C_{17}H_{16}N_2O_2$ (280.33): C, 72.84; H, 5.75; N, 9.99. Found: C, 72.70; H, 5.77; N, 10.02.

Merocyanine 2

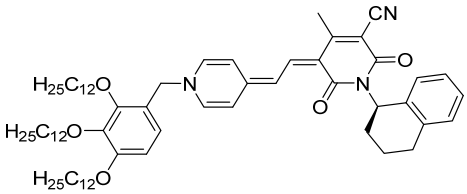

Pyridone **14** (196 mg, 699 µmol) and *N,N'*-diphenylformamidine (137 mg, 698 µmol) were stirred in Ac_2O (1.20 mL) at room temperature for 15 min. The mixture was then heated to 90 °C for additional 30 min to complete the reaction. After the reaction mixture cooled to room temperature, pyridinium salt **16** (520 mg, 636 µmol) and KOAc (98.1 mg, 1.00 mmol) were added, and the mixture was heated at 100 °C for 14 h. The solution was concentrated *in vacuo* and the crude product purified by column chromatography on silica using dichloromethane/methanol (98.5:1.5) as eluent. After evaporation of the solvent, the compound was again dissolved in pure dichloromethane, filtrated, concentrated and dried in high vacuum (2×10^{-3} mbar) at 40 °C for 3 h.

Yield: 124 mg (121 µmol, 19%).

Mp: 70 °C.

^{1}H NMR (400 MHz, CD_2Cl_2, 295 K): δ = 7.78 (br, 2H), 7.74–7.50 (br, 2H), 7.32 (br, 2H), 7.08-6.95 (m, 4H), 6.83 (d, J = 7.6 Hz, 1H), 6.66 (d, J = 8.6 Hz, 1H), 6.27 (br, 1H), 5.12 (s, 2H), 4.03 (t, J = 7.0 Hz, 2H), 3.96 (t, J = 6.4 Hz, 2H), 3.92 (t, J = 6.6 Hz, 2H), 2.97 (m, 1H), 2.75 (d, J = 15.9 Hz, 1H), 2.54 (m, 1H), 2.42 (s, 3H), 2.06 (m, 1H), 1.93 (m, 1H), 1.87 – 1.77 (m, 3H), 1.75-1.60 (m, 4H), 1.53–1.21 (m, 54H), 0.88 (t, J = 6.9 Hz, 9H) ppm.

^{13}C NMR (151 MHz, CD_2Cl_2, 295 K): δ = 164.3, 163.3, 157.5, 156.6, 156.1, 151.9, 142.0, 140.6, 140.0, 138.8, 137.6, 129.0, 126.0, 125.5, 125.4, 125.0, 120.2, 119.7, 118.3, 112.9, 108.3, 107.6, 74.3, 74.0, 69.3, 58.8, 50.6, 32.3, 30.9, 30.7, 30.2, 30.1 (three peaks), 30.0, 29.9, 29.8, 29.7, 27.0, 26.5 (two peaks), 26.4, 23.7, 23.1, 18.9, 14.3 ppm.

HRMS (ESI, pos. Mode, MeCN): *m/z* calcd for $C_{67}H_{100}N_3O_5$ ($[M+H]^+$) 1026.7657, found 1026.7646.

Anal. calcd. for $C_{67}H_{99}N_3O_5$ (1026.52): C, 78.39; H, 9.72; N, 4.09. Found: C, 78.20; H, 9.91; N, 4.38.

UV/Vis (CH_2Cl_2, 298 K, $c_0 = 6\times10^{-6}$ M): λ_{max} (ε) = 549 nm (116000 $M^{-1}cm^{-1}$).

Silanization Procedure of Glassware

For the silanization of one commercial 1×1 cm cuvette a mixture of freshly distilled trimethylsilylchloride (4.60 mL, 50.0 mmol) and NaI (7.50 g, 50.0 mmol) in dry acetonitrile (200 mL) was placed in a 250 mL round bottom flask under nitrogen atmosphere. The cuvette was immersed and the mixture heated to 90 °C overnight. After cooling, the cuvette was washed with distilled water, acetone and CH_2Cl_2. The amount of silanization reagents was adapted for other glassware by taking into account the approximate outer and inner surface of the respective cuvettes or glass vials as well as the inner surface of the reaction flask.

Solvatochromism

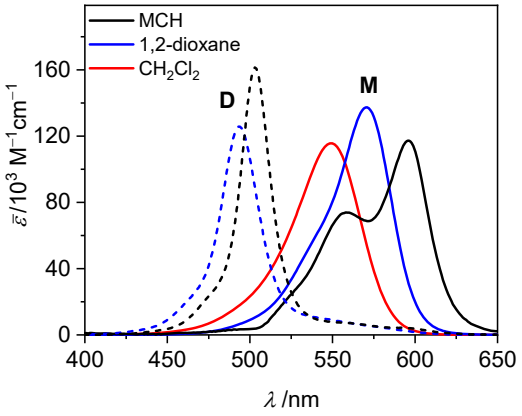

Figure A58. UV/Vis absorption spectra of merocyanine **2** as monomer (M, solid lines) and dimer (D, dashed lines) in dichloromethane (CH_2Cl_2, red, $c_0 = 1.3\times10^{-3}$ M), 1,4-dioxane (blue, global fit analysis) and MCH (MCH, black, global fit analysis) at 298 K.

UV/Vis Absorption of Higher Aggregate at Elevated Temperatures

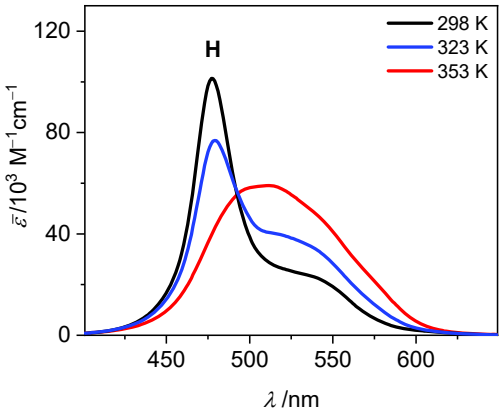

Figure A59. Calculated UV/Vis absorption spectra of the higher aggregate of merocyanine **2** from global fit analysis of the concentration-dependent spectra in MCH at 298 K (black), 323 K (blue) and 353 K (red) according to the pentamer model.

Time-Dependent UV/Vis Measurements

The higher aggregate shows kinetic stability in MCH upon dilution from $c_0 = 1.1\times10^{-3}$ M to $c_0 = 1.1\times10^{-5}$ M at 298 K. Time-dependent UV/Vis measurements show the slow transition from the higher aggregates to the dimers (Figure A60).

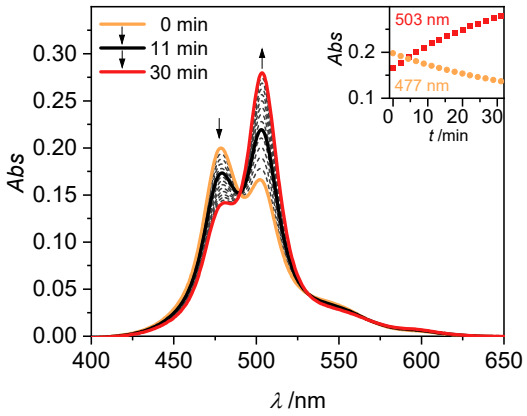

Figure A60. Time-dependent UV/Vis absorption spectra of a sample of merocyanine **2** in MCH 0 – 30 min after dilution form 1.1×10^{-3} M to 1.1×10^{-5} M at 298 K. Arrows indicate the spectral changes over time.

After rapid cooling from 353 to 298 K, two processes can be observed in the UV/Vis spectra of a concentrated solution of merocyanine **2** in MCH ($c_0 = 8.9\times10^{-4}$ M): 1) The dimer species that is formed at 353 K reassembles and 2) the absorption band of higher aggregate slowly returns from a more broad shape to its original room temperature shape of an H-aggregate with a maximum at $\lambda = 477$ nm and a shoulder at $\lambda \sim 540$ nm (Figure A61).

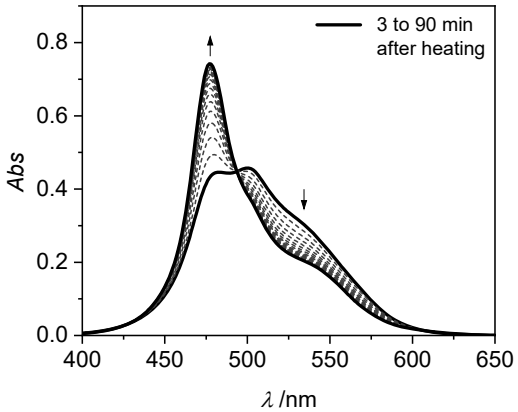

Figure A61. Time-dependent UV/Vis absorption spectra of a sample of merocyanine **2** in MCH ($c_0 = 8.9\times10^{-4}$ M) heated up to 353 K for 10 min and then measured at 298 K after rapid cooling. Arrows indicate the spectral changes over time.

Global Fit Analysis

A global fit algorithm as introduced in previous literature examples[24, 26, 97] was used to evaluate the concentration-dependent UV/Vis studies according to different aggregation models. The dimer, trimer, tetramer, pentamer and isodesmic model[16, 24] were applied.

The dimer fit[16] (2 M ⇌ D) was applied to selected data from the dilution series at 353 K in MCH, showing the transition from dimer (D) to monomer (M) (Figure A62a). The experimental apparent extinction data ($\bar{\varepsilon}$) of samples with a total molecular concentration c_0 from several dilution series is compared to the simulated curve for the dimer model according to

$$\bar{\varepsilon} = (\varepsilon_M - \varepsilon_D)\frac{\sqrt{8K_D c_0 + 1} - 1}{4K_D c_0} + \varepsilon_D, \quad (75)$$

with the extinction of the pure monomer (ε_M) and dimer (ε_D) species, as well as the dimerization constant $K_D = 4.5\times10^6$ M^{-1} obtained from global fit analysis (Figure A62b,c).

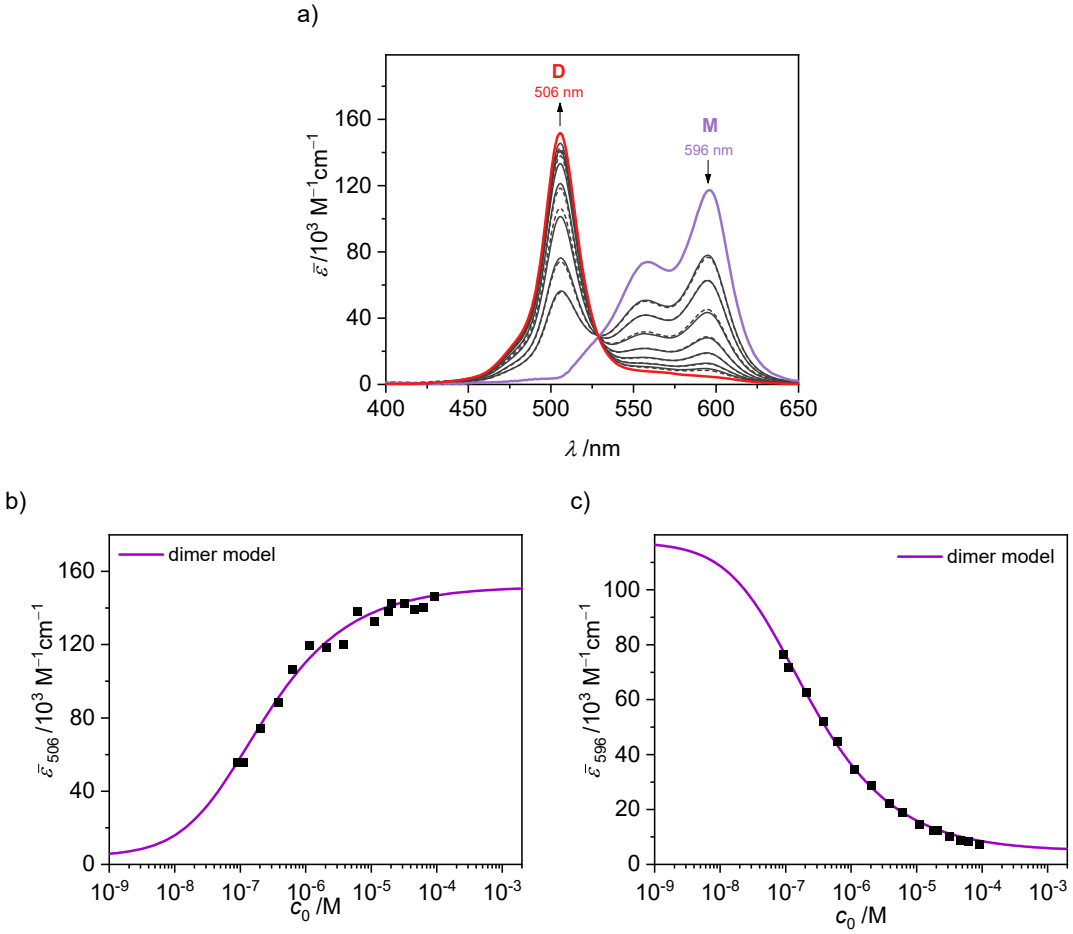

Figure A62. a) Concentration-dependent UV/Vis absorption spectra (dashed grey lines) of merocyanine **2** in MCH at 353 K in comparison with calculated spectra (solid grey lines) from global fit analysis according to the dimer model. Arrows indicate the spectral changes upon increasing the concentration from $c_0 = 9.1\times10^{-8}$ – 6.1×10^{-5} M. Colored spectra are calculated spectra for the individual monomer (M, violet) and dimer (D, red) species. b/c) Concentration-dependent

experimental extinction coefficients at 353 K at the maximum of the dimer (b, 506 nm) and monomer (c, 596 nm) absorption band in comparison with the simulated curve according to the dimer model (equation (75)).

The trimer, tetramer and pentamer fit[24] (n D ⇌ H, n = 3,4,5) were applied to selected data of the dilution series at 298 K (Figure A63), 323 K (Figure A64) and 353 K (Figure AS65) in MCH, showing the transition from the higher aggregate (H) to the dimer (D). The experimental apparent extinction data ($\bar{\varepsilon}$) of samples with a total molecular concentration c_0 from several dilution series is compared to the simulated curves for the individual models, with the extinction coefficients of the pure dimer (ε_D) and higher aggregate (ε_H) species, as well as the binding constant per binding site K_n obtained from global fit analysis. The formation of defined aggregates out of n dimers is described by expression (76). In combination with Lambert-Beer's law (77) K_n can be expressed as equation (78).

$$c_0 = 2\,c_D + 2n\,c_H, \tag{76}$$

$$c_0 \cdot \bar{\varepsilon} = 2\,c_D \cdot \varepsilon_D + 2n\,c_H \cdot \varepsilon_H, \tag{77}$$

$$K_n = \sqrt[n-1]{\frac{c_H}{{c_D}^n}} = \sqrt[n-1]{\frac{\left(c_0 - \frac{c_0(\bar{\varepsilon}-\varepsilon_H)}{(\varepsilon_D-\varepsilon_H)}\right)\cdot\frac{1}{2n}}{\left(\frac{c_0(\bar{\varepsilon}-\varepsilon_H)}{2(\varepsilon_D-\varepsilon_H)}\right)^n}}. \tag{78}$$

Additionally, the isodesmic fit[16] was applied to selected data of the dilution series at 298 K (Figure A63), 323 K (Figure A64) and 353 K (Figure AS65) in MCH, showing the transition from higher aggregate (H) to dimer (D) (n D ⇌ H). The experimental apparent extinction data ($\bar{\varepsilon}$) of samples with a total molecular concentration c_0 from several dilution series is compared to the simulated curve for the isodesmic model, with the extinction coefficients of the pure dimer (ε_D) and higher aggregate (ε_H) species, as well as the binding constant K_n obtained from global fit analysis. For the simulated curves according to the isodesmic aggregation of n dimers, the following equation applies:

$$\bar{\varepsilon} = (\varepsilon_D - \varepsilon_H)\frac{2K_n c_0 + 1 - \sqrt{4K_n c_0 + 1}}{2{K_n}^2 {c_0}^2} + \varepsilon_H. \tag{79}$$

The binding constants for the formation of the higher aggregate out of dimers (n D ⇌ H) at different temperatures, obtained from global fit analysis according to the different aggregation models, are summarized in Table A12.

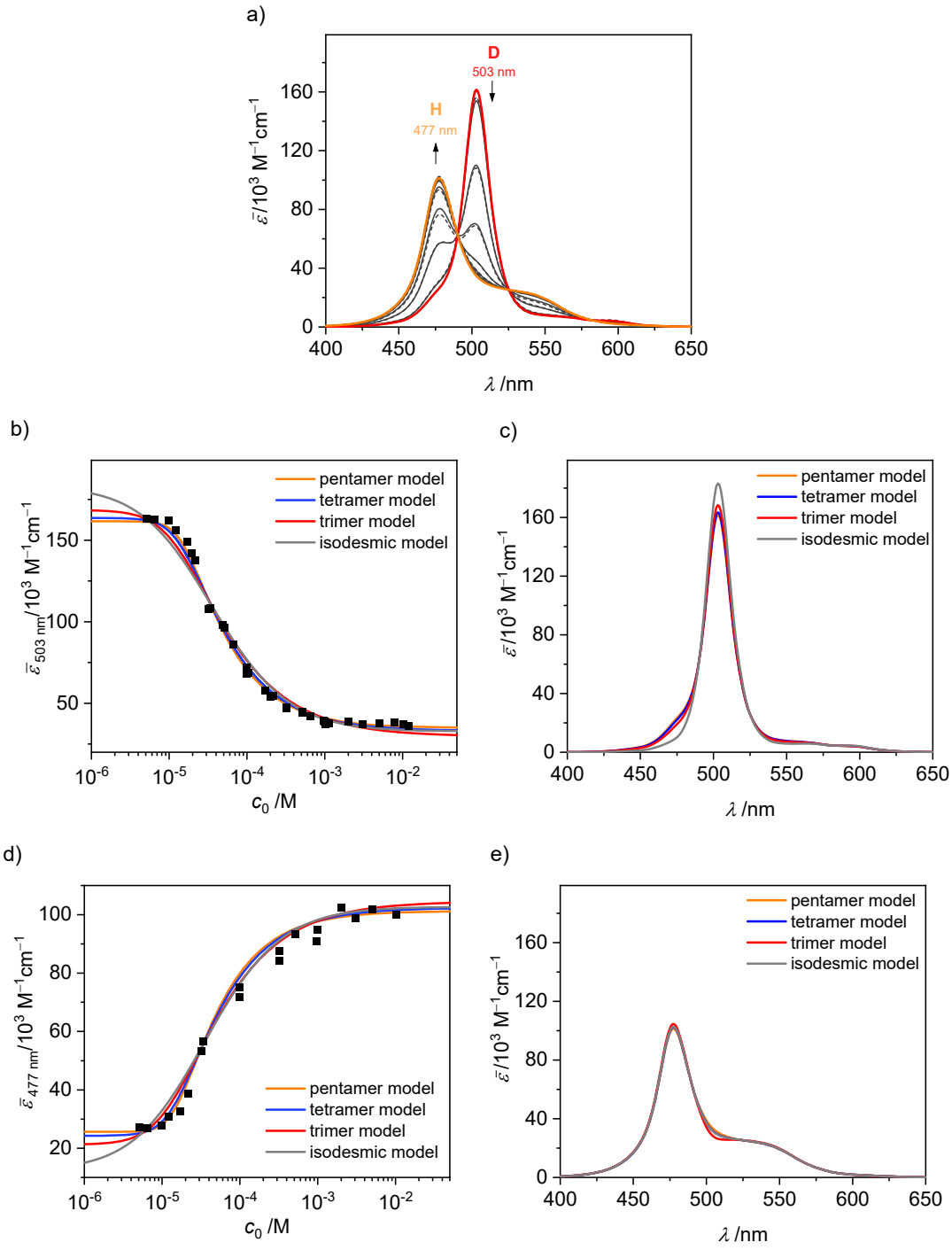

Figure A63. a) Concentration-dependent UV/Vis absorption spectra (dashed grey lines) of merocyanine **2** in MCH at 298 K in comparison with calculated spectra (solid grey lines) from global fit analysis according to the pentamer model. Arrows indicate the spectral changes upon increasing the concentration from $c_0 = 4.0\times10^{-6}$ – 5.1×10^{-3} M. Colored spectra are calculated spectra for the individual dimer (D, red) and higher aggregate (H, orange) species. b, d) Concentration-dependent experimental extinction coefficients of several independent dilution experiments at 298 K at the maximum of the dimer (b, 503 nm) or higher aggregate (d, 477 nm) absorption band in comparison with simulated curves according to different aggregation models (equation (78)and (79)). c, e) Comparison of calculated spectra of dimer (c) and higher aggregate (e) from global fit analysis according to different models.

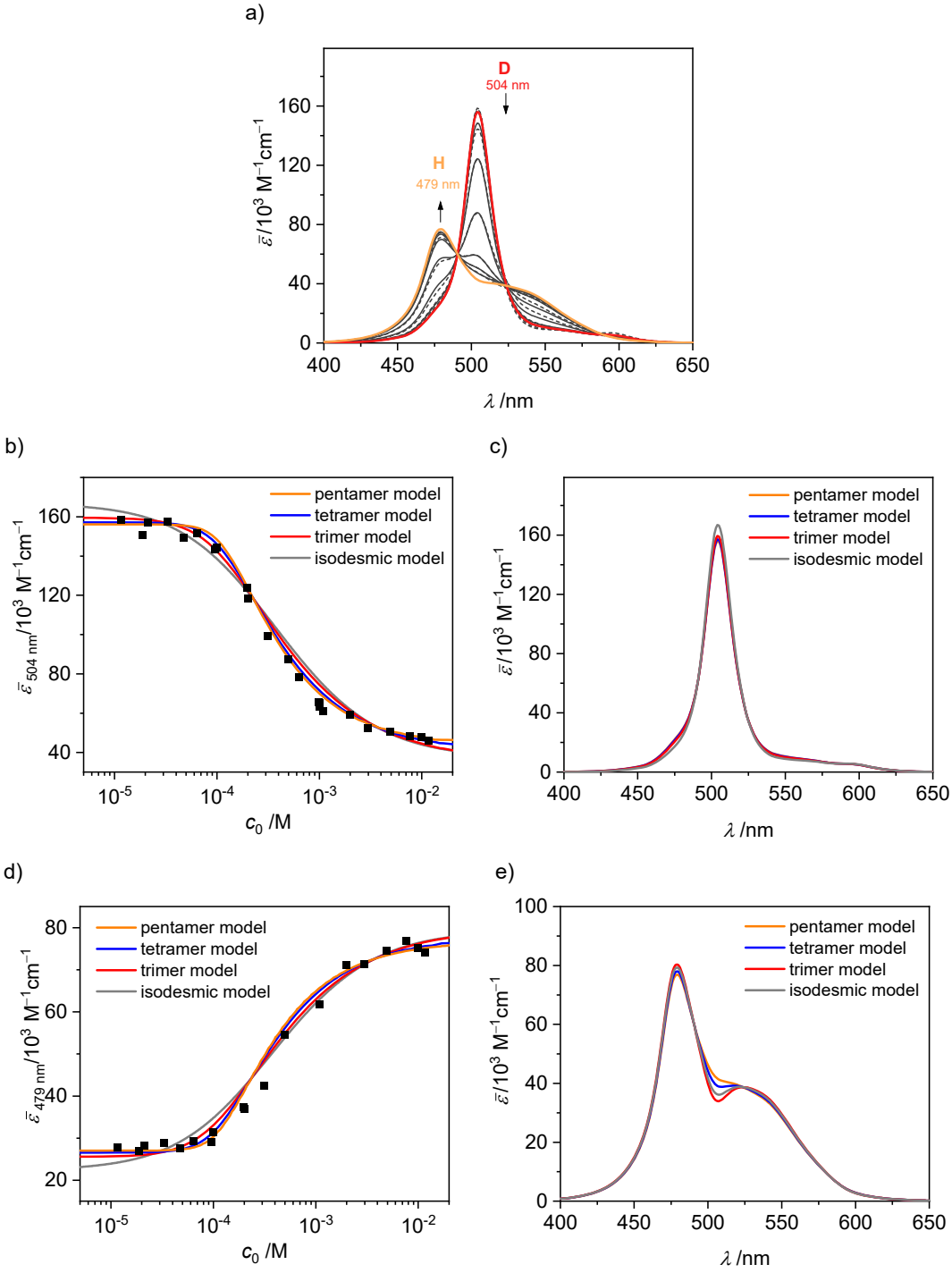

Figure A64. a) Concentration-dependent UV/Vis absorption spectra (dashed grey lines) of merocyanine **2** in MCH at 323 K in comparison with calculated spectra (solid grey lines) from global fit analysis according to the pentamer model. Arrows indicate the spectral changes upon increasing the concentration from $c_0 = 1.2\times10^{-5}$ – 1.0×10^{-2} M. Colored spectra are calculated spectra for the individual dimer (D, red) and higher aggregate (H, orange) species. b, d) Concentration-dependent experimental extinction coefficients of several independent dilution experiments at 323 K at the maximum of the dimer (b, 504 nm) or higher aggregate (d, 479 nm) absorption band in comparison with simulated curves according to different aggregation models (equation (78)and (79)). c, e) Comparison of calculated spectra of dimer (c) and higher aggregate (e) from global fit analysis according to different models.

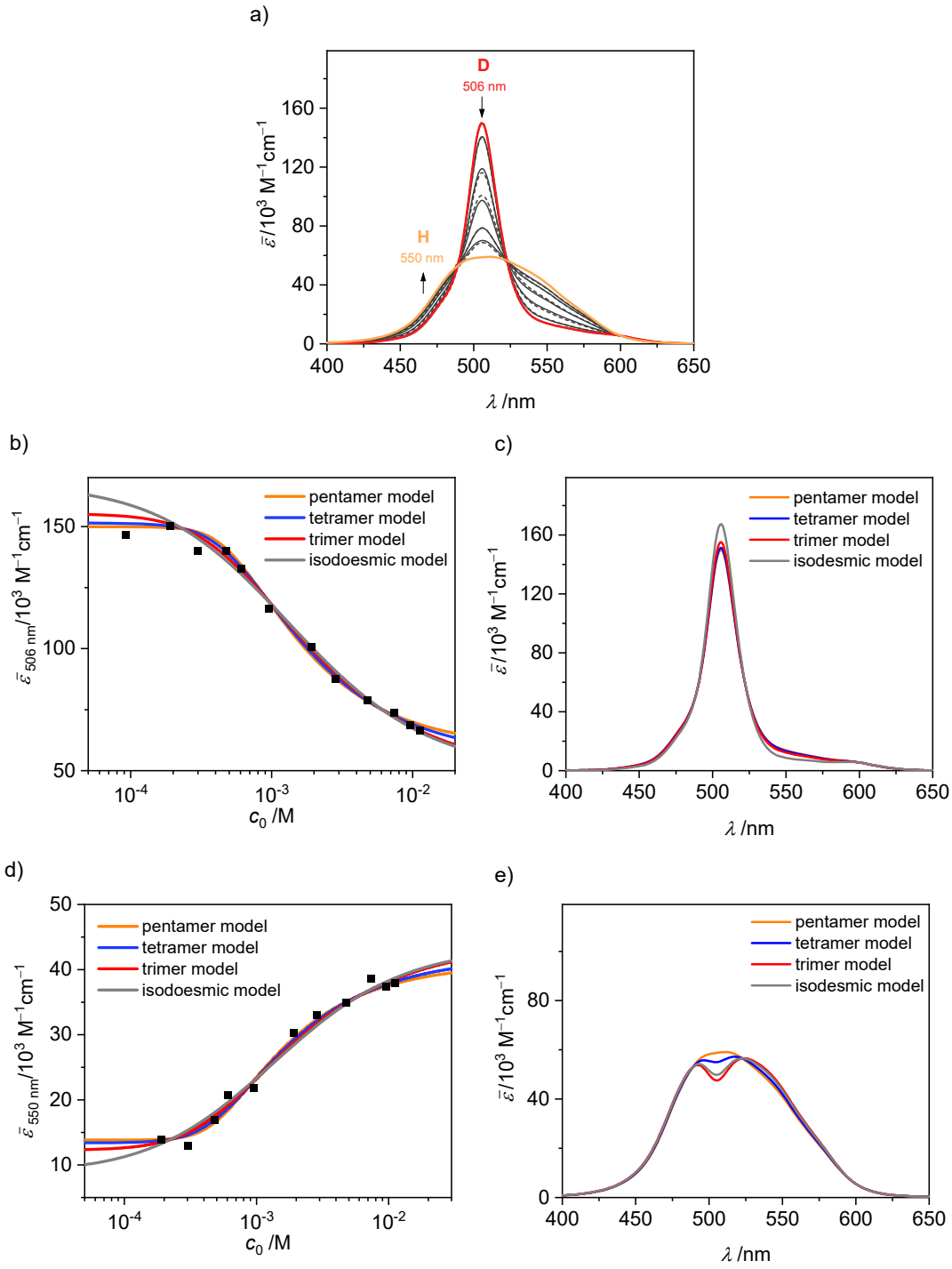

Figure AS65. a) Concentration-dependent UV/Vis absorption spectra (dashed grey lines) of merocyanine **2** in MCH at 353 K in comparison with calculated spectra (solid grey lines) from global fit analysis according to the pentamer model. Arrows indicate the spectral changes upon increasing the concentration from $c_0 = 1.9\times10^{-4}$ – 9.7×10^{-3} M. Colored spectra are calculated spectra for the individual dimer (D, red) and higher aggregate (H, orange) species. b, d) Concentration-dependent experimental extinction coefficients of several independent dilution experiments at 353 K at the maximum of the dimer (b, 506 nm) or higher aggregate (d, 550 nm) absorption band in comparison with simulates curves according to different aggregation models (equation (78)and (79)). c, e) Comparison of calculated spectra of dimer (c) and higher aggregate (e) from global fit analysis according to different models.

Table A12 Overview of the binding constants K_n for the formation of the higher aggregate (n D ⇌ H) obtained from global fit analysis of concentration-dependent UV/Vis data of **2** at different temperatures according to different aggregation models.

	K_n (298 K) /M^{-1}	K_n (323 K) /M^{-1}	K_n (353 K) /M^{-1}
Pentamer	6.0×10^4	7.5×10^3	1.8×10^3
Tetramer	5.5×10^4	6.6×10^3	1.6×10^3
Trimer	4.9×10^4	5.3×10^3	1.3×10^3
Isodesmic	3.2×10^4	3.0×10^3	0.8×10^3

Higher Aggregate in Cyclohexane

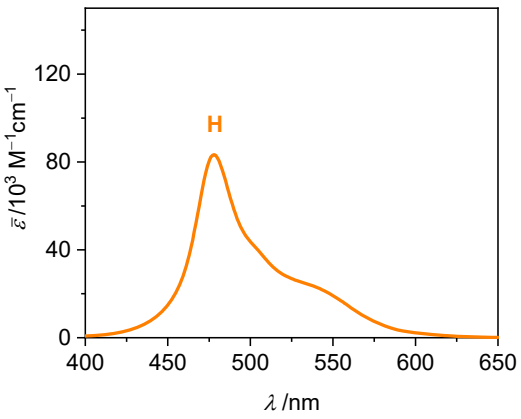

Figure A66. UV/Vis absorption spectrum of higher aggregate of **2** in cyclohexane (c_0 = 1×10^{-3} M, 298 K).

^{1}H and ^{13}C NMR

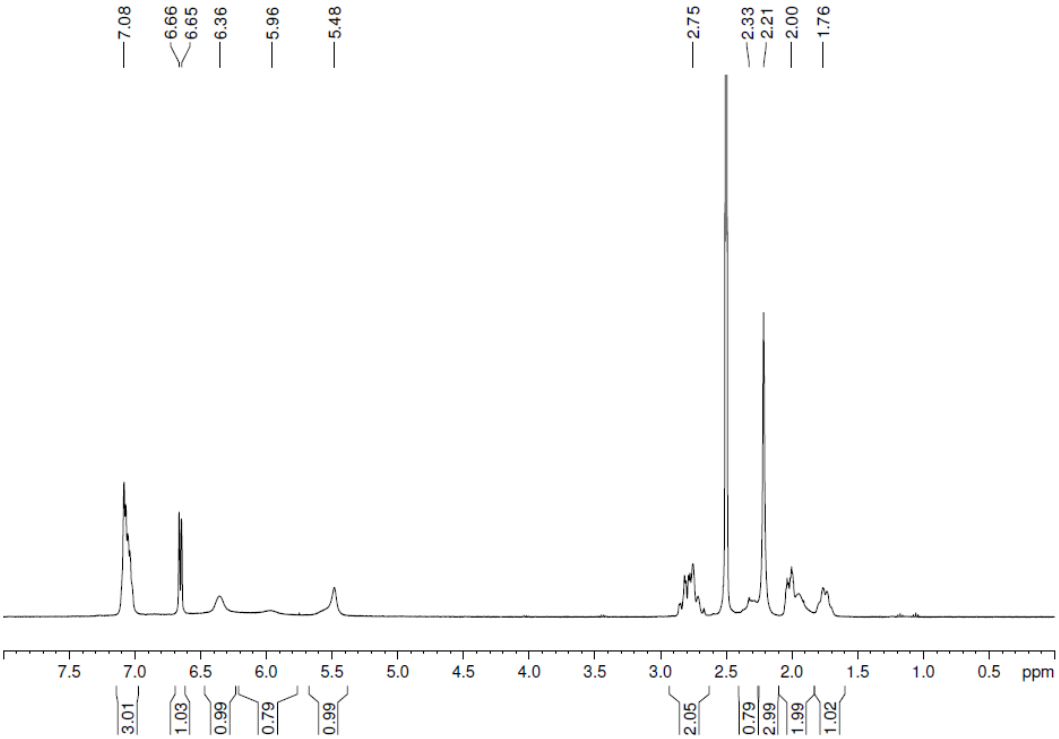

Figure A67. ^{1}H NMR (400 MHz) spectrum of compound **14** in DMSO-d_6 at 295 K.

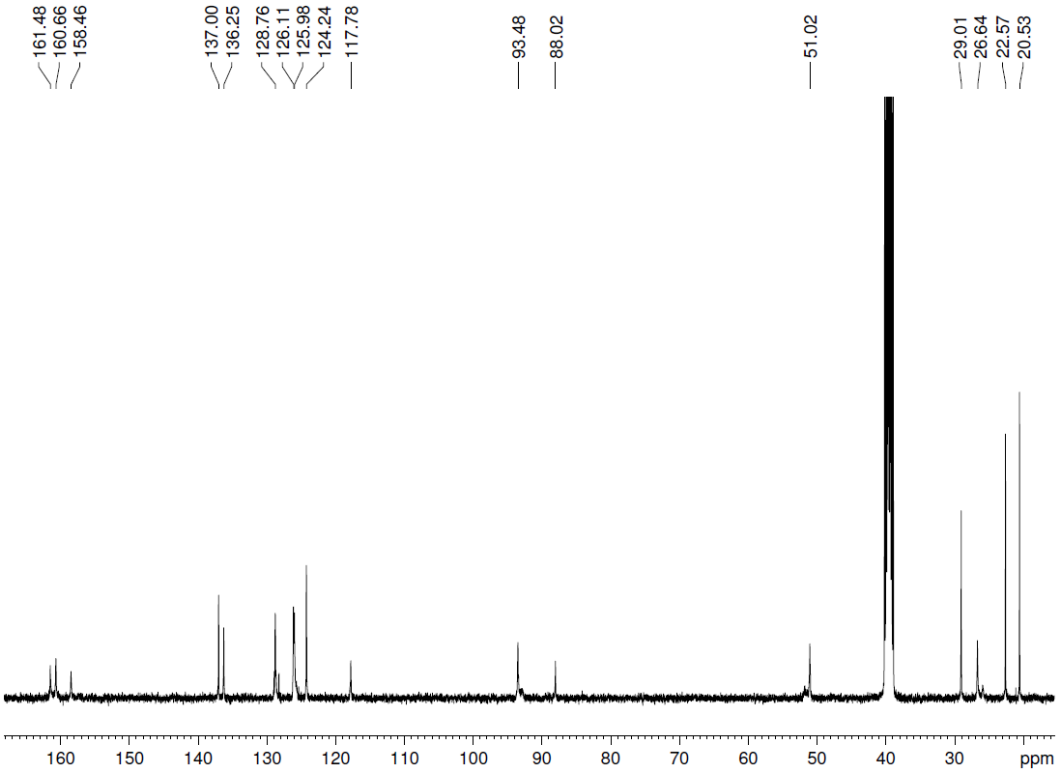

Figure A68. ^{13}C NMR (101 MHz) spectrum of compound **14** in DMSO-d_6 at 295 K.

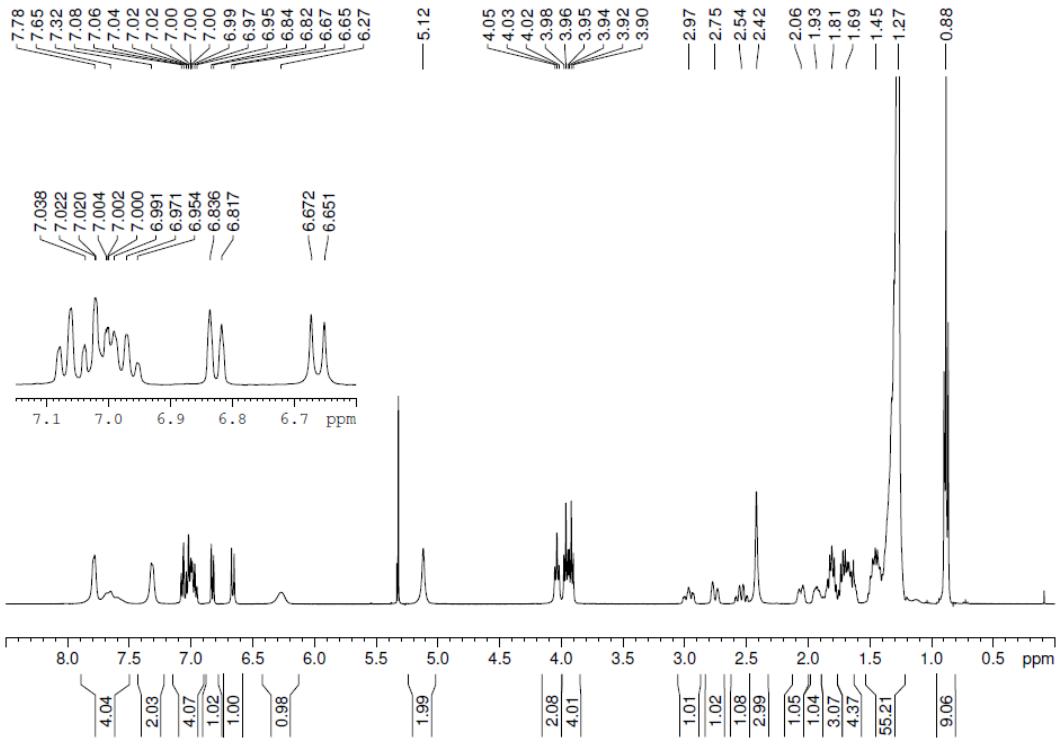

Figure A69. ^{1}H NMR (400 MHz) spectrum of merocyanine **2** in CD_2Cl_2 at 295 K.

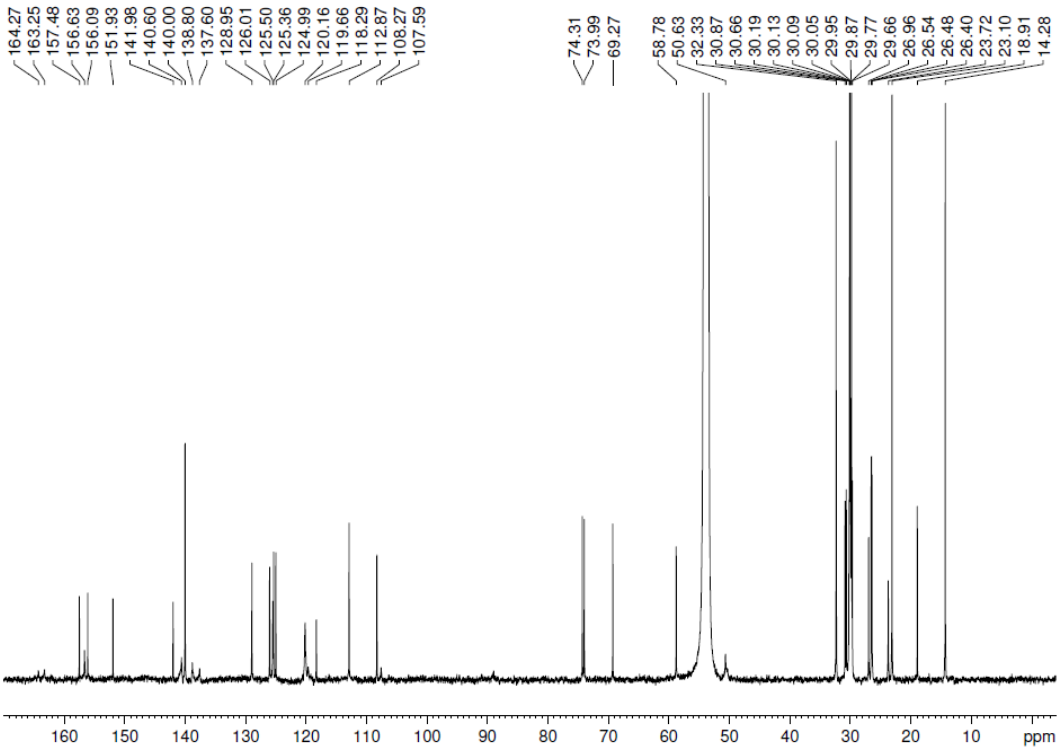

Figure A70. ^{13}C NMR (151 MHz) spectrum of merocyanine **2** in CD_2Cl_2 at 295 K.

Assignment of ^{1}H and ^{13}C NMR Signals

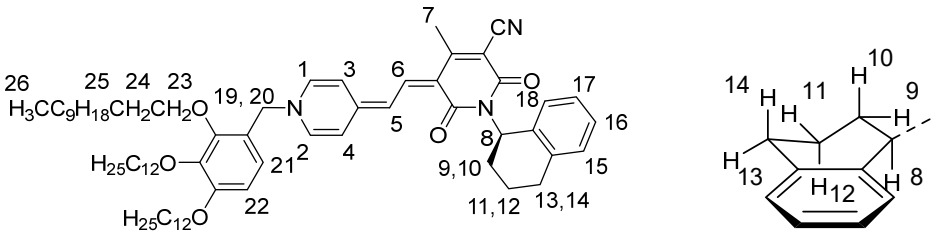

Table A13. Assignment of the ^{1}H and ^{13}C NMR signals of the monomer (M, CD_2Cl_2, 295 K) and dimer (D, MCH-d_{14}, 348 K) of merocyanine **2**.

	M in CD_2Cl_2 (298 K)		**D in MCH-d_{14} (348 K)**	
Position	δ_H /ppm (J/Hz)	δ_C /ppm	δ_H /ppm (J /Hz)	δ_C /ppm
1,2	7.78 (br, 2H)	140.00	7.30 (br, 2H)	140.8
3,4	7.32 (br, 2H)	120.16	6.87 (d, 6.4, 2H)	118.6
5	7.6 (br, 1H)	112.87	7.71 (d, 14.5, 1H)	113.2
6	7.7 (br, 1H)	140.60	7.38 (d, 14.5, 1H)	140.4
7	2.42 (s, 3H)	18.91	2.08 (s, 3H)	18.2
8	6.27 (br, 1H)	50.63	6.39 (t, 8.3, 1H)	49.9
9 10	1.93 (br, 1H) 2.54 (m, 1H)	26.96	1.91 (m, 1H) 2.60 (m, 1H)	27.6
11 12	2.06 (m, 1H) 1.81 (m, 1H)	23.72	2.05 (m, 1H) 1.79 (m, 1H)	24.6
13 14	2.75 (m, 1H) 2.97 (m, 1H)	30.18	2.67 (m, 1H) 3.11 (m, 1H)	30.8
15	7.07 (d, 7.4, 1H)	128.95	6.95 (m, 1H)	128.7
16	7.02 (t, 7.4, 1H)	125.50	6.89 (m, 1H)	125.7
17	6.97 (t, 7.4, 1H)	126.01	6.89 (m, 1H)	125.7
18	6.83 (d, 7.3, 1H)	124.99	6.93 (m, 1H)	126.2
19 20	5.12 (s, 2H)	58.78	5.16 (d, 14.0, 1H) 5.03 (d, 14.0, 1H)	58.9
21	6.95 (d, 8.5, 1H)	125.36	7.00 (d, 8.5, 1H)	126.88
22	6.66 (d, 8.5, 1H)	108.27	6.54 (d, 8.5,1H)	109.21
23	4.03 (t, 6.6, 2H) 3.96 (t, 6.4, 2H) 3.92 (t, 6.5, 2H)	74.31 69.27 73.99	4.00 – 3.89 (m, 6H)	74.2 69.6 73.9
24	1.81 (m, 2H) 1.70 (m, 4H)	29.66 30.66, 30.86	solvent overlap	
25	1.29 (m, 54)	23 – 32 (several peaks)	solvent overlap	
26	0.88 (t, 6.9, 9H)	14.28	solvent overlap	

Monomer – ^{1}H ^{1}H COSY and ROESY NMR

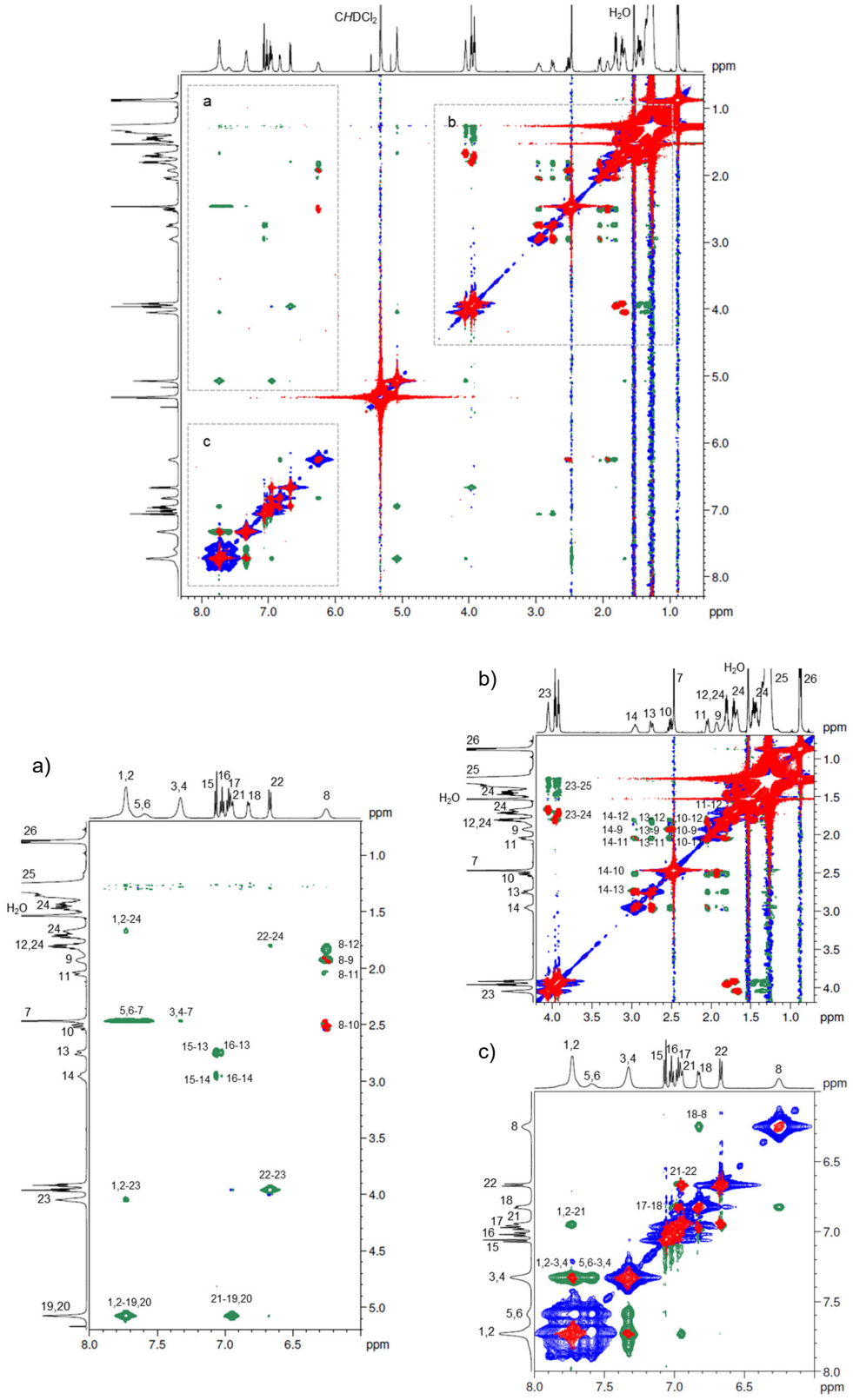

Figure A71. ^{1}H ^{1}H ROESY NMR (600 MHz) spectrum of the monomer of merocyanine **2** ($c_0 = 1.4\times10^{-3}$ M, blue = positive/green = negative) in CD_2Cl_2 at 295 K overlaid with the ^{1}H ^{1}H COSY NMR (400 MHz) spectrum of **2** ($c_0 = 9.7\times10^{-4}$ M, red) in CD_2Cl_2 at 295 K. The sections a-c) are enlarged and the cross signals assigned to the respective protons as denoted in Table A13.

Dimer – ^{1}H ^{1}H COSY and NOESY NMR

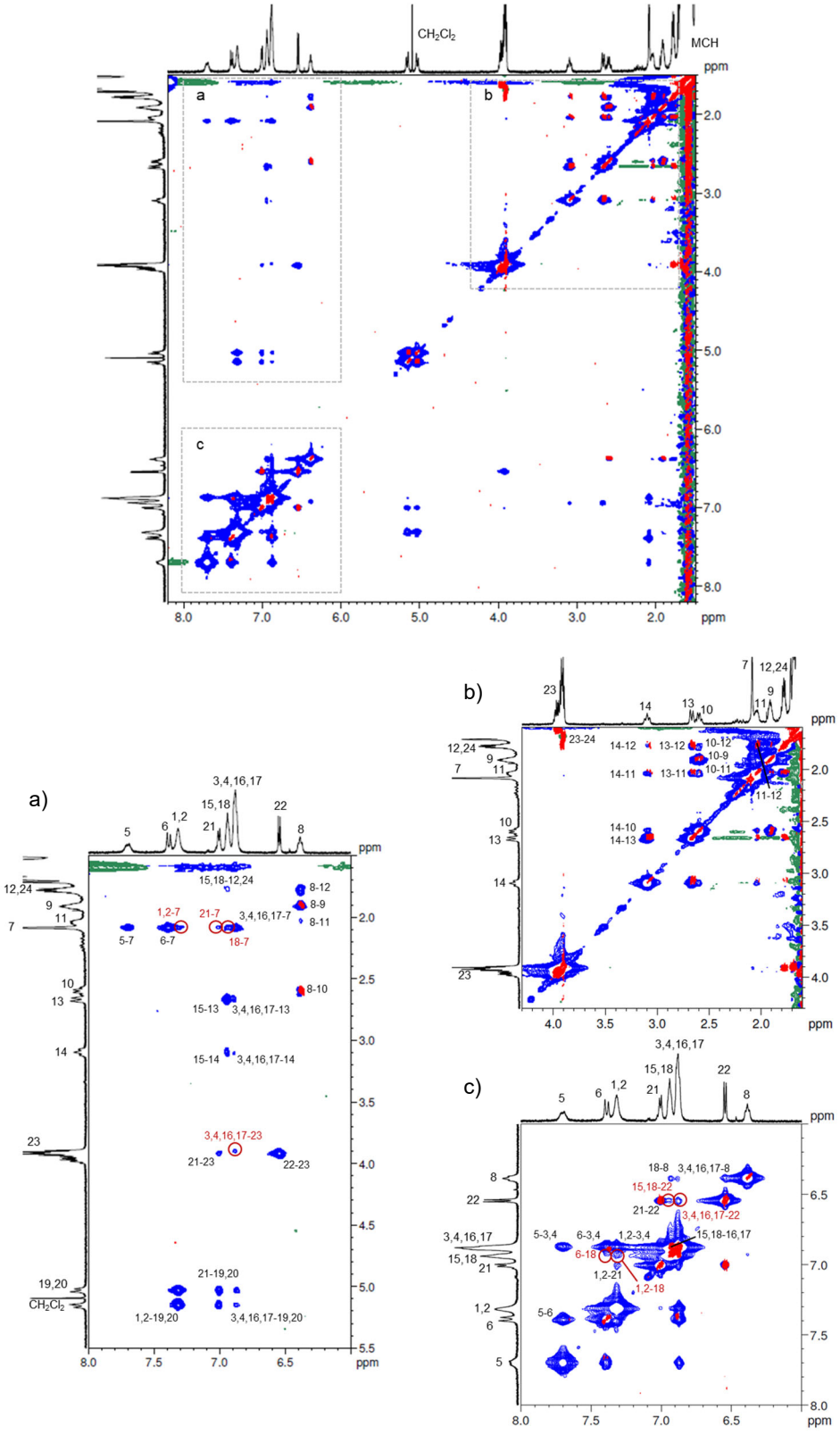

Figure A72. ^{1}H ^{1}H NOESY NMR (600 MHz) spectrum of the dimer of merocyanine **2** ($c_0 = 2.7\times10^{-4}$ M, blue = positive/green = negative) in MCH-d_{14} at 348 K overlaid with the ^{1}H ^{1}H COSY NMR (600 MHz) spectrum of the dimer of **1** ($c_0 = 5.1\times10^{-4}$ M, red) in MCH-d_{14} at 348 K. The sections a-c) are enlarged and the cross signals assigned to the respective protons as denoted in Table A13. Signals, that can not be explained by *intra*molecular proximities and therefore indicate *inter*molecular proximities between the two chromophores within the dimer are circled and labeled in red.

Monomer – ^{1}H ^{13}C HSQC NMR

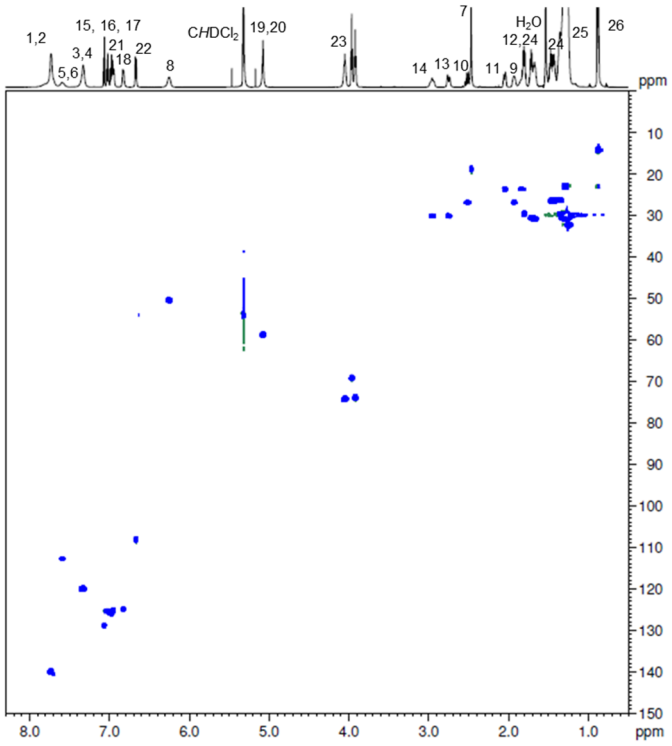

Figure A73. ^{1}H ^{13}C HSQC NMR (600 MHz) spectrum of merocyanine **2** (c_0 = 1.4×10^{-3} M) in CD_2Cl_2 at 295 K.

Dimer – ^{1}H ^{13}C HSQC NMR

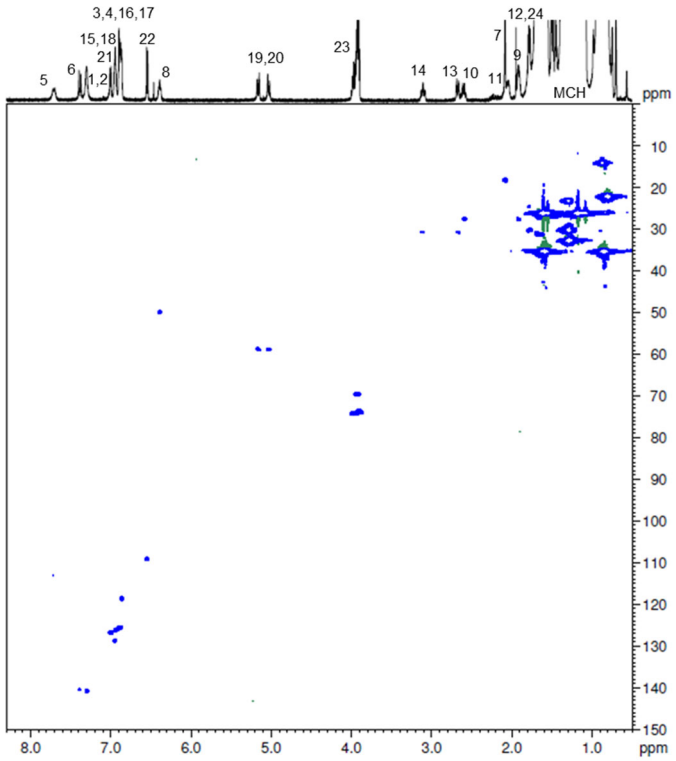

Figure A74. ^{1}H ^{13}C HSQC NMR (600 MHz) spectrum of the dimer of merocyanine **2** (c_0 = 2.3×10^{-4} M) in MCH-d_{14} at 348 K.

Higher Aggregate – ^{1}H ^{13}C HSQC NMR

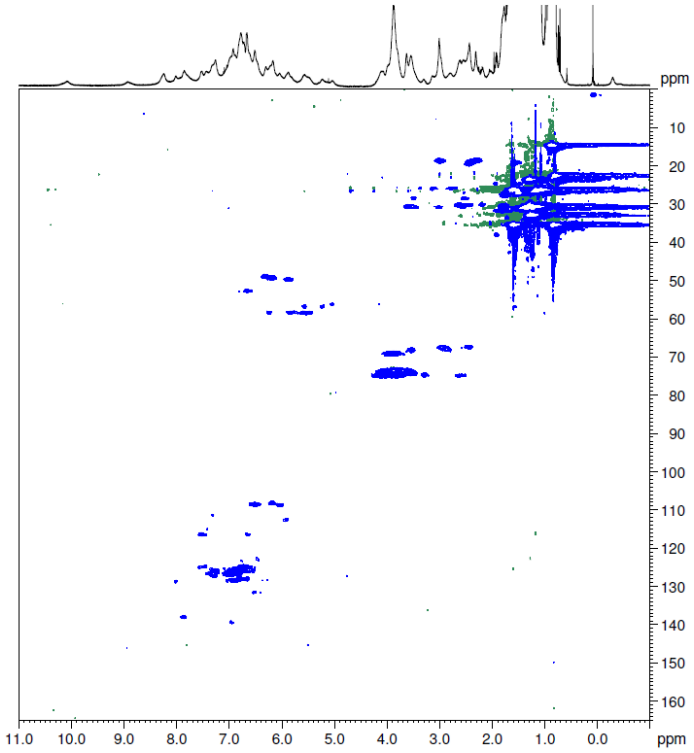

Figure A75. ^{1}H ^{13}C HSQC NMR (600 MHz) spectrum of the higher aggregate of merocyanine **2** ($c_0 = 2.1\times10^{-3}$ M) in MCH-d_{14} at 295 K.

Lifetime Measurements

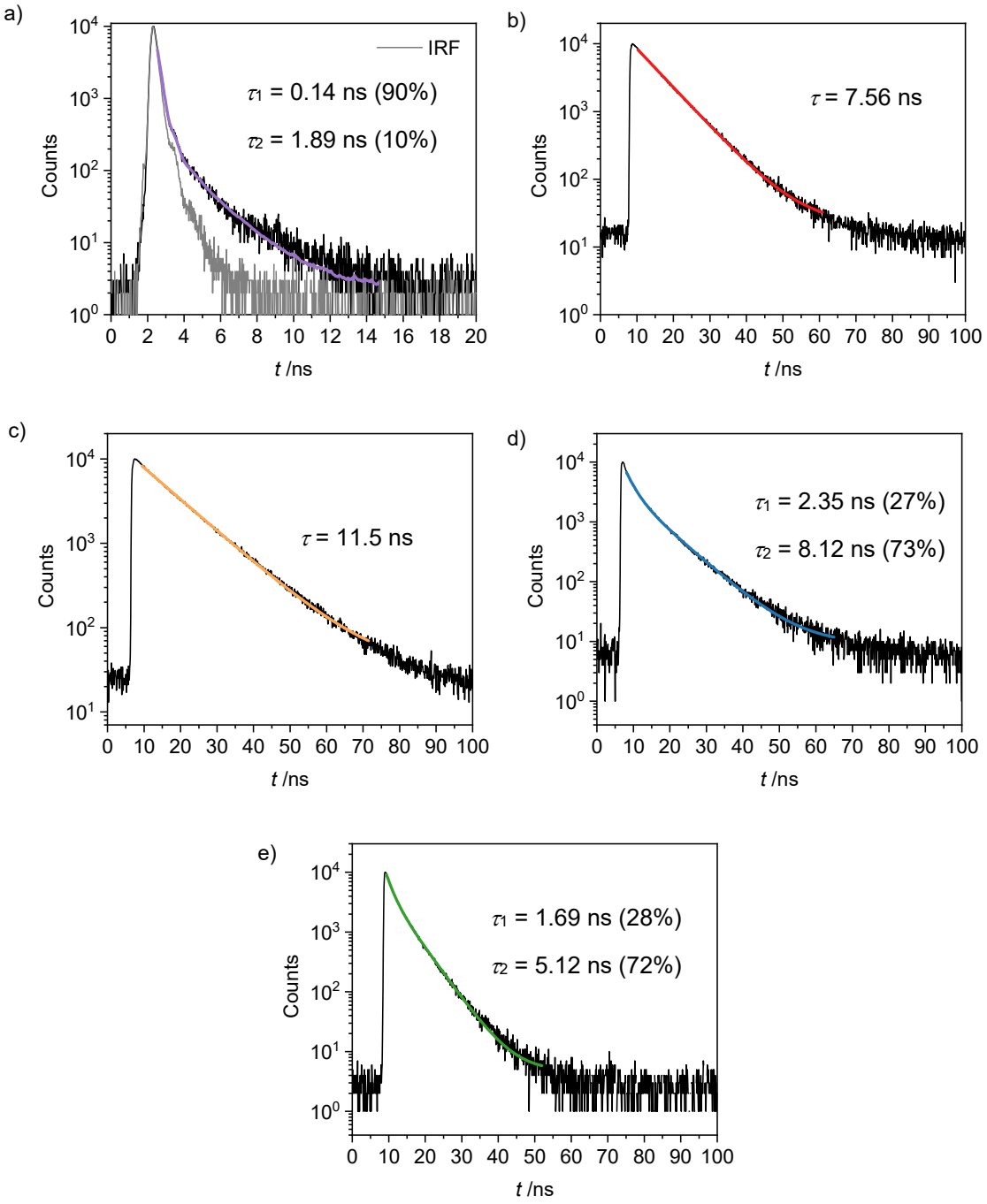

Figure A76. Fluorescence lifetime measurements (λ_{ex} = 505.8 nm, 295 K) of merocyanine **2** samples with their respective mono-/bi-exponential fits: a) Monomer in CH_2Cl_2 ($c_0 = 3.9\times10^{-7}$ M) with instrument response function (IRF, grey). b) Dimer in MCH ($c_0 = 4.8\times10^{-6}$ M). c) Higher aggregate in MCH ($c_0 = 1.0\times10^{-3}$ M). d) Freeze-dried solid from cyclohexane solution. e) Solid from CH_2Cl_2 solution.

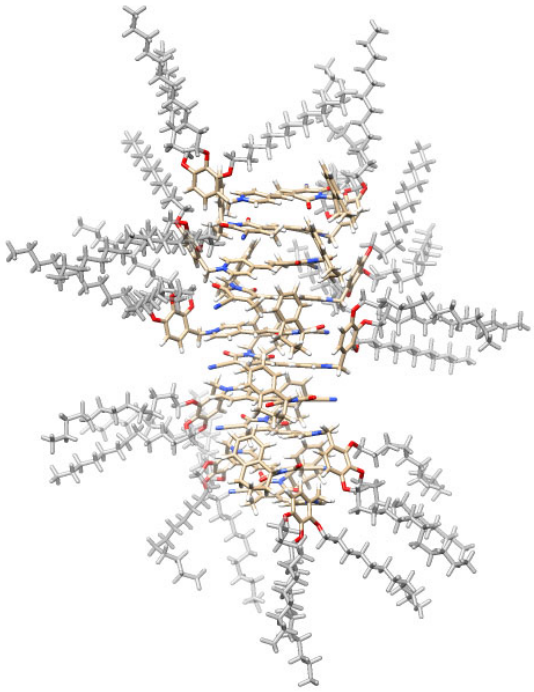

Figure A77. Geometry-optimized *P*-helical decamer stack of merocyanine **2** (PM7). The dodecyl chains of the trialkoxyphenyl substituents were replaced by methyl groups for the calculation to reduce computational effort and added manually (in grey) to the optimized structure to illustrate the sterical demand of the solubilizing substituents.

BIBLIOGRAPHY

[1] G. M. Whitesides, B. Grzybowski, *Science* **2002**, *295*, 2418-2421.
[2] R. F. Service, *Science* **2005**, *309*, 95-95.
[3] B. D. Harrison, T. M. A. Wilson, A. Klug, *Philos. Trans. R. Soc. Lond., B, Biol. Sci.* **1999**, *354*, 531-535.
[4] G. McDermott, S. M. Prince, A. A. Freer, A. M. Hawthornthwaite-Lawless, M. Z. Papiz, R. J. Cogdell, N. W. Isaacs, *Nature* **1995**, *374*, 517-521.
[5] J. W. Steed, J. L. Atwood, *Supramolecular chemistry*, John Wiley & Sons, **2022**.
[6] A. Rajak, A. Kumar Singh, L. Roy, A. Das, *ChemNanoMat* **2022**, *8*, e202200082.
[7] O. Ostroverkhova, *Chem. Rev.* **2016**, *116*, 13279-13412.
[8] A. Salehi, X. Fu, D.-H. Shin, F. So, *Adv. Funct. Mater.* **2019**, *29*, 1808803.
[9] T. M. Clarke, J. R. Durrant, *Chem. Rev.* **2010**, *110*, 6736-6767.
[10] J. H. Kim, T. Schembri, D. Bialas, M. Stolte, F. Würthner, *Adv. Mater.* **2022**, *34*, 2104678.
[11] T. Q. Trung, N.-E. Lee, *Adv. Mater.* **2017**, *29*, 1603167.
[12] D. Chen, Q. Pei, *Chem. Rev.* **2017**, *117*, 11239-11268.
[13] J. H. Kim, A. Liess, M. Stolte, A.-M. Krause, V. Stepanenko, C. Zhong, D. Bialas, F. Spano, F. Würthner, *Adv. Mater.* **2021**, *33*, 2100582.
[14] D. Bialas, E. Kirchner, M. I. S. Röhr, F. Würthner, *J. Am. Chem. Soc.* **2021**, *143*, 4500-4518.
[15] S. Kubik, *Supramolecular Chemistry*, De Gruyter, Berlin, Boston, **2020**.
[16] Z. Chen, A. Lohr, C. R. Saha-Möller, F. Würthner, *Chem. Soc. Rev.* **2009**, *38*, 564-584.
[17] R. B. Martin, *Chem. Rev.* **1996**, *96*, 3043-3064.
[18] T. F. A. De Greef, M. M. J. Smulders, M. Wolffs, A. P. H. J. Schenning, R. P. Sijbesma, E. W. Meijer, *Chem. Rev.* **2009**, *109*, 5687-5754.
[19] P. Thordarson, *Chem. Soc. Rev.* **2011**, *40*, 1305-1323.
[20] R. F. Goldstein, L. Stryer, *Biophys. J.* **1986**, *50*, 583-599.
[21] H. M. M. ten Eikelder, A. J. Markvoort, T. F. A. de Greef, P. A. J. Hilbers, *J. Phys. Chem. B* **2012**, *116*, 5291-5301.
[22] M. M. J. Smulders, M. M. L. Nieuwenhuizen, T. F. A. de Greef, P. van der Schoot, A. P. H. J. Schenning, E. W. Meijer, *Chem. Eur. J.* **2010**, *16*, 362-367.
[23] D. Zhao, J. S. Moore, *Org. Biomol. Chem.* **2003**, *1*, 3471-3491.
[24] E. Kirchner, D. Bialas, F. Fennel, M. Grüne, F. Würthner, *J. Am. Chem. Soc.* **2019**, *141*, 7428-7438.
[25] K. Cai, J. Xie, D. Zhang, W. Shi, Q. Yan, D. Zhao, *J. Am. Chem. Soc.* **2018**, *140*, 5764-5773.
[26] J. Gershberg, F. Fennel, T. H. Rehm, S. Lochbrunner, F. Würthner, *Chem. Sci.* **2016**, *7*, 1729-1737.
[27] T. Aida, E. W. Meijer, *Isr. J. Chem.* **2020**, *60*, 33-47.
[28] T. Aida, E. W. Meijer, S. I. Stupp, *Science* **2012**, *335*, 813-817.
[29] C. Rest, R. Kandanelli, G. Fernández, *Chem. Soc. Rev.* **2015**, *44*, 2543-2572.

[30] V. Vázquez-González, M. J. Mayoral, R. Chamorro, M. M. R. M. Hendrix, I. K. Voets, D. González-Rodríguez, *J. Am. Chem. Soc.* **2019**, *141*, 16432-16438.
[31] D. Zhao, J. S. Moore, *J. Org. Chem.* **2002**, *67*, 3548-3554.
[32] A. Arnaud, J. Belleney, F. Boué, L. Bouteiller, G. Carrot, V. Wintgens, *Angew. Chem. Int. Ed.* **2004**, *43*, 1718-1721.
[33] L. Herkert, J. Droste, K. K. Kartha, P. A. Korevaar, T. F. A. de Greef, M. R. Hansen, G. Fernández, *Angew. Chem. Int. Ed.* **2019**, *58*, 11344-11349.
[34] R. van der Weegen, P. A. Korevaar, P. Voudouris, I. K. Voets, T. F. A. de Greef, J. A. J. M. Vekemans, E. W. Meijer, *Chem. Comm.* **2013**, *49*, 5532-5534.
[35] I. Helmers, M. S. Hossain, N. Bäumer, P. Wesarg, B. Soberats, L. S. Shimizu, G. Fernández, *Angew. Chem. Int. Ed.* **2022**, *61*, e202200390.
[36] Y. Dorca, C. Naranjo, G. Ghosh, B. Soberats, J. Calbo, E. Ortí, G. Fernández, L. Sánchez, *Chem. Sci.* **2022**, *13*, 81-89.
[37] B. Matarranz, S. Díaz-Cabrera, G. Ghosh, I. Carreira-Barral, B. Soberats, M. García-Valverde, R. Quesada, G. Fernández, *Angew. Chem. Int. Ed.* **2023**, *62*, e202218555.
[38] H. Arima, T. Saito, T. Kajitani, S. Yagai, *Chem. Commun.* **2020**.
[39] A. Lohr, M. Grüne, F. Würthner, *Chem. Eur. J.* **2009**, *15*, 3691-3705.
[40] X. Hu, A. Schulz, J. O. Lindner, M. Grüne, D. Bialas, F. Würthner, *Chem. Sci.* **2021**, *12*, 8342-8352.
[41] A. Schulz, F. Würthner, *Angew. Chem. Int. Ed.* **2022**, *61*, e202114667.
[42] F. Würthner, *Acc. Chem. Res.* **2016**, *49*, 868-876.
[43] A. Zitzler-Kunkel, E. Kirchner, D. Bialas, C. Simon, F. Würthner, *Chem. Eur. J.* **2015**, *21*, 14851-14861.
[44] P. Jonkheijm, P. v. d. Schoot, A. P. H. J. Schenning, E. W. Meijer, *Science* **2006**, *313*, 80-83.
[45] M. M. J. Smulders, A. P. H. J. Schenning, E. W. Meijer, *J. Am. Chem. Soc.* **2008**, *130*, 606-611.
[46] B. Matarranz, G. Ghosh, R. Kandanelli, A. Sampedro, K. K. Kartha, G. Fernández, *Chem. Comm.* **2021**, *57*, 4890-4893.
[47] I. Debnath, T. Roy, J. Matern, S. A. H. Jansen, G. Fernández, K. Mahata, *Org. Chem. Front.* **2021**, *8*, 5432-5439.
[48] P. Besenius, G. Portale, P. H. H. Bomans, H. M. Janssen, A. R. A. Palmans, E. W. Meijer, *Proc. Natl. Acad. Sci. U.S.A.* **2010**, *107*, 17888-17893.
[49] K. Aratsu, N. Shimizu, H. Takagi, R. Haruki, S.-i. Adachi, S. Yagai, *Chem. Lett.* **2020**, *49*, 178-181.
[50] T. Weilandt, R. W. Troff, H. Saxell, K. Rissanen, C. A. Schalley, *Inorg. Chem.* **2008**, *47*, 7588-7598.
[51] P. A. Korevaar, C. Schaefer, T. F. A. de Greef, E. W. Meijer, *J. Am. Chem. Soc.* **2012**, *134*, 13482-13491.
[52] R. B. Prince, J. G. Saven, P. G. Wolynes, J. S. Moore, *J. Am. Chem. Soc.* **1999**, *121*, 3114-3121.
[53] C. Shao, M. Grüne, M. Stolte, F. Würthner, *Chem. Eur. J.* **2012**, *18*, 13665-13677.
[54] R. Appel, J. Fuchs, S. M. Tyrrell, P. A. Korevaar, M. C. A. Stuart, I. K. Voets, M. Schönhoff, P. Besenius, *Chem. Eur. J.* **2015**, *21*, 19257-19264.
[55] J. Buendía, L. Sánchez, *Org. Lett.* **2013**, *15*, 5746-5749.
[56] Y. Vonhausen, F. Würthner, *Chem. Eur. J.* **2023**, *29*, e202300359.
[57] G. Wu, F. Li, B. Tang, X. Zhang, *J. Am. Chem. Soc.* **2022**, *144*, 14962-14975.
[58] E. Kirchner, D. Bialas, M. Wehner, D. Schmidt, F. Würthner, *Chem. Eur. J.* **2019**, *25*, 11285-11293.
[59] R. M. Young, M. R. Wasielewski, *Acc. Chem. Res.* **2020**, *53*, 1957-1968.

[60] J. Rühe, D. Bialas, P. Spenst, A.-M. Krause, F. Würthner, *Organic Materials* **2020**, *02*, 149-158.
[61] S. J. Barrow, S. Kasera, M. J. Rowland, J. del Barrio, O. A. Scherman, *Chem. Rev.* **2015**, *115*, 12320-12406.
[62] https://commons.wikimedia.org/wiki/File:DNA_simple.svg?uselang=de, 15.02.2024.
[63] K. D. Shimizu, J. Rebek, *Proceedings of the National Academy of Sciences* **1995**, *92*, 12403-12407.
[64] M. M. Safont-Sempere, P. Osswald, K. Radacki, F. Würthner, *Chem. Eur. J.* **2010**, *16*, 7380-7384.
[65] J.-L. Mergny, L. Lacroix, *Oligonucleotides* **2003**, *13*, 515-537.
[66] F. Würthner, S. Yao, T. Debaerdemaeker, R. Wortmann, *J. Am. Chem. Soc.* **2002**, *124*, 9431-9447.
[67] S. Soldner, O. Anhalt, M. B. Sárosi, M. Stolte, F. Würthner, *Chem. Commun.* **2023**, *59*, 11656-11659.
[68] B. Engels, V. Engel, *Phys. Chem. Chem. Phys.* **2017**, *19*, 12604-12619.
[69] R. F. Fink, J. Seibt, V. Engel, M. Renz, M. Kaupp, S. Lochbrunner, H.-M. Zhao, J. Pfister, F. Würthner, B. Engels, *J. Am. Chem. Soc.* **2008**, *130*, 12858-12859.
[70] M. Son, K. H. Park, C. Shao, F. Würthner, D. Kim, *J. Phys. Chem. Lett.* **2014**, *5*, 3601-3607.
[71] Y. Hong, J. Kim, W. Kim, C. Kaufmann, H. Kim, F. Würthner, D. Kim, *J. Am. Chem. Soc.* **2020**, *142*, 7845-7857.
[72] H. Yu, J. Li, S. Li, Y. Liu, N. E. Jackson, J. S. Moore, C. M. Schroeder, *J. Am. Chem. Soc.* **2022**, *144*, 3162-3173.
[73] L. Su, J. Mosquera, M. F. J. Mabesoone, S. M. C. Schoenmakers, C. Muller, M. E. J. Vleugels, S. Dhiman, S. Wijker, A. R. A. Palmans, E. W. Meijer, *Science* **2022**, *377*, 213-218.
[74] D. Görl, F. Würthner, *Angew. Chem. Int. Ed.* **2016**, *55*, 12094-12098.
[75] P. P. N. Syamala, B. Soberats, D. Görl, S. Gekle, F. Würthner, *Chem. Sci.* **2019**, *10*, 9358-9366.
[76] F. Würthner, *J. Org. Chem.* **2022**, *87*, 1602-1615.
[77] A. M. Brown, *Comput. Methods Programs Biomed.* **2001**, *65*, 191-200.
[78] H. J. Motulsky, L. A. Ransnas, *FASEB J.* **1987**, *1*, 365-374.
[79] D. B. Hibbert, J. J. Gooding, *Data Analysis for Chemistry: An Introductory Guide for Students and Laboratory Scientists*, Oxford University Press, Cary, **2005**.
[80] H. J. Motulsky, A. Christopoulos, *Fitting models to biological data using linear and nonlinear regression. A practical guide to curve fitting*, GraphPad Software Inc., San Diego, CA, **2003**.
[81] H.-J. Schneider, A. K. Yatsimirsky, *Principles and methods in supramolecular chemistry*, J. Wiley, **2000**.
[82] G. Schwarz, S. Klose, W. Balthasar, *Eur. J. Biochem.* **1970**, *12*, 454-460.
[83] B. H. Robinson, A. Löffler, G. Schwarz, *J. Chem. Soc., Faraday Trans. 1* **1973**, *69*, 56-69.
[84] W. Spencer, J. R. Sutter, *J. Phys. Chem.* **1979**, *83*, 1573-1576.
[85] H. Naghibi, A. Tamura, J. M. Sturtevant, *Proc. Natl. Acad. Sci. U.S.A.* **1995**, *92*, 5597-5599.
[86] E. C. W. Clarke, D. N. Glew, *Trans. Faraday Soc.* **1966**, *62*, 539-547.
[87] J. Dietzsch, D. Bialas, J. Bandorf, F. Würthner, C. Höbartner, *Angew. Chem. Int. Ed.* **2022**, *61*, e202116783.
[88] P. Suppan, N. Ghoneim, *Solvatochromism*, Royal Society of Chemistry, Cambridge, **1997**.

[89] J. H. Day, *Chem. Rev.* **1963**, *63*, 65-80.
[90] A. Samat, V. Lokshin, in *Organic Photochromic and Thermochromic Compounds: Volume 2: Physicochemical Studies, Biological Applications, and Thermochromism* (Eds.: J. C. Crano, R. J. Guglielmetti), Springer US, Boston, MA, **2002**, pp. 415-466.
[91] C. Steinmetzger, C. Bäuerlein, C. Höbartner, *Angew. Chem. Int. Ed.* **2020**, *59*, 6760-6764.
[92] J. M. Scholtz, G. R. Grimsley, C. N. Pace, *Meth. Enzymol.* **2009**, *466*, 549-565.
[93] Y. Marcus, *Solvent mixtures: properties and selective solvation*, CRC Press, Boca Raton, **2002**.
[94] P. Suppan, *J. Photochem. Photobiol. A: Chem.* **1990**, *50*, 293-330.
[95] C. Reichardt, *Solvents and Solvent Effects in Organic Chemistry*, 3rd ed., WILEY-VCH Verlag, Weinheim, **2003**.
[96] F. Würthner, G. Archetti, R. Schmidt, H.-G. Kuball, *Angew. Chem. Int. Ed.* **2008**, *47*, 4529-4532.
[97] F. Fennel, S. Wolter, Z. Xie, P.-A. Plötz, O. Kühn, F. Würthner, S. Lochbrunner, *J. Am. Chem. Soc.* **2013**, *135*, 18722-18725.
[98] D. B. Hibbert, P. Thordarson, *Chem. Comm.* **2016**, *52*, 12792-12805.
[99] N. P. Kazmierczak, J. A. Chew, D. A. Vander Griend, *Anal. Chim. Acta* **2022**, *1227*, 339834.
[100] P. Thordarson, http://supramolecular.org/, 23.01.2024.
[101] D.A. Vander Griend, M. Vermeer, M. Greeley, Y. Kim, N. Wang, D. Buist, C. Ulry, http://sivvu.org/, 23.01.2024.
[102] L. Alderighi, P. Gans, A. Ienco, D. Peters, A. Sabatini, A. Vacca, *Coord. Chem. Rev.* **1999**, *184*, 311-318.
[103] Origin(Pro), Version 2020. OriginLab Corporation, Northampton, MA, USA.
[104] L. Sooväli, E.-I. Rõõm, A. Kütt, I. Kaljurand, I. Leito, *Accred. Qual. Assur.* **2006**, *11*, 246-255.
[105] https://www.originlab.com/doc/en/Origin-Help/Interpret-Regression-Result, 11.01.2024.
[106] H. H. Ku, *J. Res. Natl. Bur. Stand.* **1966**, *70*.
[107] A. V. Kulinich, A. A. Ishchenko, *Chem. Rec.* **2023**, e202300262.
[108] S. Beckmann, K.-H. Etzbach, P. Krämer, K. Lukaszuk, R. Matschiner, A. J. Schmidt, P. Schuhmacher, R. Sens, G. Seybold, R. Wortmann, F. Würthner, *Adv. Mater.* **1999**, *11*, 536-541.
[109] N. M. Kronenberg, M. Deppisch, F. Würthner, H. W. A. Lademann, K. Deing, K. Meerholz, *Chem. Commun.* **2008**, 6489-6491.
[110] C. Reichardt, *Chem. Rev.* **1994**, *94*, 2319-2358.
[111] L. G. Brooker, A. C. Craig, D. W. Heseltine, P. W. Jenkins, L. L. Lincoln, *J. Am. Chem. Soc.* **1965**, *87*, 2443-2450.
[112] T. Takada, K. Nishida, Y. Honda, A. Nakano, M. Nakamura, S. Fan, K. Kawai, M. Fujitsuka, K. Yamana, *ChemBioChem* **2021**, *22*, 2729-2735.
[113] C. J. MacNevin, D. Gremyachinskiy, C.-W. Hsu, L. Li, M. Rougie, T. T. Davis, K. M. Hahn, *Bioconjugate Chem.* **2013**, *24*, 215-223.
[114] F. Sieber, *Photochem. Photobiol.* **1987**, *46*, 1035-1042.
[115] H. Mustroph, *Physical Sciences Reviews* **2022**, *7*, 143-158.
[116] F. Würthner, R. Wortmann, K. Meerholz, *ChemPhysChem* **2002**, *3*, 17-31.
[117] H. Mustroph, *Physical Sciences Reviews* **2019**, *4*.
[118] H. Bürckstümmer, E. V. Tulyakova, M. Deppisch, M. R. Lenze, N. M. Kronenberg, M. Gsänger, M. Stolte, K. Meerholz, F. Würthner, *Angew. Chem. Int. Ed.* **2011**, *50*, 11628-11632.

[119] A. Arjona-Esteban, J. Krumrain, A. Liess, M. Stolte, L. Huang, D. Schmidt, V. Stepanenko, M. Gsänger, D. Hertel, K. Meerholz, F. Würthner, *J. Am. Chem. Soc.* **2015**, *137*, 13524-13534.
[120] F. Würthner, S. Yao, *Angew. Chem. Int. Ed.* **2000**, *39*, 1978-1981.
[121] A. S. Davydov, *Sov. Phys. Uspekhi* **1964**, *7*, 145.
[122] M. Kasha, H. R. Rawls, M. A. El-Bayoumi, *Pure Appl. Chem.* **1965**, *11*, 371-392.
[123] L. Kleine-Kleffmann, A. Schulz, V. Stepanenko, F. Würthner, *Angew. Chem. Int. Ed.* **2023**, *62*, e202314667.
[124] M. Kussler, H. Balli, *Helv. Chim. Acta* **1989**, *72*, 17-28.
[125] L. Wolthaus, A. Schaper, D. Möbius, *Chem. Phys. Lett.* **1994**, *225*, 322-326.
[126] K. Takeyuki, I. Kaoru, *Thin Solid Films* **1990**, *191*, 173-191.
[127] A. Liess, A. Lv, A. Arjona-Esteban, D. Bialas, A.-M. Krause, V. Stepanenko, M. Stolte, F. Würthner, *Nano Lett.* **2017**, *17*, 1719-1726.
[128] N. J. Hestand, F. C. Spano, *Chem. Rev.* **2018**, *118*, 7069-7163.
[129] X. Hu, J. O. Lindner, F. Würthner, *J. Am. Chem. Soc.* **2020**, *142*, 3321-3325.
[130] K. Dimroth, C. Reichardt, T. Siepmann, F. Bohlmann, *Liebigs. Ann.* **1963**, *661*, 1-37.
[131] W. Liptay, *Z. Naturforschg.* **1965**, *20a*, 1441-1471.
[132] A. Lohr, S. Uemura, F. Würthner, *Angew. Chem. Int. Ed.* **2009**, *48*, 6165-6168.
[133] B. Liu, Y. Vonhausen, A. Schulz, C. Höbartner, F. Würthner, *Angew. Chem. Int. Ed.* **2022**, *61*, e202200120.
[134] G. Fernández, M. Stolte, V. Stepanenko, F. Würthner, *Chem. Eur. J.* **2013**, *19*, 206-217.
[135] A. Lohr, T. Gress, M. Deppisch, M. Knoll, F. Würthner, *Synthesis* **2007**, *2007*, 3073-3082.
[136] F. Würthner, S. Yao, U. Beginn, *Angew. Chem. Int. Ed.* **2003**, *42*, 3247-3250.
[137] A. Lohr, M. Lysetska, F. Würthner, *Angew. Chem. Int. Ed.* **2005**, *44*, 5071-5074.
[138] A. Lohr, F. Würthner, *Angew. Chem. Int. Ed.* **2008**, *47*, 1232-1236.
[139] A. Lohr, F. Würthner, *Chem. Commun.* **2008**, 2227-2229.
[140] L. K. von Krbek, C. A. Schalley, P. Thordarson, *Chem. Soc. Rev.* **2017**, *46*, 2622-2637.
[141] H. L. Anderson, C. A. Hunter, M. N. Meah, J. K. Sanders, *J. Am. Chem. Soc.* **1990**, *112*, 5780-5789.
[142] Z. Chen, B. Fimmel, F. Würthner, *Org. Biomol. Chem.* **2012**, *10*, 5845-5855.
[143] M. F. J. Mabesoone, A. J. Markvoort, M. Banno, T. Yamaguchi, F. Helmich, Y. Naito, E. Yashima, A. R. A. Palmans, E. W. Meijer, *J. Am. Chem. Soc.* **2018**, *140*, 7810-7819.
[144] N. Ponnuswamy, G. D. Pantoş, M. M. J. Smulders, J. K. M. Sanders, *J. Am. Chem. Soc.* **2012**, *134*, 566-573.
[145] V. Dehm, M. Büchner, J. Seibt, V. Engel, F. Würthner, *Chem. Sci.* **2011**, *2*, 2094-2100.
[146] Y. Vonhausen, A. Lohr, M. Stolte, F. Würthner, *Chem. Sci.* **2021**, *12*, 12302-12314.
[147] F. Würthner, K. Meerholz, *Chem. Eur. J.* **2010**, *16*, 9366-9373.
[148] D. Bialas, C. Zhong, F. Würthner, F. C. Spano, *J. Phys. Chem. C* **2019**, *123*, 18654-18664.
[149] A. Rajak, A. Das, *ACS Polym. Au* **2022**, *2*, 223-231.
[150] S. Yao, U. Beginn, T. Gress, M. Lysetska, F. Würthner, *J. Am. Chem. Soc.* **2004**, *126*, 8336-8348.
[151] D. McPhail, A. Cooper, *J. Chem. Soc., Faraday Trans.* **1997**, *93*, 2283-2289.
[152] M. Lovatt, A. Cooper, P. Camilleri, *Eur. Biophys. J.* **1996**, *24*, 354-357.
[153] J. D. Chodera, D. L. Mobley, *Annu. Rev. Biophys.* **2013**, *42*, 121-142.

[154] F. Biedermann, W. M. Nau, H.-J. Schneider, *Angew. Chem. Int. Ed.* **2014**, *53*, 11158-11171.
[155] L. Escobar, P. Ballester, *Chem. Rev.* **2021**, *121*, 2445-2514.
[156] T. Brixner, R. Hildner, J. Köhler, C. Lambert, F. Würthner, *Adv. Energy Mater.* **2017**, *7*, 1700236.
[157] B.-K. An, J. Gierschner, S. Y. Park, *Acc. Chem. Res.* **2012**, *45*, 544-554.
[158] M. B. Smith, J. Michl, *Chem. Rev.* **2010**, *110*, 6891-6936.
[159] S. Bhosale, A. L. Sisson, P. Talukdar, A. Fürstenberg, N. Banerji, E. Vauthey, G. Bollot, J. Mareda, C. Röger, F. Würthner, N. Sakai, S. Matile, *Science* **2006**, *313*, 84-86.
[160] R. Bhosale, J. Míšek, N. Sakai, S. Matile, *Chem. Soc. Rev.* **2010**, *39*, 138-149.
[161] C. Kaufmann, W. Kim, A. Nowak-Król, Y. Hong, D. Kim, F. Würthner, *J. Am. Chem. Soc.* **2018**, *140*, 4253-4258.
[162] P. G. A. Janssen, J. Vandenbergh, J. L. J. van Dongen, E. W. Meijer, A. P. H. J. Schenning, *J. Am. Chem. Soc.* **2007**, *129*, 6078-6079.
[163] Y. Yamauchi, M. Yoshizawa, M. Fujita, *J. Am. Chem. Soc.* **2008**, *130*, 5832-5833.
[164] M. J. Ahrens, R. F. Kelley, Z. E. X. Dance, M. R. Wasielewski, *Phys. Chem. Chem. Phys.* **2007**, *9*, 1469-1478.
[165] J. E. Bullock, R. Carmieli, S. M. Mickley, J. Vura-Weis, M. R. Wasielewski, *J. Am. Chem. Soc.* **2009**, *131*, 11919-11929.
[166] X. Li, L. E. Sinks, B. Rybtchinski, M. R. Wasielewski, *J. Am. Chem. Soc.* **2004**, *126*, 10810-10811.
[167] F. Su, G. Chen, P. A. Korevaar, F. Pan, H. Liu, Z. Guo, A. P. H. J. Schenning, H.-J. Zhang, J. Lin, Y.-B. Jiang, *Angew. Chem. Int. Ed.* **2019**, *58*, 15273-15277.
[168] B. M. Rosen, C. J. Wilson, D. A. Wilson, M. Peterca, M. R. Imam, V. Percec, *Chem. Rev.* **2009**, *109*, 6275-6540.
[169] F. Würthner, *Synthesis* **1999**, *12*, 2103-2113.
[170] A. Eisfeld, J. S. Briggs, *Chem. Phys.* **2006**, *324*, 376-384.
[171] F. Gołek, P. Mazur, Z. Ryszka, S. Zuber, *Appl. Surf. Sci.* **2014**, *304*, 11-19.
[172] D. J. Keller, F. S. Franke, *Surf. Sci.* **1993**, *294*, 409-419.
[173] N. Harada, K. Nakanishi, *Acc. Chem. Res.* **1972**, *5*, 257-263.
[174] J. Luo, Z. Xie, J. W. Y. Lam, L. Cheng, H. Chen, C. Qiu, H. S. Kwok, X. Zhan, Y. Liu, D. Zhu, B. Z. Tang, *Chem. Commun.* **2001**, 1740-1741.
[175] B.-K. An, S.-K. Kwon, S.-D. Jung, S. Y. Park, *J. Am. Chem. Soc.* **2002**, *124*, 14410-14415.
[176] G. Scheibe, *Angew. Chem.* **1937**, *50*, 212-219.
[177] J. Gierschner, L. Lüer, B. Milián-Medina, D. Oelkrug, H.-J. Egelhaaf, *J. Phys. Chem. Lett.* **2013**, *4*, 2686-2697.
[178] Y. Ren, J. W. Y. Lam, Y. Dong, B. Z. Tang, K. S. Wong, *J. Phys. Chem. B* **2005**, *109*, 1135-1140.
[179] F. Würthner, *Angew. Chem. Int. Ed.* **2020**, *59*, 14192-14196.
[180] U. Rösch, S. Yao, R. Wortmann, F. Würthner, *Angew. Chem. Int. Ed.* **2006**, *45*, 7026-7030.
[181] F. Würthner, R. Sens, K. H. Etzbach, G. Seybold, *Angew. Chem. Int. Ed.* **1999**, *38*, 1649-1652.
[182] H. Ephardt, P. Fromherz, *J. Phys. Chem. Lett.* **1989**, *93*, 7717-7725.
[183] R. Khairutdinov, N. Serpone, *J. Phys. Chem. B* **1997**, *101*, 2602-2610.
[184] V. Karunakaran, J. L. Pérez Lustres, L. Zhao, N. P. Ernsting, O. Seitz, *J. Am. Chem. Soc.* **2006**, *128*, 2954-2962.

[185] J. Hoche, A. Schulz, L. M. Dietrich, A. Humeniuk, M. Stolte, D. Schmidt, T. Brixner, F. Würthner, R. Mitric, *Chem. Sci.* **2019**, *10*, 11013-11022.
[186] Z. Guo, C. Yan, W.-H. Zhu, *Angew. Chem. Int. Ed.* **2020**, *59*, 9812-9825.
[187] T. Kim, S. Kang, E. Kirchner, D. Bialas, W. Kim, F. Würthner, D. Kim, *Chem* **2021**, *7*, 715-725.
[188] E. M. Sánchez-Carnerero, A. R. Agarrabeitia, F. Moreno, B. L. Maroto, G. Muller, M. J. Ortiz, S. de la Moya, *Chem. Eur. J.* **2015**, *21*, 13488-13500.
[189] M. Inouye, K. Hayashi, Y. Yonenaga, T. Itou, K. Fujimoto, T.-a. Uchida, M. Iwamura, K. Nozaki, *Angew. Chem. Int. Ed.* **2014**, *53*, 14392-14396.
[190] J. Kumar, T. Nakashima, T. Kawai, *J. Phys. Chem. Lett.* **2015**, *6*, 3445-3452.
[191] S. Hu, L. Hu, X. Zhu, Y. Wang, M. Liu, *Angew. Chem. Int. Ed.* **2021**, *60*, 19451-19457.
[192] Y. Inai, M. Sisido, Y. Imanishi, *J. Phys. Chem.* **1990**, *94*, 2734-2735.
[193] S. Grimme, J. Antony, S. Ehrlich, H. Krieg, *J. Chem. Phys.* **2010**, *132*, 154104.
[194] F. Weigend, R. Ahlrichs, *Phys. Chem. Chem. Phys.* **2005**, *7*, 3297-3305.
[195] Gaussian 16, Revision A.03, M. J. Frisch, G. W. Trucks, H. B. Schlegel, G. E. Scuseria, M. A. Robb, J. R. Cheeseman, G. Scalmani, V. Barone, G. A. Petersson, H. Nakatsuji, X. Li, M. Caricato, A. V. Marenich, J. Bloino, B. G. Janesko, R. Gomperts, B. Mennucci, H. P. Hratchian, J. V. Ortiz, A. F. Izmaylov, J. L. Sonnenberg, D. Williams-Young, F. Ding, F. Lipparini, F. Egidi, J. Goings, B. Peng, A. Petrone, T. Henderson, D. Ranasinghe, V. G. Zakrzewski, J. Gao, N. Rega, G. Zheng, W. Liang, M. Hada, M. Ehara, K. Toyota, R. Fukuda, J. Hasegawa, M. Ishida, T. Nakajima, Y. Honda, O. Kitao, H. Nakai, T. Vreven, K. Throssell, J. A. Montgomery, Jr., J. E. Peralta, F. Ogliaro, M. J. Bearpark, J. J. Heyd, E. N. Brothers, K. N. Kudin, V. N. Staroverov, T. A. Keith, R. Kobayashi, J. Normand, K. Raghavachari, A. P. Rendell, J. C. Burant, S. S. Iyengar, J. Tomasi, M. Cossi, J. M. Millam, M. Klene, C. Adamo, R. Cammi, J. W. Ochterski, R. L. Martin, K. Morokuma, O. Farkas, J. B. Foresman, and D. J. Fox, Gaussian, Inc., Wallingford CT, 2016.
[196] S. Miertuš, E. Scrocco, J. Tomasi, *Chem. Phys.* **1981**, *55*, 117-129.
[197] S. Miertuš, J. Tomasi, *Chem. Phys.* **1982**, *65*, 239-245.
[198] J. L. Pascual-ahuir, E. Silla, I. Tuñon, *J. Comput. Chem.* **1994**, *15*, 1127-1138.
[199] GaussView, Version 6.0.16, Roy Dennington, Todd A. Keith, and John M. Millam, Semichem Inc., Shawnee Mission, KS, 2016.
[200] V. Percec, C. H. Ahn, T. K. Bera, G. Ungar, D. J. Yeardley, *Chem. Eur. J.* **1999**, *5*, 1070-1083.
[201] J. Wang*, Vol. CN104263797*, CN104263801A, China, **2015**.
[202] C. K. Zeberg-Mikkelsen, M. Barrouhou, A. Baylaucq, C. Boned, *High Temp. High Press.* **2002**, *34*, 591-601.
[203] G. Seybold, G. Wagenblast, *Dyes Pigm.* **1989**, *11*, 303-317.
[204] J. J. Stewart, *J. Mol. Model.* **2013**, *19*, 1-32.
[205] MOPAC2016, Version: 18.346, J. J. P. Stewart, Stewart Computational Chemistry, Colorado Springs, CO, USA, 2016.
[206] J.-D. Chai, M. Head-Gordon, *J. Chem. Phys.* **2008**, *128*, 084106.
[207] R. Dennington, T. Keith, J. Millam, GaussView, Version 5 (Semichem Inc.), 2009.

INDIVIDUAL CONTRIBUTIONS

The co-authors of the manuscripts included in this thesis are informed and agree with the reprint and the respective individual contributions as stated below.

Two-step anti-cooperative self-assembly process into defined π-stacked dye oligomers: insights into aggregation-induced enhanced emission

Y. Vonhausen, A. Lohr, M. Stolte, F. Würthner, *Chem. Sci.* **2021**, *12*, 12302-12314.

Autor	**Y.V.**	**A.L.**	**M.S.**	**F.W.**	∑
Design of research/Conception	1%	1%		2%	4%
Synthesis and general compound characterization	2%	3%			5%
Self-assembly studies and data evaluation	41%	13%	3%		57%
Characterization of optical properties	8%		2%		10%
Theoretical calculations	5%				5%
Publication writing	8%	2%			10%
Publication correction			2%	4%	6%
Publication coordination			1%	2%	3%
Summe	65%	19%	8%	8%	100%

Concentration-, Temperature- and Solvent-Dependent Self-Assembly: Merocyanine Dimerization as a Showcase Example for Obtaining Reliable Thermodynamic Data.

Y. Vonhausen, F. Würthner, *Chem. Eur. J.* **2023**, *29*, e202300359.

Autor	**Y.V.**	**F.W.**	∑
Design of research	3%	7%	10%
Experimental studies	35%		35%
Data evaluation	35%		35%
Publication writing	10%		10%
Publication correction		5%	5%
Publication coordination		5%	5%
Summe	83%	17%	100%

DANKSAGUNG

Mein besonderer Dank gilt meinem Doktorvater **Prof. Dr. Frank Würthner**, für die Möglichkeit zur Anfertigung dieser Arbeit unter hervorragenden Bedingungen. Vielen Dank für das entgegengebrachte Vertrauen und die damit verbundenen Freiheiten in der Bearbeitung der Themenstellung. Danke für die Unterstützung in konstruktiven Diskussionen, die Hilfe beim Verfassen von Manuskripten, die Möglichkeit zur Teilnahme an Konferenzen und Fortbildungen, sowie die Bereitstellung einer exzellenten Laborinfrastruktur. Es war eine Freude, diese vielseitige Arbeit in Deiner Gruppe anzufertigen.

Weiterhin möchte ich mich bei **Dr. Matthias Stolte** bedanken, für seine Begeisterung und Unterstützung bei vielen meiner Projekte. Ein Vorbeischauen, um etwas zu besprechen hat sich immer gelohnt. Vielen Dank für alles!

Bei **Dr. Matthias Stolte** möchte ich mich außerdem für die gewissenhafte Einarbeitung in die Spektroskopie bedanken. **Dr. David Bialas**, **Dr. Menyhárt Sárosi** und **Niyas Mundakkamattathil Abdul Salam** danke ich für die Einarbeitung und hilfreiche Diskussionen zu quantenmechanischen Rechnungen. **Dr. Kazutaka Shoyama** und **Olga Anhalt** möchte ich, wenn auch nicht Teil dieser Arbeit, trotzdem ganz herzlich für die Unterstützung bei der Einarbeitung in die Kristallographie danken.

Prof. Dr. Ann-Christin Pöppler, **Sebastian Endres** und **Dr. Matthias Grüne**, danke ich für die Diskussionen und Hilfestellungen zu NMR bezogenen Fragestellungen. **Patricia Altenberger** und **Stefanie Schmitt** danke ich für die Messungen am 600 MHz NMR Spektrometer und den reibungslosen Ablauf an den 400 MHz Spektrometern. **Dr. Juliane Adelmann** danke ich für die massenspektrometrischen Untersuchungen.

Vielen Dank an **Dr. Vladimir Stepanenko** für die Mikroskopie-Aufnahmen.

Allen technischen Angestellten des Arbeitskreises, insbesondere **Petra Seufert-Baumbach**, **Anja Rausch**, **Julius Albert**, **Maximilian Roth**, **Astrid Kudzus** und **Olga Anhalt** möchte ich für die Organisation des reibungslosen Laboralltags und die angenehme Arbeitsatmosphäre im vierten Stock und im CNC danken. Danke, dass ihr immer darauf

achtet, dass der Laden rund läuft. Vielen Dank auch an **Sarah Bullnheimer** und **Jennifer Begall** für die große Hilfe bei administrativen und organisatorischen Fragestellungen.

Stefanie Klisch, **Eugen Khitro**, **Franziska Endres**, **Florian Zeilinger**, **Andreas Sachs** und **Anna Fleck**, die ich im Rahmen von Praktika betreuen durfte, sowie der Auszubildenden **Paula Roth** und meiner Bachelor-Studentin **Sira Grätz**, danke ich für die Unterstützung bei Synthese und Spektroskopie.

Für das Korrekturlesen von Teilen dieser Arbeit danke ich **Dr. Matthias Stolte**, **Felix Brust**, **Lara Kleine-Kleffmann**, **Jessica Rühe**, **Dr. Alexander Schulz** und **Michael Wagenhäuser**.

Beim gesamten **Arbeitskreis Würthner** möchte ich mich für die Unterstützung und gute Unterhaltung bedanken und, insbesondere bei der **Laufgruppe**, für den Ausgleich zur Arbeit. Die Doktorarbeit ist ein Marathon, danke für die tolle Zeit.

Der letzte Dank geht an **Freunde** und meine **Familie** für den Rückhalt, ihr Verständnis und die Unterstützung bei diesem, wie auch bei anderen Projekten.

LIST OF PUBLICATIONS

Concentration-, Temperature- and Solvent-Dependent Self-Assembly: Merocyanine Dimerization as a Showcase Example for Obtaining Reliable Thermodynamic Data
Y. Vonhausen, F. Würthner, *Chem. Eur. J.* **2023**, *29*, e202300359.

Peptide Backbone Directed Self-Assembly of Merocyanine Oligomers into Duplex Structures
B. Liu, Y. Vonhausen, A. Schulz, C. Höbartner, F. Würthner, *Angew. Chem. Int. Ed.* **2022**, *61*, e202200120.

Two-step anti-cooperative self-assembly process into defined π-stacked dye oligomers: insights into aggregation-induced enhanced emission
Y. Vonhausen, A. Lohr, M. Stolte, F. Würthner, *Chem. Sci.* **2021**, *12*, 12302-12314.

Synthesis, Photophysical and Electronic Properties of New Red-to-NIR Emitting Donor–Acceptor Pyrene Derivatives
J. Merz, M. Dietz, Y. Vonhausen, F. Wöber, A. Friedrich, D. Sieh, I. Krummenacher, H. Braunschweig, M. Moos, M. Holzapfel, C. Lambert, T. B. Marder, *Chem. Eur. J.* **2020**, *26*, 438.

Zwitterion-Functionalized Detonation Nanodiamond with Superior Protein Repulsion and Colloidal Stability in Physiological Media
V. Merz, J. Lenhart; Y. Vonhausen, M. E. Ortiz-Soto, J. Seibel, A. Krueger, *Small* **2019**, *15*, 1901551.